

Doctoral Thesis

A NOVEL ANTIBACTERIAL SOL-GEL COATING FOR PROSTHETIC DEVICES

Author:

Amaya García Casas

Supervisor:

Dra. Antonia Jiménez Morales

Tutor:

Dra. Antonia Jiménez Morales

Department of Materials Science and Engineering

University Carlos III of Madrid

Leganés, October 2018

Doctoral Thesis

A NOVEL ANTIBACTERIAL SOL-GEL COATING FOR PROSTHETIC DEVICES

Author: Amaya García Casas

Supervisor: Dra. Antonia Jiménez Morales

Signatures of Examining Jury:

Signature

President: Dr. José Manuel Torralba Castelló

Vocal: Dr. Rafael Leiva García

Secretary: Dra. Sandra Carolina Cifuentes Cuéllar

Mark:

Leganés, October 2018

Esta memoria de tesis cumple los requisitos necesarios para obtener la Mención Internacional en el Título de Doctor que se describen en la normativa de enseñanzas universitarias de doctorado de la Universidad Carlos III de Madrid y que han sido establecidos en el artículo 15 del Real Decreto 99/2011 que establece la Ordenación de las Enseñanzas Universitarias Oficiales (BOE nº 35 del 28 de Enero de 2011, Págs. 13909-13926). Dicha Memoria de tesis ha sido informada por dos doctores que pertenecen a instituciones de educación superior internacionales:

Dr. Javier Hidalgo García, Technische Universiteit Delft, Netherlands

Dr. Rafael Leiva García, University of Manchester, United Kingdom

Dedicated to all the female scientists

*“Reserve your right to think, for even to think
wrongly is better than not to think at all”*

Hypatia of Alexandria

Agradecimientos (Acknowledgements)

La Tesis Doctoral ha sido para mí un intenso proceso de aprendizaje y madurez tanto profesional como personalmente. Durante estos cuatro años he tenido la oportunidad de compartir experiencias con varias personas que han contribuido de una forma u otra en este trabajo. Me gustaría dejar a continuación constancia y agradecer a todas estas personas por ello.

En primer lugar, quiero agradecer a mi directora de tesis, Antonia Jiménez, por brindarme la oportunidad de realizar la Tesis Doctoral en un tema tan interesante y complejo como lo es la tecnología sol-gel. Toñi, tengo que agradecerte toda la confianza que depositaste en mí desde el principio. Gracias por hacer más fácil este camino y por estar siempre disponible para transmitirme tus conocimientos. Gracias por las palabras de ánimo, por la comprensión y por la libertad que me has dado en todo momento.

Quiero agradecer también a la persona que me inició en las pericias de la investigación. Diógenes Carbonell, gracias por convencerme para iniciar una carrera en investigación. Gracias por enseñarme todo lo que sabías sobre el sol-gel.

Me gustaría agradecer a todos los integrantes del Grupo de Tecnología de Polvos de la Universidad Carlos III de Madrid por el tiempo que he compartido con ellos durante estos años. Gracias a Elena, José Manuel, Mónica, Elisa, Maru, Sophia, Paula, Sandra y Juan. Eva y Susana, gracias por vuestra paciencia. Gracias a los veteranos con los que pude compartir el inicio de la tesis y de los que tanto aprendí cuando estaban en sus respectivas etapas de escritura: a Javier por ser un ejemplo de motivación; a los García, Nerea y Roberto; a las chicas MIM, Alicia y Carolina; a Elena y Julia. Beatriz, gracias por ser una gran confidente y compañera de “las causas perdidas”. Eric, indiscutible compañero de batallas en la UC3M, muchas gracias por tu incondicional apoyo, por tus conversaciones y por tu amistad. Eres un investigador excelente. Estela, la reina del despacho 1.1A09, gracias por escucharme. Eres una luchadora con una energía desbordante y envidiable. Andrea, sucesora del legado sol-gel, gracias por los momentos compartidos en el laboratorio. Siempre tendremos dudas sobre el sol-gel pero compartirlas contigo lo ha hecho todo más llevadero. También me gustaría agradecer a mis compañeras y compañeros del Departamento de Ciencia e Ingeniería de Materiales. Gracias Cristina por todas las horas dedicadas en el microscopio. Lucía y Javier, gracias por vuestras *Master class* en orgánica. ¡Sois unos cracks!. Natalia, gracias por ser mi aliada en el frente de combate feminista. Jorge, gracias por transmitirme tu pasión científica y por tu claridad al definir conceptos. Andrés, gracias por ilustrarme con tus desbordantes datos. María (Nico) y Alberto, gracias por robarme siempre una sonrisa. Caterina y Eduardo, gracias por los “breaks” compartidos durante la última etapa. Gracias también a Marta Cartón, Carmen, Gleidys, Raquel, Morena, Nieves, Andrea Galán, Pedro, María Fernández, Marta González, Guillermo, Sara y Yahya.

I would like to thank Professor Digby D. Macdonald from the Department of Materials Science and Engineering of the University of Berkeley (United States) for the opportunity he gave me to join his team and learn the main theoretical aspects of the Electrochemical Impedance Spectroscopy. I would like also to express my gratitude to Pin Lu for the time he spent with me in the Lab.

También quiero agradecer a la Dra. Yaiza González-García del Department of Materials Science and Engineering of the Delft University of Technology (The Netherlands) su acogida durante la estancia que realicé en sus laboratorios de corrosión localizada. Gracias por todo el esfuerzo dedicado y por ayudarme a comprender mejor el complejo campo de la electroquímica.

Del Departamento de Microbiología Clínica de la Fundación Jiménez Díaz quiero agradecer al Dr. Jaime Esteban y al Dr. John J. Aguilera el tiempo dedicado en la realización de los ensayos microbiológicos. Ha sido un placer trabajar con vosotros y espero que la colaboración iniciada siga dando tan buenos frutos como hasta ahora.

Quiero dedicar un cariñoso agradecimiento a mi familia. Gracias a mis padres por creer siempre en mí y por apoyarme incondicionalmente en todo momento. Sois mi referente. Gracias a mis hermanos, Santiago y Nerea.

Me gustaría también agradecer a la cuadrilla de Pamplona por todos estos años de amistad y en especial a mi núcleo fuerte: Alba, Arantxa y Cristina, gracias por compartir conmigo durante estos años los momentos más importantes a pesar de la distancia.

Durante esta etapa en Madrid he compartido vivencias con muchas personas. Gracias a todas ellas por los momentos vividos. Con especial cariño quiero agradecer a Ruth su inestimable ayuda y amistad durante todos estos años. También quiero agradecer a Andrea su apoyo y por hacerme reflexionar en tantas cosas. Gracias por ser mi familia en Madrid.

Y para terminar quería recordar la frase de una persona maravillosa que me hizo volver a la montaña. Gracias Raúl, nunca he conocido a nadie que transmita con tanta fuerza una pasión. Y es que, “si Mahoma no va a la montaña, ya va Raúl” (09/02/2017).

Preface

This Doctoral Thesis has been developed in the Group of Powder Technology (GTP) at the Department of Materials Science and Engineering and Chemical Engineering of the University Carlos III of Madrid (UC3M) from October 2014 to September 2018. The structure of this work consists of:

- 1) An introduction with the main problems associated with prosthetic joint infections and the current strategies employed to overcome this issue. The introduction also contains a section dedicated to the sol-gel methodology and another one, to the electrochemical techniques
- 2) The motivation and partial objectives to accomplish the main goal
- 3) The experimental work and the employed techniques in this work
- 4) The results of the Doctoral Thesis, which have been divided in three chapters: characterization of the metallic substrate, sol-gel synthesis and electrochemical characterization
- 5) The main conclusions
- 6) A perspective of future lines of research

The results of the Doctoral Thesis have generated a national patent:

Authors: A. Jimenez-Morales, A. Garcia-Casas, J. Esteban, JJ. Aguilera-Correa.

Title: Procedimiento para la obtención de un recubrimiento sol-gel, composición de recubrimiento y uso de la misma

Application number: P201730628

Application date: 19/04/2017

Country: Spain

Titular entities: University Carlos III of Madrid and IIS-Foundation Jimenez Diaz

The following papers have been published during the accomplishment of this Doctoral Thesis:

2. A. Alcantara-Garcia, A. Garcia-Casas, A. Jiménez-Morales, “Electrochemical study of the synergic effect of phosphorus and cerium additions on a sol-gel coating for Titanium manufactured by powder metallurgy”, *Progress in Organic Coatings*, vol. 124, pp. 267–274, **2018**. DOI:10.1016/j.porgcoat.2018.01.026
1. D.J. Carbonell, A. Garcia-Casas, J. Izquierdo, R.M. Souto, J.C. Galván, A. Jiménez-Morales, “Scanning Electrochemical Microscopy characterization of sol-gel coatings applied on AA2024-T3 substrate for corrosion protection”, *Corrosion Science*, vol. 111, pp. 625–636, **2016**. DOI: 10.1016/j.corsci.2016.06.002

This Doctoral Thesis has also contributed to national and international conferences:

11. A. Garcia-Casas, J.J. Aguilera-Correa, A. Mediero, J. Esteban, Y. Gonzalez-Garcia and A. Jiménez-Morales. "A novel osseostimulating and antibacterial sol-gel coating for prosthetic devices". **Oral communication**. XV Congreso Nacional de Materiales (I Iberian Meeting on Materials Science). Salamanca (Spain), July **2018**
10. J.J. Aguilera Correa, A. Garcia-Casas, D. Romera García, A. Jimenez-Morales and J. Esteban. "Eradication of bacterial biofilm treated with moxifloxacin-loaded hybrid organo-inorganic sol-gel coating". **Oral communication**. 22th Congress of Spanish Society of Clinical Microbiology and Infectious Diseases. Bilbao (Spain), May **2018**
9. J.J. Aguilera-Correa, A. Garcia-Casas, D. Romera, A. Jimenez-Morales and J. Esteban. "Eradication of bacterial biofilm treated with moxifloxacin-loaded hybrid organo-inorganic sol-gel coating". **Poster**. 28th ECCMID, European Congress of Clinical Microbiology and Infectious Diseases. Madrid (Spain), April **2018**
8. A. Jiménez-Morales, A. Garcia-Casas, J.J. Aguilera-Correa, J. Esteban and Y. Gonzalez-Garcia. "A novel antibacterial sol-gel coating for prosthetic devices". **Oral communication**. BIOMAT, VII Congreso Internacional De Biomateriales. La Habana (Cuba), March 2018
7. A. Garcia-Casas, J.J. Aguilera-Correa, E. Gordo, J. Esteban, Y. Gonzalez-Garcia and A. Jiménez-Morales. "A comparative electrochemical and bacteria adherence study of Ti manufactured by powder metallurgy and Ti64 alloy". **Oral communication**. EUROCORR, European Corrosion Congress. Prague (Czech Republic), September **2017**
6. A. Garcia-Casas, J.J. Aguilera-Correa, A. Alcantara-Garcia, J. Esteban Y. Gonzalez-Garcia and A. Jiménez-Morales. "Estudio electroquímico de un recubrimiento biodegradable y antibacteriano de tipo sol-gel sobre titanio pulvimetalúrgico". **Oral communication**. VI Congreso de Pulvimetalurgia, Ciudad Real (Spain), June **2017**
5. A. Garcia-Casas, J.J. Aguilera-Correa, J. Esteban Y. Gonzalez-Garcia and A. Jiménez-Morales. "*In situ* monitoring of the degradation of a sol-gel coating doped with an antibiotic by SECM". **Oral communication**. Aetoc, Münster (Germany), April **2017**
4. JJ. Aguilera-Correa, A. Garcia-Casas, A. Jimenez-Morales, and J. Esteban. "Staphylococcus aureus 15981 adherence decrease on hybrid organo-inorganic sol-gel coating". **Poster**. EORS Bolonia (Italy), September **2016**
3. A. Garcia-Casas, A. Alcántara and A. Jiménez-Morales. "Optimization of the process parameters of a hybrid organo-inorganic sol-gel coating synthesis for biomedical P/M titanium". **Oral communication**. Junior Euromat 2016, Lausanne (Switzerland), July **2016**

2. A. Garcia-Casas, A. Alcántara, P. Lu, D. D. Macdonald, and A. Jiménez-Morales. “Design and corrosion study of a hybrid organo-inorganic sol-gel coating for biomedical P/M titanium”. **Oral communication**. XIV Congreso Nacional de Materiales 2016, Gijón (Spain), June **2016**

1. A. García-Casas, E. Gordo and A. Jiménez-Morales. “Design and corrosion study of a hybrid organo-inorganic sol-gel coating for biomedical P/M titanium”. **Oral communication**. Advances in Materials and Processing Technologies (AMPT) 2015, Madrid (Spain), December **2015**

Contents

ABSTRACT.....	1
RESUMEN.....	2
1. INTRODUCTION	5
1.1. BIOMATERIALS.....	5
1.2. PROSTHETIC JOINT INFECTIONS	7
1.3. SURFACE MODIFICATIONS AND COATINGS.....	13
1.4. SOL-GEL TECHNOLOGY.....	16
1.5. ELECTROCHEMICAL TECHNIQUES	19
REFERENCES♣.....	27
2. MOTIVATION AND OBJECTIVES.....	37
2.1 MOTIVATION.....	37
2.2 OBJECTIVES.....	38
REFERENCES.....	39
3. EXPERIMENTAL WORK.....	43
3.1 MATERIALS.....	44
3.2 SYNTHESIS CHARACTERIZATION.....	46
3.3 XEROGEL CHARACTERIZATION	46
3.4 SURFACE CHARACTERIZATION.....	47
3.5 ELECTROCHEMICAL CHARACTERIZATION.....	48
3.6 BIOLOGICAL CHARACTERIZATION.....	50
3.7 CHARACTERIZATION OF THE ANTIBIOTIC RELEASE.....	56
REFERENCES.....	57
4. CHARACTERIZATION OF THE METALLIC SUBSTRATE.....	61
ABSTRACT.....	61
4.1 MATERIALS.....	63
4.2 SURFACE CHARACTERIZATION.....	63
4.3 ELECTROCHEMICAL CHARACTERIZATION.....	65
4.4 MICROBIOLOGICAL STUDY.....	74
4.5 CONCLUSIONS.....	76
REFERENCES.....	77
5. SOL-GEL SYNTHESIS.....	81
ABSTRACT.....	81
5.1 OPTIMIZATION OF THE REFERENCE SOL-GEL COATING.....	83
5.1.1 TAGUCHI METHOD.....	83
5.1.2 CHARACTERIZATION OF THE SYNTHESIS OF SOLS.....	85
5.1.3 CHARACTERIZATION OF THE XEROGEL.....	89
5.1.4 SURFACE CHARACTERIZATION OF COATINGS.....	91
5.1.5 ELECTROCHEMICAL CHARACTERIZATION.....	92
5.1.6 CONCLUSIONS.....	97
5.2 BIO-FUNCTIONALIZATION OF SOL-GEL COATINGS WITH PHOSPHORUS-BASED COMPOUNDS.....	98
5.2.1 MATERIALS.....	98

5.2.2	CHARACTERIZATION OF THE SYNTHESIS OF SOLS.....	98
5.2.3	SURFACE CHARACTERIZATION.....	100
5.2.4	CHARACTERIZATION OF THE XEROGEL	101
5.2.5	CELLULAR STUDY	105
5.2.6	CONCLUSIONS	108
5.3	BIO-FUNCTIONALIZATION OF SOL-GEL COATINGS WITH MOXIFLOXACIN	109
5.3.1	MATERIALS.....	109
5.3.2	CHARACTERIZATION OF THE SYNTHESIS OF SOLS.....	109
5.3.3	CHARACTERIZATION OF THE XEROGEL	111
5.3.4	SURFACE CHARACTERIZATION.....	112
5.3.5	CELLULAR STUDY	115
5.3.6	CONCLUSIONS	117
	REFERENCES.....	118
6.	ELECTROCHEMICAL CHARACTERIZATION	122
	ABSTRACT	122
6.1	MATERIALS.....	124
6.2	ELECTROCHEMICAL CHARACTERIZATION.....	125
6.3	MICROBIOLOGICAL AND CELLULAR STUDY.....	139
6.4	CONCLUSIONS	143
	REFERENCES.....	144
7.	CONCLUSIONS	148
8.	FUTURE PERSPECTIVES.....	152

ABSTRACT

This Doctoral Thesis deals with the design and development of novel coatings manufactured by sol-gel technology to prevent and treat bacterial infections associated to joint prostheses. The risk of bacterial infections during the implantation of prostheses causes devastating repercussions for the patients. These bacterial infections are commonly treated systemically with the administration of antimicrobials that are somehow inefficient to locally counteract the focus of infection. Instead, local therapies are being studied because they can reach the biomaterial-tissue interface. This research project is addressed to locally overcome the risk of contracting infections by using a biodegradable sol-gel coating as carrier of an antimicrobial.

The multifunctional coating consists of two organopolysiloxanes, as the precursors of the sol-gel network, with the ability to degrade in 24 hours in contact with a physiological solution. The degradation of the coating will allow the release of the pre-loaded antimicrobial. The coating has been bio-functionalized first with an organophosphite in order to enhance the proliferation of cells during the process of implantation. Then, the selected coating has been loaded with an antibiotic of broad spectrum activity against the pathogens that causes these infections.

The degradation kinetics of the coatings has been evaluated by means of electrochemical techniques using the averaging Electrochemical Impedance Spectroscopy (EIS) and the spatially highly resolved Scanning Electrochemical Microscopy (SECM). The study revealed that the concentration of antibiotic exerted a strong influence in the degrading process, being the coating with the highest amount of antibiotic the coating that has a faster degrading process.

The non-cytotoxicity and the enhancement of the cellular proliferation have been verified with MC3T3-E1 cells. The inhibition of bacterial adhesion (prevention) and mature biofilm growth (treatment) of the main species that causes infection (*S. aureus*, *S. epidermidis* and *E. coli*) have also been confirmed. The release of the antibiotic has been tracked by absorbance spectroscopy and it revealed that the degradation of the coating is non-proportional to the release of antibiotic. Despite the low release of antibiotic to the medium, the quantity has been demonstrated to be enough to inhibit the growth of mature biofilm.

Indeed, this research study showed that the degradation kinetics of sol-gel coatings loaded with an antibiotic (moxifloxacin) can be monitored with different electrochemical techniques. Besides, thanks to the *in vitro* microbiological study and the monitorization of the release of the antibiotic, it has been verified that the quantity of antibiotic in the medium is enough to accomplish the bacterial features of the medical device. Moreover, this study confirmed the potential of the sol-gel technology to fit the release of an antimicrobial to the requirements of the prosthetic devices by modifying the parameters of the sol-gel synthesis.

RESUMEN

Esta Tesis Doctoral se centra en el diseño y desarrollo de nuevos recubrimientos obtenidos por tecnología sol-gel para prevenir y tratar infecciones bacterianas asociadas a prótesis articulares. La contracción de infecciones bacterianas durante la implantación de prótesis provoca repercusiones devastadoras a los pacientes y son generalmente tratadas mediante la administración sistémica de antimicrobianos. Este tipo de terapia es mejorable ya que no llega a alcanzar su función en el foco de la infección. Por ello, las terapias locales están adquiriendo mayor relevancia ya que alcanzan fácilmente la interfaz biomaterial-tejido. Este proyecto de investigación está orientado a combatir localmente el riesgo de infección mediante el uso de un recubrimiento de tipo sol-gel biodegradable como portador y liberador de un agente antimicrobiano.

El recubrimiento tiene carácter multifuncional y está diseñado a partir de dos organopolisiloxanos como precursores de la red sol-gel, la cual tiene la capacidad de degradarse durante las primeras 24 horas en contacto con una solución fisiológica. El recubrimiento se ha biofuncionalizado con un organofosfito para mejorar la proliferación celular durante el proceso de implantación protésica. La siguiente etapa en el diseño de la formulación fue la introducción del antibiótico durante la síntesis. El antibiótico moxifloxacino fue elegido por su amplio espectro de actividad contra los patógenos que causan las infecciones en estudio. La degradación del recubrimiento permite la liberación del antibiótico previamente incorporado a la red.

La degradación cinética de los recubrimientos se ha evaluado por medio de técnicas electroquímicas usando Espectroscopia de Impedancia Electroquímica (EIS, *Electrochemical Impedance Spectroscopy*) y Microscopía Electroquímica de Barrido (SECM, *Scanning Electrochemical Microscopy*). El estudio reveló que la concentración de antibiótico influye en el proceso de degradación siendo el recubrimiento con mayor cantidad de éste el que presenta un proceso de degradación más rápido.

La no citotoxicidad y la proliferación celular fueron verificadas con células MC3T3-E1. La inhibición de la adhesión bacteriana (prevención) y el crecimiento de la biopelícula madura (tratamiento) de las principales especies que causan estas infecciones (*S. aureus*, *S. epidermidis* y *E. coli*) también fueron confirmadas. La liberación del antibiótico se ha estudiado con espectroscopia de absorbancia UV-Vis., observándose que, a pesar de la poca cantidad de antibiótico liberada al medio, la cantidad del mismo es suficiente para inhibir el crecimiento de la biopelícula madura.

Con el presente trabajo de investigación se puede concluir que la degradación de los recubrimientos diseñados de tipo sol-gel cargados con moxifloxacino puede monitorizarse con técnicas electroquímicas. Además, gracias al estudio *in vitro* microbiológico y estudios de absorbancia, se ha comprobado que la liberación del antimicrobiano es adecuada ya que cumple su función bactericida. Este estudio confirma la idoneidad de la tecnología sol-gel para ajustar la liberación de un antimicrobiano a las necesidades temporales requerido por un sistema dispositivo protésico/medio agresivo, mediante la modulación de la síntesis del recubrimiento.

CHAPTER 1

INTRODUCTION

1.1. BIOMATERIALS.....	5
1.2. PROSTHETIC JOINT INFECTIONS.....	7
1.3. SURFACE MODIFICATIONS AND COATINGS.....	13
1.4. SOL-GEL TECHNOLOGY.....	16
1.5. ELECTROCHEMICAL TECHNIQUES.....	19
REFERENCES.....	27

1. INTRODUCTION

1.1. BIOMATERIALS

There are many definitions of **biomaterials** in the literature that express the same concept in different ways. A reliable and concrete definition was proposed in 1987 during the Second Consensus Conference of the European Society for Biomaterials where a biomaterial was defined as “a material intended to interface with biological systems to evaluate, treat, augment or replace any tissue, organ or function of the body” [1]. Biomaterials are required to not induce cytotoxicity and carcinogenesis to the host, to be chemically stable, to have appropriate mechanical properties and to resist biological corrosion.

The classification of biomaterials has also been a matter of discussion. A basic classification is the one that takes into account the chemical nature of the biomaterial. Therefore, biomaterials are classified in metals, ceramics, polymers or composites. Figure 1.1 illustrates a schematic overview of this classification and the most relevant materials used in biomedical applications are described below.

Metals are widely used in load bearing prostheses due to their high strength and resistance to fracture. Stainless steels, mainly austenitic steels, are used in short-term replacements such as in bone fracture fixations or vascular stents [2]. CoCr-based alloys are used in dental implants, while CoNiCrMo alloys are the preferred ones in prosthetic stems. Co-based materials however, are often discarded because they reduce the success of the replacements due to the occurrence of stress-shielding [3]. Ti-based materials present high specific strength and excellent corrosion resistance, and are biocompatible [4]. **Commercially pure titanium** (cp-Ti) and **Ti6Al4V alloy** are the Ti-based materials mainly employed in dental implants and orthopedic components. The performances of cp-Ti vary with the oxygen content because oxygen influences the ductility and the resistance of the metal. Therefore, cp-Ti has been standardized according to the oxygen content from grade 1 (0.18%) to grade 4 (0.40%). Finally, platinum and gold are used in dental fillers and electrodes.

Despite that **ceramics** are brittle and difficult to machine, they are very attractive because of their biocompatibility, excellent wear performances and resistance to microbial attacks. Ceramics are also inert and have strong compression features. They are often classified in: (1) bioinert such as alumina and zirconia, which are used in orthopedic and dental components; (2) biodegradable (e.g., ceramics based on hydroxyapatite and calcium phosphate); and (3) bioactive (e.g., bioglasses). Biodegradable and bioactive ceramics are employed as coatings for implants. Bioactive ceramics in addition, react with the surrounding tissue [5].

Polymers are used as biomaterials due to their versatile properties. Among other properties, they can present rigidity or flexibility, strength or high strength, biodegradability or non-biodegradability. Their shortcomings are their low strength when compared with metals or

ceramics, and their toxic by-products [5]. Collagen, alginate and chitosan are the natural biopolymers par excellence due to their excellent biocompatibility. Collagen is employed in scaffolds and alginate and chitosan in apposite for wounds. Biodegradable polymers are used for the controlled release of pharmaceutical agents thanks to their hydrolytic degradation (e.g., polylactic acid (PLA) and polyglycolic acid (PGA)).

When a material consists in two or more materials with different chemical features separated by a defined interface they are named as **composites**. Many examples illustrates this concept in the literature: hydroxyapatite (HA) has been combined with several polymers such as chitosan, collagen or polylactic acid for bone tissue engineering [6], [7]; also biopolymers containing graphene (C) have geared the attention in regenerative medicine [8]; biodegradable composites formed by a PLA matrix reinforced with 10% wt. of magnesium for osteosynthesis implants have been designed [9].

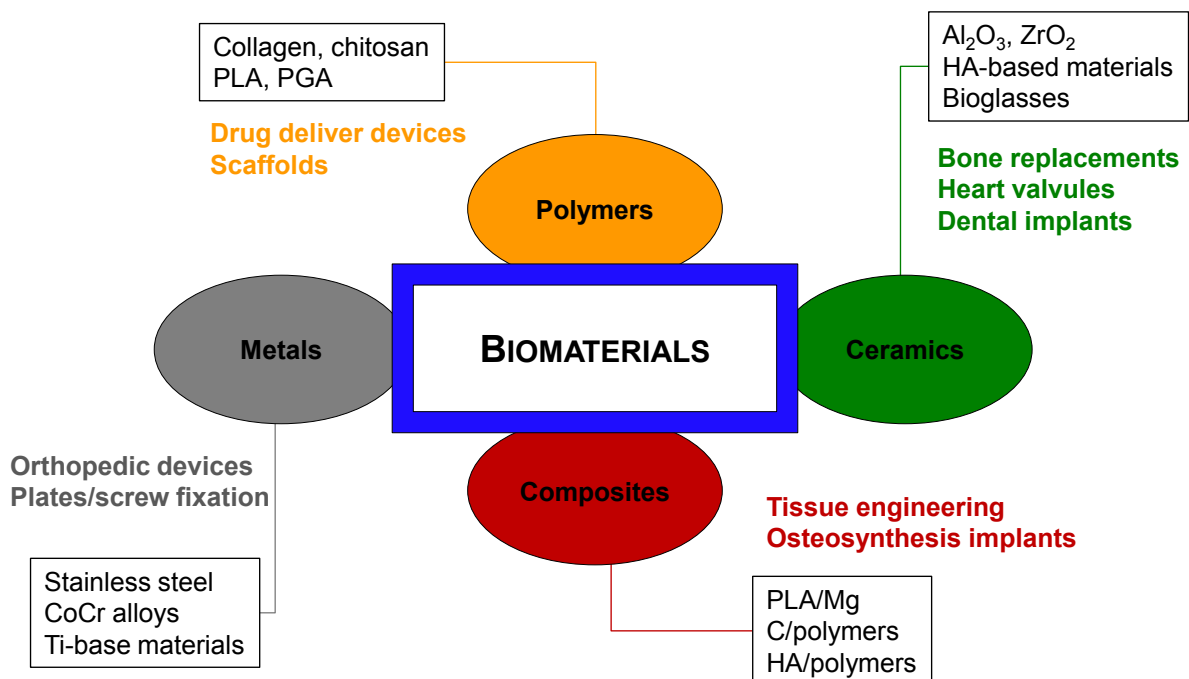


Figure 1. 1 Schematic classification of biomaterials by means of their chemical nature

L.L. Hench and J.M. Polak divided the biomaterials in three generations according to their functionalities [10]. This classification should be interpreted as a conceptual instead of a chronological classification:

- The **first generation** of biomaterials includes bioinert materials, These materials receives no response from the host, neither recognition nor rejection (metals, Al_2O_3 , ZrO_2 , poly(methyl methacrylate), polyethylene, composites).
- The **second generation** corresponds to bioactive and biodegradable materials such as biodegradable polymers and bioactive ceramics.
- The **third generation** of biomaterials ascribes to materials with the ability to stimulate physiological responses at the molecular level (e.g., scaffolds).

During the last decades the innovations in the design of materials and the developments of medical technologies have demanded the emergence of the **fourth generation** of biomaterials. This new generation is called by some authors as “smart” or “biomimetic materials” that aim to mimic the extracellular matrix of natural tissues [3].

1.2. PROSTHETIC JOINT INFECTIONS

During the implantation of prostheses, the host reacts to any strange material and produces complex mechanism as part of the physiological bone remodeling. This procedure is known as **osseointegration** and a schema of the process is shown in Figure 1.2. The implantation of a biomaterial often creates a wound whose healing experiences four overlapping and interdependent phases [4], [5]:

1. **Hemostasis:** It starts with trauma and lasts from minutes to hours. It is the first stage of the wound healing that starts with the adsorption of plasma proteins (albumin, globulin, fibrinogen, regulatory proteins and clotting factors) (stage a) and ends with the control of bleeding through coagulation (stage b).
2. **Inflammation:** It is part of the protective response of the body that aims to digest the tissue debris and the biomaterial. The process starts within 15 minutes from trauma and lasts for some days. The procedure is accompanied with the swelling and the warm of the affected area. During this stage, bacterial cells can colonize the surface of the biomaterial and develop a biofilm (stage c). The consequence is that the implant gets encapsulated into a fibrous tissue (stage d).
3. **Proliferation/initial repair:** In this phase cells proliferate on the biomaterial to enhance the recreation of the damaged tissue.
4. **Remodeling:** Cells remodel the *neotissue* into a functionalized one.

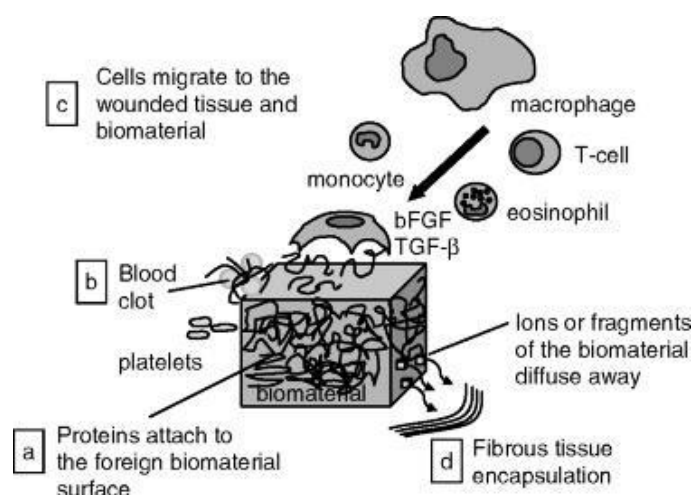


Figure 1. 2 Normal tissue-biomaterials interaction involving the four overlapping and interdependent phases of wound healing: hemostasis, inflammation, proliferation/repair, and tissue remodeling. (a)

Protein attachment to the biomaterial surface guides cellular interactions. (b) Hemostasis is accomplished by clot formation. (c) Cells found in blood and other inflammatory cells attempt to process the foreign biomaterial and repair adjacent material. (d) The host protects itself from the foreign biomaterial through encapsulation with fibrous tissue [5]

When biomaterials are placed into the host, their surface is the idyllic place to be colonized by macromolecules, microbes (bacteria, fungus) and host cells. If the surface of the biomaterial is properly colonized by the host cells, the biomaterial mitigates the risk of contracting bacterial infections. However, if microbes colonize the surface of the biomaterial, they resist against antibodies and the immune system of the host and subsequently they induce damages on the surrounding tissue [5]. The concept of “the race for the surface” was coined by A. Gristina et al. and it defines the existing competition between the host cells and the bacterial cells when colonizing an implant [11]. These procedures can be competitive and mutually exclusive. Unlike biodegradable materials, whose inflammatory processes stop once the material is fully degraded, permanent implants require to reduce the incidence of inflammatory processes in order to achieve the successful integration of the replacement. Absorbable medical devices requires to overcome other shortcomings such as how to reach a similar rate between the degradation of the material and the creation of new bone [12].

The first total replacement of a synovial joint was successfully performed by J. Charnley. in the 50s [13]. Natural synovial joints (e.g., knee, hip, shoulder, and elbow joints) are complex and fragile structures that work under critical load conditions. Their failures are common and due to fractures or degenerative diseases [14]. Replacements of natural joints are known as **arthroplasties**. They provide relief from pain and restore the function to joints in which the natural cartilage has been damaged [5]. The number of arthroplasties is expected to increase in the next decade. An international study of 18 countries reported in 2009 an average of 0.175% of primary total knee arthroplasties in the population [15]. S. Kurtz et al. forecasted a large increase in arthroplasties from 2005 to 2030 in the United States: the demand of primary hip arthroplasties is projected to almost double by 2030, and the forecast for primary knee arthroplasties is to multiply per seven the number of replacements in 25 years [16]. During the life of these replacements, the main complication is associated with the loosening of the prosthesis followed in second position by the risk of bacterial infections. **Prosthetic joint infections** (PJIs) are referred to infections in the joint of the prosthesis and the adjacent tissues. They are uncommon (1-2%) but devastating [17]. A Spanish regional study conducted in Andalucía between January 2005 and January 2010 reported that each patient affected by PJIs cost 40,542€ to the health care system [18]. Given the number of patients affected by PJIs and the burden for the patients and the health care systems, efforts are geared to reduce the incidence of these infections.

A useful classification of PJIs is based on the time to infection: (1) early-onset PJIs (< 3 months after the replacement), (2) delayed-onset PJIs (3-24 months after the procedure), and (3) late-onset PJIs (> 24 months) [19], [20]. Bacterial species can be classified in two main groups depending on the physical and chemical properties of their cell wall: Gram-positive and Gram-negative bacteria. This classification is based on how bacteria react when they are subjected to the purple/blue Gram stain. **Gram-positive bacteria** retain the stain due to the thick peptidoglycan layer of their cell wall giving rise to a purple color. **Gram-negative bacteria** meanwhile, have an inner and outer membrane with a thin peptidoglycan layer that avoids the retention of the Gram stain. Gram-negative bacteria reveal a pink color in the presence of the Gram stain. Figure 1.3 shows a schematic drawing of the structure of the cell wall of both types of bacteria.

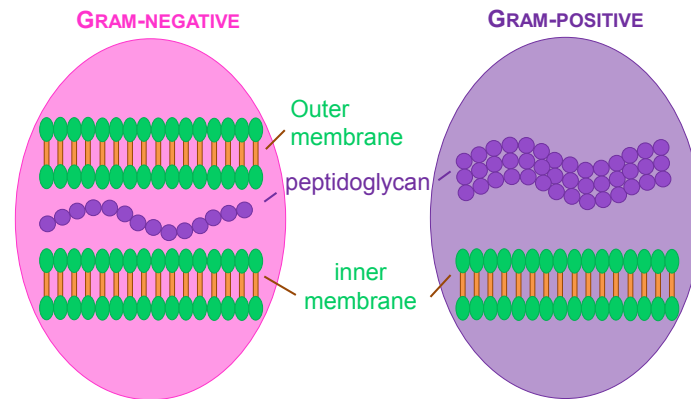


Figure 1. 3 Schematic drawing of the structure of the cell wall of Gram-negative and Gram-positive bacteria and their color stain after subjecting bacteria to the Gram's method

In order to select a suitable therapy to counteract PJI's, it is essential to identify the **etiologi- cal agents** that cause these infections. A Spanish multicenter study of 19 hospitals performed between 2003 and 2012 identified the most relevant bacteria that cause PJIs [21]. Aerobic Gram-positive cocci were isolated on 77.7% of the total PJIs and aerobic Gram-negative bacilli on 27.6% of the infections. The study revealed also an increase of PJIs associated with Gram-negative bacilli bacteria (8.3%) and **polymicrobial infections** (23.3). Four species were involved in more than 69% of all the studied cases:

- Two aerobic Gram-positive cocci bacteria: *Staphylococcus aureus* (28.1%) and *Staphylococcus epidermidis* (23.3%), and
- Two aerobic Gram-negative bacilli bacteria: *Escherichia coli* (9.1%) and *Pseudomonas aeruginosa* (8.8%)

The morphology of cocci and bacilli bacteria on the surface of a protective coating manufactured with sol-gel technology for prosthesis is shown in Figure 1.4. Cocci bacteria shows a spherical morphology (Figure 1.4(A)) while bacilli bacteria had an elongated morphology containing flagellum (Figure 1.4(B)).

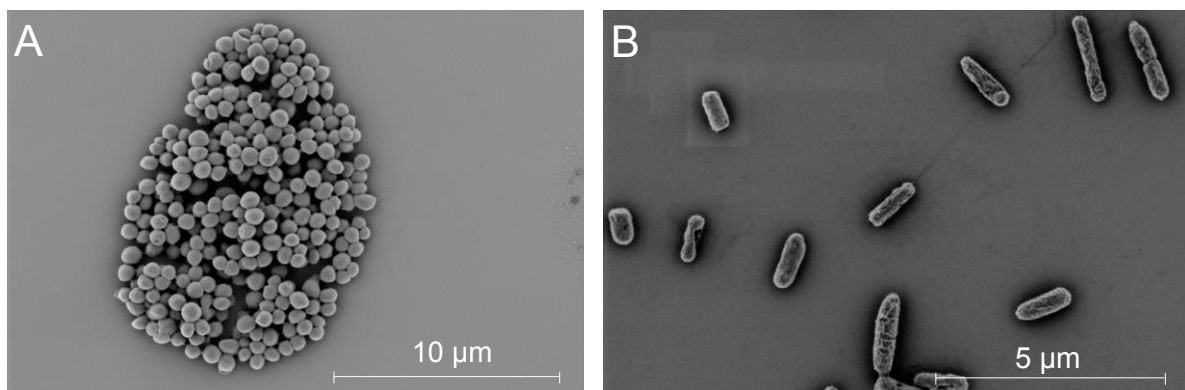


Figure 1. 4 SEM micrographs of A) *S. epidermidis* and B) *P. aeruginosa* on sol-gel coatings after an *in vitro* adhesion test

The microorganisms that induce PJI present the ability to develop biofilms. **Biofilms** are complex communities of microorganisms (monomicrobial or polymicrobial) irreversibly associated and embedded in an extracellular matrix synthesized by them. Three stages can be identified during the formation of a biofilm (see Figure 1.5) [22], [23]:

1. Attachment

First, **planktonic bacteria** (free-floating) establish contact with the surface of the material and get reversibly adsorbed (step i). Then, bacteria get irreversibly adsorbed and undergo a transformation to **sessile bacteria** (bacteria immobilized on the surface of the substrate) (step ii). The adsorption of bacteria directly depends on their morphology. The presence of pili or flagellum on the structures of bacteria (e.g., gram-negative bacteria) aids the irreversible adsorption of the bacteria to the substrate. Finally, bacteria suffer different changes on their phenotypes and start to divide and create microcolonies (step iii).

2. Maturation

During this stage bacteria release *quorum sensing* indicators that induce the synthesis of the extracellular matrix [24]. Three-dimensional structures are developed with at least the interconnection of nutrients, oxygen, pH and cellular intercommunication.

3. Dispersion

Some bacteria detach from the colony. This stage may or not occur depending on the environmental conditions.

4. New cycle

Detached bacteria on their planktonic stage start again the cycle if the environmental conditions are suitable for developing again a biofilm.

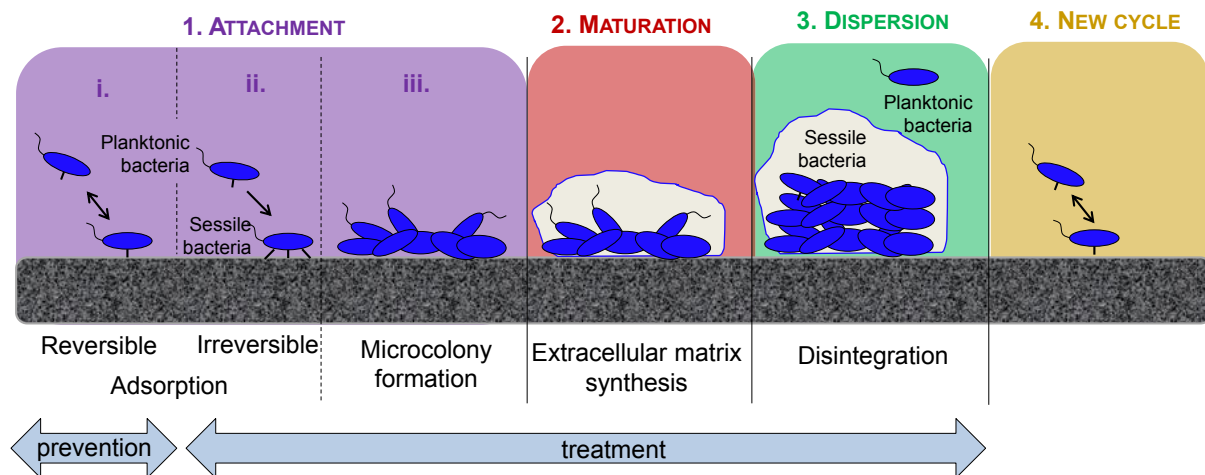


Figure 1. 5 Schematic drawing of the consecutive stages of the formation of a biofilm

Two main therapies are employed to combat bacterial biofilms: prevention and treatment.

The **prevention** of biofilm growth is based on the reduction of bacterial adsorption onto the surface of the biomaterial during the first stage of the biofilm development (step i). Metals (e.g., titanium, cobalt or stainless steel based materials), polymers (e.g., polymethylmetacrylate and polyethylene) and ceramics (e.g., hydroxyapatite-based materials) are widely used as orthopedic components but they are susceptible to the

colonization of bacteria [20]. The preventive measures taken during the replacement of prostheses are of environmental and prophylactic type. The **environmental** measures are taken during surgery and concern the operating room and the surgical personnel [25]–[27]. The surgical-site infections are minimized by employing a few preventive measures: systems of ventilation with laminar airflow and high efficient particle filters, exhaustive protocols to prepare the patient for the surgery (showers, removal of nail polish, depilation, application of detergent and antiseptic agents), and strict discipline of the surgical personnel (appropriate hygiene and attire). Besides, it is recommended to reduce the traffic of persons by keeping the surgical members between 5 or 6 and to limiting the door openings during surgery [28]. Concerning **prophylactic** measures, antibiotics are provided between 60 to 120 minutes before surgery and during the 24 hours after surgery [29]. Indeed, the American Association of Hip and Knee Surgeons (AAHKS) recommended in June of 2017 the administration of prophylactic antibiotics during the 24 hours after surgery [30].

The procedures of **treatment** aim to block the maturation of biofilms that have already started the process of infection. The selection of the treatment depends on the developing stage of the infection. If the patient contract a chronic or non-treatable infection, the prosthesis is removed without reimplantation [31]. For acute infections with a stable implant and adequate surrounding tissue, primary treatments to retain the prosthesis are employed. These treatments are referred as DAIR procedures and consist in the removal of the infected tissues (debridement), the administration of antibiotics and the retention of the implant. Successful rates of DAIR treatments range between 14% to 100% depending on the patient conditions and the selected treatment. This rate can increase if the infection is treated as soon as, the symptoms of the infection arises, which appear in less than 3 week after surgery [31]–[33]. Some studies have identified that if the administration of antibiotics stops 3-4 months after the DAIR procedure, the risk of failure is high [34]. Also, promising results have been found if systemic administrations are supplied in several dose per day (even up to 4 times per day) instead of in one dose [35].

Despite the measure of prevention and treatment employed during arthroplasties, infections are not always avoided. After surgery the tissue that surrounds the prosthesis remains avascular and/or necrotic being the antibiotic administrated orally or intravenously unable to successfully reach the inner part of a biofilm or the biomaterial-tissue interface [36]. This limitation cannot be overcome with higher systemic doses because it can lead to organic toxicity. Thus, **local antibiotic therapies** are presented as novel and promising prophylactic treatments. Local therapies are well recognized to be highly efficient because they allow the local administration of high doses of antimicrobials without inducing organic toxicity. Several studies have reported that prophylaxis combining systemic and local therapies increases the ratio of success. In addition, the emergence of antimicrobial-resistant pathogens increases the challenges to find suitable therapies to face infections.

When designing a therapy it is of paramount importance to understand the interaction between implant and cells. Implants are required to be inactive to avoid inflammatory conditions but active to allow their bio-integration. During the development of an infection, a window of opportunities is drawn prior to the irreversibly attachment of bacteria and its

phenotype change (Figure 1.5, step i). But, while hydrophobic surfaces reduce the incidence of bacterial adhesion, hydrophilic surfaces favour the attachment of cells [37],[38]. An intermediate hydrophobic surface is expected first, to reduce the adhesion of bacteria and second, to assist the attachment of cells to enhance the osseointegration of the material. The challenge on this field is the design of **multifunctional** strategies that combines the prevention and the treatment of PJIs with the improvement of the osseointegration.

Titanium-based materials are the metals used as prosthesis due to their biocompatibility, excellent mechanical properties and resistance to corrosion. **Cp-Ti** (ASTM F67) is mainly used for dental implants while **Ti6Al4V alloy** (ASTM F136) is the preferred material for components of orthopedic prostheses. They differ in their phase composition and microstructure: cp-Ti consists of only α -phase (hexagonal close-packed; HCP) and Ti6Al4V alloy of a bi-phasic microstructure $\alpha+\beta$ (body-centred cubic; BCC). Titanium and titanium alloys lack good wear resistance that can however, be enhanced by stabilizing the β phase with alloying elements such as Nb or Mo [39], [40]. The main concern when employing Ti6Al4V alloy is that the release of ions from the alloying elements can induce toxicity to the host [41]. Therefore, efforts are geared to the substitution of V for other elements that show non-cytotoxicity such as Nb or Ta [40], [42].

The Young's modulus is the main studied biomechanical property of biomaterials. The Young's moduli of the most employed metals in prosthetic devices are: 102-105 GPa for cp-Ti; 110-114 GPa for Ti6Al4V alloy; 200 GPa for stainless steel and 210 GPa for Co–Cr–Mo alloys. The low Young's modulus of Ti-based materials when compared with other metals permits to mitigate the risk of stress shielding of prostheses thanks to the small mismatch between the metal and the cortical bond (10-30 GPa) [43], [44].

Ti alloys have been subjected to many modifications of their bulk and surface features to reduce their Young's modulus and avoid the release of toxic ions [44]–[46]. In this context, **the powder metallurgy** (PM) technology offers the possibility of inducing porosity to the bulk material to reduce the mismatch between the metal and the cortical bone. PM is a near net shape and cost-effective technology that allows tailoring the mechanical properties of the final substrates [47]. Due to the industrial requirements, PM has been always focused on reducing the residual porosity that this manufacturing technology induces to metals. A. Amherd Hidalgo et al. provided an extent review of the current strategies employed to enhance the densification of Ti being the introduction of alloying elements (e.g., Ni, Cu, Co or Fe) or the application of sintering treatments the preferred modifications [48]. PM has been successfully employed to manufacture two Ti alloys, namely Ti6Al7Nb and Ti6Al4V, with similar mechanical properties to the conventional alloys manufactured by casting [49]–[51]. The versatility of the manufacturing technique offers also the possibility of inducing a gradient of mechanical properties from the surface to the bulk of the material by applying diffusion treatments through the metallic surface with Nb or Mo [39]. In this work, **pure Ti manufactured with PM** (TiPM) with 17.2% of total porosity has been employed as the substrate of sol-gel coatings. Pure Ti has been selected as the metallic substrate to simplify the study. Nevertheless, these coatings could be applied on any Ti-based metal [52].

1.3. SURFACE MODIFICATIONS AND COATINGS

Despite Ti-based materials are widely used in components for orthopedic implants, their metallic surface is inactive to assist the implant/bone integration and avoid the contraction of infections [4]. Besides, it is of main concern to design new strategies that reduce the costs to the health care system and improves the patient's well-being. The modification of the metallic surface is an easy and cost-effective procedure that changes the composition, structure and morphology of the material without modifying the excellent mechanical properties of the bulk material. Recent studies have modified metallic surfaces by applying coatings containing biopolymers such as poly(lactic acid) [4], [53], biological molecules like type I human collagen [54], [55], among others compounds. Other research approaches use innovative processing techniques to induce topographical modifications to metallic surfaces by using anodic oxidation techniques to create nanotube arrays [56], [57], additive manufacturing to create porous surfaces [58], or diffusion treatments with Nb or Mo to enhance the osseointegration of the implant with the host [40], [59], [60]. An attractive strategy among all the surface modifications is the use of anti-adhesive coatings (passive coatings) containing antimicrobial agents (active surfaces) that aim to reduce the additional surgeries and the exposure to prolonged systemic treatments with antibiotic.

Coatings with pre-incorporated **antimicrobial agents** have been widely investigated and their classification is sometimes complicated due to the extensive bibliography of the topic. E. J. Tobin published in 2016 a review of the most relevant developments in therapeutically-loaded coatings where he made a classification by means of their ultimate biological purpose [61]. Figure 1.6 illustrates this classification that consists in three categories: (1) coatings that enhance the integration of the biomaterial with the host, (2) coatings that aim to reduce infections associated to biomaterials, and (3) coatings that combine both features. In this classification he considered that coatings for orthopedic and dental implants could be bio-functionalized with the same strategies because they need to fulfill similar requirements. The little literature that have compared the materials used in both, orthopedic and dental implants, report similar osseointegration and biomechanical properties suggesting that materials could be indiscriminating employed either in dental or orthopedic components [62].

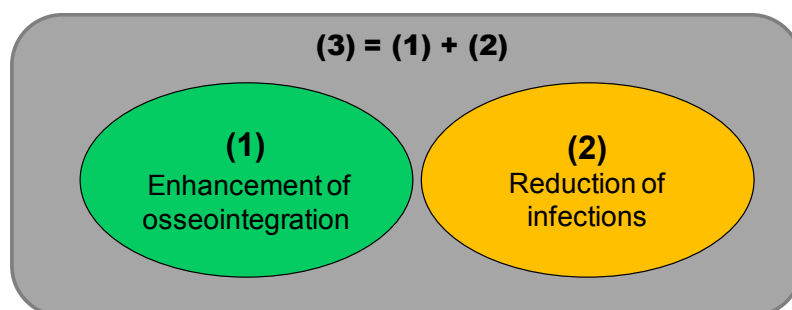


Figure 1. 6 Schema of the classification established by E. J. Tobin for therapeutically-loaded coatings

For the **enhancement of the osseointegration**, the bio-functionalization of coatings has been focus on mimicking the inorganic part of bones whose main components are calcium and orthophosphate being 1.67 the ratio between calcium and phosphorus [4]. However, materials based in calcium-phosphates have been restricted to clinical applications because of their poor adhesion to the substrate, poor mechanical properties, and non-uniformity in crystallinity and morphology [63]. Therefore alternatives free of calcium are under study being the incorporation of organic or inorganic phosphates the most promising ones. Moreover, phosphates have been recently reported to induce the osseointegration of the implant during the first stage after surgery [63], [64].

Concerning the strategies that aim to **reduce the contraction of infections** is of paramount importance designing multifunctional coatings that prevent and treat at the same time the contraction of infections and the growth of mature biofilms. **Anti-adhesive** polymers are the indisputable materials employed to reduce the colonization of bacteria. Also, nanopatterned surfaces, super-hydrophobic materials and hydrogels have been used for this purpose. Table 1.1 summarizes the main surface modifications employed to **prevent** the colonization of bacteria. The prevention of bacterial colonization has currently received more attention because of the increasing number of multi-drug resistant bacteria and the inefficiency of some antibiotics.

Table 1. 1 Main surface modifications and coatings for the prevention of bacterial attachment

Surface modification and coatings	References
Nanopatterned surfaces	
Ti based materials	[65]–[67]
Collagen	[68]
Super-hydrophobic surfaces	[38], [69], [70]
Anti-adhesive polymers:	
Polysaccharides (heparin, alginate, chitosan, hyaluronic acid)	[71]
Polymers functionalized with peptides	[72], [73]
Hydrogels	[74]

J.J.T.M Swartjes et al. gave a relevant overview of the current developments in coatings loaded with antimicrobials that aim to enhance the osseointegration of the biomaterial with the host and to reduce the risk of infections [75]. They identified the main substances used to **bio-functionalize** coatings: antimicrobial peptides, antibiotics, enzymes, nanoparticles, quaternary ammonium compounds, anti-adhesive polymers, chitosan-based substances and compounds that provide coatings with super-hydrophobicity. Also, they listed the four main strategies used when designing antimicrobial coatings. These strategies are illustrated in Figure 1.7 and are often combined to achieve better results.

- (1) The immobilization of antimicrobials on the surface
- (2) The design of coatings with the controlled release of antimicrobials
- (3) Hydrogels or other matrix structures containing bound antimicrobials
- (4) Antimicrobials tethered to a surface through spacer-molecules

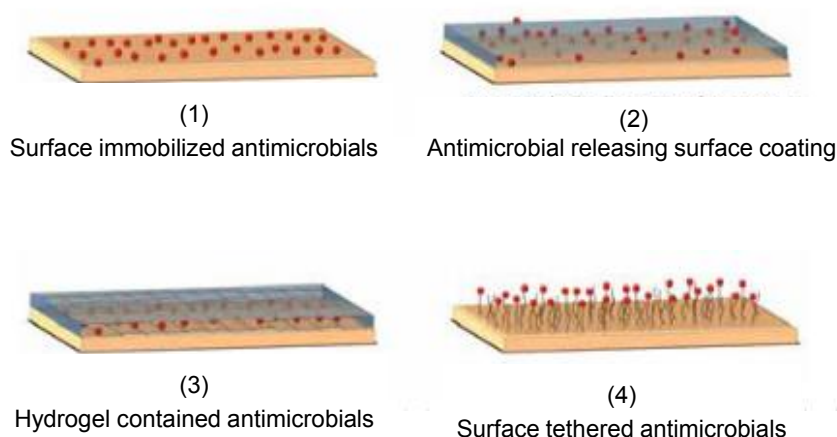


Figure 1. 7 Schematic representation of the main strategies used to bio-functionalize coatings with antimicrobials (adapted from [75])

The bio-functionalization of coatings with **antibiotics** has been the most employed among all the developed strategies in the field. The selection of the appropriate antibiotic to treat PJIs is still a challenge in hospitals. A study performed in Sweden confirmed that the main perioperative antibiotics consisted of cloxacillin (90.3%), clindamycin (7.2%), cephalosporins (2.4%) and vancomycin (0.04%) [76]. Rifampin has been positioned as the main antibiotic used against staphylococcal infections but the common development of resistance to this monotherapy demands the use of other antibiotics such as staphylococcal penicillin (e.g., flucloxacillin) or fluoroquinolones (e.g., ciprofloxacin or levofloxacin). Newer quinolones like **moxifloxacin (MOX)** are being investigated as partners of other antibiotics due to their broad spectrum activity against gram positive, gram negative, and anaerobic pathogens [77]. MOX has demonstrated superior performance in PJIs when compared with vancomycin and levofloxacin [77], [78]. The antibiotics commonly used in local prophylactic therapies are introduced either in biodegradable polymeric **carriers** such as poly(D,L-lactide), poly(ϵ -caprolactone) and poly(trimethylene carbonate) or impregnated in bone grafts [79]. Biodegradable sponges, cement spacers and beads are also used as drug carriers but once the antimicrobial agent is released the carriers must be removed [79]. Other recent approaches use multilayer arrays to simultaneously release two therapeutic compounds. A. Shukla and co-workers designed a tetralayer polymeric coating that consists in the alternation of hydrolytically degradable cations (poly(β -amino esters)) and biocompatible polyanions (alginate, chondroitin, sulfate, and dextran sulfate). The multilayer architecture has been doped with an antibiotic (vancomycin) and a nonsteroidal anti-inflammatory drug (diclofenac) [80].

In this research project, **sol-gel coatings** based in organopolysiloxanes are proposed as drug carriers and enhancers of the osseointegration of titanium-based materials. This technology is drawing the attention of the biomedical field because it is an easy synthesis process that allows tailoring the surface chemistries of the material with a low energy-consuming procedure. Depending on the selected precursors, sol-gel coatings hydrolytically degrade in contact with aqueous solutions due to an uptake of water that causes the coating to swell permitting the release of the therapeutic compound [81].

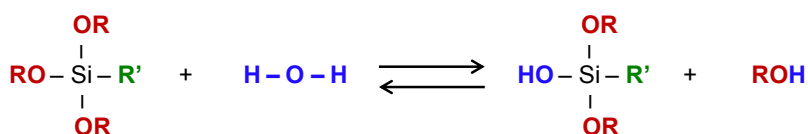
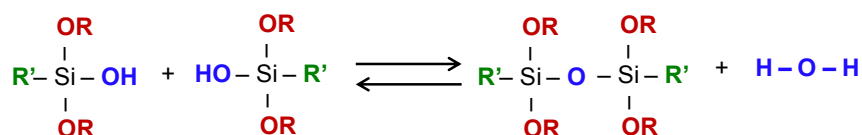
1.4. SOL-GEL TECHNOLOGY

The hybrid organo-inorganic sol-gel technology exploded in the 80s due to the expansion of the soft inorganic chemical procedures. The conditions offered by the sol-gel method (e.g., mild conditions, versatility of the colloidal state, and tailored-made properties) allow the mixing of organic and inorganic compounds under a nanoscopic scale. The sol-gel method starts from a **sol** (colloidal suspension) with metal or metalloid elements that lead to the formation of M-O-M bonds. Metallic alkoxides, $M(OR)_n$, are normally used as precursors of the sol-gel reaction. M is the nuclei element that creates the network (e.g., Si, Ti, Zr, Al, Fe, B) and R is often an alkyl group (C_xH_{2x+1}). The predominant employed alkoxides are based in silicon ($Si(OR)_n$, alkoxysilane) due to their moderate reactivity when compared with other precursors [82].

The sol-gel synthesis consists of an organic phase containing the alkoxides as the source of oxygen and alcohol as solvent, and an aqueous phase, which is the agent of the hydrolysis. Once the alkoxides undergo **hydrolysis**, **polycondensation** starts to create high molecular-weight molecules forming the polysiloxane network. Then, hydrolysis and polycondensation undergo simultaneously. Polycondensation can be extended as long as M-OH groups are available. The hydrolysis kinetic is normally catalyzed in acid medium while polycondensation kinetic requires basic conditions to be accelerated [83]. The polymerization of the sol-gel network takes places in three stages [84]:

1. Polymerization of monomers to form particles (hydrolysis-condensation)
2. Growth of particles
3. Linkage of particles into chains and creation of extended networks from the liquid medium

The reactions of hydrolysis and condensation of the sol-gel synthesis using as precursor silicon based reagents as precursors are schematized in Figure 1.8.

HydrolysisCondensation

OR = alkoxy group (e.g., OCH_2CH_3)

R' = organic chain (e.g., $\text{H}_2\text{C}=\text{C}(\text{CH}_3)\text{CO}_2(\text{CH}_2)_3$ or OCH_3)

Figure 1. 8 Hydrolysis-condensation reactions of the sol-gel synthesis using Si-based precursors

Then, a wet **gel** is created by the interaction and cross-linkage of particles. Finally, the water and solvents evaporate to produce the dry material. The sol-gel method can shape the macroscopic final material to coatings, powders, monoliths (xerogels), foams, fibers or ceramics depending on how the sol is applied and if the material is subjected to post-procedures such as heat treatments [82], [85], [86]. Figure 1.9 illustrates a schema of the different stage of the sol-gel process. In this research work, the material is shaped to a coating for metallic substrates. The coating can be applied on the substrate by different techniques: dip-coating, spin-coating or spray. The final properties of a coating will mainly depend mainly on the selected precursors, the hydrolysis-polycondensation rate prior to the deposition, and the drying treatment of the xerogel coating [87].

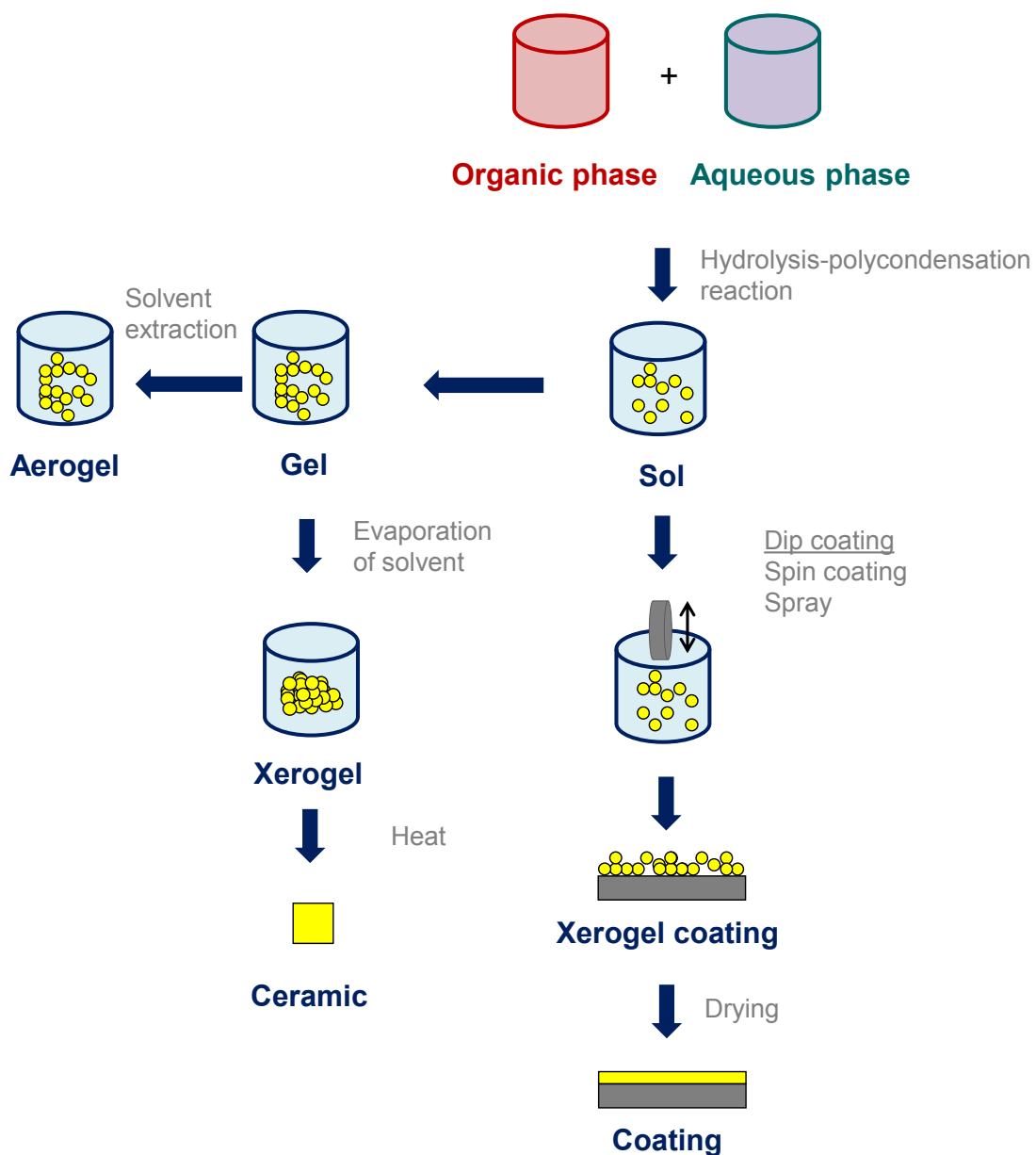


Figure 1. 9 Schematic overview of the different stages of the sol-gel process and the final macroscopic materials

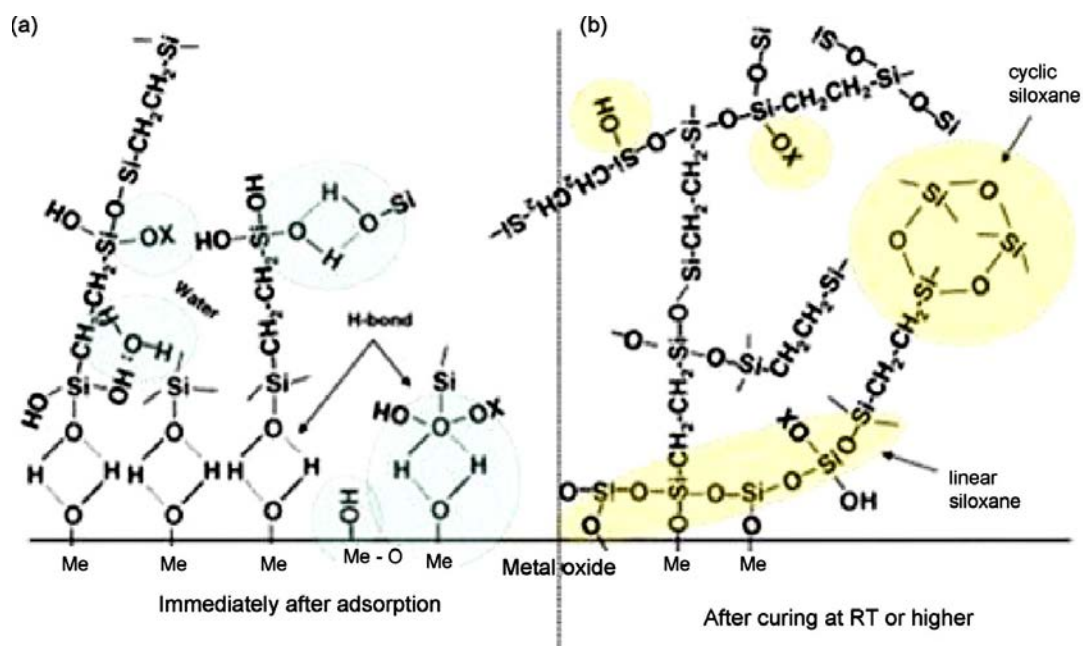


Figure 1. 10 Simplified schematic of the bonding mechanism between silane molecules and the hydroxide layer of the metallic surface: (a) before condensation: hydrogen-bonded interface; (b) after condensation: covalent-bonded interface [82]

In order to ensure the adhesion of the coating to a metallic substrate, the hydrolysis and polycondensation reactions should be optimized. A good adhesion requires to have enough **free-hydroxyls** (silanol; SiOH), which get spontaneously adsorbed onto the metal with Van der Waals bonds and enough **siloxane bonds** (Si-O-Si) to provide the network with a suitable cross-linkage. Once the sol is applied to the substrate, the condensation reactions continue and lead to the formation of strong covalent bonds between the coating and the metallic substrate. Figure 1.10 shows the bonding mechanism generally accepted to explain the covalent formation of M-O-Si bonds at the coating-metal interface [82].

Sol-gel coatings can be classified into inorganic or **hybrid organic-inorganic (O/I)** depending on the chemical nature of the employed precursors. Inorganic coatings shows excellent adhesion to the metal but coatings tend to be brittle and cracks can be generated during the drying step. Thus, coatings present poor physical barriers against corrosion. The introduction to the network of the organic components increases the density of the coatings promoting coatings free of cracks and with good physical properties. Besides, the incorporation of the organic compounds reduces the drying temperature of the coating to even room temperature. The use of low temperatures allows the introduction of inhibitors, bioactive molecules or additives to the network without altering their chemical nature [88].

Currently, researches are developing sol-gel coatings combining organic and inorganic precursors. Wang and Bierwagen reported in 2009 the main advances performed in O/I coatings. The preferred precursors used were: tetraethyl orthosilane (TEOS), tetramethyl orthosilane (TMOS), methyl triethoxysilane (MTES), methyl trimethoxysilane (MTMS), vinyl trimethoxysilane (VTMS), phenyl trimethoxysilane (PTMS), diethylphosphonatoethyl triethoxysilane (PHS), 3-(2-aminoethyl)aminopropyl trimethoxysilane (APS), 3-aminopropyl

trimethoxysilane (AEAPS), 3-glycidoxypropyl trimethoxysilane (GPTMS), 3-methacryloxypropyl trimethoxysilane (MAPTMS), 3-mercaptopropyl trimethoxysilane (MPTMS), bis-[3-(triethoxysilyl)-propyl] tetrasulfide (BTSTS) [82].

Sol-gel technology has been applied to obtain different **functional materials** such as ion selective membranes [89], electrochemical sensors [90], and coatings for the protection of metals against corrosion [82], [91]–[95]. This technology is broadening its area of application to other fields due to the request of improved performances on novel materials. Promising studies are currently been performed using the sol-gel technology in the biomedical field. Sol-gel coatings have also been loaded with active molecules such as procaine [96] and vancomycin [97]. Other research approaches have bio-functionalized coatings with HA, phosphorus and calcium compounds to enhance the osseointegration [98]–[103]. Sol-gel coatings have been used to induce osseointegration by bio-functionalizing coatings with HA [101], [102], [104]–[106], poly(ϵ -caprolactone) [107], polyethylene glycol [108], strontium [109], [110], or gelatin [111]. Nevertheless, few studies are reported on the modification of sol-gel coatings employing only phosphorus compounds. The most relevant study have used triethylphosphate, phosphoric acid and ammonium dihydrogen phosphate as phosphorus modifiers for the synthesis of silicate bioceramics [112].

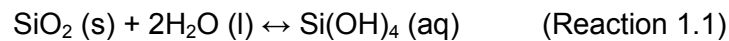
1.5. ELECTROCHEMICAL TECHNIQUES

The extracellular fluids of the human body consist on different salts (e.g., NaCl, MgCl₂, KCl, glucose, among others) dissolved in an aqueous solution containing oxygen. The physiological medium is then the perfect scenario where electrochemical phenomena can arise. The regular pH of the physiological fluid is neutral with values that vary between 7.2 and 7.4 and that can be modified due to external phenomena. For example, the appearance of wounds leads to the acidification of the medium (4.0-5.2) whereas, the contraction of infections incurs the alkalization of the medium [113].

In passive metals like **titanium**, the strong affinity of Ti to O assists the creation of a protective passive layer. The formation of this unreactive layer is essential because it protects the implant for long-term performances and prevents inflammatory processes induced by the release of toxic ions from the alloy. However, the aggressive *in vivo* conditions can alter the stability of the passive layer. Then, metals can experience corrosion phenomena that can compromise the integrity of the prosthesis. In fact, failure due to electrochemical corrosion has been reported in bio-systems involving metallic biomaterials [114], [115]. The porosity of metals is a feature that makes metals more susceptible to electrochemical corrosion than dense materials because pores entrap the ionic species of the electrolyte and reduce the oxygen supply [116]–[118]. The selection of the appropriate electrochemical technique to evaluate the electrochemical performances of a material is also important. J.-L. Wang et al. remarked on a recent study that conventional electrochemical techniques such as potentiodynamic polarization lack the resolution to deeply study the electrochemical performance of Ti alloys [119]. Innovative electrochemical techniques with

higher resolution are required in this field because it is difficult to observe differences on the electrochemical behaviour of Ti alloys due to their excellent corrosion resistance. Moreover, the literature reports contradictory results whether or not cp-Ti exhibits superior long-term performance than Ti6Al4V alloy [62]. In this research work, prior to the study of the coated specimens, the uncoated TiPM has been studied to evaluate if the porosity induced to the Ti with PM influences its electrochemical performance.

The electrochemical features of **sol-gel coatings** are ascribed to the protective layer that acts as a physical barrier to the penetration of the electrolyte through the metallic surface. Sol-gel coatings can present microdefects such as cracks or pores that allow the introduction of the electrolyte until establishing contact with the metal. Once the coating is in contact with the aqueous solution its hydrolytic degradation starts. The water hydrates the molecules of the sol-gel generating the coating to swell followed with a subsequent degradation of the coating. The hydrolytic degradation of sol-gel coatings are based on a depolymerization that can be considered as the opposite reaction of the polycondensation, which creates the siloxane bonds of the sol-gel network. The coating degrades following the hydrolysis reaction summarized in Reaction 1.1 [81]:



The **Electrochemical Impedance Spectroscopy** (EIS) is an electrochemical technique with broad applications that is growing in importance with years. EIS is used as a characterization technique of several systems such as protective materials of metals, batteries, fuel cells, etc. [120], [121].

The term **impedance** refers to the frequency dependent resistance to current flow of a circuit element (resistor, capacitor, inductor). The technique consists on the application of a small sinusoidal perturbation (potential or current) at a fixed frequency and the measurement of a sinusoidal response (potential or current). If a sinusoidal potential (E) is applied at a fixed frequency (ω), a sinusoidal current (I) is received at the same frequency but with different amplitude and phase angle (ϕ). The magnitudes of potential and current are described with Equation 1.1 and Equation 1.2, respectively [122]:

$$E = E_0 \text{sen}(\omega t) \quad (\text{Equation 1.1})$$

$$I = I_0 \text{sen}(\omega t + \phi) \quad (\text{Equation 1.2})$$

being E_0 and I_0 the maximum amplitudes of the applied potential and the received intensity, respectively, and ϕ the phase difference between both signals.

The recorded signal computes the impedance at each frequency as a complex number defined as the ratio of complex potential (E_0) and complex current (I_0) (Equation 1.3). Impedance, which uses alternating current (AC), is analogue to the resistance defined with Ohm's law, which uses direct current (DC). The main difference between impedance and resistance is that impedance is a vector magnitude with a direction (ϕ) (Equation 1.4) [122].

$$|Z| = E_0/I_0 \quad (\text{Equation 1.3})$$

$$\phi = \arctan(Z_{im}/Z_{re}) \quad (\text{Equation 1.4})$$

where Z_{im} is the imaginary component and Z_{re} , the real component of the impedance.

Figure 1.11 shows a Nyquist diagram where the components (Z_{im} and Z_{re}) of the impedance are presented as a function of the applied frequency. The modulus of the impedance ($|Z|$) is calculated as follows (Equation 1.5) [122]:

$$|Z| = \sqrt{(Z_{re})^2 + (Z_{im})^2} \quad (\text{Equation 1.5})$$

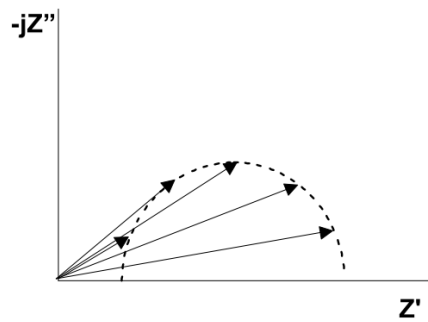


Figure 1. 11 Impedance as a function of the frequency. Nyquist diagram [122]

The experimental setup of the electrochemical cell used to measure impedances can vary depending on the tested material or the data to be recorded. When materials are tested for biomedical applications an electrochemical cell with double-wall is used in order to control the temperature at 37°C. Figure 1.12 illustrates a conventional configuration of an electrochemical cell used to measure the impedance of coated materials. A conventional setup of three electrodes is employed and the elements required are:

- (1) The **reference electrode** has a stable and well-known potential and the impedance is recorded as a function of its potential. The most employed reference electrodes are: silver chloride electrode ($\text{Ag}/\text{AgCl}/\text{sat. KCl}$; $E_0=0.197$ V vs Standard hydrogen electrode (SHE)) and saturated calomel electrode (SCE) ($\text{Cl}/\text{Hg}_2\text{Cl}_2(\text{s})/\text{Hg}(\text{l})$; $E_0=0.241$ V vs SHE).
- (2) The **counter electrode** is the electrode used to close the circuit. It records the signal received from the system. This electrode is an inert material. Polished graphite or platinum are frequently employed.
- (3) The **working electrode** is the electrode where the electrochemical reactions take place. In the case under study the working electrode is the coated metal.

- (4) The **electrolyte** is a material with free ions that acts as an electric conductor. In electrochemical studies the electrolyte is a liquid fluid, being the aqueous solution the electrolyte often employed.

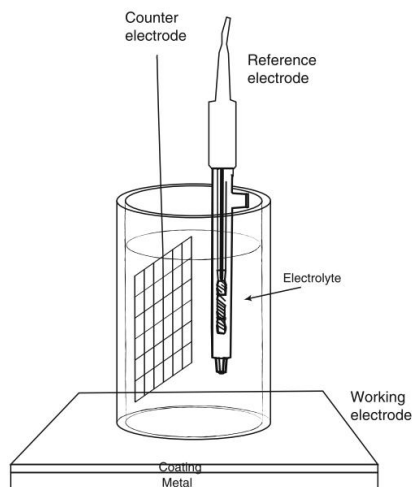


Figure 1. 12 Electrochemical cell configuration frequently used to study coated metals [121]

In order to give a physico-chemical explanation to the recorded impedances is recurrent the used of **equivalent circuits** (ECs) that combine different electrical elements. The fittings are performed using ZView software. This commercial program is based on theoretical simulations with electrical equivalent circuits, fitting techniques and complex nonlinear least-squares (CNLS) methods. The good agreement between fitted and measured data is ensured with the chi-square parameter (Chi-Sqr). Values of Chi-Sqr should be smaller than 10^{-3} to ensure the quality of the fitting [101]. Coating/metal systems are normally fitted using an EC with two relaxation times, one ascribed to the coating and the other one related with the interface metal/electrolyte. The main electrical elements of this EC are summarized in Table 1.2.

Table 1. 2 Circuit elements of the employed EC to fit the data of sol-gel coatings

	Circuit element	Frequency range
Electrolyte	Resistance of the electrolyte	High frequencies (10^5 - 10^4 Hz)
Coating	Dielectric capacitance of the coating	High-middle frequencies (10^4 - 10^1 Hz) 1 st constant time
	Resistance of the coating	
Interface metal/electrolyte	Capacitance of the double layer	Middle-low frequencies (10^1 - 10^{-2} Hz) 2 nd constant time
	Resistance of the charge transfer	

Each electrical element is identified at a specific frequency range and the physico-chemical meaning of each element is here explained:

- I. Resistance of the electrolyte: It is the resistance of the electrolyte registered between the reference electrode and the working electrode. It depends on the concentration and type of ions, the temperature and the geometry of the electrodes. In the absence of solid electrodes or gradients of concentration the electrolyte can be considered to be electrically neutral.
- II. Dielectric capacitance of the coating: The capacitance of a material is often substituted with a constant phase element (CPE) to take into account the defects of its surface such as kink, jags, ledges, local charge heterogeneities, among others. This element is described with Equation 1.6:

$$Z(\omega) = \frac{1}{Y_0(j\omega)^n} \quad (\text{Equation 1.6})$$

where j is the complex number ($j^2=-1$), Y_0 is the constant of the CPE, ω is the angular frequency of the applied signal ($\text{rad}\cdot\text{s}^{-1}$), $n=\alpha/(\pi/2)$ is the potential factor of the CPE and α is the phase angle of the CPE. The n factor is an empirical adjustable parameter that indicates the deviation from the ideal capacitive behaviour (i. e., when $n=1$) and is comprised between 0.5 and 1.

The capacitance of the materials can be estimated with the parallel-plate capacitance approximation (Equation 1.7) that consists of two thin parallel conductive plates separated by a dielectric material [120].

$$\text{CPE1} = \frac{A\varepsilon\varepsilon_0}{d} \quad (\text{Equation 1.7})$$

where $\varepsilon_0 = 8.85 \times 10^{-10} \text{ F}\cdot\text{cm}^{-1}$; ε is the permittivity of the coating, which is assumed to be 2-10 [123]; A (cm^2) is the area of the tested coating and d (cm) is the thickness of the tested coating.

The absorption of water on the coating (water uptake) increases the capacitance of the coating because the relative permittivity of the water at 25°C is higher (78.7) than the one of the coating. The water uptake is correlated with the degradation kinetics of sol-gel coatings. Thus, the evolution of the water uptake with time can be studied by monitoring the CPE of the coating with time.

- III. Resistance of the coating: Coatings manufactured by sol-gel technology normally present micro/nano-pores that allow the electrolyte to penetrate and interact with the metallic substrate. Upon immersion, the resistance of these pores varies and decreases with the exposure time to the electrolyte. If corrosion products are formed, the pores are blocked with these products and as a result the resistance of the coating increases.

- IV. Double layer capacitance: When a solid is introduced into the electrolyte electrochemical processes appear at the electrode/electrolyte interface. A structure similar to an electrical condenser is created with a distribution of a charge associated with a discrete layer of ions that balances the charge associated with the electrons at the metallic surface. Several models try to explain this phenomenon, being the simplest model the one proposed by Helmholtz.
- V. Charge-transfer resistance: This circuit element is related to the single kinetically-controlled electrochemical reactions that takes places across a certain interface. This element is inversely proportional to the corrosion rate.

Prior to the study of the coated material, the uncoated material is studied and taken as reference. In the case under study titanium is the metallic substrate. Titanium is a passive metal that, as it was discussed before, spontaneously forms a passive and protective oxide layer in contact with aqueous solutions. **Passivity** can be defined as “the phenomenon whereby a thermodynamically reactive metal (i.e., one whose Gibbs’ energy of reaction with components of the environment, such as oxygen and/or water, is negative) attains kinetic stability because of the formation of a reaction product phase on the surface” [124]. When a **coating** is applied on the metallic surface, analogue ECs to the ones used on the passive metal can be selected but replacing the contribution of the passive oxide with the coating one.

EIS can be used to evaluate the hydrolytic degradation of the sol-gel coating subjected to a physiological solution. L.C. Córdoba et al. already used this technique to study the degradation of sol-gel coatings applied on AZ31 and ZE41 Mg alloys [125]. They observed that once the delamination process of the coating reached large areas of the substrate, the electrochemical response was close to the signal recorded on the uncoated material. Others studies also reported that the first stage during the degradation of sol-gel coatings can be monitored by calculating the water up-take of coatings. This parameter is directly proportional to the capacitance of the coating, as it was previously described [126]. The electrochemical study performed with EIS can give a first approach in terms of the electrochemical behaviour of the coating in a physiological solution and its hydrolytic degradation rate.

The other electrochemical technique used in this research project is the **Scanning Electrochemical Microscopy** (SECM). SECM is a contactless scanning probe technique used to probe and study the reactions of surfaces. SECM was designed on the Bard Laboratories in the last 80’s. SECM is based on the electrochemical measure of current from the system through an **ultramicroelectrode** (UME). The UME is normally a platinum wire with a radius on the order of a few nanometers to 25 μm contained in a polished glass. The current is provided by species contained in the electrolyte. These species receive the name of **mediators** and undergo an electrochemical reaction (e.g., oxidation-reduction reaction). Ferrocene is an example of a mediator used that gets oxidized to its ferrocenium ion under a potential of 0.5 V. The others electrodes employed are a reference electrode and a counter electrode, similar to the ones used in EIS.

SECM can operate in two modes: generator/collector or **feedback mode**. This theoretical part is going to focus on the feedback mode because it is the mode that has been used in the experimental work. When the tip is on the bulk solution, the recorded signal is directly proportional to the concentration of the mediator because the reaction is kinetically controlled by the diffusion of the oxidized specie contained on the bulk solution to the electrode surface. The current decays due to the formation of a diffusion layer of mediator around the electrode, and rapidly attains a steady-state (limit current, $i_{T,\infty}$) value given by Equation 1.8 [127]:

$$i_{T,\infty} = 4nFDca \quad (\text{Equation 1.8})$$

where n , is the number of electrons in the reaction; F , the Faraday constant; D , the diffusion coefficient of the reducible species; and, c , its concentration; and a , the radius of the UME.

The presence of a substrate perturbs the signal recorded by the UME. This perturbation gives information about the electrochemical features of the sample [128]. When approaching the tip to the sample, if the surface of the substrate is **active**, the recorded current is greater than the limit current ($i > i_{T,\infty}$) and the microscope operates in **positive feedback mode**. The resulting current is greater because it is the contribution of the reaction provided by the mediator and the reactions of the active species of the substrate. Figure 1.13(A) illustrates the positive feedback response of a metal. However, if the substrate presents insulating features, the recorded current decreases and tends to zero when approaching the tip of the UME to the substrate. This mode is called **negative feedback mode** and is schematized in Figure 1.13(B). In this mode the substrate besides experiencing no active reactions, blocks the reaction of the mediator.

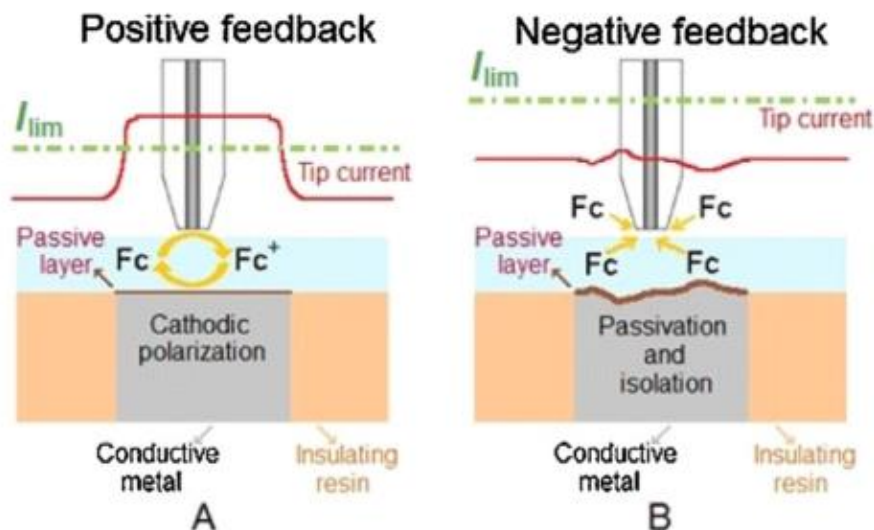


Figure 1. 13 Electrochemical responses observed for the tip current as a function of substrate polarization during amperometric SECM operation over titanium alloys exposed to a physiological solution containing ferrocenemethanol as redox mediator. (A) Positive feedback effect recorded over cathodically polarized conductive areas because of ferrocenium reduction on the substrate; (B) negative feedback effect recorded over the oxide-covered surface, which blocks the diffusion pathways for ferrocenemethanol from the bulk of the solution (adapted from [129])

During the last 10 years, it has been reported the useful characterization that SECM provides to the field of coated metals. R.M. Souto et al. have contributed to both, the theoretical and experimental development of the technique. In 2010 they contributed with an extended revision of the technique [130]. SECM has been used to study the activity of sol-gel coatings doped with inhibitors [92], [131] and metals exposed to physiological solutions [132], [133]. SECM is a potential and innovative electrochemical technique with high spatial resolution that differs from other scanning probes techniques (e.g., scanning tunneling (STM) or atomic force microscopy (AFM)) in the possibility of quantifying the chemistry of the substrates [128].

REFERENCES

- [1] P. Tranquilli Leali and A. Merolli, "Fundamentals of biomaterials," *Biomater. Hand Surg.*, pp. 1–11, 2009.
- [2] M. Navarro, A. Michiardi, O. Castan, and J. A. Planell, "Review. Biomaterials in orthopaedics," *J. R. Soc. Interface*, vol. 5, pp. 1137–1158, 2008.
- [3] B. M. Holzapfel, J. C. Reichert, J. T. Schantz, U. Gbureck, L. Rackwitz, U. Nöth, F. Jakob, M. Rudert, J. Groll, and D. W. Hutmacher, "How smart do biomaterials need to be? A translational science and clinical point of view," *Adv. Drug Deliv. Rev.*, vol. 65, no. 4, pp. 581–603, 2013.
- [4] R. Tejero, E. Anitua, and G. Orive, "Toward the biomimetic implant surface: Biopolymers on titanium-based implants for bone regeneration," *Prog. Polym. Sci.*, vol. 39, no. 7, pp. 1406–1447, 2014.
- [5] J. Enderle and J. Bronzino, *Introduction to Biomedical Engineering*, 3rd Ed. 2011.
- [6] J. Venkatesan and S. K. Kim, "Nano-hydroxyapatite composite biomaterials for bone tissue engineering - A review," *J. Biomed. Nanotechnol.*, vol. 10, no. 10, pp. 3124–3140, 2014.
- [7] H. Zhou, J. G. Lawrence, and S. B. Bhaduri, "Fabrication aspects of PLA-CaP/PLGA-CaP composites for orthopedic applications: A review," *Acta Biomater.*, vol. 8, no. 6, pp. 1999–2016, 2012.
- [8] X. Ding, H. Liu, and Y. Fan, "Graphene-Based Materials in Regenerative Medicine," *Adv. Healthc. Mater.*, vol. 4, no. 10, pp. 1451–1468, 2015.
- [9] S. C. Cifuentes, R. Gavilán, M. Lieblich, R. Benavente, and J. L. González-Carrasco, "In vitro degradation of biodegradable polylactic acid/magnesium composites: Relevance of Mg particle shape," *Acta Biomater.*, vol. 32, pp. 348–357, 2016.
- [10] L. L. Hench and J. M. Polak, "Third-Generation Biomedical Materials," *Science (80-.)*, vol. 295, no. 5557, pp. 1014–1017, 2002.
- [11] J. Gallo, M. Holinka, and C. S. Moucha, "Antibacterial surface treatment for orthopaedic implants," *Int. J. Mol. Sci.*, vol. 15, no. 8, pp. 13849–13880, 2014.
- [12] A. R. Amini, J. S. Wallace, and S. P. Nukavarapu, "Short-Term and Long-Term Effects of Orthopedic Biodegradable Implants," *J. Long. Term. Eff. Med. Implants*, vol. 21, no. 2, pp. 93–122, 2011.
- [13] J. Charnley, "Anchorage of the Femoral Head Prosthesis to the Shaft of the Femur," *Br J Bone Jt Surg*, vol. 42–B, no. 1, pp. 28–30, 1960.
- [14] M. Long and H. J. Rack, "Titanium alloys in total joint replacement--a materials science perspective," *Biomaterials*, vol. 19, no. 18, pp. 1621–1639, 1998.
- [15] S. M. Kurtz, K. L. Ong, E. Lau, M. Widmer, M. Maravic, E. Gómez-Barrena, M. De Fátima De Pina, V. Manno, M. Torre, W. L. Walter, R. De Steiger, R. G. T. Geesink, M. Peltola, and C. Röder, "International survey of primary and revision total knee replacement," *Int. Orthop.*, vol. 35, no. 12, pp. 1783–1789, 2011.
- [16] S. Kurtz, K. Ong, E. Lau, F. Mowat, and M. Halpern, "Projections of Primary and Revision Hip and Knee Arthroplasty in the United States from 2005 to 2030," *J Bone Jt. Surg Am.*, vol. 89, no. 4, p. 780–5., 2007.
- [17] D. Rodríguez-Pardo, C. Pigrau, J. Lora-Tamayo, A. Soriano, M. D. del Toro, J. Cobo, J. Palomino, G. Euba, M. Riera, M. Sánchez-Somolinos, N. Benito, M. Fernández-Sampedro, L. Sorli, L. Guio, J. A. Iribarren, J. M. Baraia-Etxaburu, A. Ramos, A. Bahamonde, X. Flores-Sánchez, P. S. Corona, and J. Ariza, "Gram-negative prosthetic joint infection: outcome of a debridement, antibiotics and implant retention approach. A large multicentre study," *Clin. Microbiol. Infect.*, vol. 242, p. 815, 2014.
- [18] J. Garrido-Gómez, M. A. Arrabal-Polo, M. S. Girón-Prieto, J. Cabello-Salas, J. Torres-Barroso, and J. Parra-Ruiz, "Descriptive analysis of the economic costs of periprosthetic joint infection of the knee for the public health system of Andalusia," *J. Arthroplasty*, vol. 28, no. 7, pp. 1057–

- 1060, 2013.
- [19] A. J. Tande and R. Patel, "Prosthetic joint infection," *Clin. Microbiol. Rev.*, vol. 27, no. 2, pp. 302–345, 2014.
- [20] H. O. Gbejuade, A. M. Lovering, and J. C. Webb, "The role of microbial biofilms in prosthetic joint infections: A review," *Acta Orthop.*, vol. 86, no. 2, pp. 147–158, 2015.
- [21] N. Benito, M. Franco, A. Ribera, A. Soriano, D. Rodriguez-Pardo, L. Sorlí, G. Fresco, M. Fernández-Sampedro, M. Dolores del Toro, L. Guío, E. Sánchez-Rivas, A. Bahamonde, M. Riera, J. Esteban, J. M. Baraia-Etxaburu, J. Martínez-Alvarez, A. Jover-Sáenz, C. Dueñas, A. Ramos, B. Sobrino, G. Euba, L. Morata, C. Pigrau, P. Coll, I. Mur, and J. Ariza, "Time trends in the aetiology of prosthetic joint infections: a multicentre cohort study," *Clin. Microbiol. Infect.*, vol. 22, no. 8, p. 732.e1-732.e8, 2016.
- [22] N. Palanisamy, N. Ferina, A. Amirulhusni, Z. Mohd-Zain, J. Hussaini, L. Ping, and R. Durairaj, "Antibiofilm properties of chemically synthesized silver nanoparticles found against *Pseudomonas aeruginosa*," *J. Nanobiotechnology*, vol. 12, no. 1, p. 2, 2014.
- [23] C. Beloin, S. Renard, J. M. Ghigo, and D. Lebeaux, "Novel approaches to combat bacterial biofilms," *Curr. Opin. Pharmacol.*, vol. 18, pp. 61–68, 2014.
- [24] C. E. Zobell and E. C. Allen, "The Significance of Marine Bacteria in the Fouling of Submerged Surfaces.," *J. Bacteriol.*, vol. 29, no. 3, pp. 239–51, 1935.
- [25] S. J. McConoughey, R. Howlin, J. F. Granger, M. M. Manring, J. H. Calhoun, M. Shirliff, S. Kathju, and P. Stoodley, "Biofilms in periprosthetic orthopedic infections.," *Future Microbiol.*, vol. 9, no. 8, pp. 987–1007, 2014.
- [26] E. Mejia, A. Williams, and M. Long, "Decreasing Prosthetic Joint Surgical Site Infections: An Interdisciplinary Approach," *AORN J.*, vol. 101, no. 2, pp. 213–222, 2015.
- [27] S. I. Berríos-Torres, C. A. Umscheid, D. W. Bratzler, B. Leas, E. C. Stone, R. R. Kelz, C. E. Reinke, S. Morgan, J. S. Solomkin, J. E. Mazuski, E. P. Dellinger, K. M. F. Itani, E. F. Berbari, J. Segreti, J. Parvizi, J. Blanchard, G. Allen, J. A. J. W. Kluytmans, R. Donlan, and W. P. Schechter, "Centers for Disease Control and Prevention Guideline for the Prevention of Surgical Site Infection, 2017," *JAMA Surg.*, vol. 152, no. 8, p. 784, 2017.
- [28] D. Chauveaux, "Preventing surgical-site infections: Measures other than antibiotics," *Orthop. Traumatol. Surg. Res.*, vol. 101, no. 1, pp. S77–S83, 2015.
- [29] J. L. Del Pozo and R. Patel, "Infection Associated with Prosthetic Joints," *N. Engl. J. Med.*, vol. 361, no. 8, pp. 787–794, 2009.
- [30] A. J. Yates, "Postoperative prophylactic antibiotics in total joint arthroplasty," *Arthroplast. Today*, vol. 4, no. 1, pp. 130–131, 2018.
- [31] J. W. Kuiper, "Treatment of acute periprosthetic infections with prosthesis retention: Review of current concepts," *World J. Orthop.*, vol. 5, no. 5, p. 667, 2014.
- [32] B. A. S. Knobben, A. J. De Vries, and P. Wierd, "Predicting failure in early acute prosthetic joint infection treated with debridement, antibiotics and implant retention: external validation of the KLIC score," *J. Arthroplasty*, vol. 33, no. 8, pp. 2582–2587, 2018.
- [33] J. W. P. Kuiper, S. J. Vos, R. Saouti, D. A. Vergroesen, H. C. A. Graat, Y. J. Debets-Ossenkopp, E. J. G. Peters, and P. A. Nolte, "Prosthetic joint-associated infections treated with DAIR (debridement, antibiotics, irrigation, and retention)," *Acta Orthop.*, vol. 84, no. 4, pp. 380–386, 2013.
- [34] I. Byren, P. Bejon, B. L. Atkins, B. Angus, S. Masters, P. McLardy-Smith, R. Gundle, and A. Berendt, "One hundred and twelve infected arthroplasties treated with 'DAIR' (debridement, antibiotics and implant retention): Antibiotic duration and outcome," *J. Antimicrob. Chemother.*, vol. 63, no. 6, pp. 1264–1271, 2009.
- [35] L. B. Engesæter, S. A. Lie, B. Espehaug, O. Furnes, S. E. Vollset, and L. I. Havelin, "Antibiotic prophylaxis in total hip arthroplasty: Effects of antibiotic prophylaxis systemically and in bone cement on the revision rate of 22,170 primary hip replacements followed 0-14 years in the

- Norwegian Arthroplasty Register,” *Acta Orthop. Scand.*, vol. 74, no. 6, pp. 644–651, 2003.
- [36] K. C. Papat, M. Eltgroth, T. J. LaTempa, C. A. Grimes, and T. A. Desai, “Titania nanotubes: A novel platform for drug-eluting coatings for medical implants?,” *Small*, vol. 3, no. 11, pp. 1878–1881, 2007.
- [37] I. V. Sukhorukova, A. N. Sheveyko, P. V. Kiryukhantsev-korneev, and I. Y. Zhitnyak, “Toward bioactive yet antibacterial surfaces,” *Colloids Surfaces B Biointerfaces*, vol. 135, pp. 158–165, 2015.
- [38] C. P. Stallard, K. A. McDonnell, O. D. Onayemi, J. P. O’Gara, and D. P. Dowling, “Evaluation of protein adsorption on atmospheric plasma deposited coatings exhibiting superhydrophilic to superhydrophobic properties,” *Biointerphases*, vol. 7, no. 1–4, pp. 1–12, 2012.
- [39] J. Ureña, E. Tejado, J. Y. Pastor, F. Velasco, S. Tsipas, A. Jiménez-Morales, and E. Gordo, “Role of beta-stabilizer elements in microstructure and mechanical properties evolution of PM modified Ti surfaces designed for biomedical applications,” *Powder Metall.*, pp. 90–99, 2018.
- [40] J. Ureña, S. Tsipas, A. Jiménez-Morales, E. Gordo, R. Detsch, and A. R. Boccaccini, “Cellular behaviour of bone marrow stromal cells on modified Ti-Nb surfaces,” *Mater. Des.*, vol. 140, pp. 452–459, 2018.
- [41] D. Zhang, C. S. Wong, C. Wen, and Y. Li, “Cellular responses of osteoblast-like cells to 17 elemental metals,” *J. Biomed. Mater. Res. - Part A*, vol. 105, no. 1, pp. 148–158, 2017.
- [42] V. S. A. Challa, S. Mali, and R. D. K. Misra, “Reduced toxicity and superior cellular response of preosteoblasts to Ti-6Al-7Nb alloy and comparison with Ti-6Al-4V,” *J. Biomed. Mater. Res. - Part A*, vol. 101 A, no. 7, pp. 2083–2089, 2013.
- [43] M. Niinomi, Y. Liu, M. Nakai, H. Liu, and H. Li, “Biomedical titanium alloys with Young’s moduli close to that of cortical bone,” *Regen. Biomater.*, vol. 3, no. 3, pp. 173–185, 2016.
- [44] M. Kulkarni, A. Mazare, P. Schmuki, and A. Iglič, “Biomaterial surface modification of titanium and titanium alloys for medical applications,” *Nanomedicine*, pp. 111–136, 2014.
- [45] V. Goriainov, R. Cook, J. M. Latham, D. G. Dunlop, and R. O. C. Oreffo, “Bone and metal: An orthopaedic perspective on osseointegration of metals,” *Acta Biomater.*, vol. 10, no. 10, pp. 4043–4057, 2014.
- [46] M. R. Kalu, J. P. Schreckenbach, and H. Graf, “Titanium dental implant surfaces obtained by anodic spark deposition – From the past to the future,” *Mater. Sci. Eng. C*, vol. 69, pp. 1429–1441, 2016.
- [47] L. Bolzoni, E. M. Ruiz-Navas, and E. Gordo, “Quantifying the properties of low-cost powder metallurgy titanium alloys,” *Mater. Sci. Eng. A*, vol. 687, pp. 47–53, 2017.
- [48] A. Amherd Hidalgo, R. Frykholm, T. Ebel, and F. Pyczak, “Powder Metallurgy Strategies to Improve Properties and Processing of Titanium Alloys: A Review,” *Adv. Eng. Mater.*, vol. 19, no. 6, pp. 1–14, 2017.
- [49] L. Bolzoni, E. M. Ruiz-Navas, and E. Gordo, “Evaluation of the mechanical properties of powder metallurgy Ti-6Al-7Nb alloy,” *J. Mech. Behav. Biomed. Mater.*, vol. 67, pp. 110–116, 2017.
- [50] L. Bolzoni, E. M. Ruiz-Navas, and E. Gordo, “Feasibility study of the production of biomedical Ti-6Al-4V alloy by powder metallurgy,” *Mater. Sci. Eng. C*, vol. 49, pp. 400–407, 2015.
- [51] L. Bolzoni, E. M. Ruiz-Navas, and E. Gordo, “Powder metallurgy CP-Ti performances: Hydride-dehydride vs. sponge,” *Mater. Des.*, vol. 60, pp. 226–232, 2014.
- [52] R. G. Neves, B. Ferrari, A. J. Sanchez-Herencia, and E. Gordo, “Colloidal approach for the design of Ti powders sinterable at low temperature,” *Mater. Lett.*, vol. 107, pp. 75–78, 2013.
- [53] E. N. Bolbasov, P. V. Maryin, K. S. Stankevich, A. I. Kozelskaya, E. V. Shesterikov, Y. I. Khodyrevskaya, M. V. Nasonova, D. K. Shishkova, Y. A. Kudryavtseva, Y. G. Anissimov, and S. I. Tverdokhlebov, “Surface modification of electrospun poly-(L-lactic) acid scaffolds by reactive magnetron sputtering,” *Colloids Surfaces B Biointerfaces*, vol. 162, pp. 43–51, 2018.

- [54] J. Sharan, V. Koul, A. K. Dinda, O. P. Kharbanda, S. V. Lale, R. Duggal, M. Mishra, G. Gupta, and M. P. Singh, "Bio-functionalization of grade V titanium alloy with type I human collagen for enhancing and promoting human periodontal fibroblast cell adhesion – an in-vitro study," *Colloids Surfaces B Biointerfaces*, vol. 161, pp. 1–9, 2018.
- [55] S. B. Goodman, Z. Yao, M. Keeney, and F. Yang, "The future of biologic coatings for orthopaedic implants," *Biomaterials*, vol. 34, no. 13, pp. 3174–3183, 2013.
- [56] T. Kumeria, H. Mon, M. S. Aw, K. Gulati, A. Santos, H. J. Griesser, and D. Losic, "Advanced biopolymer-coated drug-releasing titania nanotubes (TNTs) implants with simultaneously enhanced osteoblast adhesion and antibacterial properties," *Colloids Surfaces B Biointerfaces*, vol. 130, pp. 255–263, 2015.
- [57] P. Liu, Y. Hao, Y. Zhao, Z. Yuan, Y. Ding, and K. Cai, "Surface modification of titanium substrates for enhanced osteogenetic and antibacterial properties," *Colloids Surfaces B Biointerfaces*, vol. 160, pp. 110–116, 2017.
- [58] X. Wang, S. Xu, S. Zhou, W. Xu, M. Leary, P. Choong, M. Qian, M. Brandt, and Y. M. Xie, "Topological design and additive manufacturing of porous metals for bone scaffolds and orthopaedic implants: A review," *Biomaterials*, vol. 83, pp. 127–141, 2016.
- [59] J. Ureña, C. Mendoza, B. Ferrari, Y. Castro, S. A. Tsipas, A. Jiménez-Morales, and E. Gordo, "Surface Modification of Powder Metallurgy Titanium by Colloidal Techniques and Diffusion Processes for Biomedical Applications," *Adv. Eng. Mater.*, vol. 19, no. 6, p. 1600060, 2017.
- [60] J. Ureña, S. Tsipas, A. Jiménez-Morales, E. Gordo, R. Detsch, and A. R. Boccaccini, "In-vitro study of the bioactivity and cytotoxicity response of Ti surfaces modified by Nb and Mo diffusion treatments," *Surf. Coatings Technol.*, vol. 335, pp. 148–158, 2018.
- [61] E. J. Tobin, "Recent coating developments for combination devices in orthopedic and dental applications: A literature review," *Adv. Drug Deliv. Rev.*, vol. 112, pp. 88–100, 2016.
- [62] F. A. Shah, M. Trobos, P. Thomsen, and A. Palmquist, "Commercially pure titanium (cp-Ti) versus titanium alloy (Ti6Al4V) materials as bone anchored implants - Is one truly better than the other?," *Mater. Sci. Eng. C*, vol. 62, pp. 960–966, 2016.
- [63] M. V. Cardoso, J. de Rycker, A. Chaudhari, E. Coutinho, Y. Yoshida, B. Van Meerbeek, M. F. Mesquita, W. J. da Silva, K. Yoshihara, K. Vandamme, and J. Duyck, "Titanium implant functionalization with phosphate-containing polymers may favour in vivo osseointegration," *J. Clin. Periodontol.*, vol. 44, no. 9, pp. 950–960, 2017.
- [64] Y. K. Liu, Q. Z. Lu, R. Pei, H. J. Ji, G. S. Zhou, X. L. Zhao, R. K. Tang, and M. Zhang, "The effect of extracellular calcium and inorganic phosphate on the growth and osteogenic differentiation of mesenchymal stem cells in vitro: Implication for bone tissue engineering," *Biomed. Mater.*, vol. 4, no. 2, 2009.
- [65] V. K. Truong, R. Lapovok, Y. S. Estrin, S. Rundell, J. Y. Wang, C. J. Fluke, R. J. Crawford, and E. P. Ivanova, "The influence of nano-scale surface roughness on bacterial adhesion to ultrafine-grained titanium," *Biomaterials*, vol. 31, no. 13, pp. 3674–3683, 2010.
- [66] D. Karazisis, S. Petronis, H. Agheli, L. Emanuelsson, B. Norlindh, A. Johansson, L. Rasmusson, P. Thomsen, and O. Omar, "The influence of controlled surface nanotopography on the early biological events of osseointegration," *Acta Biomater.*, vol. 53, pp. 559–571, 2017.
- [67] C. Perez-Jorge, M. A. Arenas, A. Conde, J. M. Hernández-Lopez, J. J. de Damborenea, S. Fisher, A. M. A. Hunt, J. Esteban, and G. James, "Bacterial and fungal biofilm formation on anodized titanium alloys with fluorine," *J. Mater. Sci. Mater. Med.*, vol. 28, no. 1, 2017.
- [68] J. Hendriks, J. Riesle, and C. A. van Blitterswijk, "Co-culture in cartilage tissue engineering," *J. Tissue Eng. Regen. Med.*, vol. 4, no. 7, pp. 524–531, 2010.
- [69] E. J. Falde, S. T. Yohe, Y. L. Colson, and M. W. Grinstaff, "Superhydrophobic materials for biomedical applications," *Biomaterials*, vol. 104, pp. 87–103, 2016.
- [70] S. A. Mahadik, F. Pedraza, S. S. Mahadik, B. P. Relekar, and S. S. Thorat, "Biocompatible superhydrophobic coating material for biomedical applications," *J. Sol-Gel Sci. Technol.*, vol. 81, no. 3, pp. 791–796, 2017.

- [71] G. A. Junter, P. Thébault, and L. Lebrun, "Polysaccharide-based antibiofilm surfaces," *Acta Biomater.*, vol. 30, pp. 13–25, 2016.
- [72] A. K. Muszanska, E. T. J. Rochford, A. Gruszka, A. A. Bastian, H. J. Busscher, W. Norde, H. C. Van Der Mei, and A. Herrmann, "Antiadhesive polymer brush coating functionalized with antimicrobial and RGD peptides to reduce biofilm formation and enhance tissue integration," *Biomacromolecules*, vol. 15, no. 6, pp. 2019–2026, 2014.
- [73] F. D'Este, D. Oro, G. Boix-Lemonche, A. Tossi, and B. Skerlavaj, "Evaluation of free or anchored antimicrobial peptides as candidates for the prevention of orthopaedic device-related infections," *J. Pept. Sci.*, vol. 23, no. 10, pp. 777–789, 2017.
- [74] V. Pandit, J. M. Zuidema, K. N. Venuto, J. Macione, G. Dai, R. J. Gilbert, and S. P. Kotha, "Evaluation of Multifunctional Polysaccharide Hydrogels with Varying Stiffness for Bone Tissue Engineering," *Tissue Eng. Part A*, vol. 19, no. 21–22, pp. 2452–2463, 2013.
- [75] J. J. T. M. Swartjes, P. K. Sharma, T. G. Kooten, H. C. Mei, M. Mahmoudi, H. J. Busscher, and E. T. J. Rochford, "Current Developments in Antimicrobial Surface Coatings for Biomedical Applications," *Curr. Med. Chem.*, vol. 22, no. 18, pp. 2116–2129, 2015.
- [76] O. Robertsson, O. Thompson, A. W-Dahl, M. Sundberg, L. Lidgren, and A. Stefánsdóttir, "Higher risk of revision for infection using systemic clindamycin prophylaxis than with cloxacillin: A report from the Swedish Knee Arthroplasty Register on 78,000 primary total knee arthroplasties for osteoarthritis," *Acta Orthop.*, vol. 88, no. 5, pp. 562–567, 2017.
- [77] F. Greimel, C. Scheuerer, A. Gessner, M. Simon, T. Kalteis, J. Grifka, A. Benditz, H. R. Springorum, and J. Schaumburger, "Efficacy of antibiotic treatment of implant-associated *Staphylococcus aureus* infections with moxifloxacin, flucloxacillin, rifampin, and combination therapy: An animal study," *Drug Des. Devel. Ther.*, vol. 11, pp. 1729–1736, 2017.
- [78] M. Wouthuyzen-Bakker, E. Tornero, L. Morata, P. V. Nannan Panday, P. C. Jutte, G. Bori, G. A. Kampinga, and A. Soriano, "Moxifloxacin plus rifampin as an alternative for levofloxacin plus rifampin in the treatment of a prosthetic joint infection with *Staphylococcus aureus*," *Int. J. Antimicrob. Agents*, vol. 51, no. 1, pp. 38–42, 2018.
- [79] K. Anagnostakos and K. Schrder, "Antibiotic-impregnated bone grafts in orthopaedic and trauma surgery: A systematic review of the literature," *Int. J. Biomater.*, no. 2012: 53806, 2012.
- [80] A. Shukla, R. C. Fuller, and P. T. Hammond, "Design of multi-drug release coatings targeting infection and inflammation," *J. Control. Release*, vol. 155, no. 2, pp. 159–166, 2011.
- [81] M. J. Juan-Díaz, M. Martínez-Ibáñez, M. Hernández-Escolano, L. Cabedo, R. Izquierdo, J. Suay, M. Gurruchaga, and I. Goñi, "Study of the degradation of hybrid sol-gel coatings in aqueous medium," *Prog. Org. Coatings*, vol. 77, no. 11, pp. 1799–1806, 2014.
- [82] D. Wang and G. P. Bierwagen, "Sol-gel coatings on metals for corrosion protection," *Prog. Org. Coatings*, vol. 64, no. 4, pp. 327–338, 2009.
- [83] G. Malucelli, "Hybrid Organic/Inorganic Coatings Through Dual-Cure Processes: State of the Art and Perspectives," *Coatings*, vol. 6, no. 1, p. 10, 2016.
- [84] C. J. Brinker and G. W. Scherer, *Sol-gel Science: The Physics and Chemistry of Sol-gel Processing*. 1990.
- [85] M. Faustini, D. Grosso, and R. Backov, "'Integrative sol – gel chemistry': a nanofoundry for materials science," *J Sol-Gel Sci Technol*, pp. 216–226, 2014.
- [86] C. Brinker and G. Scherer, "Sol-Gel Science: The Physics and Chemistry of Sol-Gel Processing," *Advanced Materials*, vol. 3, no. 10, p. 912, 1990.
- [87] M. J. Juan-Díaz, M. Martínez-Ibáñez, I. Lara-Sáez, S. da Silva, R. Izquierdo, M. Gurruchaga, I. Goñi, and J. Suay, "Development of hybrid sol-gel coatings for the improvement of metallic biomaterials performance," *Prog. Org. Coatings*, vol. 96, pp. 42–51, 2015.
- [88] S. Zheng and J. Li, "Inorganic-organic sol gel hybrid coatings for corrosion protection of metals," *J. Sol-Gel Sci. Technol.*, vol. 54, no. 2, pp. 174–187, 2010.
- [89] A. Jiménez-Morales, J. C. Galván, and P. Aranda, "A new silver-ion selective sensor based on

- a polythiacrown-ether entrapped by sol-gel,” *Electrochim. Acta*, vol. 47, no. 13–14, pp. 2281–2287, 2002.
- [90] J. Wang, “Electrochemical biosensing based on noble metal nanoparticles,” *Microchim. Acta*, vol. 177, no. 3–4, pp. 245–270, 2012.
- [91] H. Rahimi, R. Mozaffarinia, A. Hojjati Najafabadi, R. Shoja Razavi, and E. Paimozd, “Optimization of process factors for the synthesis of advanced chrome-free nanocomposite sol-gel coatings for corrosion protection of marine aluminum alloy AA5083 by design of experiment,” *Prog. Org. Coatings*, vol. 76, no. 2–3, pp. 307–317, 2013.
- [92] D. J. Carbonell, A. García-Casas, J. Izquierdo, R. M. Souto, J. C. Galván, and A. Jiménez-Morales, “Scanning electrochemical microscopy characterization of sol-gel coatings applied on AA2024-T3 substrate for corrosion protection,” *Corros. Sci.*, vol. 111, pp. 625–636, 2016.
- [93] D. Raps, T. Hack, J. Wehr, M. L. Zheludkevich, A. C. Bastos, M. G. S. Ferreira, and O. Nuyken, “Electrochemical study of inhibitor-containing organic-inorganic hybrid coatings on AA2024,” *Corros. Sci.*, vol. 51, no. 5, pp. 1012–1021, 2009.
- [94] M. Raimondo, F. Veronesi, G. Boveri, G. Guarini, A. Motta, and R. Zanoni, “Superhydrophobic properties induced by sol-gel routes on copper surfaces,” *Appl. Surf. Sci.*, vol. 422, pp. 1022–1029, 2017.
- [95] A. Alcántara-García, A. García-Casas, and A. Jiménez-Morales, “Electrochemical study of the synergic effect of phosphorus and cerium additions on a sol-gel coating for Titanium manufactured by powder metallurgy,” *Prog. Org. Coatings*, vol. 124, pp. 267–274, 2018.
- [96] M. Hernández-Escolano, M. Juan-Díaz, M. Martínez-Ibáñez, A. Jiménez-Morales, I. Goñi, M. Gurruchaga, and J. Suay, “The design and characterisation of sol-gel coatings for the controlled-release of active molecules,” *J. Sol-Gel Sci. Technol.*, vol. 64, no. 2, pp. 442–451, 2012.
- [97] S. Radin and P. Ducheyne, “Controlled release of vancomycin from thin sol-gel films on titanium alloy fracture plate material,” *Biomaterials*, vol. 28, no. 9, pp. 1721–1729, 2007.
- [98] X. Yang, P. Huang, H. Wang, S. Cai, Y. Liao, Z. Mo, X. Xu, C. Ding, C. Zhao, and J. Li, “Antibacterial and anti-biofouling coating on hydroxyapatite surface based on peptide-modified tannic acid,” *Colloids Surfaces B Biointerfaces*, vol. 160, pp. 136–143, 2017.
- [99] L. Forte, S. Sarda, C. Combes, F. Brouillet, M. Gazzano, O. Marsan, E. Boanini, and A. Bigi, “Hydroxyapatite functionalization to trigger adsorption and release of risedronate,” *Colloids Surfaces B Biointerfaces*, vol. 160, pp. 493–499, 2017.
- [100] A. Szcześ, L. Hołysz, and E. Chibowski, “Synthesis of hydroxyapatite for biomedical applications,” *Adv. Colloid Interface Sci.*, vol. 249, pp. 321–330, 2017.
- [101] A. El Hadad, E. Peón, F. García-Galván, V. Barranco, J. Parra, A. Jiménez-Morales, and J. Galván, “Biocompatibility and Corrosion Protection Behaviour of Hydroxyapatite Sol-Gel-Derived Coatings on Ti6Al4V Alloy,” *Materials (Basel)*, vol. 10, no. 2, p. 94, 2017.
- [102] R. I. M. Asri, W. S. W. Harun, M. A. Hassan, S. A. C. Ghani, and Z. Buyong, “A review of hydroxyapatite-based coating techniques: Sol-gel and electrochemical depositions on biocompatible metals,” *J. Mech. Behav. Biomed. Mater.*, vol. 57, pp. 95–108, 2016.
- [103] T. T. Phan, F. Bentiss, and C. Jama, “Structural and anticorrosion performance characterization of phosphosilicate sol-gel coatings prepared from 3-(trimethoxysilyl) propyl methacrylate and bis[2-(methacryloyloxy)ethyl] phosphate,” *Prog. Org. Coatings*, vol. 89, pp. 123–131, 2015.
- [104] C. Domínguez-Trujillo, E. Peón, E. Chicardi, H. Pérez, J. A. Rodríguez-Ortiz, J. J. Pavón, J. García-Couce, J. C. Galván, F. García-Moreno, and Y. Torres, “Sol-gel deposition of hydroxyapatite coatings on porous titanium for biomedical applications,” *Surf. Coatings Technol.*, vol. 333, pp. 158–162, 2018.
- [105] D. C. Romoñi, J. Iskra, M. Bele, I. Demetrescu, and I. Milošev, “Elaboration and characterization of fluorohydroxyapatite and fluoroapatite sol-gel coatings on CoCrMo alloy,” *J. Alloys Compd.*, vol. 665, pp. 355–364, 2016.

- [106] A. Bral and M. Y. Mommaerts, "In vivo biofunctionalization of titanium patient-specific implants with nano hydroxyapatite and other nano calcium phosphate coatings: A systematic review," *J. Cranio-Maxillofacial Surg.*, vol. 44, no. 4, pp. 400–412, 2016.
- [107] M. Catauro, F. Bollino, R. Giovanardi, and P. Veronesi, "Modification of Ti6Al4V implant surfaces by biocompatible TiO₂/PCL hybrid layers prepared via sol-gel dip coating: Structural characterization, mechanical and corrosion behavior," *Mater. Sci. Eng. C*, vol. 74, pp. 501–507, 2017.
- [108] M. Catauro, F. Bollino, F. Papale, C. Ferrara, and P. Mustarelli, "Silica-polyethylene glycol hybrids synthesized by sol-gel: Biocompatibility improvement of titanium implants by coating," *Mater. Sci. Eng. C*, vol. 55, pp. 118–125, 2015.
- [109] S. Omar, F. Repp, P. M. Desimone, R. Weinkamer, W. Wagermaier, S. Ceré, and J. Ballarre, "Sol-gel hybrid coatings with strontium-doped 45S5 glass particles for enhancing the performance of stainless steel implants: Electrochemical, bioactive and in vivo response," *J. Non. Cryst. Solids*, vol. 425, pp. 1–10, 2015.
- [110] O. Kaygili, S. Keser, M. Kom, Y. Eroksuz, S. V. Dorozhkin, T. Ates, I. H. Ozercan, C. Tatar, and F. Yakuphanoglu, "Strontium substituted hydroxyapatites: Synthesis and determination of their structural properties, in vitro and in vivo performance," *Mater. Sci. Eng. C*, vol. 55, pp. 538–546, 2015.
- [111] M. Martínez-ibañez, I. Aldalur, F. J. Romero-Gavilán, J. Suay, I. Goñi, and M. Gurruchaga, "Design of nanostructured siloxane-gelatin coatings: Immobilization strategies and dissolution properties," *J. Non. Cryst. Solids*, vol. 481, pp. 368–374, 2017.
- [112] K. Sinkó, A. Meiszterics, J. Rohonczy, B. Kobzi, and S. Kubuki, "Effect of phosphorus precursors on the structure of bioactive calcium phosphate silicate systems," *Mater. Sci. Eng. C*, vol. 73, pp. 767–777, 2017.
- [113] J. Bronzino, *The Biomedical Engineering Handbook*, Second Edi. Boca Raton, Florida: CRC Press, 2000.
- [114] J. Jacobs, J. Gilbert, and R. Urban, "Current Concepts Review-Corrosion of Metal Orthopaedic Implants," *J Bone Jt. Surg*, vol. 80, pp. 268–82, 1998.
- [115] K. Yokoyama, T. Ichikawa, H. Murakami, Y. Miyamoto, and K. Asaoka, "Fracture mechanisms of retrieved titanium screw thread in dental implant," *Biomaterials*, vol. 23, no. 12, pp. 2459–2465, 2002.
- [116] Y. H. Li, G. B. Rao, L. J. Rong, and Y. Y. Li, "The influence of porosity on corrosion characteristics of porous NiTi alloy in simulated body fluid," *Mater. Lett.*, vol. 57, no. 2, pp. 448–451, 2002.
- [117] K. H. W. Seah, R. Thampuran, and S. H. Teoh, "The influence of pore morphology on corrosion," *Corros. Sci.*, vol. 40, no. 4–5, pp. 547–556, 1998.
- [118] A. C. Alves, I. Sendão, E. Ariza, F. Toptan, P. Ponthiaux, and A. M. P. Pinto, "Corrosion behaviour of porous Ti intended for biomedical applications," *J. Porous Mater.*, vol. 23, no. 5, pp. 1261–1268, 2016.
- [119] J.-L. Wang, R. L. Liu, T. Majumdar, S. A. Mantri, V. A. Ravi, R. Banerjee, and N. Birbilis, "A closer look at the in vitro electrochemical characterisation of titanium alloys for biomedical applications using in-situ methods," *Acta Biomater.*, vol. 54, pp. 469–478, 2017.
- [120] M. E. Orazem and B. Tribollet, *Electrochemical impedance spectroscopy*, vol. 48. 2008.
- [121] E. Cano, D. Lafuente, and D. M. Bastidas, "Use of EIS for the evaluation of the protective properties of coatings for metallic cultural heritage: A review," *J. Solid State Electrochem.*, vol. 14, no. 3, pp. 381–391, 2010.
- [122] A. Jiménez-Morales and J. C. Galán Sierra, "Espectroscopía de impedancia electroquímica aplicada al estudio de la corrosión y protección de superficies metálicas," in *Ciencia e ingeniería de superficie de los materiales metálicos*, J. J. de D. (CSIC) A. J. Vázquez, Ed. 2000, pp. 426–440.

- [123] A. Perrotta, S. J. García, and M. Creatore, “Ellipsometric Porosimetry and Electrochemical Impedance Spectroscopy Characterization for Moisture Permeation Barrier Layers,” *Plasma Process. Polym.*, vol. 12, no. 9, pp. 968–979, 2015.
- [124] E. Barsoukov and J. R. Macdonald, Eds., *Impedance Spectroscopy Theory, Experiment, and Applications*, Second Edi. 2010.
- [125] L. C. Córdoba, M. F. Montemor, and T. Coradin, “Silane/TiO₂ coating to control the corrosion rate of magnesium alloys in simulated body fluid,” *Corros. Sci.*, vol. 104, pp. 152–161, 2016.
- [126] F. Romero-Gavilán, S. Barros-Silva, J. Garcia-Cañadas, B. Palla, R. Izquierdo, M. Gurruchaga, I. Goñi, and J. Suay, “Control of the degradation of silica sol-gel hybrid coatings for metal implants prepared by the triple combination of alkoxy silanes,” *J. Non. Cryst. Solids*, vol. 453, pp. 66–73, 2016.
- [127] R. M. Souto, S. V Lamaka, and S. González, “Uses of Scanning Electrochemical Microscopy in Corrosion Research,” *Microsc. Sci. Technol. Appl. Educ.*, vol. 3, pp. 1769–1780, 2010.
- [128] C. G. Zoski, “Review—Advances in Scanning Electrochemical Microscopy (SECM),” *J. Electrochem. Soc.*, vol. 163, no. 4, pp. H3088–H3100, 2016.
- [129] J. Izquierdo, M. B. González-Marrero, M. Bozorg, B. M. Fernández-Pérez, H. C. Vasconcelos, J. J. Santana, and R. M. Souto, “Multiscale electrochemical analysis of the corrosion of titanium and nitinol for implant applications,” *Electrochim. Acta*, vol. 203, pp. 366–378, 2015.
- [130] Y. González-García, J. J. Santana, J. González-Guzmán, J. Izquierdo, S. González, and R. M. Souto, “Scanning electrochemical microscopy for the investigation of localized degradation processes in coated metals,” *Prog. Org. Coatings*, vol. 69, no. 2, pp. 110–117, 2010.
- [131] I. Recloux, Y. Gonzalez-Garcia, M.-E. Druart, F. Khelifa, P. Dubois, J. M. C. Mol, and M.-G. Olivier, “Active and passive protection of AA2024-T3 by a hybrid inhibitor doped mesoporous sol-gel and top coating system,” *Surf. Coatings Technol.*, vol. 303, no. Part B, pp. 352–361, 2015.
- [132] D. Mareci, G. Bolat, J. Izquierdo, C. Crimu, C. Munteanu, I. Antoniac, and R. M. Souto, “Electrochemical characteristics of bioresorbable binary MgCa alloys in Ringer’s solution: Revealing the impact of local pH distributions during in-vitro dissolution,” *Mater. Sci. Eng. C*, vol. 60, pp. 402–410, 2016.
- [133] J. Izquierdo, G. Bolat, D. Mareci, C. Munteanu, S. González, and R. M. Souto, “Electrochemical behaviour of ZrTi alloys in artificial physiological solution simulating in vitro inflammatory conditions,” *Appl. Surf. Sci.*, vol. 313, pp. 259–266, 2014.

CHAPTER 2

MOTIVATION AND OBJECTIVES

2.1	MOTIVATION.....	37
2.2	OBJECTIVES.....	38
	REFERENCES.....	39

2. MOTIVATION AND OBJECTIVES

2.1 MOTIVATION

The increase in the **life expectancy** of the population in the developed countries is accompanied with an increase of chronic diseases, which in most of the cases require the application of surgical procedures. The **enhancement of the patient's well-being** is of main concern in hospitals and among the surgical procedures performed this research has been focus on the improvement of **arthroplasties**. The number of arthroplasties for total knee and hip replacements has been projected to increase from 2005 to 2030 in the United States. The total knee arthroplasties (TKA) will almost double by 2030 whereas, the numbers of hip replacements will be multiplied per seven in 25 years [1]. This trend was also forecasted in different developed countries around the world: an international survey of TKA performed in 18 countries ranged the annual growth of TKA per country from 5.3% (France) to 17% (Portugal). In this study Spain reached the 11.5% of annual growth and United States the 7.9% [2].

The success of a prosthetic replacement is sometimes compromised due to the appearance of several complications during the procedure. The contraction of **bacterial infections** is the second cause of failure on prosthetic replacements [3]. The incidence of prosthetic joint infections (PJIs) is low (1-2%) but they incur **high costs** to the health care system and alter the well-being of patients. The current therapies used to counteract these infections are based in the administration of DAIR procedures (debridement, antibiotic and implant retention) that are often inefficient [4]–[6]. The success of DAIR procedures varies from 14% to 100% and depends on several external factors. To increase the ratio of success, **local prophylactic therapies** are being proposed as alternative therapies in combination with systemic therapies (e.g., oral and intravenous administration of antibiotics). A clear window of opportunities has been identified at early stages of the development of bacterial infections where the adsorption of bacteria is still reversible [7], [8]. An attractive strategy is the use of **multifunctional** materials that can assist both, the prevention and the treatment of bacterial infections.

Besides the complications due to the colonization of the biomaterial by bacterial cells, the integration of the biomaterial with the host is of paramount importance [9], [10]. Arthroplasties often employ **titanium-based materials** because they have excellent corrosion and mechanical properties. Ti-based materials however, lack **active surfaces** to assist the osseointegration of the replacement [9]. An easy procedure to provide the metal with activity is to apply surface modifications or coatings to the metallic surface. In this context, **sol-gel coatings** have been proposed as surface modification of Ti-based prostheses. The sol-gel methodology is a versatile technology that allows the “customization” of coatings with a manufacturing procedure that employs room temperature [11]. The technology offers the possibility of **bio-functionalizing** coatings with different compounds depending on the requirements of the biomedical device.

2.2 OBJECTIVES

The main goal of this Doctoral Thesis is the design of **multifunctional** and **biodegradable sol-gel coatings** for prosthetic devices. The sol-gel coating is developed as a local prophylactic therapy to **prevent** and **treat bacterial infections** associated to joint prostheses. Besides, coatings are designed to enhance the **osseointegration** of the material with the host. This objective is accomplished with the following partial objectives:

- i. To optimize the sol-gel matrix employing a **Taguchi** method and varying different parameters of the sol-gel synthesis (the molar ratio of the precursors, the reaction time of the sol-gel synthesis and the temperature of the drying step). The goal is to minimize the number of the prepared routes and evaluate the influence of each parameter on the hydrophilicity/hydrophobicity of the coatings.
- ii. To bio-functionalize the sol-gel coating with **phosphorus-based compounds** to enhance the osseointegration of the biomaterial with the host.
- iii. To bio-functionalize the sol-gel coating with an antibiotic, **moxifloxacin (MOX)**, to treat and prevent prosthetic joint infections associated with bacteria.
- iv. To study the **degradation kinetics** of sol-gel coatings with two **electrochemical techniques**: (1) an averaging technique, Electrochemical Impedance Spectroscopy (EIS), and a high spatially-resolved technique, Scanning Electrochemical Microscopy (SECM). Tests have been performed in phosphate buffered solution (PBS) at 37°C.
- v. To study the biological behaviour of coatings loaded with MOX. For this purpose the therapeutic prevention has been evaluated with the study of the **bacterial adhesion** of the main species that causes infection (*Staphylococcus aureus*, *Staphylococcus epidermidis* and *Escherichia coli*); the therapeutic treatment has been evaluated by exposing coatings to **mature biofilms** of the same bacterial species used in the bacterial adhesion test. Moreover the **non-cytotoxicity** and the **cellular proliferation** of coatings have been verified with MC3T3-E1 cells.

REFERENCES

- [1] S. Kurtz, K. Ong, E. Lau, F. Mowat, and M. Halpern, "Projections of Primary and Revision Hip and Knee Arthroplasty in the United States from 2005 to 2030," *J Bone Jt. Surg Am.*, vol. 89, no. 4, p. 780–5., 2007.
- [2] S. M. Kurtz, K. L. Ong, E. Lau, M. Widmer, M. Maravic, E. Gómez-Barrena, M. De Fátima De Pina, V. Manno, M. Torre, W. L. Walter, R. De Steiger, R. G. T. Geesink, M. Peltola, and C. Röder, "International survey of primary and revision total knee replacement," *Int. Orthop.*, vol. 35, no. 12, pp. 1783–1789, 2011.
- [3] D. Rodríguez-Pardo, C. Pigrau, J. Lora-Tamayo, A. Soriano, M. D. del Toro, J. Cobo, J. Palomino, G. Euba, M. Riera, M. Sánchez-Somolinos, N. Benito, M. Fernández-Sampedro, L. Sorli, L. Guio, J. A. Iribarren, J. M. Baraia-Etxaburu, A. Ramos, A. Bahamonde, X. Flores-Sánchez, P. S. Corona, J. Ariza, C. Amat, M. N. Larrosa, M. Puig, O. Murillo, X. Cabo, M. Á. Goenaga, M. Elola, G. De la Herrán, J. M. García-Arenzana, S. García-Ramiro, J. C. Martínez-Pastor, E. Tornero, J. M. García-Lechuz, M. Marín, M. Villanueva, I. López, R. Cisterna, J. M. Santamaría, M. J. Gómez, A. Puente, P. Cano, J. P. Horcajada, P. González-Mínguez, E. Portillo, L. Puig, M. Franco, M. Jordán, P. Coll, J. Amador-Mellado, C. Fuster-Foz, L. García-Paíno, I. Nieto, M. Á. Muniain, A. I. Suárez, J. Praena, M. J. Gómez, A. Puente, M. A. Maseguer, E. Garagorri, V. Pintado, C. Marinescu, A. Ramírez, F. Montaner, E. Múñez, T. Álvarez, R. García, E. Puente, C. Salas, M. C. Fariñas, J. M. Pérez, B. V. Achabal, and J. M. Montejo Baranda, "Gram-negative prosthetic joint infection: Outcome of a debridement, antibiotics and implant retention approach. A large multicentre study," *Clin. Microbiol. Infect.*, vol. 20, no. 11, pp. O911–O919, 2014.
- [4] J. W. Kuiper, "Treatment of acute periprosthetic infections with prosthesis retention: Review of current concepts," *World J. Orthop.*, vol. 5, no. 5, p. 667, 2014.
- [5] B. A. S. Knobben, A. J. De Vries, and P. Wierd, "Predicting failure in early acute prosthetic joint infection treated with debridement, antibiotics and implant retention: external validation of the KLIC score," *J. Arthroplasty*, vol. 33, no. 8, pp. 2582–2587, 2018.
- [6] J. W. P. Kuiper, S. J. Vos, R. Saouti, D. A. Vergroesen, H. C. A. Graat, Y. J. Debets-Ossenkopp, E. J. G. Peters, and P. A. Nolte, "Prosthetic joint-associated infections treated with DAIR (debridement, antibiotics, irrigation, and retention)," *Acta Orthop.*, vol. 84, no. 4, pp. 380–386, 2013.
- [7] N. Palanisamy, N. Ferina, A. Amirulhusni, Z. Mohd-Zain, J. Hussaini, L. Ping, and R. Durairaj, "Antibiofilm properties of chemically synthesized silver nanoparticles found against *Pseudomonas aeruginosa*," *J. Nanobiotechnology*, vol. 12, no. 1, p. 2, 2014.
- [8] C. Beloin, S. Renard, J. M. Ghigo, and D. Lebeaux, "Novel approaches to combat bacterial biofilms," *Curr. Opin. Pharmacol.*, vol. 18, pp. 61–68, 2014.
- [9] R. Tejero, E. Anitua, and G. Orive, "Toward the biomimetic implant surface: Biopolymers on titanium-based implants for bone regeneration," *Prog. Polym. Sci.*, vol. 39, no. 7, pp. 1406–1447, 2014.
- [10] J. Enderle and J. Bronzino, *Introduction to Biomedical Engineering*, 3rd Ed. 2011.
- [11] D. Wang and G. P. Bierwagen, "Sol-gel coatings on metals for corrosion protection," *Prog. Org. Coatings*, vol. 64, no. 4, pp. 327–338, 2009.

CHAPTER 3

EXPERIMENTAL WORK

3.1	MATERIALS.....	43
3.2	SYNTHESIS CHARACTERIZATION	44
3.3	XEROGEL CHARACTERIZATION	46
3.4	SURFACE CHARACTERIZATION	47
3.5	ELECTROCHEMICAL CHARACTERIZATION.....	48
3.6	BIOLOGICAL CHARACTERIZATION.....	50
3.7	CHARACTERIZATION OF THE ANTIBIOTIC RELEASE.....	56
	REFERENCES	57

3. EXPERIMENTAL WORK

In this section the materials used to produce the new biomaterials and the experimental methods employed to evaluate their properties are described. Figure 3.1 schematically depicts the performed experimental work. All the employed reagents have analytical grade and were used as received.

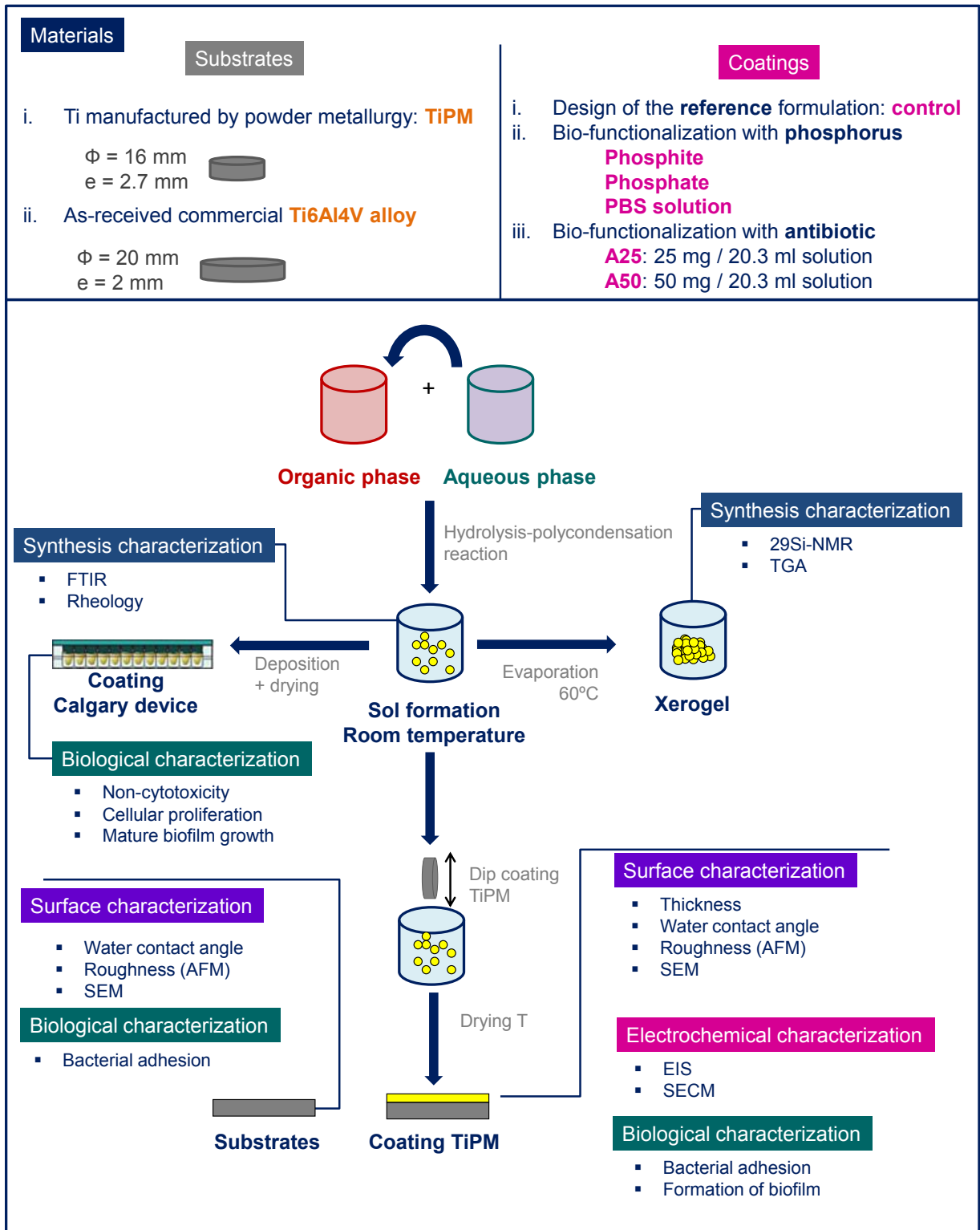


Figure 3. 1 Scheme of the experimental work performed during the Doctoral Thesis

3.1 MATERIALS

Coatings were prepared following the sol-gel methodology. The selected precursors of the hybrid sol-gel synthesis were **3-methacryloxypropyltrimethoxy silane** (MAPTMS, 98%, Acros Organics) and **tetramethyl orthosilane** (TMOS, 98%, Acros Organics). The selection was made based on previous works where the same precursors were employed to synthesize coatings for aluminum and titanium alloys [1]–[3]. Figure 3.2 shows the chemical structure of the employed organopolysiloxanes. The organic chain of MAPTMS (figure 3.2 (A)) provides the organic component to the sol-gel network. The inorganic part is created once the reaction starts thanks to the creation of siloxane bonds (Si-O-Si). MAPTMS has 3 alkoxy groups susceptible of being hydrolysed to subsequently create the siloxane bonds. TMOS (Figure 3.2 (B)) meanwhile, has 4 hydrolysable groups. The optimization of the control sol-gel synthesis was accomplished with a Taguchi orthogonal array procedure in where 3 parameters of the synthesis were varied: the molar ratio of the precursors (MAPTMS and TMOS), the reaction time of the synthesis and the drying temperature of coatings. The molar ratio of the reagents of the synthesis is: 1 mole of the precursors (MAPTMS+TMOS), 3 moles of ethanol and 3 moles of water.

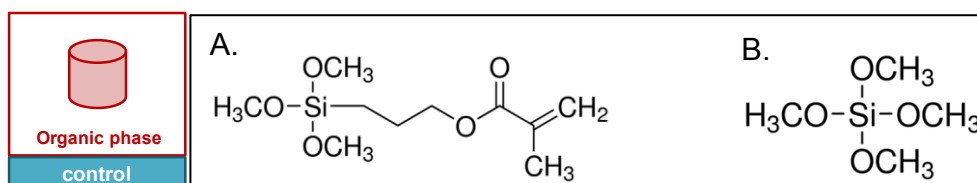


Figure 3. 2 Chemical structure of the precursors: A) 3-methacryloxypropyltrimethoxy silane (MAPTMS) and B) tetramethyl orthosilane (TMOS)

The first bio-functionalization of coatings was performed by adding an organophosphorus to the control synthesis as the phosphorus-based compound. Two coatings were prepared by adding two different compounds: **tris(trimethylsilyl) phosphite** (92%, Sigma Aldrich) and **tris(trimethylsilyl) phosphate** (98%, Sigma Aldrich). Figure 3.3 shows the chemical structure of the two organophosphorus compounds used that were dispersed in the organic phase of the sol-gel synthesis.

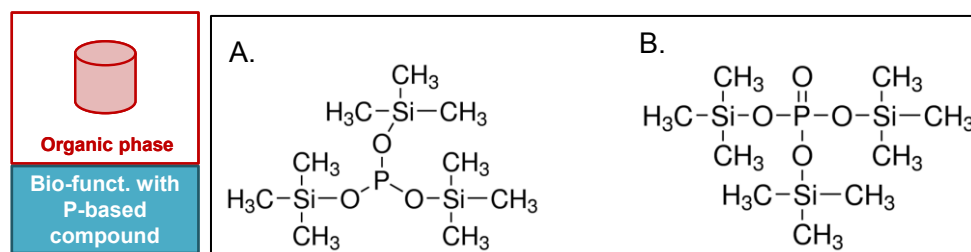



Figure 3. 3 Chemical structure of A) tris(trimethylsilyl) phosphite and B) tris(trimethylsilyl) phosphate

The other bio-functionalization was prepared by replacing part of the water added to the synthesis with a phosphate buffered solution (Dulbecco's PBS-Phosphate Buffered Saline, Sigma Aldrich) that contains **phosphate ions**. Table 3.1 lists the composition of the PBS solution that contains a concentration of ions that is similar to the one contained in the human blood plasma [4].

Table 3. 1 Composition of the PBS solution

 Aqueous phase Bio-funct. with P-based compound	Inorganic salts	Concentration (g/L)
	KCl	0.2
	KH ₂ PO ₄	0.2
	NaCl	8.0
	Na ₂ HPO ₄ (anhydrous)	1.1

The prepared bio-functionalized coatings are summarized in table 3.2. The organic compounds were dispersed in the organic phase in a molar ratio of 1:52 in relation with the organopolysiloxanes (MAPTMS + TMOS) before the aqueous phase was added to the synthesis. The aqueous compound (PBS solution) was dispersed in the water added to the synthesis. Sols without phase segregation were obtained. The moles of phosphorus contained in the PBS solution were calculated and are shown in Table 3.2.

Table 3. 2 Coatings bio-functionalized with phosphorus based compounds

Identification	Compound added	Quantity added $n_{Si}:n_P$
SG-C	-	-
SG-phosphite	tris(trimethylsilyl) phosphite	52:1
SG-phosphate	tris(trimethylsilyl) phosphate	52:1
SG-PBS	phosphate ions	10 ⁴ :1

* n_{Si} : sum of moles of both organopolysiloxanes (MAPTMS + TMOS)
 n_P : moles of the phosphorus compound

Moxifloxacin (MOX, moxifloxacin Hydrochloride, Sigma Aldrich) is the antimicrobial agent selected for the second bio-functionalization of coatings. Two coatings doped with this antibiotic were prepared. MOX was dissolved in water because it presents higher solubility in aqueous solutions than in organic ones [5]. Figure 3.4 shows the chemical structure of MOX and Table 3.3 summarizes the prepared coatings with MOX.

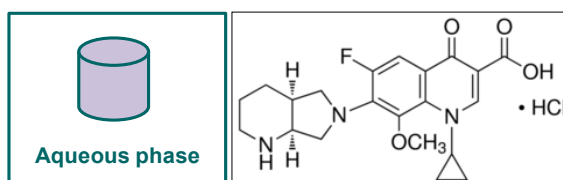


Figure 3. 4 Chemical structure of MOX

Table 3. 3 Coatings doped with MOX

Identification	MOX (mg)/ 20.3 ml of sol-gel solution
A25	25
A50	50

Once sols were prepared and optimized, the metallic substrate was dipped into the solutions and withdrawn at a rate of $200 \text{ mm}\cdot\text{s}^{-1}$ and then dried at a fixed temperature (varied from 60 to $180 \text{ }^\circ\text{C}$) for one hour. Titanium manufactured by a conventional powder metallurgical route (TiPM) was employed as substrate. TiPM substrates were prepared applying a cold uniaxial load of $7.9 \text{ ton}/\text{cm}^2$ followed by a sintering step at 1250°C for 120 minutes under high vacuum as described elsewhere [6]. The starting powders had a particle size below $75 \text{ }\mu\text{m}$ and were supplied by AP&C Inc. The metallic substrates were ground with silicon carbide paper of 1000 grit and cleaned with acetone in ultrasonic bath. In addition, commercial discs of Ti6Al4V alloy (Surgival Co., S.A.U., Valencia, Spain) were used as-received for a comparison study with TiPM. The as-received material was cleaned with acetone in ultrasonic bath.

3.2 SYNTHESIS CHARACTERIZATION

The **evolution of the hydrolysis-polycondensation reaction** was studied with Fourier-Transform Infrared Spectroscopy (FTIR) to establish the optimal reaction time prior to the deposition of sols on the substrate. Each sample was prepared by adding a drop of the synthesis to a pressed KBr disc. KBr powders were previously dried at 150°C for at least 2 hours to remove any content of humidity. Spectra were recorded using 10 scans with a PerkinElmer spectrum GX FT-IR System at room temperature covering the wave number range of $4000\text{--}500 \text{ cm}^{-1}$, with a resolution of 4 cm^{-1} and an interval of 0.1 cm^{-1} . Measures were performed by triplicate.

The **viscosity** of sols was measured using a HAAKE Viscotester iQ from Thermo Scientific with a parallel plate geometry and profiled surfaces. The viscosity was obtained by controlling the shear rate from 1 to 600 s^{-1} . Measures were performed by triplicate and mean values of each sol were calculated.

3.3 XEROGEL CHARACTERIZATION

Gels were dried at 60°C for 4 hours and ground in an agate mortar prior to their characterization. **Thermogravimetric analyses** (TGA) were performed using the model STA 6000 from PerkinElmer. Around 10 mg of xerogel (dry gel) was placed on alumina crucibles and heated at a $10^\circ\text{C}/\text{min}$ rate from 30 to 800°C in air atmosphere. Measurements were made by duplicated.

Solid-state ^{29}Si MAS-NMR (magic angle spinning, nuclear magnetic resonance) was recorded using a Bruker Avance-400 pulse spectrometer equipped with fast Fourier transform unit. Frequency used was 79.48 MHz for silicon nuclei (9.4T magnetic field). Samples were spun at 10 kHz around an axis inclined $54^\circ44'$ with respect to the external magnetic field. Spectra were acquired with a pulse length of $5 \text{ }\mu\text{s}$ (90 degree pulse), a relaxation delay of 10 seconds and 6000 accumulations. Spectra were referenced to TMS. Signals obtained with **^{29}Si MAS-NMR** depend on the organopolysiloxanes used as precursors of the sol-gel synthesis. These organopolysiloxane have different amount of

alkoxy groups that can be hydrolysed. The hydrolysed groups can then react with other hydrolysed groups of either MAPTMS or TMOS molecules and form the siloxane bond (Si-O-Si). T species correspond to Si atoms that are capable of creating three siloxane bonds while Q species correspond to species that can form four siloxane bonds. In this study, T signals reveal the chemical entourage of MAPTMS and Q signals the ones of TMOS. The nomenclature for T species is T^n where n can take values of 0, 1, 2 and 3 depending on the amount of siloxane groups created per silicon nuclei. For TMOS, Q^m is the identification of the species and m can take values from 0 to 4. Table 3.4 shows the chemical shifts reported in the bibliography of MAPTMS and Table 3.5 summarizes the chemical shifts of TMOS [1], [7].

Table 3. 4 Chemical shift (δ) of MAPTMS employing silicon nuclei

	$R'-Si-(OR)_3$	$\begin{array}{c} O-Si- \\ \\ R'-Si-(OR)_2 \end{array}$	$\begin{array}{c} (O-Si-)_2 \\ \\ R'-Si-OR \end{array}$	$\begin{array}{c} (O-Si-)_3 \\ \\ R'-Si \end{array}$
Signal	T^0	T^1	T^2	T^3
δ (ppm)	-42	-49	-58	-67

Table 3. 5 Chemical shift (δ) of TMOS employing silicon nuclei

	$Si-(OR)_4$	$\begin{array}{c} O-Si- \\ \\ Si-(OR)_3 \end{array}$	$\begin{array}{c} (O-Si-)_2 \\ \\ Si-(OR)_2 \end{array}$	$\begin{array}{c} (O-Si-)_3 \\ \\ Si-OR \end{array}$	$\begin{array}{c} (O-Si-)_4 \\ \\ Si \end{array}$
Signal	Q^0	Q^1	Q^2	Q^3	Q^4
δ (ppm)	-82	-86	-92	-101	-110

3.4 SURFACE CHARACTERIZATION

The **water contact angle** of coatings was determined by measuring the static contact angle of distilled water onto sol-gel surfaces using an automatic contact angle meter (DATAPHYSICS OCA 20 Goniometer). A sessile drop of 3 μ L was deposited at 1 μ L/s on the surfaces at room temperature. The contact angle was determined by the half angle method and at least on 2 different locations per sample. The value given is the mean of at least 5 measurements. The hydrophobic/hydrophilic nature of the materials is a key parameter on the “race to the surface” between bacteria and cells. It is reported on the bibliography that while bacteria are more attracted to hydrophobic surfaces, cells recognize better hydrophilic surfaces [8], [9].

The **thickness** of coatings was measured with an ultrasonic thickness equipment from Neurtek Instruments. The value given is the average of 7 samples per designed coating.

The **surface** of coatings was inspected with Teneo FEI microscope with W filament. Images were captured applying 2-5 kV and 0.2 nA. The microscope, equipped with Energy-Dispersive X-ray Spectroscopy (EDS) Basic and an Octane Plus detector with an area of 30 mm², allowed the semi-quantitative analysis of the chemical composition.

The **roughness** of the surface of coatings was measured with Atomic Force Microscopy (AFM) using the Dimension Edge (Bruker, USA) instrument operating in tapping mode. The AFM tip was antimony (n) doped with Si-cantilever. Maps of 100×100 μm² were recorded at a scan rate of 1 Hz. The average roughness represented by the root mean square (rms) roughness of the surface was calculated using Gwyddion software (Department of Nanometrology, Czech Metrology Institute, Czech Republic).

3.5 ELECTROCHEMICAL CHARACTERIZATION

Impedances were recorded using an Autolab PGSTAT302N potentiostat/galvanostat (Ecochemie, Utrecht, The Netherlands). A conventional three-electrode setup, using an Ag/AgCl/KCl(sat.) electrode as reference ($E_0=+0.197$ V vs. NHE), and a Pt wire as counter electrode. The working electrode was the sample under study: TiPM (area = 1 cm²), Ti6Al4V alloy (area = 2 cm²), and the different coatings (area = 1 cm²). Impedances were normalized per unit area. All the reported potentials are thus relative to the Ag/AgCl/KCl(sat.) reference electrode potential. An aqueous solution at 0.9 %wt. of NaCl or a PBS solution (Dulbecco's Phosphate Buffered Saline, Sigma Aldrich, USA) was used as electrolyte. Temperature was controlled at 37± 0.5°C and the cell was placed in a Faraday cage. Impedances were recorded at regular intervals of 2 hours during 1 day and even to longer times (e.g., 1 week) in the case of the metallic substrate. An AC amplitude of ±10 mV with respect to the open circuit potential (OCP) was used. A frequency scan from 10 kHz to 10 mHz was applied with values spaced logarithmically with 10 points per decade. OCP was recorded before and after each impedance. EIS data were fitted and analysed in terms of equivalent circuits (ECs) using ZView software (Scribner Associates, Charlottesville, VA, USA). Figure 3.5 shows the set-up of the electrochemical cells and the electrodes used in EIS experiments. Measures were made per triplicate.

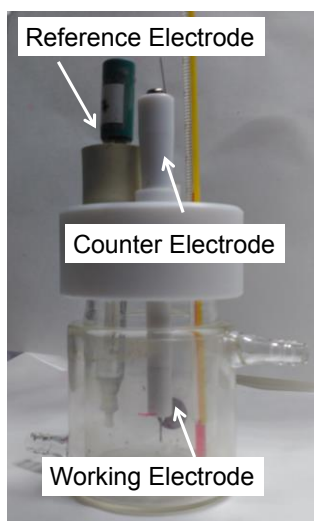


Figure 3. 5 Set-up of the EIS experiment

SECM measurements were recorded with the Scanning Electrochemical Workstation Model 370 (Princeton Applied Research, AMETEK Inc., USA). A Pt-ultramicroelectrode (UME) of 5 μm radius supplied by Sensolytics GmbH (Germany) was used as working electrode. An Ag/AgCl/KCl(sat.) as the reference electrode, and a Pt wire as the counter electrode completed the electrochemical cell. All reported potentials are thus relative to the Ag/AgCl/KCl(sat.) reference electrode potential. SECM operated in feedback mode using 5 mM ferrocenemethanol (97%, Sigma Aldrich, USA) as electrochemical mediator in PBS solution. Ferrocenemethanol, and its corresponding oxidized species, ferrocenium ion, are both soluble in the solution. The substrates were mounted facing up in the SECM setup using a teflon holder with a 1.6 cm diameter O-ring limiting the total exposed area. The holder with the sample was placed into a double-walled electrochemical cell to control the temperature at $37 \pm 0.5^\circ\text{C}$. The distance between sample and tip was established by approaching curve measurements. The tip potential was +0.5 V (vs. Ag/AgCl/KCl (sat.)), which corresponds to the oxidation of the ferrocene complex to its ferrocenium form under diffusion-controlled conditions. The curves were recorded at constant approximation rate of $1 \mu\text{m}\cdot\text{s}^{-1}$, starting from the bulk of the solution. SECM maps were obtained with the UME located at a distance corresponding to a change in the current of approximately 80% respect to the limiting current. The chosen criteria assure that the measured current is influenced by the surface reactivity, but the UME is still far enough from the surface to avoid the influence of the sample topography. Maps of $1 \times 1 \text{ mm}^2$ were recorded every 2 hours for 1 day. The normalized current scale of maps was established from 0 to 1 for comparison. The scan width step size was 25 μm and maps were obtained at scan velocity of $100 \mu\text{m}\cdot\text{s}^{-1}$. Before and after each experiment (24 hours) a cyclic voltammetry from 0 to 0.5 V was applied from the bulk of the solution to control the state of the Pt-UME. Tip-current values in this work have been normalized (I_N) by dividing them by the measured limiting current. Figure 3.6 shows the set-up of the electrochemical cells and the electrodes used in the SECM experiment.

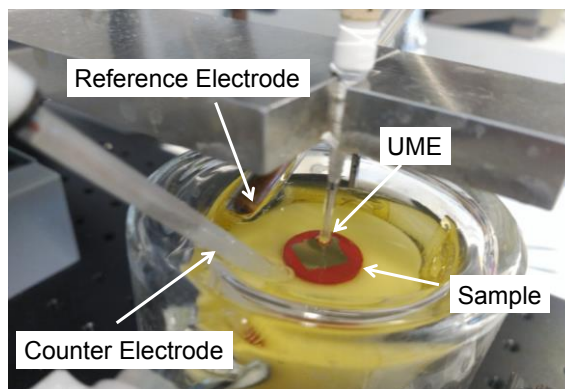


Figure 3. 6 Set-up of the SECM experiment

Samples used in both electrochemical techniques, EIS and SECM, were coated with a red stopping off lacquer from Mac Dermid to avoid the corrosion through the edge of the samples.

3.6 BIOLOGICAL CHARACTERIZATION

Bacterial adhesion

The bacterial adhesion on the **metallic substrates** was tested with two collection strains. The collection strains were *S. aureus* 15981 [10], and *E. coli* ATCC 25922. All the strains were kept frozen at -80°C until experiments were performed. The bacterial adhesion experiments were performed following the modified protocol developed by Kinnari *et al.* [11]. Figure 3.7 illustrates the followed protocol.

- (1) First, each strain was grown overnight in blood tryptic soy agar (BTSA) at 37°C and $5\%\text{CO}_2$ and then transferred to tubes containing tryptic soy broth (TSB) (Biomérieux, Marcy-l'Étoile, France) and left overnight at 37°C and $5\%\text{CO}_2$. After culture, bacterial broth was harvested 10 minutes at 3500 rpm at room temperature. Supernatant was discarded and the pellet was washed three times with sterile saline (SS) at 0.9 wt.% of NaCl (B.Braun, Melsungen, Germany). Bacteria were then suspended and diluted with SS to adjust the colony forming units (CFUs) to 0.5 McF (turbidity units) (equivalent to $\sim 1.0 - 1.6 \times 10^8$ CFU/ml) of bacterial inoculum.
- (2) Then, 5 mL of inoculum was incubated 90 minutes onto the surfaces of the metallic substrates (TiPM and Ti6Al4V alloy) in a sterile non-treated 6-well dish (Thermo Fisher Scientific, Massachusetts, USA) at 37°C and $5\%\text{CO}_2$ to allow the adhesion in a static model [11]–[13].
- (3) After incubation, the substrates were washed three times with SS to remove unattached bacteria. Finally, discs were stained with 150 μL of the Live/Dead BacLight® bacterial viability kit (Thermo Fisher Scientific, Massachusetts, USA) and rinsed with sterile water [13]. The excitation/emission maxima for these dyes are 480/500 nm for SYTO 9 stain and 490/635 nm for propidium iodide.
- (4) Ten photographs (40×magnifications) were taken in a DM 2000 fluorescence microscope (Leica Microsystems, Wetzlar, Germany) for each substrate. The percentage of total surface

covered with adhered bacteria and the percentages of dead and live bacteria were calculated and analysed using ImageJ software (National Institutes of Health, Bethesda, Maryland, USA). Experiments were performed in triplicate for each strain.

- (5) Microbiological statistical analysis was performed using Stata Statistical Software: Release 11 (College Station, TX: StataCorp LP, USA). Non-parametric Wilcoxon test was used for a pairwise comparison of the adhered bacteria and viability. A level of statistical significance of $p < 0.001$ was considered. The values of the adhered bacteria and viability are cited as medians and interquartile range.

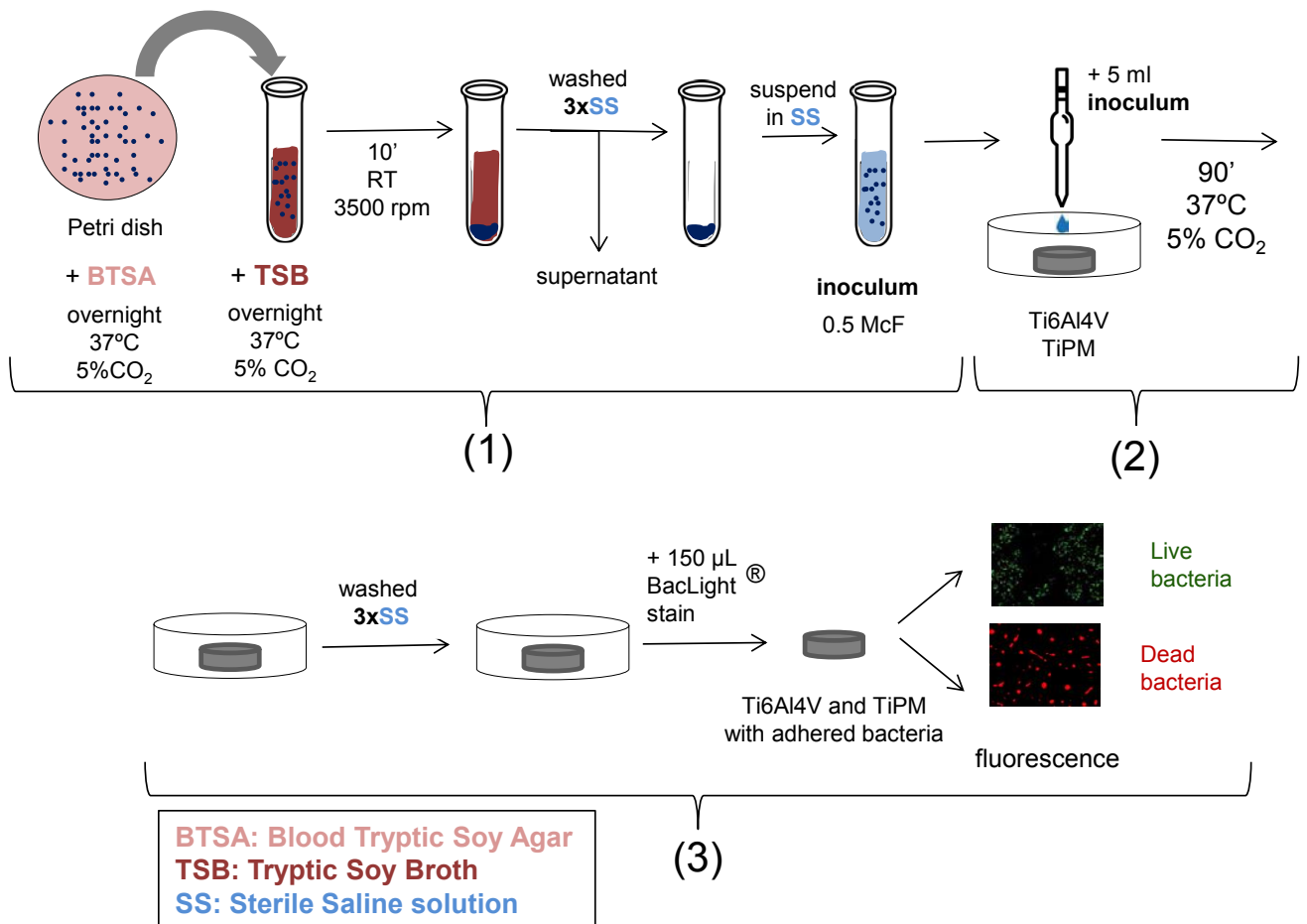


Figure 3. 7 Schema of the protocol of the bacterial adhesion test

Biofilm formation: biofilm development and mature biofilm growth treatment

The biofilm development studies were carried out on the surfaces of **coatings** while the mature biofilm growth was performed on a polymeric device coated with sols. The same three bacterial strains were tested in both tests: *S. aureus* 15981 [10], *S. epidermidis* ATCC 35984 and *Escherichia coli* ATCC 25922. All the strains were kept frozen at -80°C until experiments were performed.

- (1) The biofilm development test (**prevention**) is illustrated in Figure 3.8 and the followed protocol was carried out:
 - a. Strains were grown overnight in petri dishes with BTSA at 37°C and 5% CO_2 . Then the biofilm was induced overnight by adding TSB supplemented with 1% (wt./vol.) of glucose at 37°C and 5% CO_2 until adjusting the inoculum to 0.5 McF (turbidity units) (equivalent to $\sim 1.0 - 1.6 \times 10^8$ CFU/ml). The inoculum (5 ml) was deposited on the coatings and incubated 24 hours at 37°C and 5% CO_2 . Then coatings were washed three times with SS (B.Braun, Germany).
 - i. The **adhered CFUs** (sessile bacteria) were estimated by scraping the top disc surface with sterile wooden sticks to corroborate the viability differences on each coating. These wooden sticks with scrapped bacteria were sonicated 5 minutes at 50-60 Hz in a 50-mL Falcon™ conical tube (Thermo Fisher Scientific, USA) with 10 mL of SS, with an Ultrasons-H 3000840 low-power bath sonicator (J. P. Selecta, Spain) at room temperature [14]. The wooden sticks were removed and the inoculum was serially diluted with SS (namely, 10^{-1} , 10^{-2} , 10^{-3} , 10^{-4} , 10^{-5} , 10^{-6} and 10^{-7}). Five drops of 5 μl of each inoculum was placed in a petri dish and incubated 24 hours at 37°C and 5% CO_2 . Adhered CFUs per area unit were estimated using the drop plate method [15]. This experiment was performed by triplicate for each strain and coating.
 - ii. For estimating the planktonic bacterial concentration, the absorbance of the **supernatant** (planktonic bacteria) was measured at 600 nm in eight replicates in a Nunc™ 96-Well Polypropylene MicroWell™ Plate (Thermo Fisher Scientific, USA). This experiment was performed by triplicate for each strain and coating.

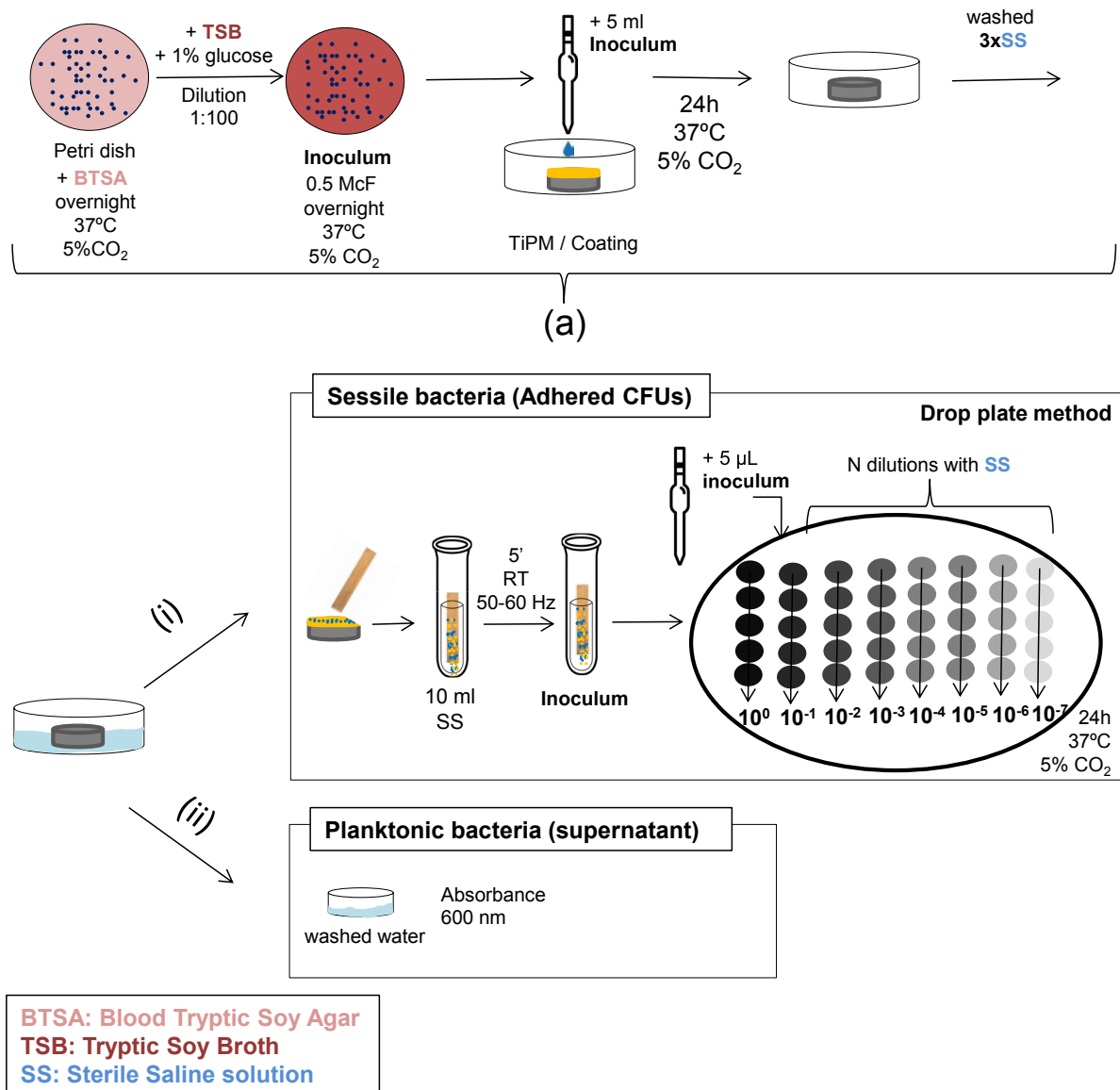


Figure 3. 8 Schema of the protocol for the biofilm development test (prevention)

- (2) The protocol to evaluate the effect of the MOX-loaded sol-gel on mature biofilm viability (**treatment**) is shown in Figure 3.9 and consists of the following stages:
- Strains were grown overnight in petri dishes with BTSA at 37°C and 5%CO₂. The biofilm was induced overnight by adding TSB supplemented with 1% (wt./vol.) of glucose at 37°C and 5% CO₂ until reaching 0.5 McF (turbidity units) (equivalent to ~ 1.0 – 1.6 × 10⁸ CFU/ml).
 - Biofilms were then grown on bottom black MicroWell (black Nunc™ F96 MicroWell™, Thermo Fisher Scientific, USA) using 200 µL of the inoculum per well. The medium was incubated 24 hours at 37°C and 5% CO₂ [16]. Then, the mature biofilm of each well was rinsed twice with 200 µL of SS at 0.9 wt.% NaCl and 200 µL of brain heart infusion (BHI) at 1% (wt./vol.) containing 60% of bovine serum adult (BSA) (Sigma Aldrich, USA).

- c. A MBECTM biofilm Incubator lid (Innovotech, Canada) was coated by dipping in wells filled with 200 μL of each sol. Lids were then dried for 24 hours at room temperature.
- d. The bottom black MicroWell was closed with the lid containing the sol-gel and incubated 48 hours at 37°C, 5% CO_2 and 80 rpm. Viable bacterial concentration was estimated after adding 10 μL of alamarBlue® (BIO-RAD, USA) per well and incubating 3 hours at 37°C, 5% CO_2 and 80 rpm [17]. Fluorescence was measured using an excitation and emission wavelength of 560 nm and 590 nm, respectively, using EnSpire Multimode Plate Reader (Perkin Elmer, USA). Pegs of the uncoated material were used as positive control. This experiment was performed in eight wells per coating and by triplicate for each strain.

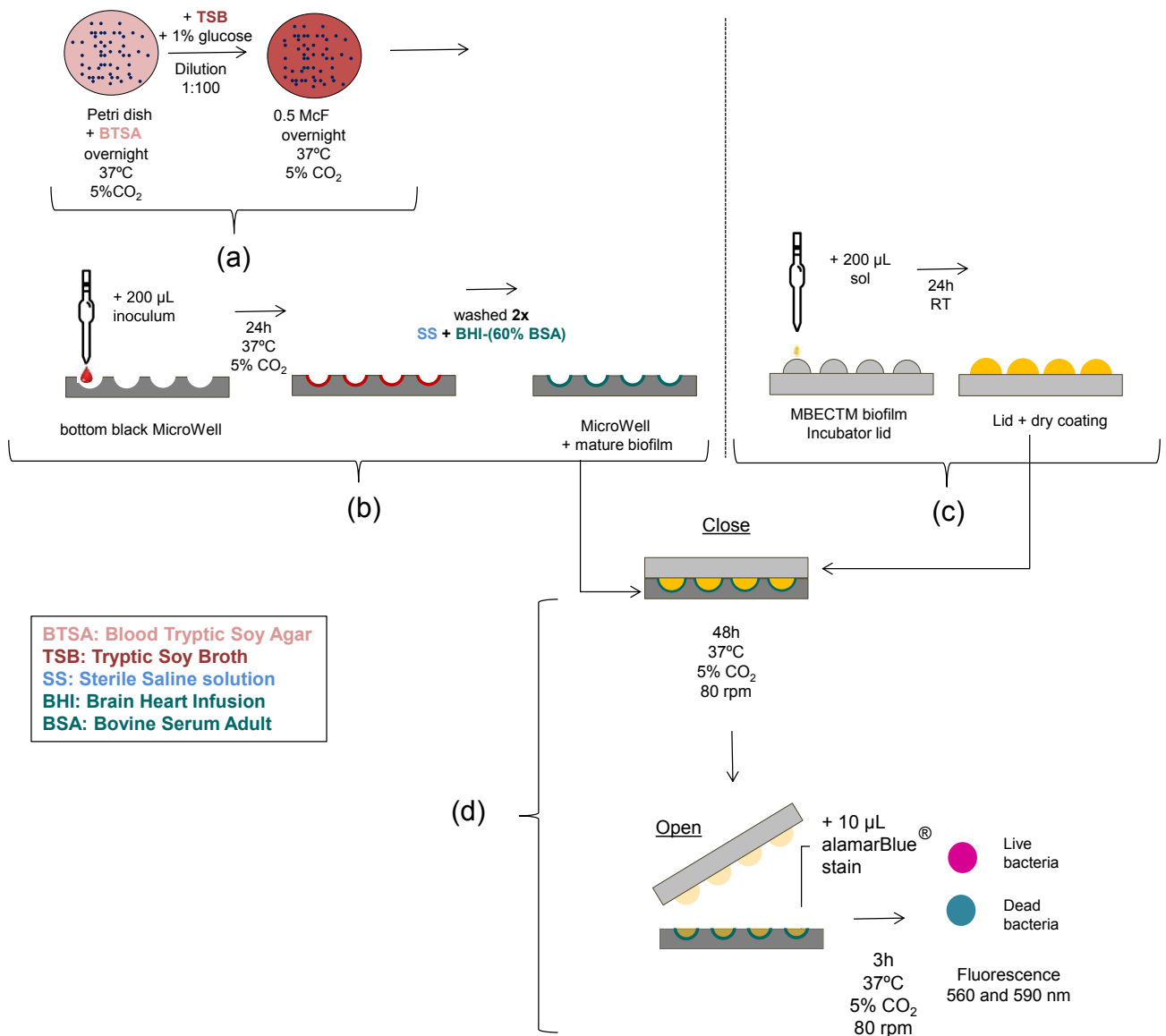


Figure 3. 9 Schema of the protocol for the biofilm mature biofilm growth (treatment) test

Cytotoxicity and cellular proliferation

The viability of MC3T3-E1 cells was performed following the detailed protocol that is illustrated Figure 3.10:

- (1) MC3T3-E1 cells were seeded in a concentration of 10^4 cells/cm² on 96 well plates with α -minimum essential medium (α MEM, Invitrogen, Thermo Fisher Scientific Inc. USA) with 10% of fetal bovine serum (FBS) and 1% of penicillin-streptomycin (PS). Cells were incubated overnight at 37°C and 5% CO₂. After cell adhesion, the medium was replaced by 50 mg/mL ascorbic acid (AA) (Sigma-Aldrich, USA) and 10 mM β -glycerol-2-phosphate (GP) (Sigma-Aldrich, USA) for promoting osteoblastic differentiation.
- (2) A MBECTM biofilm Incubator lids (Innovotech, Canada) were coated by dipping in wells filled with 200 μ L of each sol-gel. Lids were dried for 24 hours at room temperature.
- (3) The 96 well plates were closed with lids containing the sol and incubated 48 hours at 37°C, 5% CO₂. After incubation:
 - a. The **cytotoxicity** was tested by CytoTox 96® NonRadioactive Cytotoxicity Assay (Promega, USA). Fluorescence intensity was measured at 492 nm in Tecan Infinite 200 Reader (Life Sciences, Switzerland).
 - b. The **cellular proliferation** was determined by adding 10 μ L alamarBlue® solution (BIO-RAD, USA) at 10% (vol./vol.) to the cellular culture and incubating 4 hours at 37°C and 5% CO₂. Fluorescence intensity was measured with excitation and emission wavelengths of 560 and 590 nm, respectively, in EnSpire Multimode Plate Reader (Perkin Elmer, USA). This experiment was performed in triplicate testing each treatment in eight wells per replicate.

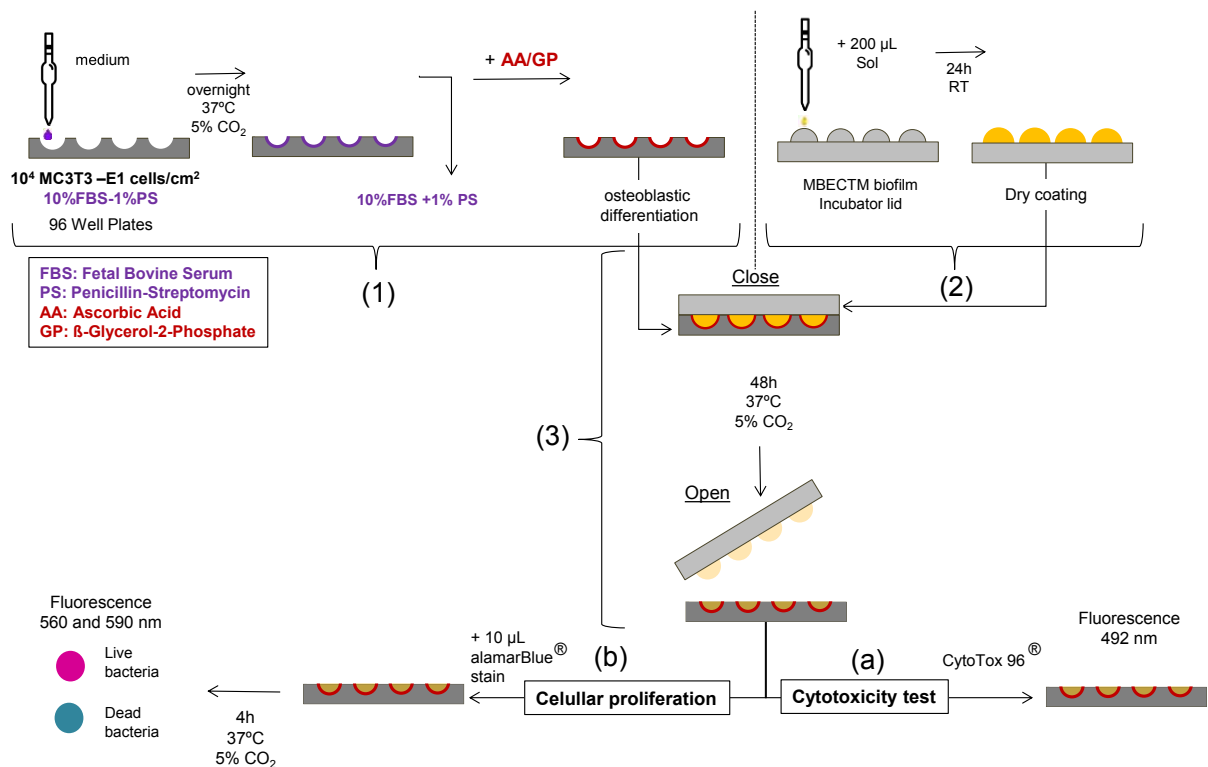


Figure 3.10 Schema of the protocol for the cytotoxicity and the cellular proliferation study

Figure 3.11 shows a picture of the polymeric device employed to treat the mature biofilm and the MC3T3-E1 cells.



Figure 3. 11 Picture of the polymeric device employed (Calgary device) to treat the mature biofilm and the MC3T3-E1 cells

3.7 CHARACTERIZATION OF THE ANTIBIOTIC RELEASE

The release of MOX from coatings loaded with MOX (A25 and A50) in a PBS solution (Dulbecco's Phosphate Buffered Saline, Sigma Aldrich, USA) was tracked by measuring the absorbance of MOX at 292 nm with an UV-Vis absorption spectroscopy JASGO V-650 [5]. Coatings were exposed to 10 ml of PBS solution at 37°C and placed into polypropylene tubes. The absorbance was measured at different times (6, 12, 24 and 48 hours) using cuvettes of quartz. A calibration curve is shown in Figure 3.12. The calibration was done varying the concentration of MOX between 4×10^{-6} mg to 4×10^{-3} mg. Then, the concentration of MOX of each specimen was normalized taken into account the dilution.

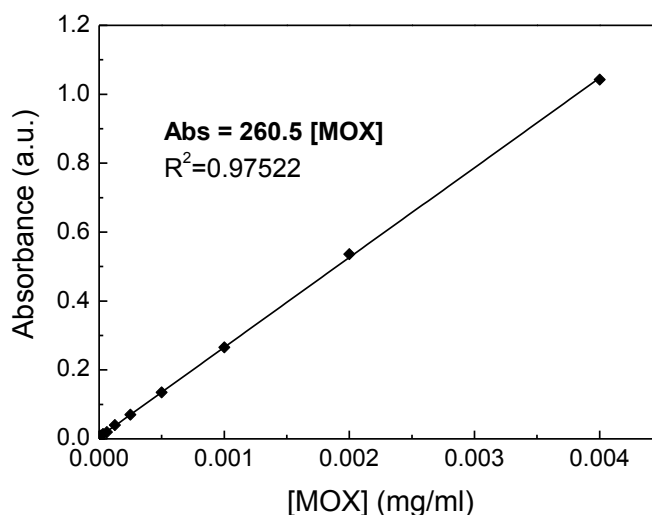


Figure 3. 12 Calibration curve of MOX in PBS solution

REFERENCES

- [1] A. A. El hadad, D. Carbonell, V. Barranco, A. Jiménez-Morales, B. Casal, and J. C. Galván, "Preparation of sol–gel hybrid materials from γ -methacryloxypropyltrimethoxysilane and tetramethyl orthosilicate: study of the hydrolysis and condensation reactions," *Colloid Polym. Sci.*, vol. 289, no. 17–18, pp. 1875–1883, 2011.
- [2] A. El Hadad, E. Peón, F. García-Galván, V. Barranco, J. Parra, A. Jiménez-Morales, and J. Galván, "Biocompatibility and Corrosion Protection Behaviour of Hydroxyapatite Sol-Gel-Derived Coatings on Ti6Al4V Alloy," *Materials (Basel)*, vol. 10, no. 2, p. 94, 2017.
- [3] D. J. Carbonell, A. García-Casas, J. Izquierdo, R. M. Souto, J. C. Galván, and A. Jiménez-Morales, "Scanning electrochemical microscopy characterization of sol-gel coatings applied on AA2024-T3 substrate for corrosion protection," *Corros. Sci.*, vol. 111, pp. 625–636, 2016.
- [4] T. Kokubo and H. Takadama, "How useful is SBF in predicting in vivo bone bioactivity?," *Biomaterials*, vol. 27, no. 15, pp. 2907–15, 2006.
- [5] F. Varanda, M. J. Pratas De Melo, A. I. Caço, R. Dohrn, F. A. Makrydaki, E. Voutsas, D. Tassios, and I. M. Marrucho, "Solubility of antibiotics in different solvents. 1. Hydrochloride forms of tetracycline, moxifloxacin, and ciprofloxacin," *Ind. Eng. Chem. Res.*, vol. 45, no. 18, pp. 6368–6374, 2006.
- [6] L. Bolzoni, E. M. Ruiz-Navas, and E. Gordo, "Powder metallurgy CP-Ti performances: Hydride-dehydride vs. sponge," *Mater. Des.*, vol. 60, pp. 226–232, 2014.
- [7] M. Criado, I. Sobrados, and J. Sanz, "Polymerization of hybrid organic–inorganic materials from several silicon compounds followed by TGA/DTA, FTIR and NMR techniques," *Prog. Org. Coatings*, vol. 77, no. 4, pp. 880–891, 2014.
- [8] I. V. Sukhorukova, A. N. Sheveyko, P. V. Kiryukhantsev-korneev, and I. Y. Zhitnyak, "Colloids and Surfaces B: Biointerfaces Toward bioactive yet antibacterial surfaces," vol. 135, pp. 158–165, 2015.
- [9] C. P. Stallard, K. A. McDonnell, O. D. Onayemi, J. P. O’Gara, and D. P. Dowling, "Evaluation of protein adsorption on atmospheric plasma deposited coatings exhibiting superhydrophilic to superhydrophobic properties," *Biointerphases*, vol. 7, no. 1–4, pp. 1–12, 2012.
- [10] J. Valle, A. Toledo-Arana, C. Berasain, J. M. Ghigo, B. Amorena, J. R. Penadés, and I. Lasa, "SarA and not σ B is essential for biofilm development by *Staphylococcus aureus*," *Mol. Microbiol.*, vol. 48, no. 4, pp. 1075–1087, 2003.
- [11] T. J. Kinnari, J. Esteban, E. Gomez-Barrena, N. Zamora, R. Fernandez-Roblas, A. Nieto, J. C. Doadrio, A. López-Noriega, E. Ruiz-Hernández, D. Arcos, and M. Vallet-Regí, "Bacterial adherence to SiO₂-based multifunctional bioceramics," *J. Biomed. Mater. Res. - Part A*, vol. 89, no. 1, pp. 215–223, 2009.
- [12] M. A. Arenas, C. Pérez-Jorge, A. Conde, E. Matykina, J. M. Hernández-López, R. Pérez-Tanoira, J. J. de Damborenea, E. Gómez-Barrena, and J. Esteba, "Doped TiO₂ anodic layers of enhanced antibacterial properties," *Colloids Surfaces B Biointerfaces*, vol. 105, pp. 106–112, 2013.
- [13] J. J. Aguilera-Correa, A. Conde, M. A. Arenas, J. J. De-Damborenea, M. Marin, A. L. Doadrio, and J. Esteban, "Bactericidal activity of the Ti-13Nb-13Zr alloy against different species of bacteria related with implant infection," *Biomed. Mater.*, vol. 12, no. 4, 2017.
- [14] J. Esteban, E. Gomez-Barrena, J. Cordero, N. Z. Martín-de-Hijas, T. J. Kinnari, and R. Fernandez-Roblas, "Evaluation of quantitative analysis of cultures from sonicated retrieved orthopedic implants in diagnosis of orthopedic infection," *J. Clin. Microbiol.*, vol. 46, no. 2, pp. 488–492, 2008.
- [15] B. Herigstad, M. Hamilton, and J. Heersink, "How to optimize the drop plate method for enumerating bacteria," *J. Microbiol. Methods*, vol. 44, no. 2, pp. 121–129, 2001.
- [16] C. Perez-Jorge, M. A. Arenas, A. Conde, J. M. Hernández-Lopez, J. J. de Damborenea, S. Fisher, A. M. A. Hunt, J. Esteban, and G. James, "Bacterial and fungal biofilm formation on anodized titanium alloys with fluorine," *J. Mater. Sci. Mater. Med.*, vol. 28, no. 1, 2017.
- [17] R. K. Pettit, C. A. Weber, M. J. Kean, H. Hoffmann, G. R. Pettit, R. Tan, K. S. Franks, and M. L. Horton, "Microplate alamar blue assay for *Staphylococcus epidermidis* biofilm susceptibility testing," *Antimicrob. Agents Chemother.*, vol. 49, no. 7, pp. 2612–2617, 2005.

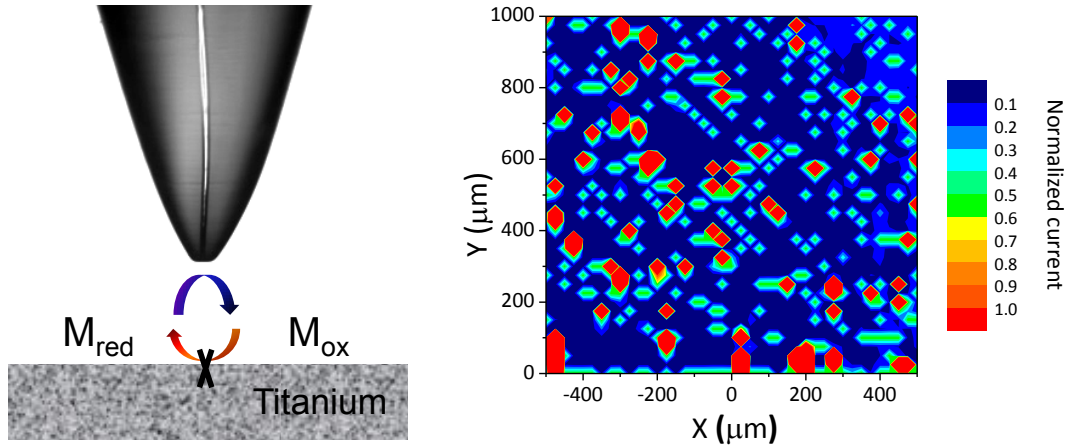
CHAPTER 4

CHARACTERIZATION OF THE METALLIC SUBSTRATE

ABSTRACT.....	61
4.1 MATERIALS.....	63
4.2 SURFACE CHARACTERIZATION.....	63
4.3 ELECTROCHEMICAL CHARACTERIZATION.....	65
4.4 MICROBIOLOGICAL STUDY.....	74
4.5 CONCLUSIONS.....	76
REFERENCES.....	77

4. CHARACTERIZATION OF THE METALLIC SUBSTRATE

ABSTRACT



An electrochemical characterization of **titanium manufactured by powder metallurgy** (TiPM) was performed to elucidate if the porosity induced to the material was detrimental to its electrochemical performance. Commercial **Ti6Al4V alloy** was used as the reference material. The surface reactivity was studied with Scanning Electrochemical Microscopy (SECM) operating in feedback-mode. Results revealed that both materials presented metastable events in PBS solution and 37°C. Electrochemical Impedance Spectroscopy (EIS) tests concluded that TiPM had superior long-term performance despite developing more metastable events than Ti6Al4V alloy. The biological study supported TiPM as an alternative material to Ti6Al4V alloy in prosthetic devices.

4.1 MATERIALS

A conventional **powder metallurgy** (PM) route based on a pressing and subsequent sintering step was employed to prepare **titanium** substrates (TiPM). A cold uniaxial load of 7.9 ton/cm^2 followed by a sintering step at 1250°C for 120 minutes under high vacuum was used [1]. The starting powders of pure titanium were supplied by AP&C Inc. and had a particle size below $75 \mu\text{m}$. The surface of TiPM was ground with silicon carbide paper of 1000 grit and cleaned with acetone in ultrasonic bath. The as-received discs of **Ti6Al4V alloy** (Surgival Co., S.A.U., Valencia, Spain) were cleaned with acetone in ultrasonic bath.

4.2 SURFACE CHARACTERIZATION

First, the surface of the metallic substrates was studied to evaluate how the manufacturing processes determined their features. Images of the surface of Ti6Al4V alloy and TiPM and the water drop of the contact angle test on their surfaces are shown in Figure 4.1. The values of the contact angle are shown in Table 4.1 and revealed that **Ti6Al4V alloy was more hydrophobic than TiPM**. The water contact angle of Ti6Al4V alloy almost doubled the values obtained on the surface of TiPM. Images captured with BSE mode (Figure 4.1(A) and Figure 4.1(C)) showed that Ti6Al4V alloy had one contrast while TiPM presented two contrasts. EDS analyses (Table 4.1) revealed the composition analysis of both specimens.

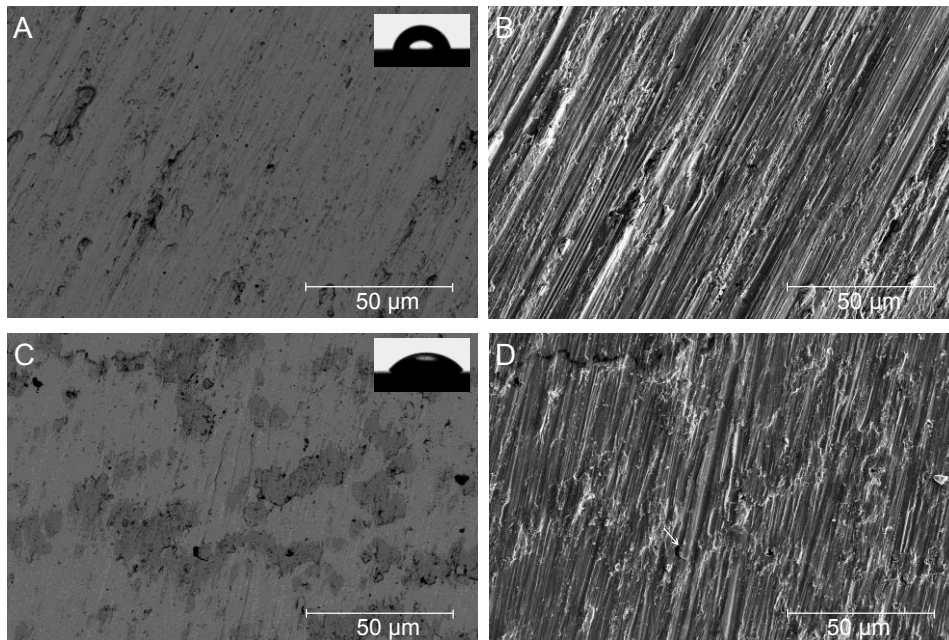


Figure 4. 1 SEM micrographs of: (A-B) Ti6Al4V alloy and (C-D) TiPM using BSE and SE mode, respectively. An image of the water drop of each material is shown

The analysis on the surface of Ti6Al4V alloy identified the elements Ti, Al and V, while in TiPM only Ti element was detected. In both cases, **oxygen** was also detected, which is an indication of the presence of an **oxide layer** [2]–[4]. EDS analyses of the different regions observed on TiPM surface showed that dark areas in the SEM image contained more oxygen than the bright ones, which suggests that TiPM sample presented an heterogeneous oxide layer with patched areas containing thicker oxides.

Table 4. 1 Chemical analysis, RMS roughness and water contact angle of Ti6Al4V alloy and TiPM specimens

Element (at.%)	Ti6Al4V alloy	TiPM	
		Bright	Dark
Ti	81.2 ± 0.6	95.3 ± 0.2	69.9 ± 0.1
Al	9.5 ± 0.2	-	-
V	3.9 ± 0.1	-	-
O	5.4 ± 0.9	4.7 ± 0.2	30.1 ± 0.1
RMS Roughness (nm)	195 ± 34	293 ± 25	
Water contact angle (°)	85.6 ± 6.4	48.7 ± 5.0	

The AFM images for both samples are presented in Figure 4.2. Ti6Al4V alloy and TiPM showed similar topography as can be seen in the cross-sections in Figure 4.2 (bottom). Table 4.1 summarizes the root mean square roughness (RMS) calculated as an average of the RMS values obtained from several areas of 10x10 μm^2 of the AFM image. The **roughness of TiPM was found to be 100 nm higher** the one obtained on Ti6Al4V alloy. The resulting surface features of TiPM, which presents higher roughness and higher hydrophilicity than Ti6Al4V alloy, can assist the attachment of cells and improve the process of osseointegration. However, this apparent advantage can be detrimental to the process of osseointegration if bacterial cells colonize first the surface of the biomaterial. This competition, which can be mutually exclusive, between host cells and bacterial cells was coined by A. Gristina et al. as the “the race for the surface” [5]. The bacterial adhesion of the main etiological agents that cause prosthetic joint infections is evaluated in section 4.4 to confirm if these bacteria have also affinity to the surface of TiPM.

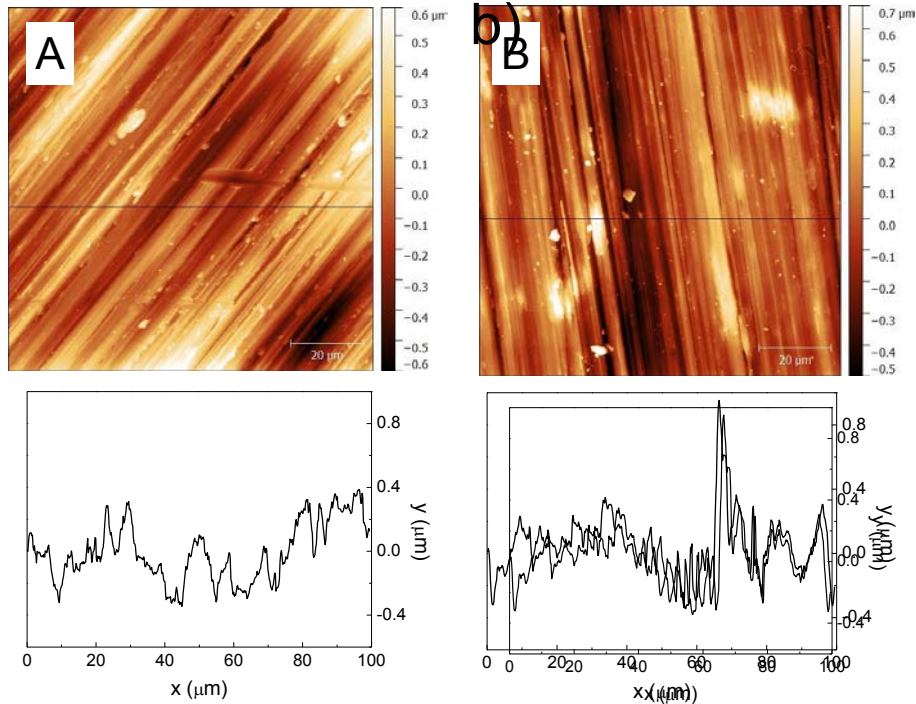


Figure 4. 2 (top) Topographic AFM images of a) Ti6Al4V alloy and b) TiPM specimens. (bottom) Plot of the selected cross-section lines from AFM images

4.3 ELECTROCHEMICAL CHARACTERIZATION

The electrochemical performance of the metallic substrates was studied by means of two electrochemical techniques: a high spatially-resolved one, the **scanning electrochemical microscopy** (SECM) and a conventional averaging technique, the **electrochemical impedance spectroscopy** (EIS). The characterization was performed by immersing specimens in PBS solution (Dulbecco's Phosphate Buffered Saline, Sigma Aldrich, USA) and 37°C.

Scanning Electrochemical Microscopy (SECM)

Experiments consisted of mapping with the SECM a selected area of the surface of the specimens at different immersion times in PBS solution. With the SECM operating in **feedback mode**, the electroreactivity of the surface was *in-situ* measured and referred as normalized current (I_N).

SECM maps of **Ti6Al4V alloy** at four immersion times (2, 6, 18, and 24 hours) are shown in Figure 4.3(A). From the beginning of the test (2 hours) it was observed, as expected for passive materials, the insulating features (normalized current below one, $I_N < 1$) of Ti6Al4V alloy. Only one localized area with activity (normalized current above one, $I_N > 1$) was observed. The electrochemical response recorded on Ti6Al4V alloy completely changed from 2 to 6 hours. After 2 hours of exposure, the response was influenced by the topography of

the metal while after 6 hours the recorded response was due to the homogenous oxide layer created among the surface of the metal. By increasing the exposure time to the electrolyte, the surface of Ti6Al4V alloy showed more active areas. The presence of active areas on passive materials can be due to the breakdown of the protective layer. The activity did not progress with time revealing that these events were metastable. The occurrence of metastable events is defined as “small microscopic events that initiate and repassivate at potentials below the breakdown potential” [6]. The correlation of these active areas with the induction of metastable events is supported by the work of G.T. Burstein and co-workers [7]. They have reported the induction of metastable events in Ti alloys exposed to physiological solutions, namely Ringer’s solution. They also established that these breakdowns were temperature-dependant.

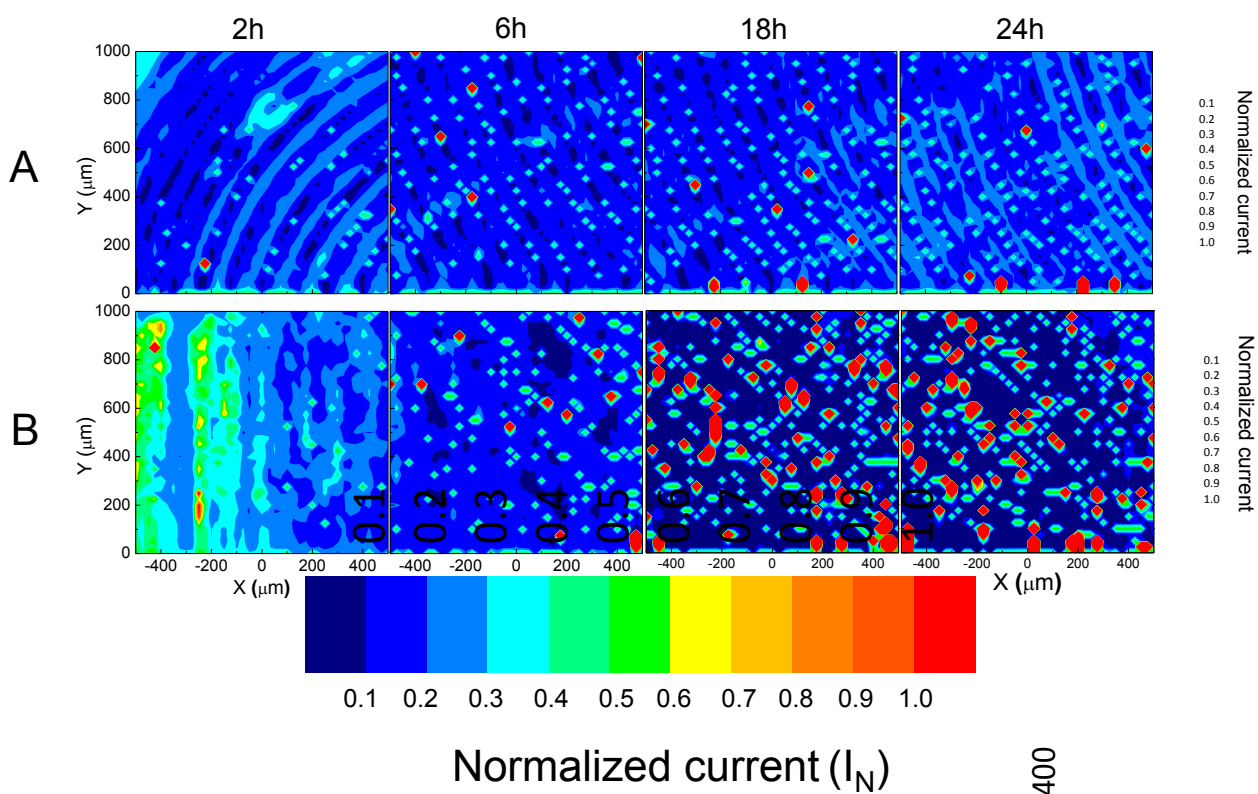


Figure 4. 3 SECM maps of $1 \times 1 \text{mm}^2$ recorded on A) Ti6Al4V alloy and B) TiPM after 2, 6, 18 and 24 hours exposed to PBS solution and 37°C

Figure 4.3(B) shows maps recorded on the surface of **TiPM** at the same immersion times. It was revealed that TiPM had lower insulating features than Ti6Al4V alloy at early immersion times (e.g., 2 hours) even though TiPM had more oxygen content on its surface as it was previously observed by SEM. The poor insulating nature observed in TiPM can be correlated with its roughness. The roughness of TiPM was found to be almost 100 nm greater the one of Ti6Al4V alloy. The roughness of TiPM generated high specific areas among the surface of the metal slowing down the creation of the oxide layer. As it was observed on Ti6Al4V alloy, the active areas of TiPM also increased with time. In the case of TiPM more active areas

than in Ti6Al4V alloy were observed. Besides, it was observed that TiPM became considerably more insulating (dark blue) than Ti6Al4V alloy after performing the 24 hours-SECM test.

The active areas have been estimated following Equation 4.1:

$$\% \text{ active area} = \frac{\text{number of points with } I_N > 1}{\text{total number of points recorded at 24 hours}} \times 100 \quad (\text{Equation 4.1})$$

The percentage of **active area** recorded on each material is shown in Figure 4.4. The reactivity of Ti6Al4V alloy remained almost unaltered during the 24 hours of test and its percentage of active area remained below 1%. In TiPM the percentage of active area suffered a 5-fold increase from 6 to 18 hours. After 18 hours this percentage was stabilized and the affected area was the 5.2% of the total tested area.

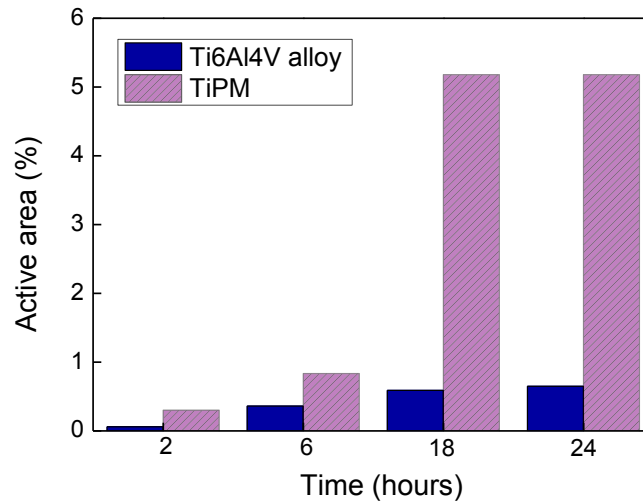


Figure 4. 4 Active area recorded on Ti6Al4V alloy and TiPM after 2, 6, 18 and 24 hours exposed to the PBS solution and 37°C. The percentage of active area was calculated as the cumulative number of points with $I_N > 1$ with respect to the total recorded points

With the SECM test it was confirmed the heterogeneous insulating features of both materials. It seems that the roughness of each material influences the creation of the oxide layer. The oxide layer of TiPM showed low insulating features at the beginning of the test (from 2 to 6 hours) but with time this oxide layer was more inactive than the oxide layer of Ti6Al4V alloy. Also, the high spatial resolution of the technique allowed identifying **metastable events** among the surface of both materials, being the oxide layer of TiPM more susceptible to these metastable events.

Electrochemical Impedance Spectroscopy (EIS)

Impedances of both materials were recorded each 2 hours during a day and exposed to the same conditions used in SECM maps: PBS solution and 37°C. Impedances at four times were selected (2, 6, 18 and 24 hours).

Impedances of the commercial **Ti6Al4V alloy** are shown in Figure 4.5. Nyquist plots are depicted in Figure 4.5(A) and the logarithmic Bode plot of the modulus of the impedance and the semi logarithmic Bode plot of the phase angle are shown in Figure 4.5(B) and Figure 4.5(C), respectively. It was observed that the modulus of the impedance slightly increased from 2 to 24 hours. Also the bell of the phase angle plot became wider. This confirms that Ti6Al4V alloy was stable during the 24 hours-test because diagrams barely varied.

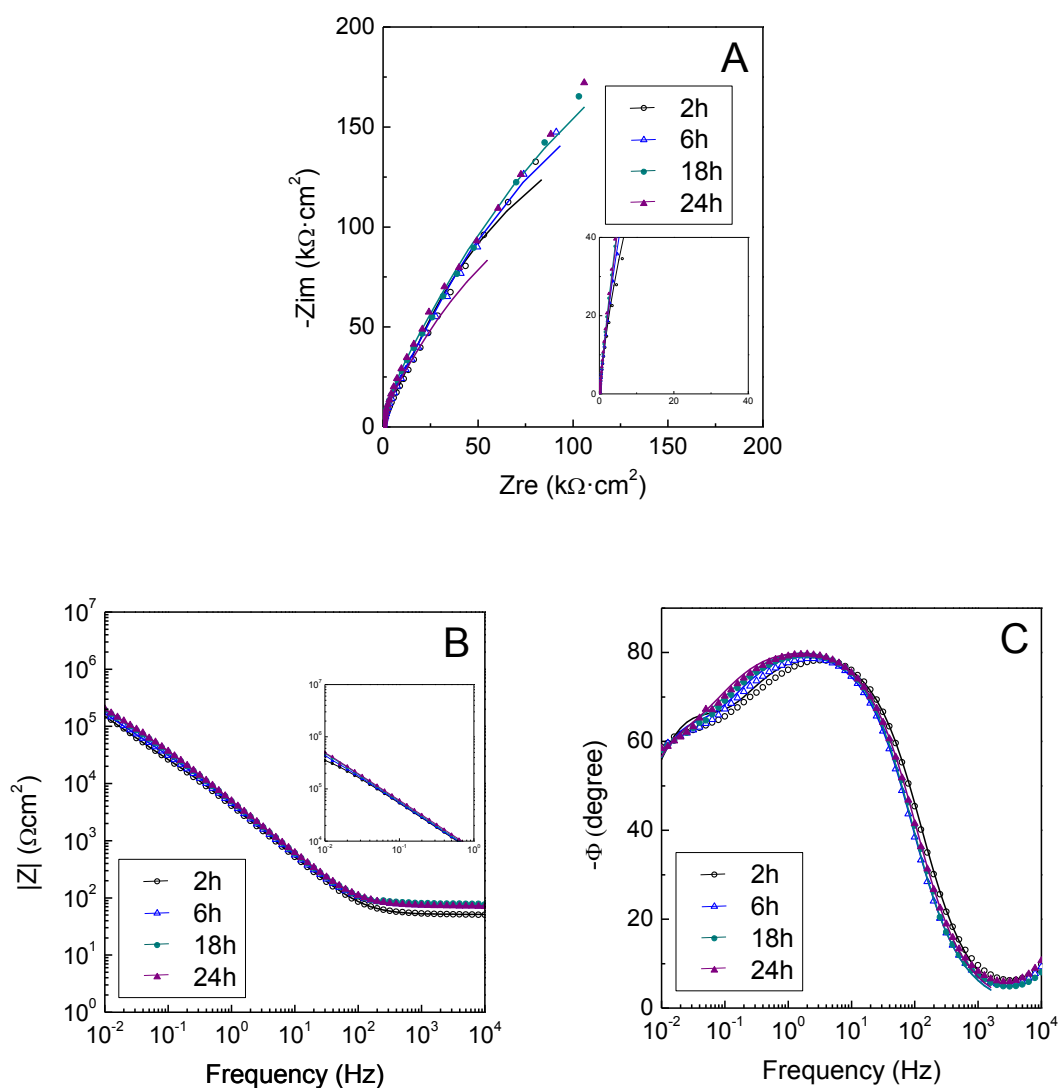


Figure 4. 5 Measured (discrete points) and fitted (solid lines) impedance spectra of Ti6Al4V alloy after 2, 6, 18 and 24 hours exposed to PBS solution and 37°C

Plots of **TiPM** are presented in Figure 4.6. This material showed no variations on the averaging impedance (Figure 4.6(B)). Differences were observed however, in Nyquist plot (Figure 4.6(A)) where the imaginary and the real components of the impedance are depicted: the amplitude of Nyquist arc increased with the immersion time in the testing solution. Differences were also observed in the phase angle diagram (Figure 4.6(C)) where it was observed that the bell became wider and near to a pure capacitor. Values of the phase angle were very close to 90 degrees. Comparing the averaging electrochemical response of Ti6Al4V alloy and TiPM, it can be stated that TiPM had better barrier properties under the testing solution than Ti6Al4V alloy. Indeed, this is in good agreement with SECM maps where it was observed that TiPM was more insulating (dark blue) than Ti6Al4V alloy after the 24 hours-test.

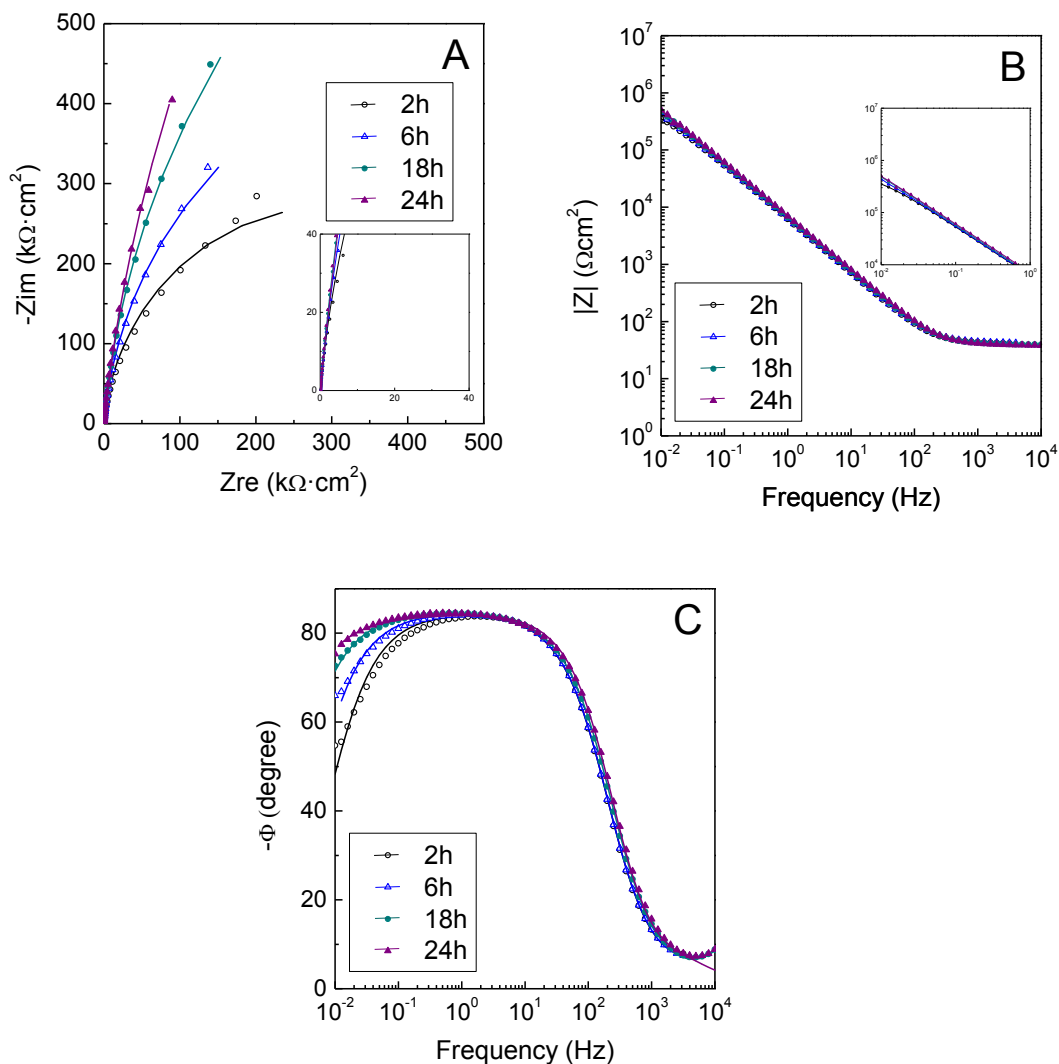


Figure 4. 6 Measured (discrete points) and fitted (solid lines) impedance spectra of TiPM after 2, 6, 18 and 24 hours exposed to PBS solution monitored at 37°C

Specimens were left one week in PBS solution to evaluate the long-term electrochemical performances of both materials. In Figure 4.7 are shown the impedances of metals after 24 hours and 1 week of exposure to the testing electrolyte. Despite Ti6Al4V alloy had a stable behaviour, its averaging barrier properties were lower when compared with TiPM. This is evidenced when observing that TiPM had a more open arc in Nyquist plot (Figure 4.7(A)) and a higher modulus of the impedance (Figure 4.7(B)) even after 1 week.

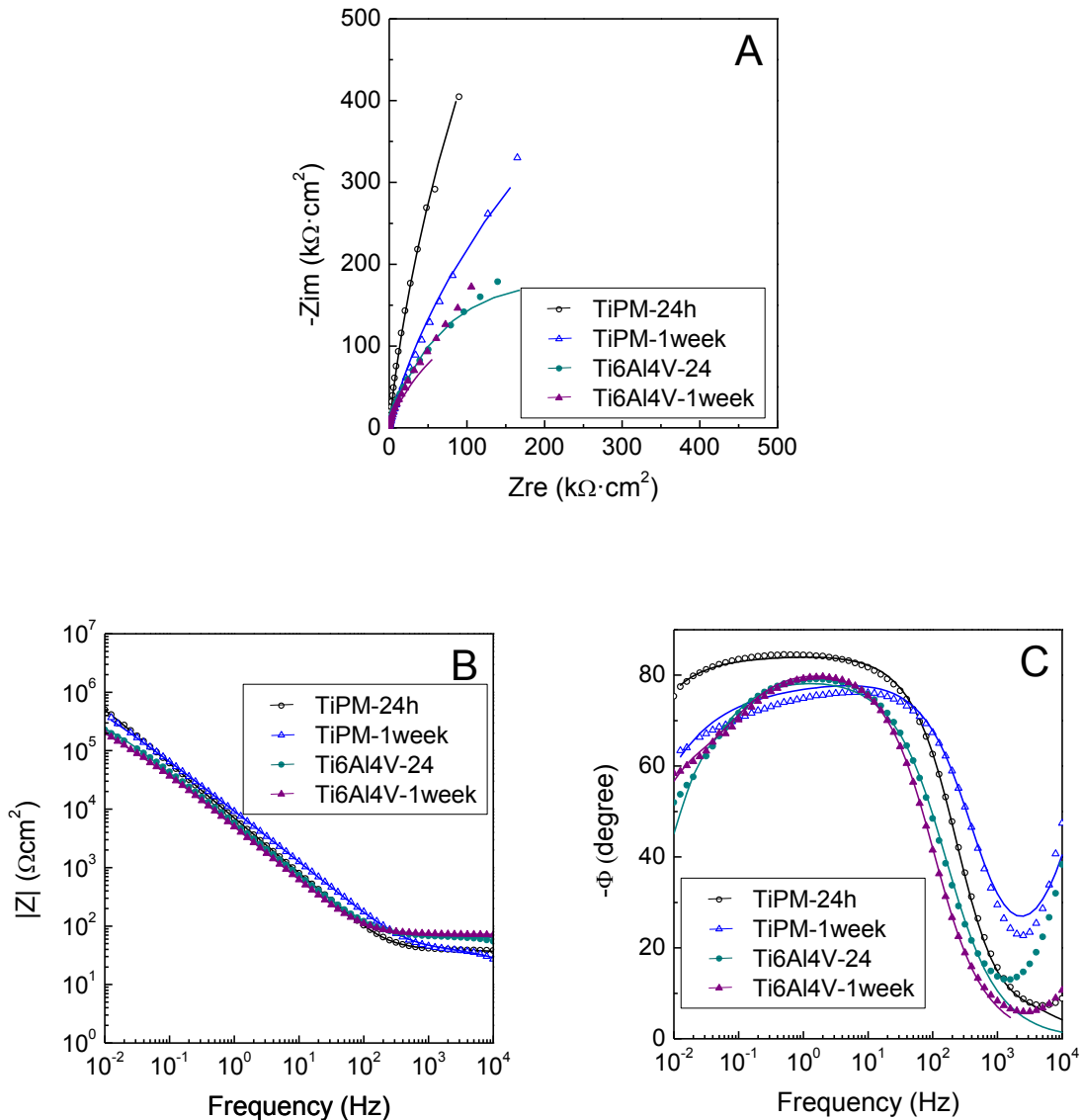


Figure 4. 7 Measured (discrete points) and fitted (solid lines) impedance spectra of Ti6Al4V alloy and TiPM after 24 hours and 1 week exposed to PBS solution monitored at 37°C

One relaxation time is observed in Bode plots of both specimens, but the wide bells observed in both materials, which became even wider from 2 to 24 hours, suggests that two phenomena are masked. Many descriptive models are employed to characterize passive

metals with two relaxation times [8]. Two of the most accepted ECs used for passive metals are commented and illustrated in Figure 4.8 [9]. In both ECs the resistance of the electrolyte is identified as R_e .

Model A: This EC is used when the oxide layer is **compact**. R_1 and CPE1 represent the electrical double layer whereas R_2 and CPE2 are ascribed to the dielectric features of the passive layer. The two constant times are connected in series because each phenomenon is assumed to take place consecutively.

Model B: This EC is employed for metals that have a **porous** oxide layer. The first constant time is associated with the ionic resistance (R_1) of the pores of the passive layer impregnated with the electrolyte and the capacitance (CPE1) of the passive layer (pore-free zones). The second constant time corresponds to the electrochemical double-layer capacitance (CPE2) and the resistance of the charge-transfer (R_2) of the corrosion process, both in the base of the pores. Both phenomena are identified simultaneously, thus the two constant times are placed in parallel.

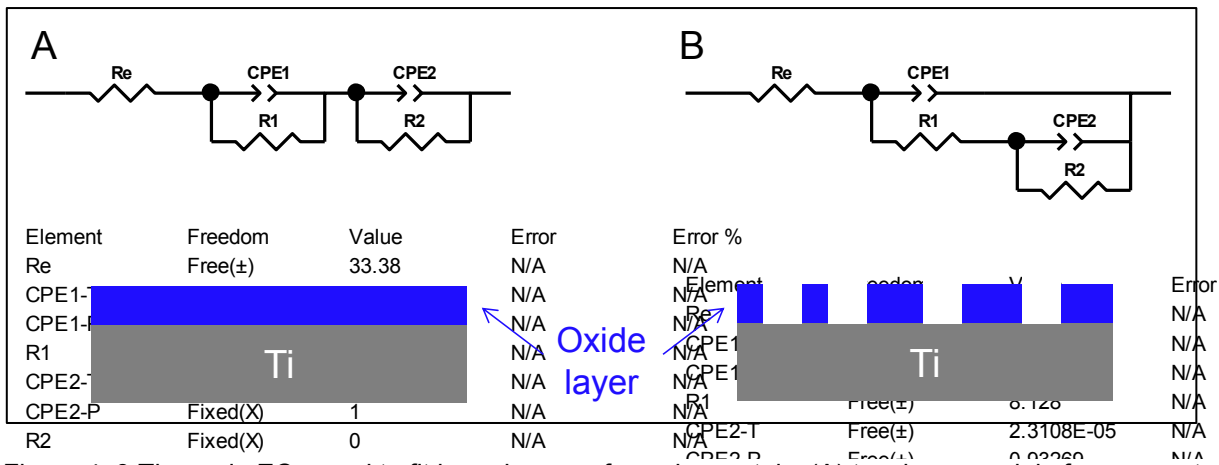


Figure 4. 8 The main ECs used to fit impedances of passive metals: (A) two-layer model of a compact oxide layer and (B) two-layer model of a porous oxide layer

Titanium-based materials are reported to spontaneously develop a thin oxide layer when the material is exposed to an aqueous solution. This oxide layer is reported to be on the nano-meter scale ranging between 1 and 10 nm [10]–[12]. Due to the thin layer of oxide formed, in this research work the uncoated material has been fitted with the EC of Figure 4.8(B) assuming that the metallic substrate develops a porous oxide layer among the surface.

The good agreement between fitted and measured data is ensured with a chi-square value below 0.001 ($\text{Chi-Sqr} < 10^{-3}$). The values are shown in Table 4.2. Constant phase elements (CPEs) were employed to take into account the intrinsic non-homogeneities of the oxide layer and the oxidized metal surface.

Table 4. 2 Parameters of the EC of Ti6Al4V alloy and TiPM after 2, 6, 18, and 24 hours and 1 week exposed to the testing solution and 37°C

Circuit element	$ Z _{10\text{mHz}}$ $\times 10^5$	Re Ωcm^2	R1 Ωcm^2	CPE1 μFcm^{-2}	n1	R2 Ωcm^2	CPE2 μFcm^{-2}	n2	χ^2 $\times 10^{-3}$	
Ti6Al4V	2h	1.5	25.8	2.8×10^4	89.2	0.912	1.7×10^5	65.9	0.859	1.48
	6h	1.7	36.9	4.4×10^4	81.9	0.915	2.0×10^5	63.9	0.850	0.92
	18h	1.9	35.5	6.5×10^4	76.2	0.915	2.1×10^5	62.3	0.866	0.78
	24h	2.0	36.3	7.5×10^4	74.2	0.915	2.7×10^5	51.9	0.788	0.60
	1w	2.3	32.4	1.5×10^5	66.4	0.897	1.2×10^5	145.1	0.981	1.23
TiPM	2h	3.5	40.4	21.4	12.9	--	6.3×10^5	15.9	0.881	1.36
	6h	3.5	38.3	8.2	4.6	--	1.0×10^6	23.4	0.929	0.28
	18h	4.7	32.6	9.2	1.5	--	2.1×10^6	25.2	0.938	0.18
	24h	4.2	30.4	10.1	1.1	--	3.2×10^6	24.4	0.937	0.83
	1w	3.7	21.3	0.8	13.7	0.780	1.4×10^6	9.2	0.941	1.67

Impedances of TiPM recorded from 2 to 24 hours were fitted using a pure capacitor in the constant time associated with the oxide layer (CPE1/R1) because when fitting the data, the factor n of CPE1 took values of one. After 1 week of immersion in the testing electrolyte, TiPM lost its capacitive features and the data was poorly correlated with the fitting as it can be observed in the phase angle plot at low frequencies Figure 4.7(C). By contrast, the fitting of Ti6Al4V alloy improved with the immersion time, being the fitting at 2 hours the one that worse simulated the data as it can be observed again in the phase angle plot at low frequencies (Figure 4.7(C)).

The parameters obtained with the fittings are listed in Table 4.2. The resistance of the electrolyte had low values ($34.3 \pm 4.3 \Omega\text{cm}^2$) due to the presence of chloride and phosphate ions in solution. This magnitude is reasonable according with the values reported in the literature [13]. The **resistance of the oxide layer** of Ti6Al4V alloy increased with the immersion time and reached its highest value after 1 week. Despite TiPM showed higher averaging impedance than Ti6Al4V alloy during the whole test, the resistance of its oxide decreased with the immersion time. Besides, R1 of TiPM was found to be 3 orders of magnitude lower than the R1 of the oxide of Ti6Al4V alloy. These differences between the averaging impedance and the resistance of the oxide can be associated with the presence of metastable events in both materials as it has been observed with SECM. In fact, the higher insulating features of TiPM observed with SECM is supported with the higher impedance registered in EIS. The presence of more metastable events in TiPM is ascribed with the poor resistance of the oxide created among the surface of TiPM when compared with the resistance of the oxide of Ti6Al4V alloy. Both materials lost their barrier features after 1 week

of exposure to the electrolyte. This was confirmed with the decrease on their capacitive parameters (C1 or CPE1) and the shift of the phase angle at low frequencies to lower values. The phase angle of TiPM shifted from 77.4 to 63.4 degrees and the angle of Ti6Al4V alloy, from 58.4 to 52.0 degrees.

The **capacitance of the oxide layer** can be estimated with the capacitance formula of a parallel-plate capacitor (Equation 4.2):

$$C = \varepsilon_r \varepsilon_0 (A/d) \quad (\text{Equation 4.2})$$

where C is the capacitance of the oxide ($\text{F} \cdot \text{cm}^{-2}$), ε_0 the vacuum permittivity ($\varepsilon_0 = 8.8542 \cdot 10^{-14} \text{F} \cdot \text{cm}^{-1}$), ε_r the relative permittivity of the oxide layer, A (cm^2) is the area of the testing materials, and d (cm) the thickness of the oxide. Considering the titanium oxide thickness to be 1-10 nm and its dielectric constant (ε_r) between 10 and 100, it is expected the capacitance of the oxide to be 10^{-5} - $10^{-6} \text{F} \cdot \text{cm}^{-2}$ [10]–[12]. These values correlated with the values of CPE1 estimated with the fittings.

The **capacitance of the double-layer capacitance** (CPE2) is proportional to the corrosion rate, meaning that a reduction on the CPE2 is an evidence of a lower corrosion rate. The CPE2 of TiPM after 1 week reached the magnitude order of 10^{-6}Fcm^{-2} while the values registered on Ti6Al4V alloy after 1 week achieved values of 10^{-4}Fcm^{-2} . These values of capacitance are similar to the values reported in the literature for the capacitance of the double-layer capacitance of bare metals, which range between 10^{-6} and 10^{-4}Fcm^{-2} [14]. The corrosion process experienced by Ti6Al4V alloy increased with the immersion time being the increase of CPE2 accompanied with a decrease of the **resistance of the charge transfer**. For TiPM, CPE2 decreased from 2 hours to 1 week while R2 increased. The parameters of the second constant time revealed that the averaging corrosion process was less developed in TiPM than in Ti6Al4V alloy after 1 week. This agreement is supported with SECM results because after 24 hours it was observed that the insulating response (94.8% of the total area recorded after 24 hours of exposure to the physiological solution) of TiPM was more insulating (dark blue) than the one recorded in Ti6Al4V alloy.

SECM allowed studying the evolution rate of the active areas of Ti6Al4V alloy and TiPM in PBS solution and 37°C. Results showed that TiPM was more susceptible to evidence activity than Ti6Al4V alloy. TiPM showed more percentage of active areas with the time exposed to the PBS solution (from 2 to 24 hours) than Ti6Al4V alloy. Impedances revealed meanwhile, that TiPM had better averaging resistance than Ti6Al4V alloy. Despite these differences, both materials presented similar electrochemical features.

The surface of both materials after being exposed 1 week to the PBS solution and 37°C is shown in Figure 4.9. As expected after the electrochemical study, TiPM presented more metastable events (Figure 4.9(A)) than Ti6Al4V alloy (Figure 4.9(B)). A magnification of one metastable event of TiPM is shown in Figure 4.9(C-D).

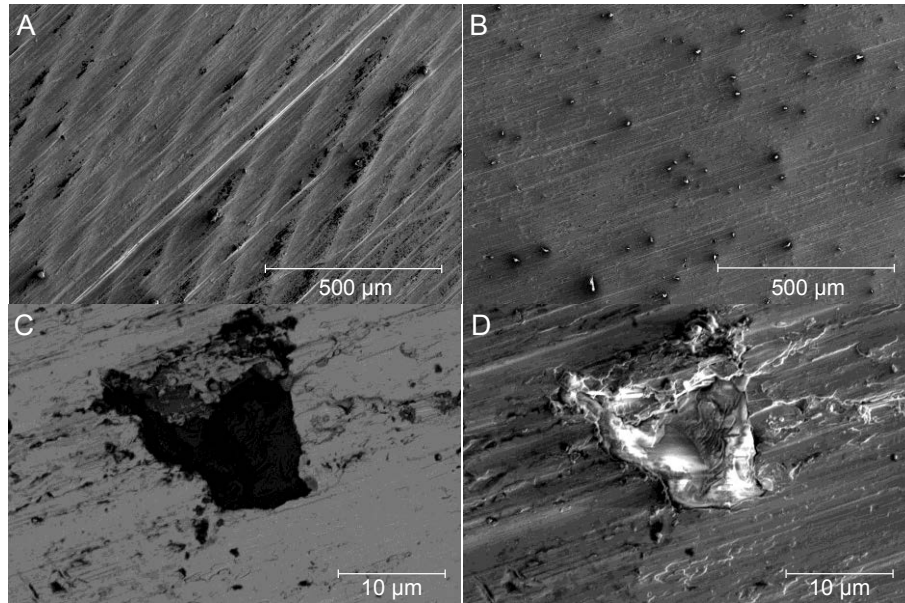


Figure 4. 9 SEM micrographs of: A) Ti6Al4V alloy and B) TiPM after 1 week exposed to the PBS solution at 37 °C and C-D) detail of a metastable event on TiPM using BSE and SE modes, respectively

4.4 MICROBIOLOGICAL STUDY

After concluding that Ti6Al4V alloy and TiPM showed similar electrochemical behaviour, a microbiological study was performed to ensure that TiPM can be proposed as an alternative material to Ti6Al4V alloy in prosthetic devices. The **bacterial adhesion** of two of the main species that causes prosthetic joint infections was studied [15]: *S. aureus*, and *E. coli*. The percentage of area covered by bacteria after the culture is shown in Figure 4.10(A). No differences between Ti6Al4V alloy and TiPM were observed because when performing the statistical contrast of each bacteria between both materials the probability was found to be above 0.001 ($p=0.0863$ for *S. aureus* 15981 and $p=0.0584$ for *E. coli* ATCC 25922).

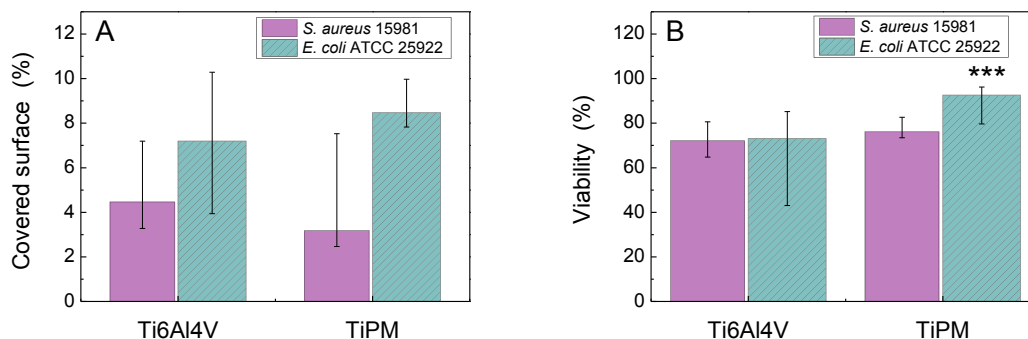


Figure 4. 10 A) Bacterial adhesion per area unit on Ti6Al4V alloy and TiPM of *S. aureus* 15981, and *E. coli* ATCC 25922. B) Viability percentages of *S. aureus* 15981, and *E. coli* ATCC 25922 in presence of Ti6Al4V alloy and TiPM. Control was considered in the absence of material.

***: Probability ($p < 0.001$) for statistical contrast between Ti6Al4V alloy and TiPM

The viability of the adhered bacteria on both materials was also tested (Figure 4.10(B)). Similar viability was observed with *S. aureus* 15981 on both materials because the probability was found to be higher than 0.001 ($p=0.3671$). By contrast, the viability of *E. coli* ATCC 25922 on TiPM was 20% significantly higher than on Ti6Al4V alloy ($p=0.0005$). The literature reports that Gram-positive coccus (e.g., *S. aureus*) is prone to adhere easily to any metallic implants [16] whereas Gram-negative bacillus (e.g., *E. coli*) is influenced by the hydrophilic/hydrophobic features of the surface [17]. Thus, the microbiological response depended on the bacteria tested and also on the different hydrophilic/hydrophobic nature of the metallic substrates.

4.5 CONCLUSIONS

Titanium manufactured by powder metallurgy (TiPM) has been tested by means of electrochemical and microbiological tests and compared with the commercial Ti6Al4V alloy mainly used in prosthetic replacements. The study confirmed that **TiPM can be presented as an alternative material to Ti6Al4V alloy**. The following conclusions can be drawn from this study:

- (1) The different manufacturing method, casting for Ti6Al4V alloy and powder metallurgy for TiPM, influenced their surface characterization. The surface characterization of both materials revealed differences in terms of oxygen content, roughness and hydrophilicity/hydrophobicity. These differences determined the electrochemical behaviour of the materials. SECM allowed an electrochemical characterization with high spatial resolution that confirmed the presence of metastable events in both materials. Impedances revealed that **TiPM had superior long-term averaging electrochemical performance** despite being more susceptible to metastable events than Ti6Al4V alloy.
- (2) Despite that TiPM is more coarse and hydrophilic, it was confirmed that the bacterial adhesion of *S. aureus* and *E. coli* to its surface was similar to the observed in Ti6Al4V alloy. The good electrochemical and microbiological performance of TiPM aims to continue the development of Ti-based materials manufactured by PM without adding toxic alloying elements because of the possibility of “customizing” the surface properties of the metal.

REFERENCES

- [1] L. Bolzoni, E. M. Ruiz-Navas, and E. Gordo, "Powder metallurgy CP-Ti performances: Hydride-dehydride vs. sponge," *Mater. Des.*, vol. 60, pp. 226–232, 2014.
- [2] I. Cvijović-Alagić, Z. Cvijović, J. Bajat, and M. Rakin, "Composition and processing effects on the electrochemical characteristics of biomedical titanium alloys," *Corros. Sci.*, vol. 83, pp. 245–254, 2014.
- [3] D. D. Macdonald, "Passivity: enabler of our metals based civilisation," *Corros. Eng. Sci. Technol.*, vol. 49, no. 2, pp. 143–155, 2014.
- [4] J. M. Calderon Moreno, E. Vasilescu, P. Drob, P. Osiceanu, C. Vasilescu, S. I. Drob, and M. Popa, "Surface analysis and electrochemical behavior of Ti-20Zr alloy in simulated physiological fluids," *Mater. Sci. Eng. B Solid-State Mater. Adv. Technol.*, vol. 178, no. 18, pp. 1195–1204, 2013.
- [5] J. Gallo, M. Holinka, and C. S. Moucha, "Antibacterial surface treatment for orthopaedic implants," *Int. J. Mol. Sci.*, vol. 15, no. 8, pp. 13849–13880, 2014.
- [6] J.-L. Wang, R. L. Liu, T. Majumdar, S. A. Mantri, V. A. Ravi, R. Banerjee, and N. Birbilis, "A closer look at the in vitro electrochemical characterisation of titanium alloys for biomedical applications using in-situ methods," *Acta Biomater.*, vol. 54, pp. 469–478, 2017.
- [7] G. T. Burstein, C. Liu, and R. M. Souto, "The effect of temperature on the nucleation of corrosion pits on titanium in Ringer's physiological solution," *Biomaterials*, vol. 26, no. 3, pp. 245–256, 2005.
- [8] C. Boissy, B. Ter-Ovanesian, N. Mary, and B. Normand, "Correlation between predictive and descriptive models to characterize the passive film – Study of pure chromium by electrochemical impedance spectroscopy," *Electrochim. Acta*, vol. 174, pp. 430–437, 2015.
- [9] F. Mohammadi, T. Nickchi, M. M. Attar, and A. Alfantazi, "EIS study of potentiostatically formed passive film on 304 stainless steel," *Electrochim. Acta*, vol. 56, no. 24, pp. 8727–8733, 2011.
- [10] A. I. Mardare, A. Savan, A. Ludwig, A. D. Wieck, and A. W. Hassel, "A combinatorial passivation study of Ta-Ti alloys," *Corros. Sci.*, vol. 51, no. 7, pp. 1519–1527, 2009.
- [11] V. Spagnol, E. Sutter, C. Debiemme-Chouvy, H. Cachet, and B. Baroux, "EIS study of photo-induced modifications of nano-columnar TiO₂ films," *Electrochim. Acta*, vol. 54, no. 4, pp. 1228–1232, 2009.
- [12] A. Wypych, I. Bobowska, M. Tracz, A. Opasinska, S. Kadlubowski, A. Krzywania-Kaliszewska, J. Grobelny, and P. Wojciechowski, "Dielectric Properties and Characterisation of Titanium Dioxide Obtained by Different Chemistry Methods," *J. Nanomater.*, vol. 2014, pp. 1–9, 2014.
- [13] Y. Bai, X. Gai, S. Li, L. C. Zhang, Y. Liu, Y. Hao, X. Zhang, R. Yang, and Y. Gao, "Improved corrosion behaviour of electron beam melted Ti-6Al-4V alloy in phosphate buffered saline," *Corros. Sci.*, vol. 123, pp. 289–296, 2017.
- [14] M. E. Orazem and B. Tribollet, *Electrochemical impedance spectroscopy*, vol. 48. 2008.
- [15] N. Benito, M. Franco, A. Ribera, A. Soriano, D. Rodriguez-Pardo, L. Sorlí, G. Fresco, M. Fernández-Sampedro, M. Dolores del Toro, L. Guío, E. Sánchez-Rivas, A. Bahamonde, M. Riera, J. Esteban, J. M. Baraia-Etxaburu, J. Martínez-Alvarez, A. Jover-Sáenz, C. Dueñas, A. Ramos, B. Sobrino, G. Euba, L. Morata, C. Pigrau, P. Coll, I. Mur, and J. Ariza, "Time trends in the aetiology of prosthetic joint infections: a multicentre cohort study," *Clin. Microbiol. Infect.*, vol. 22, no. 8, p. 732.e1-732.e8, 2016.
- [16] E. Barth, Q. M. Myrvik, W. Wagner, and A. G. Gristina, "In vitro and in vivo comparative colonization of *Staphylococcus aureus* and *Staphylococcus epidermidis* on orthopaedic implant materials," *Biomaterials*, vol. 10, no. 5, pp. 325–328, 1989.
- [17] A. Zita and M. Hermansson, "Effects of bacterial cell surface structures and hydrophobicity on attachment to activated sludge flocs," *Appl. Environmental Microbiol.*, vol. 63, no. 3, pp. 1168–1170, 1997.

CHAPTER 5

SOL-GEL SYNTHESIS

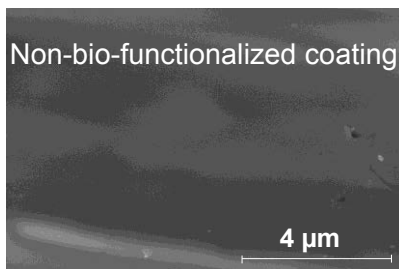
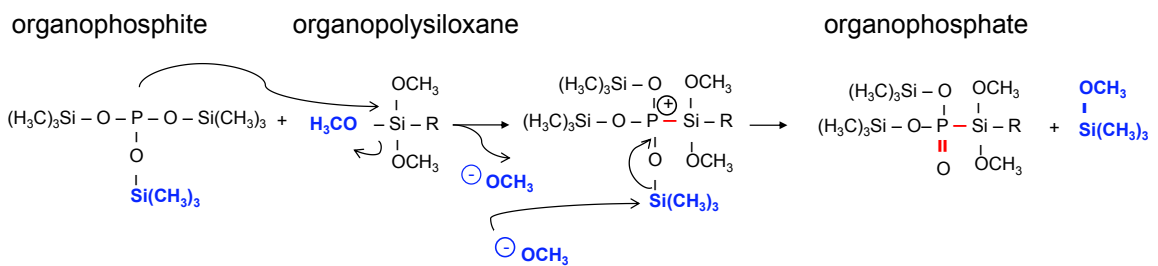
ABSTRACT.....	80
5.1 OPTIMIZATION OF THE REFERENCE SOL-GEL COATING	82
5.1.1 TAGUCHI METHOD	82
5.1.2 CHARACTERIZATION OF THE SYNTHESIS OF SOLS	84
5.1.3 CHARACTERIZATION OF THE XEROGEL	88
5.1.4 SURFACE CHARACTERIZATION OF COATINGS	90
5.1.5 ELECTROCHEMICAL CHARACTERIZATION.....	91
5.1.6 CONCLUSIONS	96
5.2 BIO-FUNCTIONALIZATION OF SOL-GEL COATINGS WITH PHOSPHORUS-BASED-COMPOUNDS.....	97
5.2.1 MATERIALS	97
5.2.2 CHARACTERIZATION OF THE SYNTHESIS OF SOLS	97
5.2.3 SURFACE CHARACTERIZATION	99
5.2.4 CHARACTERIZATION OF THE XEROGEL	100
5.2.5 CELLULAR STUDY	104
5.2.6 CONCLUSIONS	107
5.3 BIO-FUNCTIONALIZATION OF SOL-GEL COATINGS WITH MOXIFLOXACIN.....	108
5.3.1 MATERIALS.....	108
5.3.2 CHARACTERIZATION OF THE SYNTHESIS OF SOLS	108
5.3.3 CHARACTERIZATION OF THE XEROGEL	110
5.3.4 SURFACE CHARACTERIZATION	111
5.3.5 CELLULAR STUDY.....	114
5.3.6 CONCLUSIONS.....	116
REFERENCES	117

5. SOL-GEL SYNTHESIS

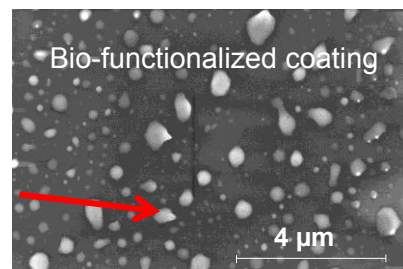
ABSTRACT

Hybrid organo-inorganic sol-gel coatings are studied in this work using **MAPTMS** and **TMOS** as precursors. The optimization of the sol-gel method was performed employing a **Taguchi method** that allowed reducing the number of the prepared syntheses from 27 to 9. Three factors of the synthesis, namely the molar ratio of the organopolysiloxanes, the reaction time of the synthesis, and the drying temperature of the coating, were modified and their influence on the hydrophilicity/hydrophobicity of coatings was studied with one-way ANOVA analysis. The contribution of the molar ratio of the organopolysiloxanes was found to be the predominant among the evaluated factors. Besides, the viability of the sol-gel method was evaluated by monitoring the evolution of the reaction and the viscosity. It was observed that higher additions of MAPTMS contributed to slow the reaction rate down and compromised the cross-linkage and stability of the network. All the coatings showed an elevated water contact angle when compared with the uncoated specimen, which is expected to **prevent the adhesion of bacteria**. The best coatings were selected and subjected to an electrochemical study in 0.9 wt.% NaCl. Only one of the coatings showed appropriate electrochemical features and was selected as the reference coating for the subsequent bio-functionalizations.

The **bio-functionalization** of coatings with a **phosphorus-based compound** was performed with three compounds. Three coating have been prepared by adding **tris(trimethylsilyl) phosphite**, **tris(trimethylsilyl) phosphate**, and an aqueous solution containing phosphate ions (**PBS solution**). Results showed that only the addition of the organophosphites integrated the phosphorus compound onto the sol-gel due to the transformation of trivalent phosphorus to pentavalent phosphorus following a **Michaelis-Arbuzov reaction**.



Localized sites with high P content



The synthesis modified with the addition of the organophosphite was selected and coatings with different concentration of phosphite were prepared. Coatings were subjected to a **cellular study** and it was observed that the increase on the phosphorus content led to a small increase on the cellular proliferation. The inspection of the surfaces of the coatings revealed that by increasing the quantity of organophosphite, the adhesion to the substrate was compromised. An intermediate quantity of organophosphite was considered to be the most suitable to be applied on metallic prostheses.

The second part of the bio-functionalization of coatings was the addition of an antibiotic, **moxifloxacin** (MOX). MOX was selected as the active agent to **treat bacterial infections** due to their broad spectrum activity against gram positive, gram negative and anaerobic pathogens. The addition of MOX to the synthesis did not alter the evolution of the reaction and the cross-linkage of the network. It was verified that the addition of MOX did not compromise the non-cytotoxicity and the cellular proliferation of the materials.

5.1 OPTIMIZATION OF THE REFERENCE SOL-GEL COATING

5.1.1 TAGUCHI METHOD

Taguchi method was employed to minimize the number of sol-gel routes prepared in order to optimize the reference sol-gel synthesis. Three parameters of the sol-gel method, which are reported to determine the final properties of sol-gel coatings, were modified: the molar ratio of the organopolysiloxanes, the reaction time of syntheses and the drying temperature of coatings [1]–[3]. The **hydrophilic/hydrophobic degree** of coatings was the selected parameter to be evaluated with Taguchi method because it is a key parameter on the “race to the surface” between bacteria and cells [4]. The bibliography reports that bacteria prefer hydrophobic surfaces while cells are more attracted to hydrophilic surfaces [5], [6].

A Taguchi orthogonal array procedure with 3 levels was employed. The selected parameters of the process for each level are summarized in Table 5.1. The orthogonal array used with Taguchi method was calculated by raising the number of factors to the number of levels with Equation 5.1. A L9 orthogonal array was obtained, which resulted in the preparation of nine sol-gel routes.

$$\text{level}^{\text{factor}} = 3^3 \quad (\text{Equation 5. 1})$$

Table 5. 1 Designed experimental factors and levels of Taguchi method

Parameters of the process	Level 1	Level 2	Level 3
Molar ratio of MAPTMS:TMOS	1:1	1:2	2:1
Reaction time (hours)	1	8	24
Drying temperature (°C/1h)	60	120	180

The nine sol-gel routes and the water contact angle of each coating are listed in Table 5. 2. Coatings showed intermediate hydrophilicity with values that ranged between 62.2 and 78.6 degrees. In order to identify the process parameter that reduced the variability of the response, the water contact angle, the signal-to-noise (S/N) ratio of the water contact angle was calculated. The S/N ratio was calculated with Equation 5. 2. The aim is to target the response to intermediate hydrolytic/hydrophobic values. This equation is identified as the *nominal is better* procedure.

$$S/N = -10 \log_{10}(\sigma^2) \quad (\text{Equation 5. 2})$$

where σ is the standard deviation of the measured response.

Table 5. 2. Water contact angle and S/N ratio of each prepared coating

Sol-gel route	Molar ratio of MAPTMS:TMOS	Reaction time (h)	Drying Temp.(°C)	Water contact angle (°)	S/N ratio (dB)
S1		1	60	62.2	-7.9
S2	1:1	8	120	72.4	8.3
S3		24	180	64.1	-1.4
S4		1	120	72.7	-7.8
S5	1:2	8	180	71.0	-4.6
S6		24	60	68.9	-12.4
S7		1	180	75.2	1.5
S8	2:1	8	60	76.6	-5.2
S9		24	120	78.6	-4.0

Coatings S3 and S7 presented the lowest S/N ratio, meaning they showed the lowest variability on the response. Then, an analysis of variance (ANOVA) was performed to evaluate the contribution of each factor to the response. The degree of freedom (DF) of each factor was calculated as one less the level associated to each factor. The sequential sum of squares ($SeqSS_{factor}$) identifies the variability in the data associated to each factor and was calculated using Equation 5. 3. The total sum of $SeqSS$ ($SeqSS_{total}$) is the sum of the variability ascribed to each data and was calculated with Equation 5. 4. The contribution of each factor to the response was calculated using Equation 5. 5 [7].

$$SeqSS_{factor} = \sum n_i (\bar{y}_i - \bar{y})^2 \quad (\text{Equation 5. 3})$$

$$SeqSS_{total} = \sum_i \sum_j (y_{ij} - \bar{y})^2 \quad (\text{Equation 5. 4})$$

$$contribution(\%) = \frac{SeqSS_{factor}}{SeqSS_{total}} \times 100 \quad (\text{Equation 5. 5})$$

where n_i is the number of observations for the i th factor level, \bar{y}_i is the mean of all the observations at the i th factor level, \bar{y} is the mean of all the observation, and y_{ij} is the value of the observation at the i th factor level.

ANOVA results are shown in Table 5. 3 and identified the **molar ratio** as the factor influencing more the hydrolytic/hydrophobic properties with a **contribution of 71.2%**. The drying temperature of coatings and the reaction time of syntheses contributed less to the variability of the response with values of 20.8 and 8.0 %, respectively. Taguchi method revealed that in spite of varying the parameters of the synthesis, all the coatings showed intermediate hydrophilic angles.

Table 5. 3 ANOVA result of each studied factor

Parameters of the process	DF	SeqSS _{factor}	Contribution (%)
Molar ratio of MAPTMS:TMOS	2	168.1	71.2
Reaction time (hour)	2	19.0	20.8
Drying Temp. (°C)/1h	2	49.1	8.0
Total	6	236.2	100.0

5.1.2 CHARACTERIZATION OF THE SYNTHESIS OF SOLS

The evolution of the hydrolysis-polycondensation rate was monitored with Fourier-Transform Infrared Spectroscopy (FTIR) after 1, 8 and 24 hours of reaction. Figure 5. 1 depicts the FTIR spectra of the three prepared syntheses.

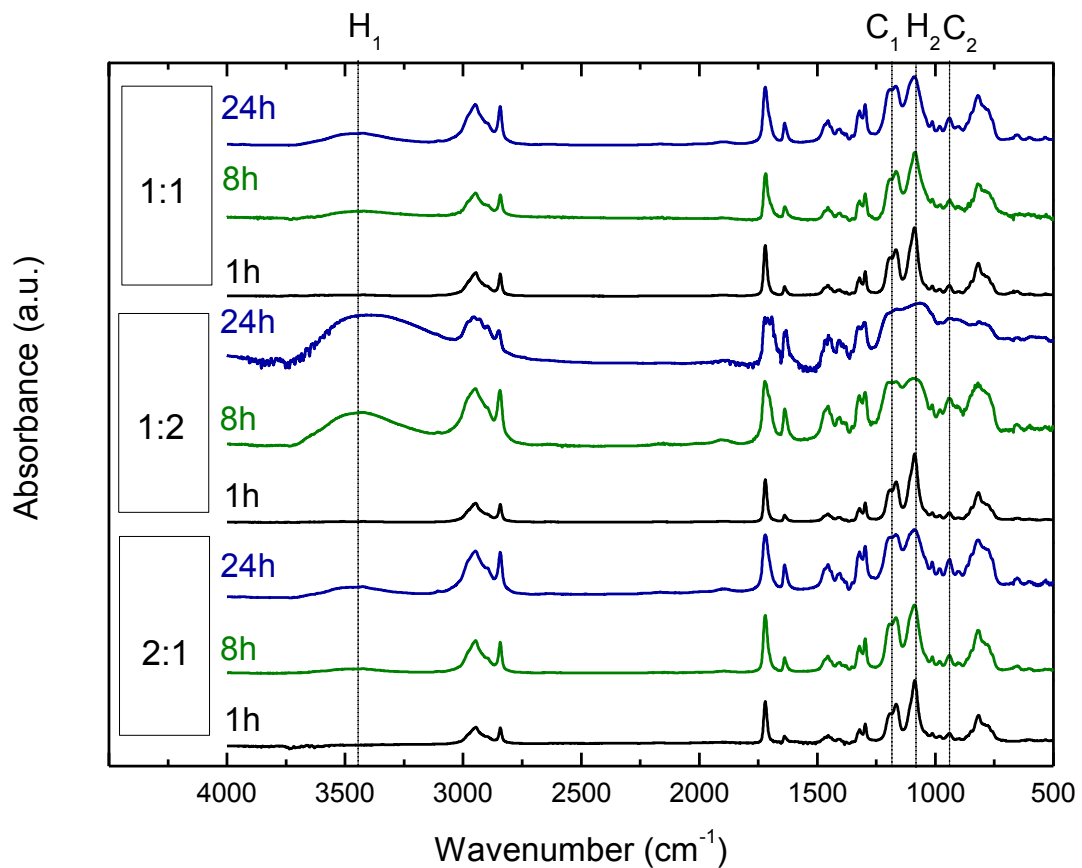


Figure 5. 1 FTIR spectra of the sol-gel synthesis with a molar ratio (MAPTMS:TMOS) of 1:1, 1:2, 2:1 at different reaction times (1, 8 and 24 hours)

Spectra revealed the most relevant bond-type signals associated with the hydrolysis-polycondensation reaction. The assignments of the most relevant peaks are summarized in Table 5. 4. During hydrolysis, Si-OH bonds are created and their evidence is observed with the apparition of a broad band between 3100 and 3600 cm^{-1} (H_1). While Si-OH bonds are created, Si-O-CH₃ bonds from the starting organopolysiloxanes are broken. The peak associated to Si-O-CH₃ bond is identified at 1080 cm^{-1} (H_2). Once hydrolysis starts, polycondensation simultaneously undergoes reaction. Polycondensation is associated with the formation of Si-O-Si bonds (peaks situated at 1187 cm^{-1} (C_1) and 980 cm^{-1} (C_2)). At short times of reaction (1 hour) no evidence of hydrolysis was observed in the syntheses because band H_1 was not revealed. After 8 hours of reaction, synthesis 1:2 showed the first evidences of hydrolysis and polycondensation reactions with the appearance of the main bond-type associated with both reactions: appearance of the hydrolysis band (H_1) and the polycondensation peak (C_1). Syntheses 1:1 and 2:1 showed however, no evidence of reaction until 24 hours of reaction was reached. After 24 hours, the first signs of hydrolysis were identified with the slightly appearance of band H_1 .

Table 5. 4 Assignment of the FTIR peaks revealed in Figure 5. 1

Identification	Wavenumber / cm^{-1}	Assignment
H_1	3100-3600	$\nu_{\text{O-H}}(\text{Si-OH})$
C_1	1187	$\nu_{\text{as}}(\text{Si-O-Si})$
H_2	1080	$\nu_{\text{as-Si-O}}(\text{Si-O-CH}_3)$
C_2	980	$\nu_{\text{s}}(\text{Si-O-Si})$

*s: symmetric; as: asymmetric

The relevance of this study was to establish the **optimal reaction time** of the synthesis prior to the deposition of sols on the substrates. It is required a compromise between the creation of free-hydroxides (Si-OH) during hydrolysis and the formation of siloxane bonds (Si-O-Si) during polycondensation. The good adhesion between coating and metal is reached with the creation of strong covalent bonds between the free-hydroxides of sols and the ones of the metallic substrate. By contrast, the creation of enough siloxane bonds ensures the good cross-linkage of the sol-gel network. For this purpose, the normalized height of the most relevant peaks associated to hydrolysis (band H_1) and polycondensation (peak C_1) were calculated. Table 5.5 shows the normalized heights and the **H_1/C_1 ratio** of each synthesis. The evolution of the H_1/C_1 ratio during hydrolysis-polycondensation reactions follows four stages:

- (1) At early stages of reaction, the hydrolysis band is barely appreciated. Peak C_1 is higher than band H_1 ($H_1 < C_1$) because peak C_1 is overlapped by other signals provided by bonds of the starting organopolysiloxanes. Signals of the non-hydrolysed groups of the starting organopolysiloxanes were already identified in previous works [8].
- (2) Once hydrolysis starts, band H_1 starts to increase in detriment of peak C_1 ($H_1 > C_1$).

- (3) Then, a compromise between both reactions is reached and both signals have similar heights ($1 < H_1/C_1 < 2$).
- (4) Once hydrolysis ends, C_1 is higher than H_1 ($H_1 < C_1$) until full gelation is reached. At full gelation, H_1 almost disappears.

At the fourth stage, sols are too condensed and with very few Si-OH bonds to create covalent bonds with the metallic substrate. In this research project, the optimal reaction stage has been established when peak C_1 reaches similar height than peak H_1 ($1 < H_1/C_1 < 2$). The H_1/C_1 ratio of each synthesis is calculated in Table 5.5. It was observed that only synthesis 1:2 reached after 24 hours of reaction an appropriated reaction rate, which corresponds with synthesis S6. Comparing synthesis 1:1 and 2:1, the latter is the one that experienced the lowest reaction evolution. This can be observed by comparing the H_1/C_1 ratio calculated at 24 hours: 0.262 for synthesis 1:1 (synthesis S3) against 0.171 for synthesis 2:1 (synthesis S9).

Table 5. 5 H_1/C_1 ratio calculated with the normalized heights of Figure 5.1

Sol	H_1	C_1	H_1/C_1 ratio
S1	0.017	0.512	0.033
S2	0.086	0.590	0.146
S3	0.170	0.649	0.262
S4	0.013	0.427	0.030
S5	0.494	0.631	0.783
S6	0.778	0.518	1.502
S7	0	0.388	0
S8	0.064	0.633	0.101
S9	0.103	0.603	0.171

The **viscosity** of sols is a time-dependant parameter during the **sol-to-gel transition**. The viscosity of sols increases with time due to the growth and connection of particles. Sols behave as non-Newtonian liquids and by measuring the viscosity as a function of the applied shear rate, sols can be classified as: (1) **shear thinning fluids** if their viscosities decreased with the applied shear rate or (2) **shear thickening fluids** if their viscosities increases with the applied shear rate [9]. The evolution of the viscosity of each synthesis with the reaction time (from 1 to 24 hours) is depicted in Figure 5.2. At early stages of reaction (1-8 hours) sols behaved as shear thinning fluids and their mean viscosity reached 1 mPa·s. At 24 hours of reaction, the viscosity of sols 1:1 (Figure 5.2(A)) and 1:2 (Figure 5.2 (B)) decreased one order of magnitude from 1 to 10 mPa·s. Their behaviour changed to shear thickening fluids. By contrast, the viscosity of the sol with the highest amount of MAPTMS (Figure 5.2(C)) remained almost unaltered.

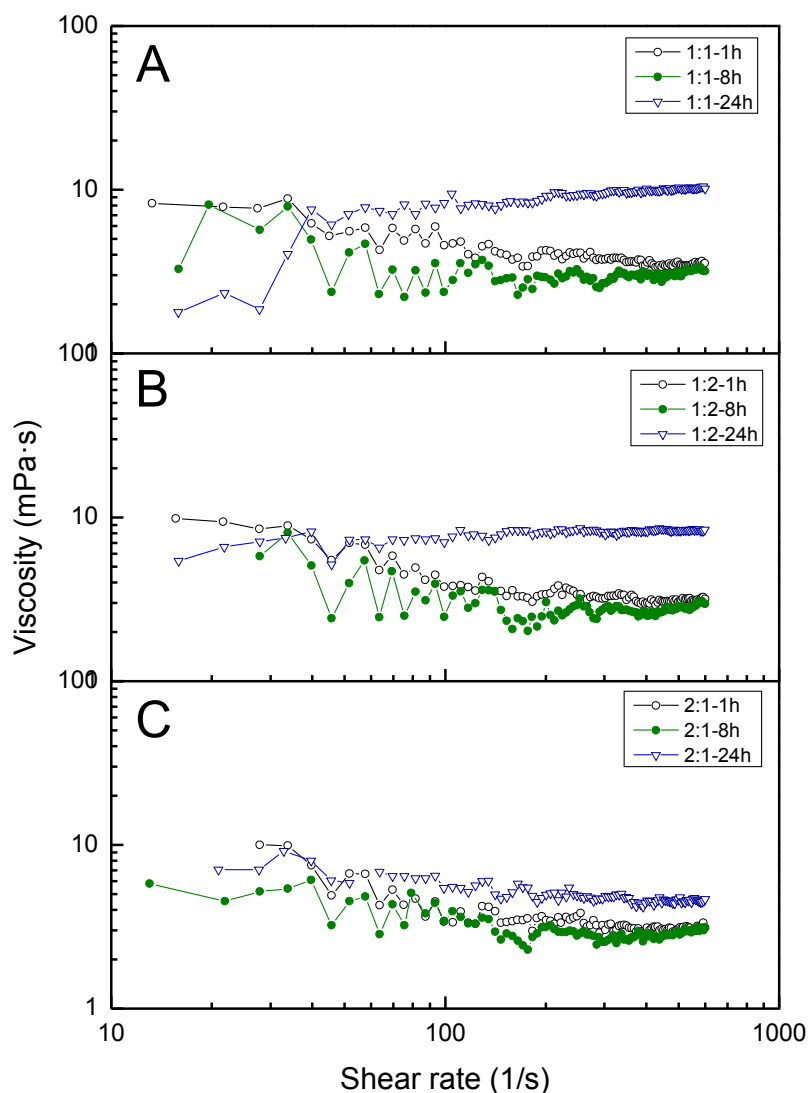


Figure 5. 2 Relation between the viscosity and the applied shear rate on sols with a molar ratio (MAPTMS:TMOS) of A) 1:1, B) 1:2, and C) 2:1 after 1, 8, and 24 hours of reaction

It seems that sols experience two consecutive stages during the sol-gel synthesis. Sols changed from shear thinning to shear thickening fluids. These stages can be correlated with the different steps of the hydrolysis-polycondensation reaction. The shear thinning behaviour is associated with early stages of reaction with low hydrolysis evolution ($H_1 < C_1$). Then, the shear thickening behaviour is observed when enough polycondensation undergoes simultaneously with hydrolysis ($1 < H_1/C_1 < 2$). This discussion is in good agreement with FTIR results because synthesis 1:2 evidenced the highest reaction evolution while synthesis 2:1 barely experienced hydrolysis.

The discrepancy was observed in synthesis 1:1. The viscosity evolution was found to be similar to the one of synthesis 1:2. However, the reaction evolution of synthesis 1:1 was found to be close to the one of synthesis 2:1. The correlation between the rheological and the FTIR study seems not to be adequate when the sol-gel synthesis is nearby reaching the second stage of the synthesis ($1 < H_1/C_1 < 2$).

5.1.3 CHARACTERIZATION OF THE XEROGEL

The thermogravimetric analysis (TGA) and the differential weight loss (DTG or first derivate) plots of the xerogels are shown in Figure 5. 3. The study allows quantifying the inorganic contribution to the network (Si-O-Si bonds) and ensuring that during the drying step the organic chains of MAPTMS are not degraded. The xerogels showed three degrading regions. The **first stage** (Region I) was observed around 220°C and is associated with the elimination of the condensation by-products of the synthesis (alcohol and water) and the unreacted organopolysiloxanes ($p_{b_{\text{TMOs}}}= 121^{\circ}\text{C}$, $p_{b_{\text{MAPTMS}}}=190^{\circ}\text{C}$) [10]–[12]. This stage barely contributed to the total mass loss of the xerogel 1:1 but it was more patent in xerogels 2:1 and 1:2 where the elimination of solvents was more gradual. The **second degrading stage** (Region II) was identified with a sharp inflection around 350°C and corresponds to the partial thermal degradation of organic matter (oligomers and unreacted organopolysiloxanes). And the subsequent **third stage** (Region III) was observed between 350°C and 500°C and is due to the complete thermal degradation of the organic matter. These two stages (Region II and III) were identified in all the xerogels being the peak of the xerogel 1:1 the most pronounced. The rearrangement of the organic chain of MAPTMS in the xerogel 1:1 could have retarded the appearance of the first stage, which seems to be added to the second region. Concerning the total mass loss, it was observed that the xerogel 1:2 had the highest percentage of residue at 800°C, meaning that this synthesis had more inorganic contribution (siloxane bonds) than the others. The inorganic contribution is not degraded within the range of temperatures of the test. Thus, the percentage of residue at 800°C can be taken as a first indicator of the creation of siloxane bonds, which will be supported with a ^{29}Si -NMR test. The percentage of the inorganic contributions increased with the content of TMOS added to the synthesis as follows: 55.8 wt.% for the xerogel 1:1, 58.8 wt.% for the xerogel 2:1 and 65.4 wt.% for the xerogel 1:2. Moreover, it was confirmed that the temperature used to dry coatings (60°C) did not alter the organic chain of MAPTMS because at 60°C it was not observe a thermal degrading process.

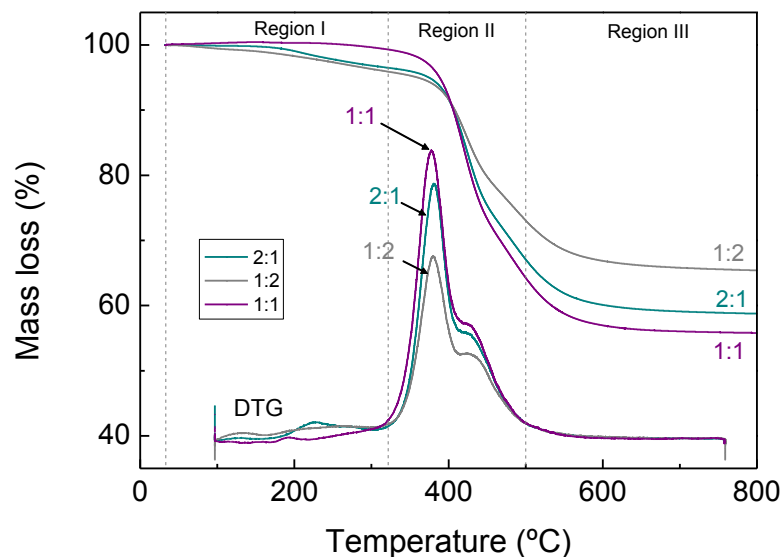


Figure 5. 3 TGA and DTG profiles of the xerogels 1:1, 1:2 and 2:1. The xerogels were dried at 60°C for 4 hours

The entourage of the sol-gel network has been evaluated with NMR of silicon nuclei to study the degree of inorganic polymerization of the network. Spectra obtained with ^{29}Si MAS-NMR of the xerogels 1:1, 1:2, and 2:1 are shown in Figure 5. 4. According to the organopolysiloxanes used two species are identified, T and Q, as described in Chapter 3. Each T^n and Q^m species showed well defined shift ranges that were in good agreement with the bibliography [8], [10]. Signal T^1 , T^2 and T^3 of MAPTMS were identified at -49, -58, and -67 ppm. Signals Q^2 , Q^3 , and Q^4 of TMOS were observed at -92, -101, and -110 ppm. The absence of non-hydrolysable species of MAPTMS (T^0) confirmed that each molecule of MAPTMS have created at least one siloxane bond. For TMOS, no signal of the non-hydrolysable specie (Q^0) and the mono-siloxane specie (Q^1) were identified.

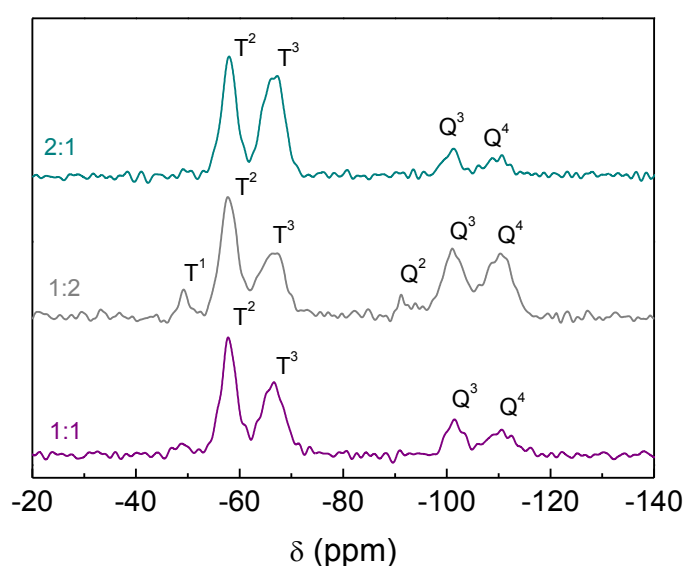


Figure 5. 4 Solid state ^{29}Si NMR spectra of the xerogels 1:1, 1:2 and 2:1. The xerogels were dried at 60°C for 4 hours

The relative proportions of T and Q species are listed in Table 5.6. By adding more MAPTMS to the formulation (the xerogels 1:1 and 2:1) T^3 increased and generated three dimensional siloxane networks. Signals of TMOS however, were poorly identified in these xerogels. In these two syntheses the cross-linkage was mainly formed by the contribution of MAPTMS (close to 80%). Synthesis 1:2 meanwhile, presented an equal contribution of T (58.2%) and Q (41.8%) species to the cross-linkage. Despite showing better defined signals of TMOS, the averaging cross-linkage of the xerogel 1:2 was found to be less branched because T^1 and Q^2 signals were also identified. The xerogel 1:2 (with the lowest amount of MAPTMS) showed the best compromise (equal contribution) between the formation of inorganic polymerization of MAPTMS and TMOS molecules.

Table 5. 6 Relative proportions of Tⁱ and Q^j species, and Tⁿ and Q^m ratio obtained from Figure 5. 4

Xerogel	Relative proportion ^a (%)						Ratio ^b (%)	
	T ¹	T ²	T ³	Q ²	Q ³	Q ⁴	T ⁿ	Q ^m
1:1	--	47.3	29.0	--	13.9	9.8	76.3	23.7
1:2	6.9	33.8	17.5	5.5	18.9	17.4	58.2	41.8
2:1	--	45.0	37.6	--	9.9	7.5	82.6	17.4

$$^a \text{ relative proportion (\%)} : T^i = (T^i / (\sum_{i=1}^3 T + \sum_{j=2}^4 Q)) \cdot 100$$

$$Q^j = (Q^j / (\sum_{i=1}^3 T + \sum_{j=2}^4 Q)) \cdot 100$$

$$^b \text{ ratio (\%)} : T^n = (\sum_{i=1}^3 T / (\sum_{i=1}^3 T + \sum_{j=2}^4 Q)) \cdot 100$$

$$Q^m = (\sum_{j=2}^4 Q / (\sum_{i=1}^3 T + \sum_{j=2}^4 Q)) \cdot 100$$

5.1.4 SURFACE CHARACTERIZATION OF COATINGS

Once the syntheses and the xerogels were characterized, sols were applied to TiPM. The surfaces of coatings were inspected with SEM and images are shown in Figure 5. 5. Two contrasts were identified: dark areas corresponded to the coating whereas bright areas to the metallic substrate. At first glance it was observed that by increasing the reaction time of the sol-gel synthesis from 1 hour (Figure 5. 5 (A)-(D)-(G)) to 24 hours (Figure 5. 5 (C)-(F)-(I)) TiPM was better coated by the sols. Concerning the drying temperature of the coatings, it seems that this parameter did not influence the surface features of coatings. Comparing for example coatings S3, S5, and S7, which were dried at 180°C, the adhesion of the coating to the substrate was different: S3 uniformly and homogeneously covered the whole surface of TiPM (Figure 5. 5(C)); S5 (Figure 5. 5(E)) and S7 (Figure 5. 5(G)) presented however, poor adhesion of the coatings to TiPM. Taking into account the molar ratio of the organopolysiloxanes it was observed that the synthesis containing the highest amount of MAPTMS (synthesis 2:1) presented even at 24 hours of reaction the lowest percentage of area covered with the coating (Figure 5. 5(I)).

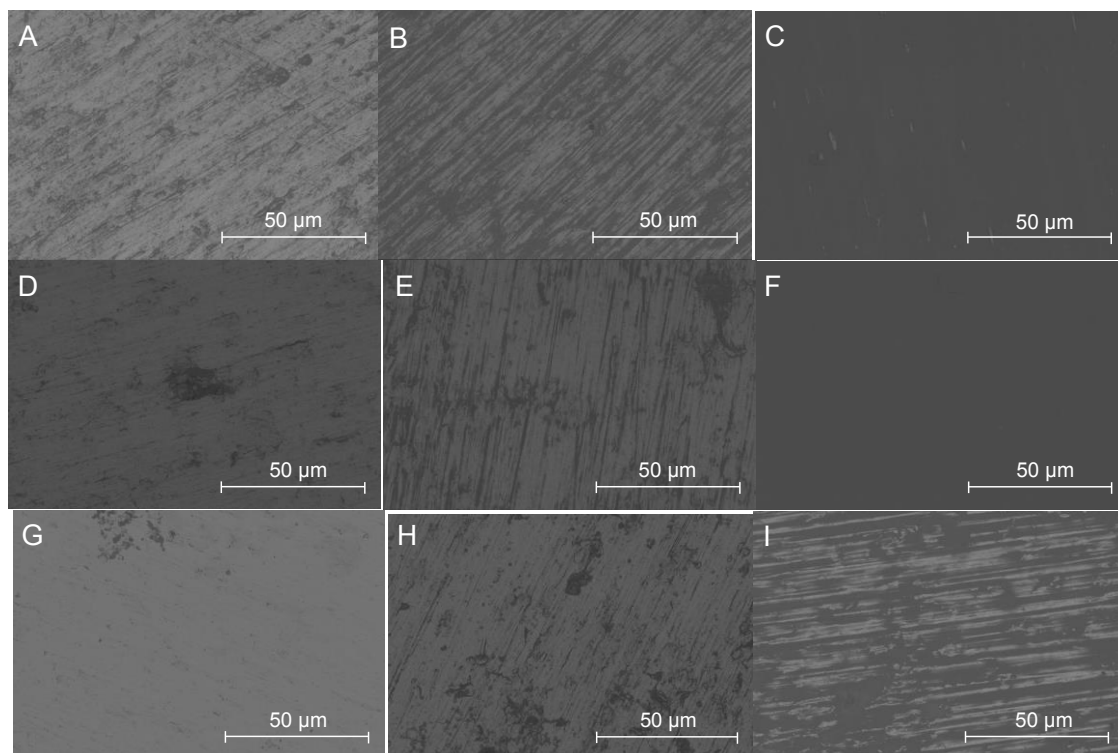


Figure 5. 5 SEM micrographs of coatings prepared with synthesis A) S1, B) S2, C) S3, D) S4, E) S5, F) S6, G) S7, H) S8, and I) S9

5.1.5 ELECTROCHEMICAL CHARACTERIZATION

Electrochemical Impedance Spectroscopy (EIS) was employed to evaluate the degrading rate of coatings under the exposure of an electrolyte containing 0.9 wt.% of NaCl, since it represents the major compound of the physiological solution in terms of chloride ions. Coatings S3 and S6 were selected to perform impedances on their surfaces because they completely covered TiPM. The bare titanium was also tested and taken as reference. Impedances were recorded each 2 hours for 1 day and the impedances at three times (4, 12 and 24 hours) were selected. Despite the metallic substrate (TiPM) was evaluated in Chapter 4, in this section impedances of TiPM are shown again in Figure 5. 6. TiPM is used as reference to study the electrochemical behaviour of the coatings. Spectra of TiPM are briefly commented here. The electrochemical results of TiPM have been in-depth explained in Chapter 4 and showed that TiPM was stable during the 24 hour-test.

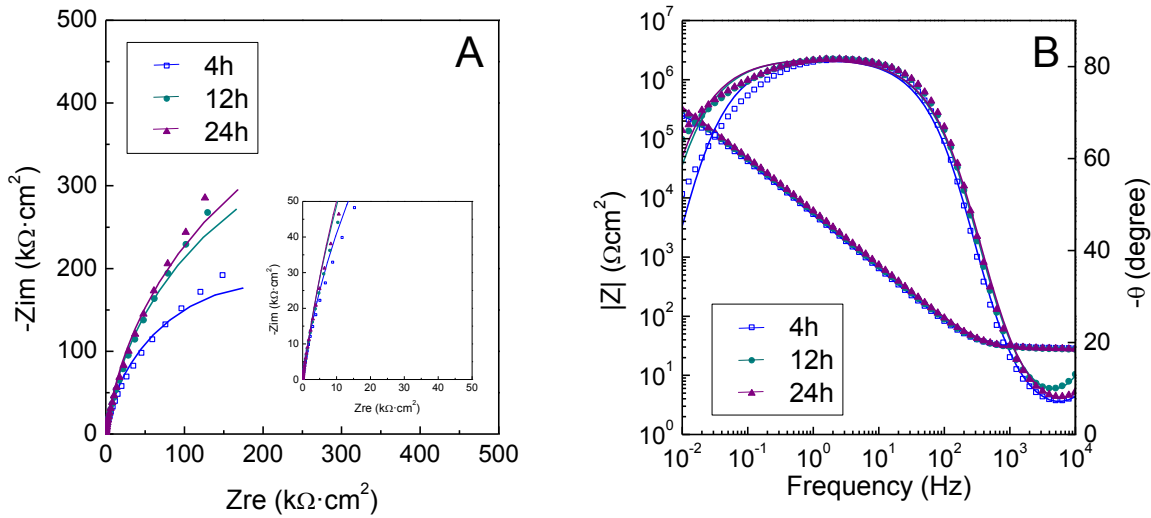


Figure 5. 6. Measured (discrete points) and fitted (solid lines) impedance spectra of TiPM after 4, 12, and 24 hours exposed to 0.9 wt.% NaCl solution at 37°C

Impedance of Ti was fitted using the EC with two relaxation times of Figure 5. 7. The wide bell overlaps two phenomena. At high-middle frequencies is identified the constant time ascribed to the protective oxide layer (CPE1, R1) and at middle-low frequencies the constant time related with the interaction electrolyte/metal (CPE2, R2).

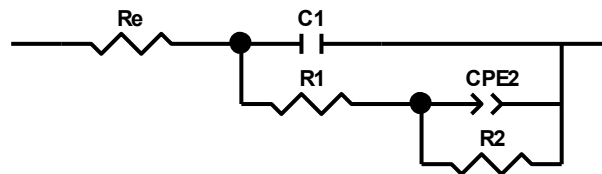


Figure 5. 7. Equivalent circuit (EC) used to model the impedance data of TiPM

Impedance of coatings S3 and S6 were fitted using the EC of Figure 5. 8. The constant time identified at high-middle frequencies is ascribed to the features of the coating, being the capacitance and the resistance of the coating identified as CPE1 and R1. The constant time identified at middle-low frequencies corresponds to the pore resistance and the capacitance of the interface electrolyte/metallic substrate. The electrical elements of this constant time are CPE2 and R2. The explanation of the selection of this EC for the system coating/metal is discussed in section 6.2 of Chapter 6.

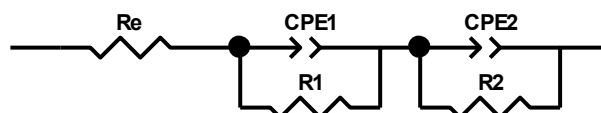


Figure 5. 8 Equivalent circuit (EC) used to model the impedance data of coatings S3 and S6

Impedance of coating S3 is showed in Figure 5. 9(A) (Nyquist plot) and Figure 5. 9(B) (Bode plot). At early stages of immersion (4 hours), coating S3 revealed two constant times although the one identified at high-middle frequencies was barely appreciated. By increasing the immersion of the coating in the aqueous solution, its features shifted to more capacitive features. This suggests that coating S3 presented poor adhesion and high porosity because in 24 hours the coating completely degraded and the recorded signal was similar to the one registered in TiPM. Plots of coating S6 are shown in Figure 5. 9(C and D). During the whole tests (24 hours) two constant times are identified, meaning TiPM was still coated with coating S6 after the test. The circuit elements obtained in the fitting are listed in Table 5. 7. The interpretation of each parameter has been in-depth discussed in Chapter 6 where coatings bio-functionalized with the phosphorus compound and the antibiotic has been studied. In this section, EIS measures were used as a first qualitative approach to evaluate the degrading process of the coatings. Only the absorption of water has been studied in this chapter.

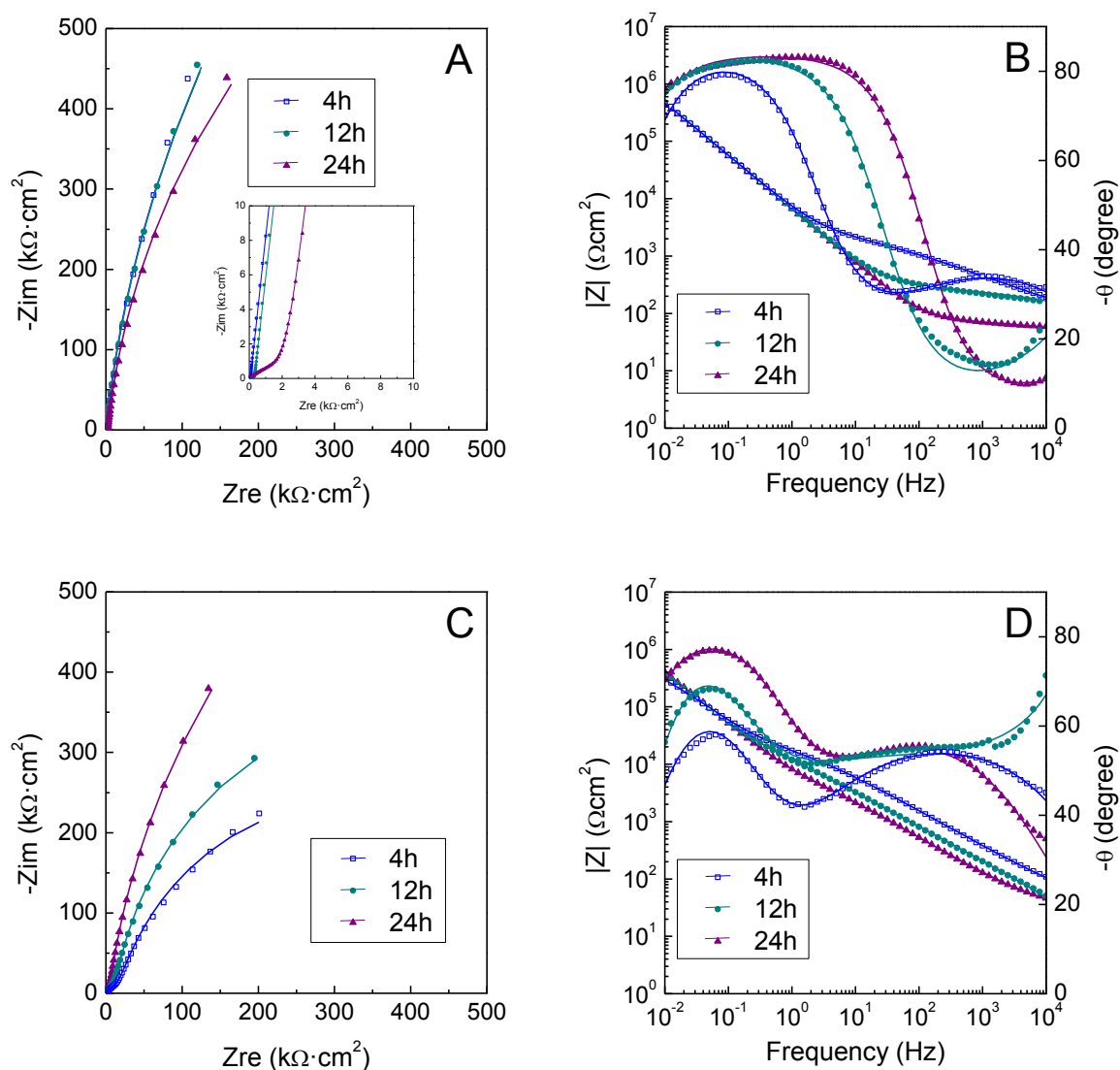


Figure 5. 9 Measured (discrete points) and fitted (solid lines) impedance spectra of coating A) S3, and B) S6 after 4, 12, and 24 hours exposed to 0.9 wt.% NaCl solution at 37°C

Table 5. 7 Electrical parameters obtained from the ECs used to fit impedances of TiPM and coatings S3 and S6 after 4, 12, and 24 hours of immersion in 0.9 wt.% NaCl solution

Time (hours)	Ti			S3			S6		
	4	12	24	4	12	24	4	12	24
$ Z _{10\text{mHz}} (\times 10^5)$	2.5	3.2	3.2	5.0	5.0	4.0	3.2	3.2	4.0
$R1/\text{k}\Omega\text{cm}^2$	410	792	914	1807	2950	2648	618	790	1880
$\text{CPE1}/\mu\text{Fcm}^{-2}$	36.2	33.7	32.1	27.1	27.1	27.5	28.3	32.6	30.1
n1	0.913	0.911	0.910	0.934	0.929	0.931	0.837	0.929	0.919
$R2 / \text{k}\Omega\text{cm}^2$	0.13	0.06	0.27	2.6	7.4	0.06	16.6	17.9	4.7
$\text{CPE2}/\mu\text{Fcm}^{-2}$	0.003	0.018	0.001	35.1	0.99	124.1	12.7	30.7	37.9
n2	-	-	-	0.472	0.145	0.396	0.620	0.578	0.628
$\text{Chi-Sqr.} \times 10^{-3}$	3.0	3.1	3.6	0.103	11.6	0.841	0.203	0.898	0.433

Sol-gel coatings are known to start their degradation in aqueous solution with the **uptake of water**, which is proportional to the CPE of coatings (CPE1) [13]. An increase of CPE1 is correlated with a higher amount of water uptake. The ultimate goal of the coatings that are being designed in this work is to degrade within 24 hours in order to release the antibiotic previously incorporated in the synthesis (section 5.3, Chapter 5). Thus, a faster water uptake will lead to a faster degradation of coatings. The accumulative CPE1 values were calculated using Equation 5.6:

$$\Delta\text{CPE1} = \frac{\text{CPE1}_t - \text{CPE1}_0}{\text{CPE1}_0} \times 100 \quad (\text{Equation 5.6})$$

where CPE1_0 is the capacitance of coatings after 2 hours of exposure to the electrolyte and CPE1_t the capacitance at the different recorded times.

Figure 5. 10 depicts the accumulative CPE1 percentage with the immersion time of coatings S3 and S6. Coating S3 evidenced almost no water uptake, which confirms the prior agreement where it was argued that upon immersion (4 hours) the coating was almost fully degraded. Coating S6 showed meanwhile, a remarkable increase of the accumulative CPE1 value that reached its highest value after 12 hours of exposure to the testing electrolyte. Then, the water uptake diminished gradually and remained stable. Indeed, coating S6 experienced a first degrading stage due to the water uptake during the first 12 hours of exposure to the aqueous solution. Then, the first layers of the coating started to degrade but TiPM was still covered with the coating. The full coverage of TiPM was evidenced with the presence of the constant time associated with the coating at 24 hours. This suggests that once the first layer of the coating degraded the next layer starts again the degrading procedure.

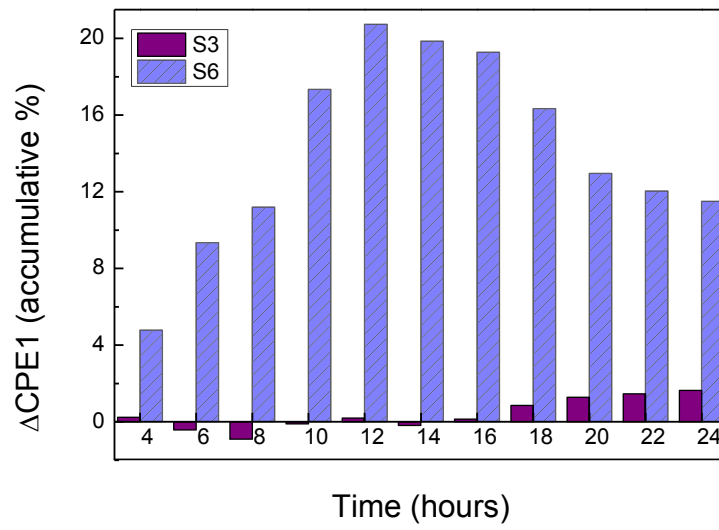


Figure 5. 10 Evolution of the accumulative CPE1 of coatings S3 and S6 immersed in 0.9 wt.% NaCl at 37°C during 24 hours

5.1.6 CONCLUSIONS

Taguchi method allowed reducing from 27 to 9 the prepared sol-gel routes. The study was based on evaluating the influence of three parameters of the sol-gel procedure (the molar ratio of the organopolysiloxanes, the reaction time of the synthesis and the drying temperature of the coatings) on the hydrophilic/hydrophobic features of the coatings. The following conclusions can be drawn from this study:

- (1) All the coatings showed **intermediate hydrophilic degree** (from 62.2 to 78.6 degrees) as desired for preventing bacterial adhesion on metallic prostheses.
- (2) The characterization of the synthesis with FTIR and rheological study, allowed **discarding the systems with 2 moles of MAPTMS and 1 mole of TMOS**. It was observed that higher additions of the organic compound (MAPTMS) slowed considerably down the reaction rate of the synthesis and the subsequent formation of siloxane bonds. In addition, the rheological study confirmed that synthesis 2:1 did not reach an appropriate viscosity (viscosity > 1 mPa·s) to coat TiPM.
- (3) Only the synthesis with the **lowest organic content** (the xerogel 1:2) showed equal contribution of TMOS and MAPTMS to the cross-linkage of the network.
- (4) The inspection of the surfaces of coatings with SEM allowed selecting the coatings with uniform and homogenous features and free of cracks. The selected systems were:
 - a. Coating S3: 1 mole MAPTMS / 1 mole TMOS, 24 hours of reaction and 180°C of drying temperature.
 - b. Coating S6: 1 mole MAPTMS / 2 moles TMOS, 24 hours of reaction and 60°C of drying temperature.
- (5) The electrochemical study with EIS permitted evaluating the stability of coating S3 and S6 during the first 24 hours of exposure to the aqueous solution:
 - a. **Coating S6** showed a suitable degrading rate in the electrolyte during the critical period (24 hours) to avoid the adhesion of bacteria at the surface of the coating. This coating was the selected for the bio-functionalization with phosphorus-based compounds.

5.2 BIO-FUNCTIONALIZATION OF SOL-GEL COATINGS WITH PHOSPHORUS-BASED COMPOUNDS

5.2.1 MATERIALS

Next step on the design of the sol-gel formulation was the bio-functionalization of coatings with the addition of phosphorus-based compounds. Three coatings were prepared by adding three different compounds: tris(trimethylsilyl) phosphite, tris(trimethylsilyl) phosphate and a solution containing phosphate ions. Table 5.8 summarizes the bio-functionalized coatings. The coating denoted as SG-C is the reference coating previously optimized with Taguchi method. The control coating, denoted as S6 in previous section (section 5.1, Chapter 5), contains 1 mole of MAPTMS and 2 moles of TMOS. The bio-functionalized syntheses were left 24 hours to undergo the hydrolysis-polycondensation reaction. Sols were applied to the substrate by dipping the substrates into the solution. Then, coatings were dried at 60°C during 1 hour.

Table 5. 8 The prepared bio-functionalized coatings with phosphorus-based compounds

Identification	Compound added	Quantity added $n_{Si}:n_P$
SG-C	-	-
SG-phosphite	tris(trimethylsilyl) phosphite	52:1
SG-phosphate	tris(trimethylsilyl) phosphate	52:1
SG-PBS	phosphate ions	10 ⁴ :1

* n_{Si} : moles of both organopolysiloxanes employed (MAPTMS and TMOS)

n_P : moles of the phosphorus compound

5.2.2 CHARACTERIZATION OF THE SYNTHESIS OF SOLS

FTIR spectra (Figure 5. 11) of the bio-functionalized syntheses were compared with the non-bio-functionalized synthesis identified as control (SG-C). At first glance it can be observed that the addition of the PBS solution (SG-PBS) considerably decreased the evolution of the reaction. The synthesis with the organophosphorus compounds (SG-phosphite and SG-phosphate) was similar to the evolution of the control synthesis. An additional peak appeared at 1256 cm⁻¹ in these two bio-functionalized syntheses. The literature reports the identification of a stretching vibration of the P=O bond between 1320 and 1140 cm⁻¹ in FTIR spectra [14]–[16]. The appearance of the P=O implies that the phosphorus compounds could be properly integrated as phosphates into the sol-gel network. However, further studies such as NMR should be performed to elucidate how the phosphite and the phosphate have been incorporated into the network (section 5.2.4, Chapter 5).

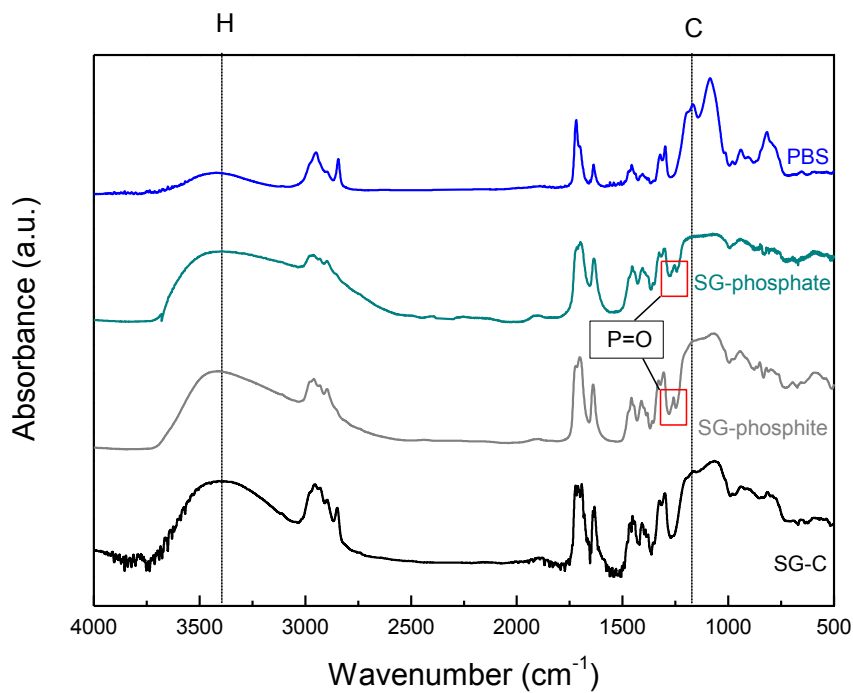


Figure 5. 11 FTIR spectra of synthesis SG-C and synthesis bio-functionalized with the phosphite, the phosphate and the PBS solution after 24 hours of reaction

The optimal reaction rate has been previously established (section 5.1.2, Chapter 5) when the ratio between H (band associated with hydrolysis) and C (main peak associated with polycondensation) is between 1 and 2 ($1 < H_1/C_1 < 2$). Table 5.9 summarizes the H/C ratio calculated for each synthesis. The calculation of the H/C ratio confirmed that the evolution rate of the synthesis with PBS was poor (first stage of the reaction, $H < C$). The synthesis had barely started the reaction even though indices of hydrolysis and polycondensation were observed. The addition of the organophosphorus compounds slightly retarded the evolution of the sol-gel synthesis, being the addition of the organophosphite the bio-functionalized synthesis less altered.

Table 5. 9 H/C ratio calculated with the normalized heights of Figure 5. 11

Sol	H	C	H/C ratio
SG-C	0.700	0.464	1.509
SG-phosphite	0.673	0.509	1.322
SG-phosphate	0.608	0.718	0.847
SG-PBS	0.184	0.708	0.260

5.2.3 SURFACE CHARACTERIZATION

TiPM was coated with the different bio-functionalized syntheses after 24 hours of reaction. The coated surfaces were inspected by SEM (Figure 5. 12) and remarkable differences between each other were observed.

The reference coating (Figure 5. 12(A)) presented a homogenous surface without cracks. When performing EDS analyses, the elements C, Si and O corresponding to the organic precursors of the sol-gel synthesis were identified. The coating bio-functionalized with the organophosphite is shown in Figure 5. 12(B) and the surface features completely changed. Two contrasts were observed and EDS analyses revealed the presence of phosphorus on both, the bright areas and the matrix. The coating bio-functionalized with the organophosphate (Figure 5. 12(C)) presented similar features than coating modified with the phosphite but with larger spots. The coating bio-functionalized with PBS (Figure 5. 12(D)) showed cracks and EDS analyses confirmed the presence of TiPM among the surface (areas identified with white arrows in the SEM images and as Sb in Table 5.10). The spots of coating with the phosphite seemed to be integrated onto the coating and were located on the surface of coatings. The coating with the phosphate however, presented two well-differentiated phases with the bright areas barely integrated in the coating.

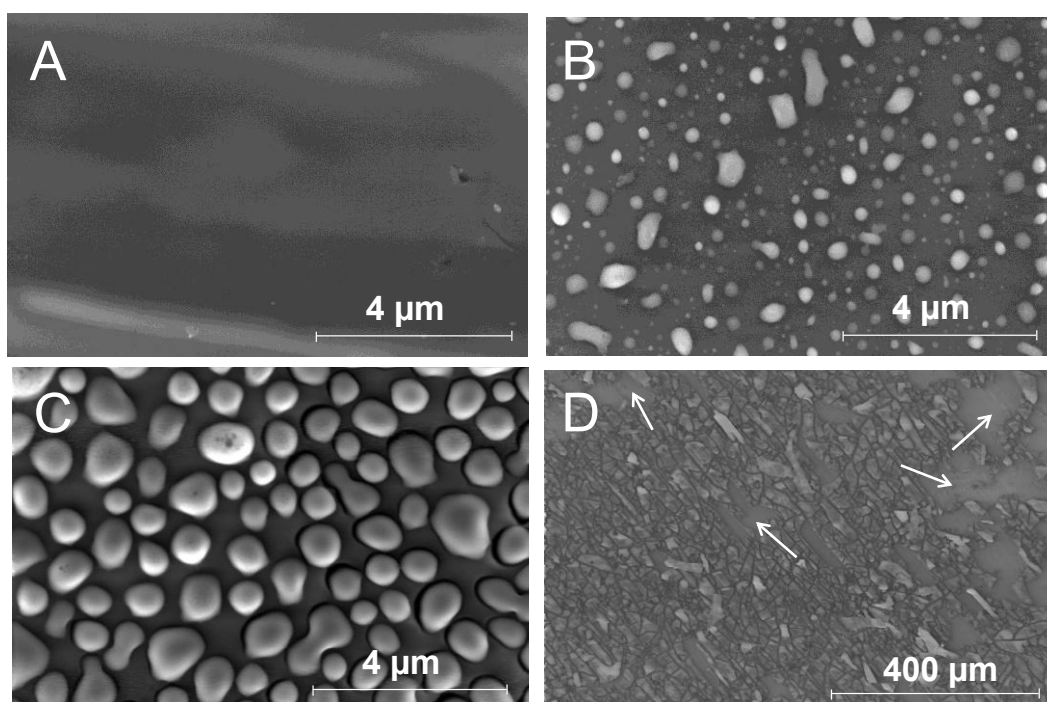


Figure 5. 12 SEM micrographs of coatings: A) control and coatings bio-functionalized with B) phosphite, C) phosphate and E) PBS. The white arrows indicates the presence of TiPM

Table 5. 10 EDS analyses of the surface of the prepared coatings

Elements (At.%)	SG-C	SG-phosphite		SG-phosphate		SG-PBS	
	SG	S	SG	S	SG	Sb	SG
C	Bal.	Bal.	Bal.	Bal.	Bal.	Bal.	Bal.
O	61.1	47.6	47.8	47.0	46.8	22.1	31.4
Si	10.5	13.3	15.2	11.5	13.2	9.1	20.1
P	--	1.5	0.6	2.30	2.0	--	--
Ti	--	--	--	--	--	37.4	--

*SG: sol-gel; S: bright spots; Sb: substrate

The water contact angle of the modified surfaces was also studied but only of the coatings that showed good adhesion to the metallic substrate. Coatings modified with the organophosphate and the PBS solution were not subjected to this study because their adhesion to TiPM was poor and after the deposition of the water drop it was evidenced that the coating was removed from the metal. The values of the water contact angle of the uncoated metal, the coating non-bio-functionalized and the coating bio-functionalized with the phosphite are shown in Table 5. 11. The application of sols to the substrate increased the water contact angle of TiPM: the water contact angle shifted from 47.7 to 68.9 degrees. The addition of the organic compound increased even more the water contact angle of the surface to 87.5 degrees due to the non-polarity of the phosphite. This value, which is very close to a hydrophobic surface (angle > 90 degrees), is expected to be the most appropriate surface, among the studied ones, to prevent the adhesion of bacteria [5].

Table 5. 11 Water contact angle of the prepared coatings

Coating	Water contact angle (°)
Uncoated substrate (TiPM)	47.7 ± 5.0
SG-C	68.9 ± 4.2
SG-phosphite	87.5 ± 3.5

5.2.4 CHARACTERIZATION OF THE XEROGEL

The TGA and DTG plots of the xerogels obtained during the three syntheses are shown in Figure 5. 13. This study was performed to evaluate how the addition of the phosphorus-based compounds influenced the cross-linkage (creation of siloxane bonds). The non-bio-functionalized xerogel (SG-C) was depicted and used as reference. The same three thermal stages identified in the optimization of the reference synthesis were observed (section 5.1.3, Chapter 5).

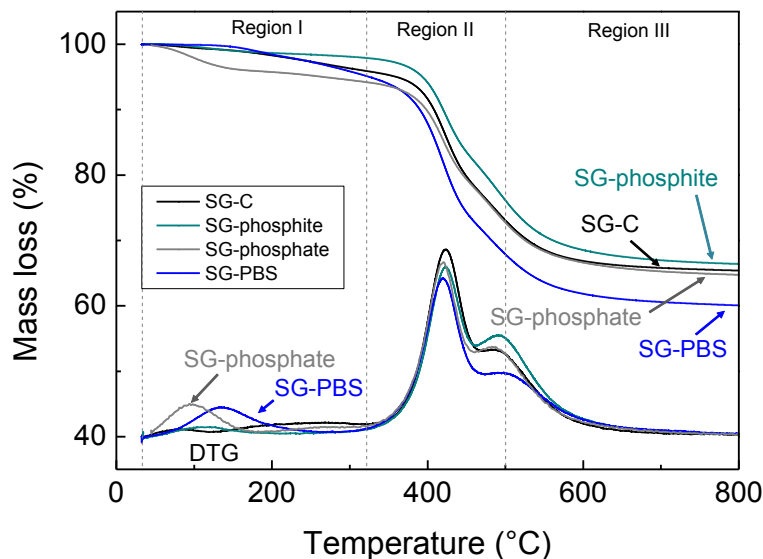


Figure 5. 13 TGA and DTG profiles of the xerogels obtained during the non-bio-functionalized synthesis (SG-C), and syntheses bio-functionalized with the phosphite (SG-phosphite), the phosphate (SG-phosphate) and the PBS solution (SG-PBS) dried at 60°C for 4 hours

The study revealed that only the xerogel modified with the organophosphite (SG-phosphite) followed the behaviour of the reference xerogel (SG-C). The xerogels biofunctionalized with the phosphate (SG-phosphate) and the PBS solution (SG-PBS) presented a remarkable mass loss in the first region. The mass loss in this region can be ascribed either to the elimination of entrapped solvent or by-products of the condensation reaction. The NMR of Si nuclei was performed to elucidate the source of this degrading stage and results are presented latter. The phosphite enhanced in a 1 wt.% the inorganic contribution of SG-C suggesting that the phosphite acted as a cross-linker of the sol-gel network. The addition of the phosphate meanwhile, unaltered the total amount of mass loss. By contrast, the addition of the PSB solution reduced in a 5.3 wt.% the inorganic contribution to the network.

Spectra obtained with ^{29}Si MAS-NMR of each xerogel are shown in Figure 5. 14. Again, spectrum of the reference synthesis (SG-C) was depicted for the sake of comparison. The spectra showed that the cross-linkage of the xerogels biofunctionalized with the organophosphorus compounds (SG-phosphite and SG-phosphate) had similar features than the control reference. The xerogel SG-PBS showed meanwhile, a poor signal. The addition of the solution containing phosphate ions blocked the creation of siloxane bonds (Si-O-Si) and it was evidenced with the low signals obtained in the spectrum. Signals corresponding to the creation of the siloxane bonds of TMOS were barely observed and the dominant signal observed in the chemical shifts of MAPTMS was ascribed to non-hydrolysed molecules of MAPTMS (T^0). This results supports that the mass loss observed in the TGA in Region I corresponded to entrapped water. During the synthesis containing PBS solution, part of the water used as reactive in the sol-gel reaction was replaced by PBS solution. This solution contains several ions, such as Ca^{2+} , PO_4^{3-} , Na^+ , Cl^- that slowed the reaction down, as it was observed with the FTIR study. Even after drying the sol to obtain the xerogel, this synthesis was unable to create siloxane bonds.

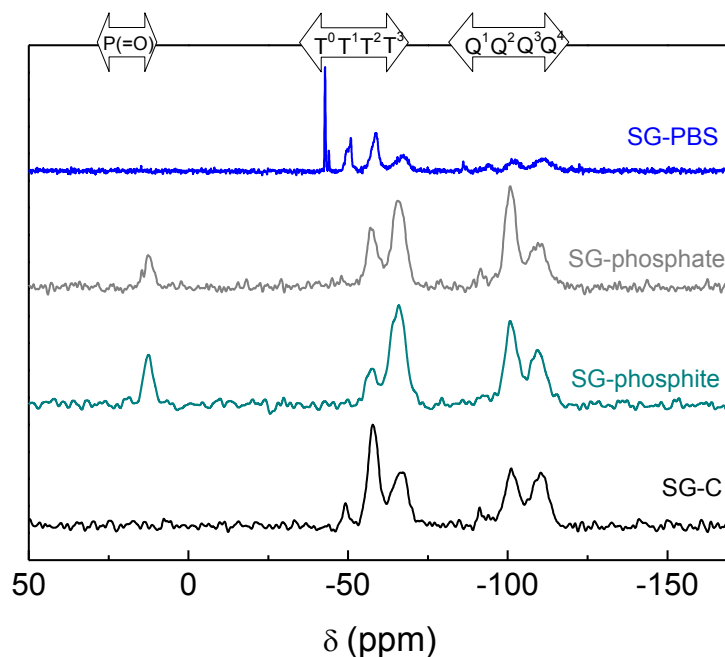


Figure 5. 14 Solid state ^{29}Si NMR spectra of the xerogels of the control synthesis (SG-C) and synthesis bio-functionalized with the phosphite (SG-phosphite), the phosphate (SG-phosphate) and the PBS solution (SG-PBS) dried at 60°C for 4 hours

The relative proportions of T, Q and P(=O) species are listed in Table 5. 12. The poor cross-linkage degree of SG-PBS was confirmed. The dominant signal in SG-PBS is due to non-hydrolysed molecules of TMOS (T^0). Up to this point of the design of the formulation, the synthesis bio-functionalized the PBS solution was discarded because it led to a poor cross-linkage of the sol-gel network. The ions contained in the PBS solution blocked the hydrolysis-polycondensation reaction and created neither enough free-hydroxyl bonds nor siloxane bonds. The poor adhesion of this coating with the substrate due to the low formation of free-hydroxyl bonds during the reaction of hydrolysis was evidenced during the inspection of its surface with SEM, in where TiPM was identified.

The spectrum of the xerogels with the organic compounds revealed T^3 and Q^3 as the main signals of MAPTMS and TMOS, respectively. These xerogels showed the formation of tridimensional networks contrary to the reference xerogel, which formed a less branched network: signal T^1 disappeared in benefit of T^3 . These two spectra evidenced in addition the appearance of a signal at 12.5 ppm. This signal, denoted as P(=O) in the NMR spectra, corresponds to the creation of a **-P(=O)- bond** in the entourage of the Si nuclei of the sol-gel network [17], [18]. The addition of the organophosphorus compounds enhanced the cross-linkage of the network and this was confirmed with the disappearance of T^1 and Q^2 signals and the identification of species with more siloxane bonds per silicon atom (T^2 , T^3 , Q^3 and Q^4). Concerning the contribution of the **-P(=O)- linkage** to the averaging cross-linkage (denoted of as P(=O) in Table 5.12), in GS-phosphite it contributed in a 15.2% and in GS-phosphate, in a 7.8%. The appearance of this signal supports the results obtained with FTIR where the creation of a P=O bond was revealed.

Table 5. 12 Relative proportions of T^i , Q^j and $P(=O)$ species calculated in Figure 5. 14

Xerogel	Relative proportion ^a (%)								Ratio ^b (%)		
	T^0	T^1	T^2	T^3	Q^1	Q^2	Q^3	Q^4	$P(=O)$	T^n	Q^m
SG-C	--	--	38.7	19.9	--	--	21.5	19.9	--	58.6	41.4
SG-phosphite	--	--	10.7	31.2	--	--	26.1	16.8	15.2	41.9	42.9
SG-phosphate	--	--	16.7	25.3	--	8.3	30.0	11.8	7.8	42.0	50.1
SG-PBS	47.5	14.8	17.1	7.0	3.1	1.9	4.2	4.4	--	86.4	13.6

$$^a \text{ relative proportion (\%): } T^i = (T^i / (\sum_{i=0}^3 T + \sum_{j=1}^4 Q + P(=O))) \cdot 100;$$

$$Q^j = (Q^j / (\sum_{i=0}^3 T + \sum_{j=1}^4 Q + P(=O))) \cdot 100;$$

$$P(=O) = (P(=O) / (\sum_{i=0}^3 T + \sum_{j=1}^4 Q + P(=O))) \cdot 100$$

$$^b \text{ ratio (\%): } P(=O) = (P(=O) / (\sum_{i=0}^3 T + \sum_{j=1}^4 Q + P(=O))) \cdot 100;$$

$$T^n = (\sum_{i=0}^3 T / (\sum_{i=0}^3 T + \sum_{j=1}^4 Q + P(=O))) \cdot 100;$$

$$Q^m = (\sum_{i=1}^4 Q / (\sum_{i=0}^3 T + \sum_{j=1}^4 Q + P(=O))) \cdot 100$$

The organophosphorus compounds are integrated into the sol-gel network following different mechanisms. First, the incorporation of the organophosphate to the sol-gel network is explained. When the organophosphate is exposed to water, the organic chain (TMS:trimethylsilyl) can get hydrolysed by releasing as by-products trimethylsilanol molecules (TMS-OH, $b_{p_{TMS-OH}}=99^\circ\text{C}$). Then, the hydrolysed organophosphate can react with a hydrolysed organopolysiloxane and create a new bond (P-O-Si) following a condensation reaction. Figure 5.15 illustrates the proposed reaction between a molecule of organophosphate and a molecule of organopolysiloxane. The proposed reaction elucidate that the mass contribution of the TGA during the first thermal stage at 100°C (Figure 5.13) can be associated with the elimination of several by-products (alcohol and water) during the condensation reactions. Despite that this synthesis reached an appropriated cross-linkage it has been discarded do to the poor adhesion of the coating with the metallic substrate.

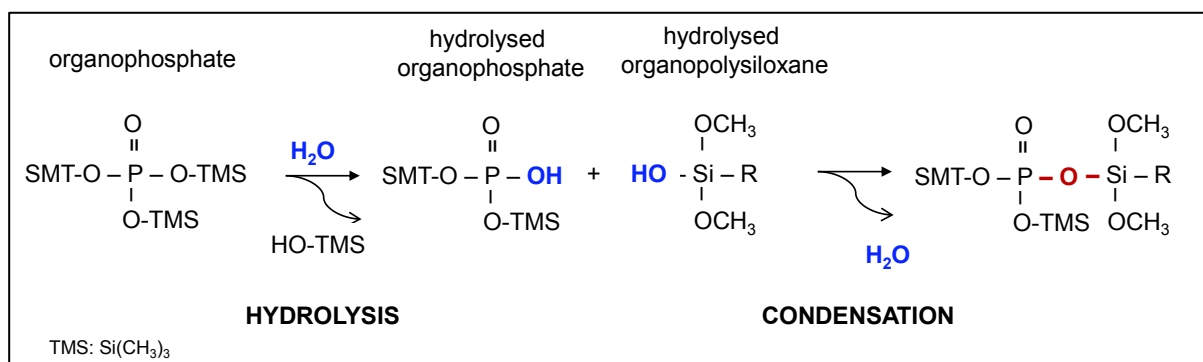


Figure 5. 15 Reaction proposed for the incorporation of the organophosphate into the sol-gel network following a hydrolysis and polycondensation reaction between the hydrolysed organophosphate and the hydrolysed silane

The synthesis modified with the organophosphite experienced a prior reaction that led to the oxidation of trivalent phosphorus to pentavalent phosphorus. This explains the identification of the P(=O) bond in the ^{29}Si NMR spectra (Figure 5.14). The incorporation of the organophosphite into the sol-gel network is then accomplished with a **Michaelis-Arbuzov reaction** between a molecule of organophosphite and a molecule of an organopolysiloxane [19]. During this reaction, the phosphite is oxidized to a phosphate via a Second-order Nucleophilic Substitution (SN2). The phosphite acts as nucleophile and the organopolysiloxane as electrophile. During the sol-gel synthesis two organopolysiloxanes are employed, MAPTMS and TMOS. TMOS shows better features to behave as electrophile than MAPTMS because TMOS is less sterically hindered and its central silicon has more positive charge density than MAPTMS. This allows that MAPTMS molecules react between each other and generate the increase of signal T^3 . The lone pair of electrons of the phosphite attacks the electroactive silicon of the organopolysiloxane. A phosphonium intermediate is formed thanks to the leaving alcoxide group ($-\text{OCH}_3$) of the organopolysiloxane. Then, this alcoxide reacts, via another SN2 reaction, with the silicon atom of a TMS group giving rise to the formation of the P(=O) bond. The overall result is the conversion of trivalent phosphorus to pentavalent phosphorus. The proposed mechanism is summarized in Figure 5.16.

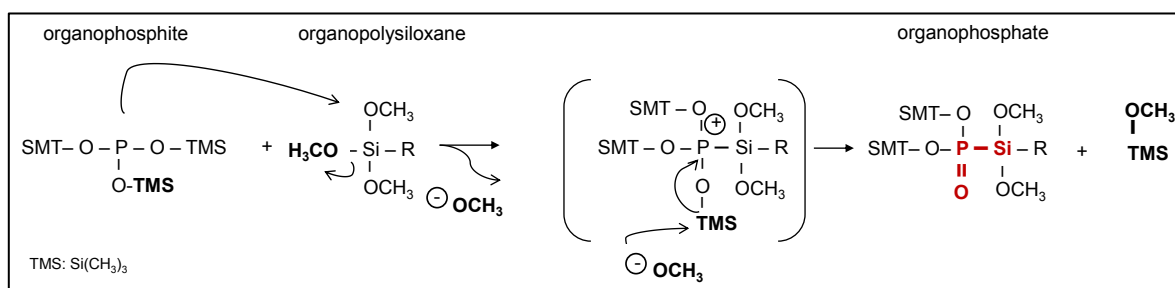


Figure 5. 16 Proposed reaction mechanism based on a Michaelis-Arbuzov reaction for the synthesis bio-functionalized with the organophosphite

The bio-functionalization with the **organophosphite was selected as the most suitable** to continue with the next step of the design of the formulation (the incorporation of the antibiotic). In order to select the most appropriate quantity of compound added to the synthesis, **the concentration of the organophosphite was modified** to study if the amount of phosphorus conditioned the proliferation of cells.

5.2.5 CELLULAR STUDY

The amount of organophosphite added to the synthesis was varied from 0 to 9.4 mmoles (0, 0.5, 0.9, 1.9, 3.8, 5.6 and 9.4 mmoles) to evaluate the influence of the phosphorus content on the cellular proliferation. Table 5. 13 summarizes the prepared synthesis.

Table 5. 13 The prepared sol-gel synthesis

Identification	$n_{Si}:n_P$	n_P (mmoles)
P_0	52:0	0
$P_{0.5}$	52:0.5	0.5
P_1	52:1	0.9
P_2	52:2	1.9
P_4	52:4	3.8
P_6	52:6	5.6
P_{10}	52:10	9.4

* n_{Si} : moles of organopolysiloxanes (MAPTMS and TMOS)

n_P : moles of tris(trimethylsilyl) phosphite

The surface of the coatings was inspected by SEM and images are shown in Figure 5. 17. When adding only 0.5 mmoles of the organophosphite (Figure 5. 17(A)), the surface features of the coating were similar to the control coating (see Figure 5. 12(A)). By increasing the amount of the organophosphite, the surface features considerably changed. It was observed the apparition of greater areas with spherical topographies that generated poor adhesion of the coating with the metallic substrate.

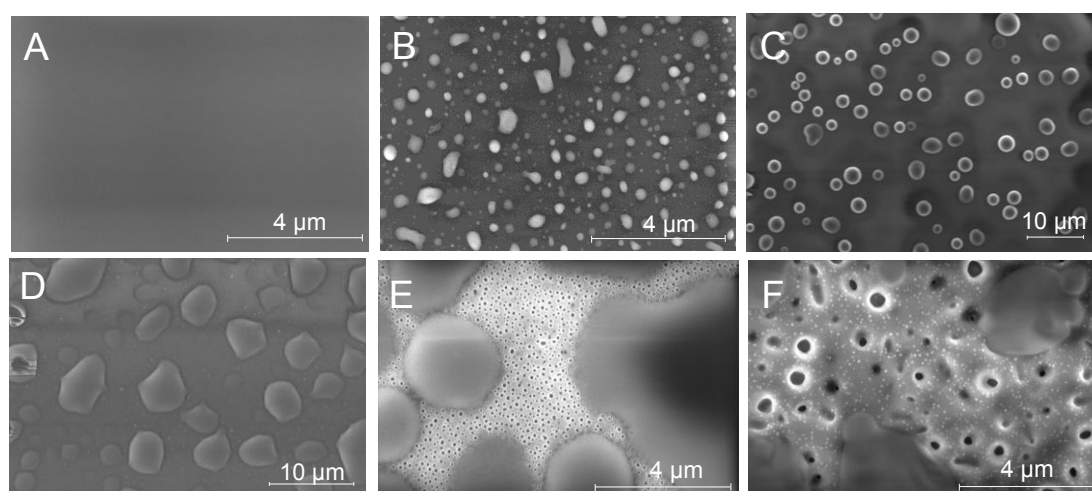


Figure 5. 17 SEM micrographs of coatings: A) $P_{0.5}$, B) P_1 , C) P_2 , D) P_4 , E) P_6 and F) P_{10}

The cellular proliferation in the presence of each material containing different amounts of the organophosphite is shown in Figure 5. 18. It was observed that cells proliferated more by increasing the amount of phosphite added to the synthesis. This trend was supported with a t-Student's test. The results obtained in this statistical test are shown in Table 5.14. In this statistical study each material was compared with each other. If the probability is below 0.05 ($p < 0.05$) that means that there is no enhancement on the proliferation of cells between the compared materials. First, comparing all the synthesis with the control material (P_0) it was observed that only when adding 0.5 mmoles of phosphite the cellular proliferation of cells increased. Also the proliferation of cells was found no significant between $P_{0.5}$ and $\geq P_4$, and between P_2 and P_6 .

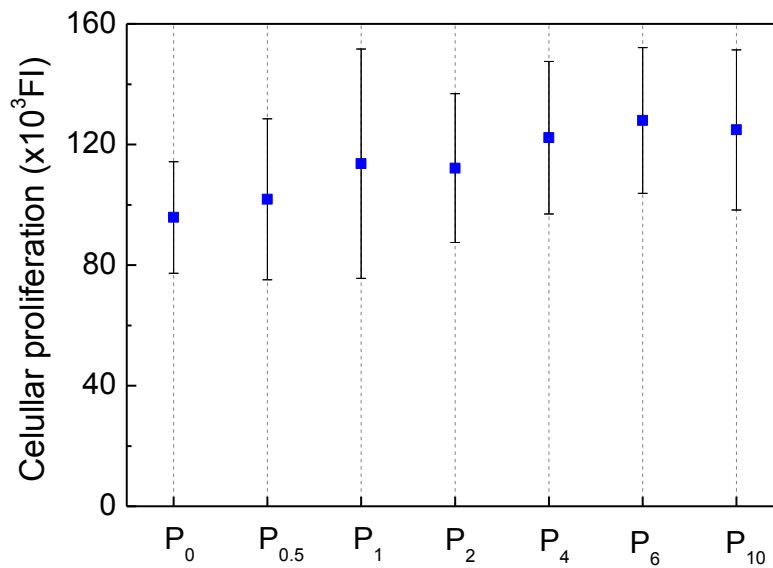


Figure 5. 18 Cellular proliferation of MC3T3-E1 cells on the control synthesis and synthesis: P_{0.5}, P₁, P₂, P₄, P₆, and P₁₀

Table 5. 14 Results of Student's t-test for cell proliferation in the presence of the different concentration of organophosphite. *: inequality of variance

Material	P ₀	P _{0.5}	P ₁	P ₂	P ₄	P ₆
P _{0.5}	0.1857					
P ₁	0.0223	0.1092				
P ₂	0.0109	0.1121	0.555			
P ₄	0.0002	0.0102	0.2164	0.131		
P ₆	<0.0001	0.0004	0.0641*	0.0258	0.2385	
P ₁₀	<0.0001	0.0022	0.1219	0.0682	0.3802	0.6639

It was demonstrated that the bio-functionalization of the synthesis with **tris(trimethylsilyl) phosphite induced the proliferation of MC3T3-E1 cells** due to the presence of phosphates created during the synthesis. Due to the fact that by adding higher amount of the organophosphite the proliferation of cells was not considerably enhance, the selection of the concentration was made evaluating the adhesion of the coating with the substrate. The addition of 0.9 mmoles (P₁) was considered the most convenient because it did not compromise the adhesion with the substrate.

5.2.6 CONCLUSIONS

The bio-functionalization of sol-gel coatings with phosphorus-based compounds was performed with three different compounds. The following conclusions can be drawn from this study:

- (1) The bio-functionalization with **PBS solution** (aqueous solution containing phosphate ions) was discarded because the presence of ions in the solution **slowed the synthesis down** and **blocked the cross-linkage** of the network.
- (2) The bio-functionalization with the organophosphate (tris(trimethylsilyl) phosphate) was also discarded because the compound **compromised the adhesion** of the coating with the metal.
- (3) The successful incorporation of phosphorus into the coating was only achieved by adding the **organophosphite** (tris(trimethylsilyl) phosphite). Phosphates were created *in situ* following a **Michaelis-Arbuzov reaction** that allowed the integration of the phosphates into the siloxane network. Besides, the organophosphite barely altered the evolution of the synthesis when compared with the control synthesis.
- (4) The proliferation of cells was slightly enhanced by increasing the amount of organophosphite. Despite that the cellular proliferation was enhanced, higher amount of organophosphite acted in detriment to the adhesion of the coating to the metallic substrate. Hence, an **intermediate concentration of organophosphite (0.9 mmoles) was selected** to ensure a suitable adhesion to the prosthesis.

5.3 BIO-FUNCTIONALIZATION OF SOL-GEL COATINGS WITH MOXIFLOXACIN

5.3.1 MATERIALS

The following step in the bio-functionalization of the sol-gel coating was the addition of an antibiotic, **moxifloxacin** (MOX). Two coatings were prepared by dissolving MOX in the aqueous phase of the sol-gel synthesis. MOX was dissolved in water rather than in the organic phase because of its higher solubility in aqueous solutions [20]. Table 5. 15 summarizes the prepared coatings with MOX: A25 contains 25 mg of MOX per 20.3 ml of sol (0.0017 mg of MOX per coating) and A50, 50 mg of MOX per 20.3 ml of sol (0.0034 mg of MOX per coating). The coating P, non-bio-functionalized with MOX, was taken as the reference coating.

Table 5. 15 The prepared bio-functionalized coatings with moxifloxacin

Identification	MOX (mg) / sol-gel (ml)
P	--
A25	25
A50	50

5.3.2 CHARACTERIZATION OF THE SYNTHESIS OF SOLS

The influence of the addition of MOX to the evolution of the synthesis was studied with FTIR and rheology. The FTIR spectrum obtained for each synthesis is shown in Figure 5.19(A) and it revealed that the addition of MOX did not alter the evolution of the hydrolysis-polycondensation reaction. The H/C ratio was calculated and values are shown in Table 5.16. The similarity of the H/C ratios confirmed that the addition of MOX did not modify the evolution of the reaction. The FTIR spectra also revealed the presence of the P(=O) bond, as it was observed in the previous section.

The bio-functionalization of the synthesis with MOX however, modified the viscosity of sols. Figure 5.19(B) depicts the behaviour of sols under different shear rates. Sols experienced at low shear rate (from 0 to 250 s⁻¹) a shear thickening behaviour, which is associated with fluids that experience an increase on their viscosities when the applied shear rate increases. Sols behave as Newtonian fluids when the applied shear rates to sol increased from 250 to 600 s⁻¹. Despite showing similar viscosity features, the mean viscosity value differed. The addition of MOX increases the viscosity of sols, being sol A25 the one with the highest viscosity followed by sol A50 and P2. The highest viscosity can be correlated with a higher growth and connection of particles.

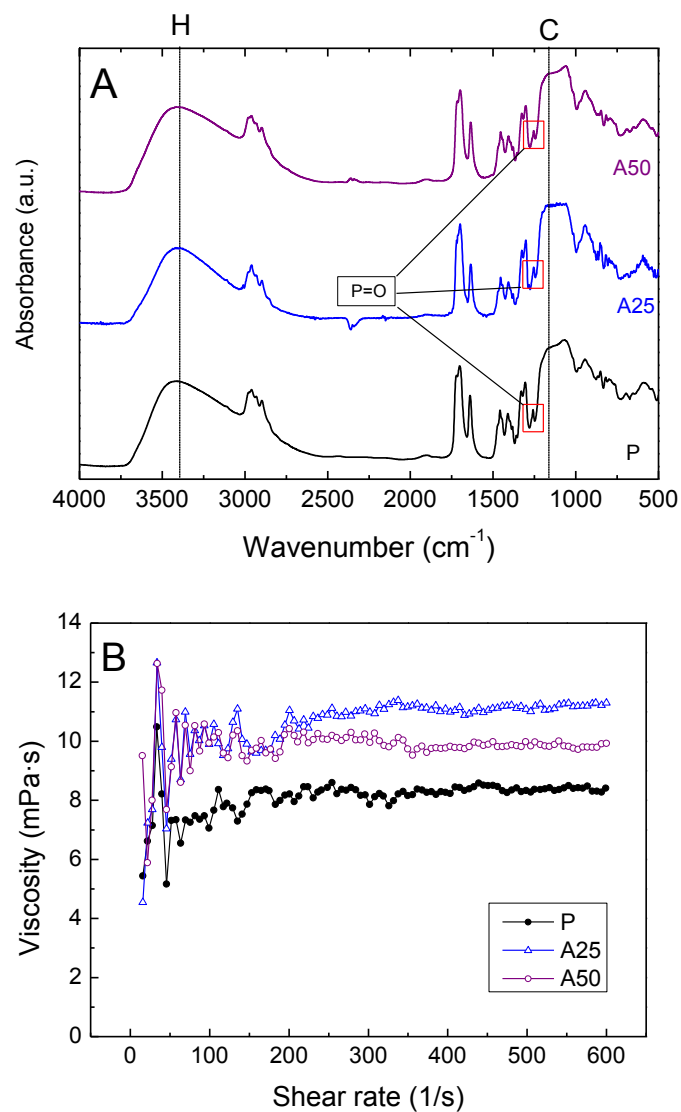


Figure 5. 19 A) FTIR spectra of the synthesis P, A25, and A50 after 24 hours of reaction and B) relation between the viscosity and the applied shear rate on the reference sol (P) and sols bio-functionalized with MOX (A25 and A50) after 24 hours of reaction

Table 5. 16 The H/C ratio calculated with the normalized heights of Figure 5.19(A)

Sol	H	C	H/C ratio
P	0.673	0.509	1.322
A25	0.645	0.567	1.138
A50	0.604	0.493	1.225

5.3.3 CHARACTERIZATION OF THE XEROGEL

The TGA and DTG plots of the xerogels are shown in Figure 5.20(A). No significant differences were observed between each other. The xerogels presented the main degradation stage at the same temperature, around 450°C, and similar total mass losses. Also similar ^{29}Si NMR spectra were obtained of each xerogel (Figure 5.20(B)).

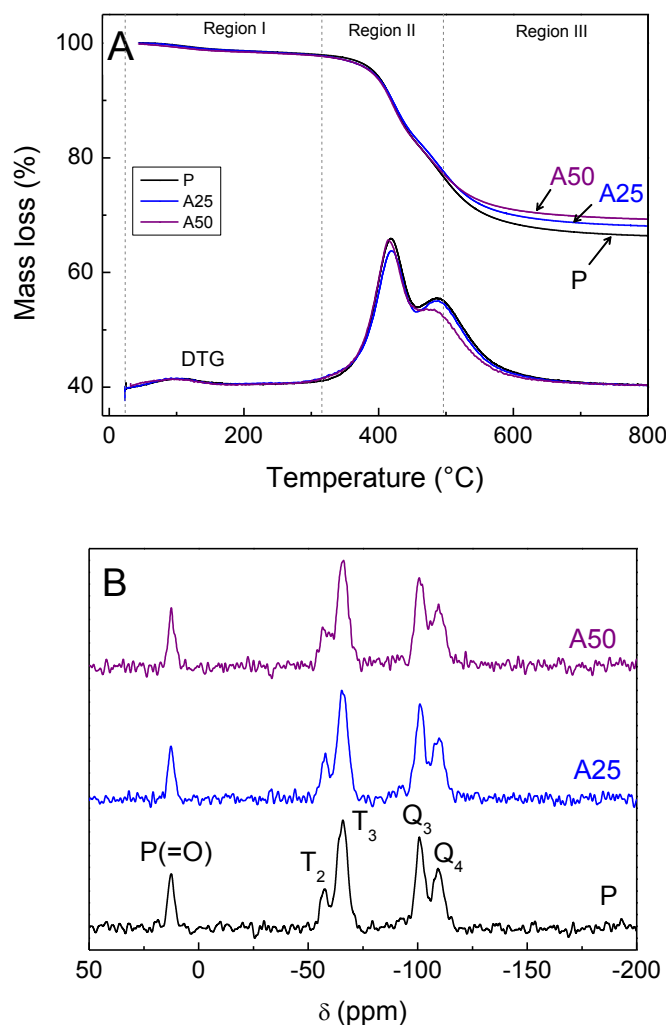


Figure 5. 20 A) TGA and DTG profiles and B) Solid state ^{29}Si NMR spectra of the xerogels of synthesis P, A25, and A50 dried at 60°C for 4 hours

The peaks associated to the control sample (P) were already identified in previous section (section 5.1.3, Chapter 5). Signals of the creation of siloxane bonds in MAPTMS are ascribed to T signals while Q signals corresponds to the formation of siloxane bonds in TMOS. Peak labelled as P(=O) corresponds to the formation of phosphates following a Michaelis Arbusov reaction as it was previously described (section 5.2.4, Chapter 5). The addition of MOX was found to not alter the cross-linkage of coatings. Table 5.17 summarizes the contribution of each signal to the total cross-linkage of the sol-gel network. The xerogels P, A25 and A50 had similar contribution of T, Q and P(=O) signals.

Table 5. 17 Relative proportions of T^i , Q^j and $P(=O)$ species calculated from Figure 5.20(B)

Xerogel	Relative proportion ^a (%)				Ratio ^b (%)		
	T^2	T^3	Q^3	Q^4	$P(=O)$	T^n	Q^m
P	10.7	31.2	26.1	16.8	15.2	41.9	42.9
A25	12.3	30.4	26.5	16.5	14.3	42.7	43.0
A50	10.6	30.4	25.2	17.4	16.4	41.0	42.6

$$^a \text{ relative proportion (\%)} : T^i = (T^i / (\sum_{i=2}^3 T + \sum_{j=3}^4 Q + P(=O))) \cdot 100;$$

$$Q^j = (Q^j / (\sum_{i=2}^3 T + \sum_{j=3}^4 Q + P(=O))) \cdot 100;$$

$$P = (P(=O) / (\sum_{i=2}^3 T + \sum_{j=3}^4 Q + P(=O))) \cdot 100$$

$$^b \text{ ratio (\%)} : P(=O) = (P(=O) / (\sum_{i=2}^3 T + \sum_{j=3}^4 Q + P(=O))) \cdot 100;$$

$$T^n = (\sum_{i=2}^3 T / (\sum_{i=2}^3 T + \sum_{j=3}^4 Q + P(=O))) \cdot 100;$$

$$Q^m = (\sum_{i=3}^4 Q / (\sum_{i=2}^3 T + \sum_{j=3}^4 Q + P(=O))) \cdot 100$$

5.3.4 SURFACE CHARACTERIZATION

SEM images of the sol-gel coatings corresponding to samples P, A25, and A50 are shown in Figure 5.21. Surfaces showed the same colour features: a grey contrast corresponding to the sol-gel matrix and localized spherical spots with a bright contrast. The resulting topography of the surfaces was created during the drying step of the coatings due to the evaporation of solvent. EDS analyses (Table 5.18) were performed on the bright spots (labelled as 1 and 2) and on the matrix (labelled as 3). The chemical elements C, O and Si were detected in all locations of the surface for all the specimens. These elements correspond to the composition of the sol-gel network.

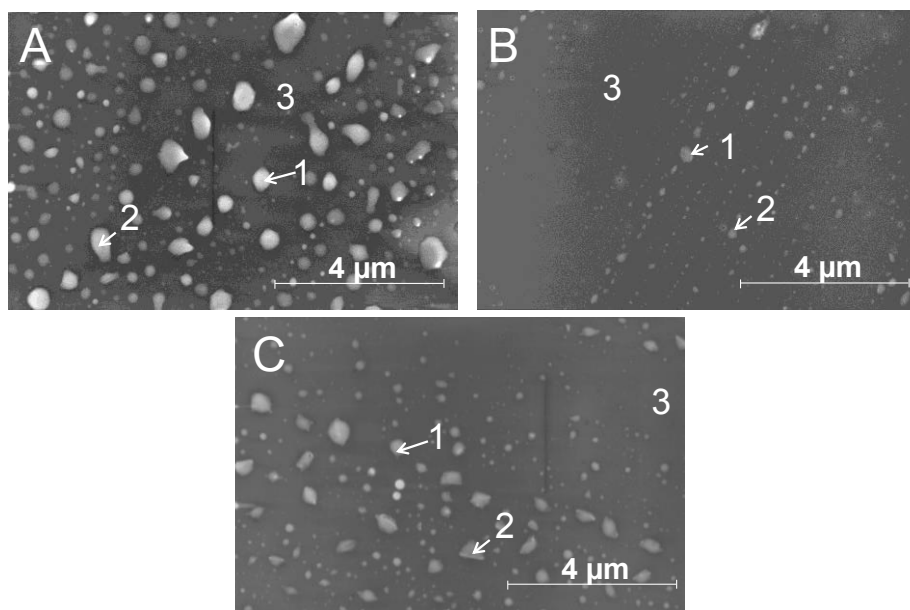


Figure 5. 21 SEM micrographs of coatings: A) P, B) A25, and C) A50. Images were taken operating in the secondary electron emission mode

Table 5. 18 Chemical analysis of coatings P, A25, and A50 performed with EDS. The wt% of the elements at different locations of the surface is presented: (1)-(2) at the spots and (3) at the matrix

Element (wt.%)	P			A25			A50		
	1	2	3	1	2	3	1	2	3
C	38.4	38.4	38.4	37.3	37.6	34.1	40.5	36.1	36.4
O	47.2	47.2	47.2	47.4	47.1	50.7	45.3	47.0	47.6
Si	12.1	12.1	12.1	14.5	14.4	15.2	12.3	15.4	16.0
P	2.3	2.3	2.3	0.8	0.9	--	1.9	1.5	--

Phosphorus was integrated into the sol-gel network thanks to a Michaelis-Arbuzov reaction between the organopolysiloxanes and the organophosphite that transforms the organophosphite to organophosphate [19]. This reaction has been explained in more detail in section 5.2.4, Chapter 5. Phosphorus was detected in all the samples. In coating P, phosphorus was found across the whole surface: the matrix and the spots. In the MOX-loaded coatings, phosphorus was identified only on the local spots. The localization of phosphorus in these areas was generated because the solvent (ethanol and water) is more entrapped on the areas where the sol-gel network contains the organophosphate cross-linked with the organopolysiloxanes. The solvent finds more difficulties to escape from these areas and generates these spots.

Also, the water contact angle of coatings was measured to evaluate if the addition of MOX altered the hydrophilic/hydrophobic features of the surfaces. The obtained values are shown in Table 5.19. It can be observed that coatings kept their hydrophilic/hydrophobic features when adding MOX to the formulation. The high values of the water contact angle of the coatings, which are very close to 90 degrees, are expected to ensure the prevention of bacterial adhesion, which will be evaluated in Chapter 6 [5].

The topography and roughness of the bare metal and the coated TiPM samples were studied by AFM measurements. Figure 5.22 shows AFM images and the variation on the Y-axis by means of distance obtained on a defined line.

Table 5. 19 RMS roughness values and thickness of the coatings P, A25 and A50

Material	RMS (nm)	Thickness (μm)	Water contact angle ($^\circ$)
TiPM	292.9 ± 25.4	--	48.7 ± 5.0
P	14.5 ± 4.8	12.0 ± 0.8	79.3 ± 3.4
A25	6.3 ± 2.5	16.5 ± 1.3	82.0 ± 2.2
A50	11.4 ± 2.4	12.4 ± 0.5	80.4 ± 2.7

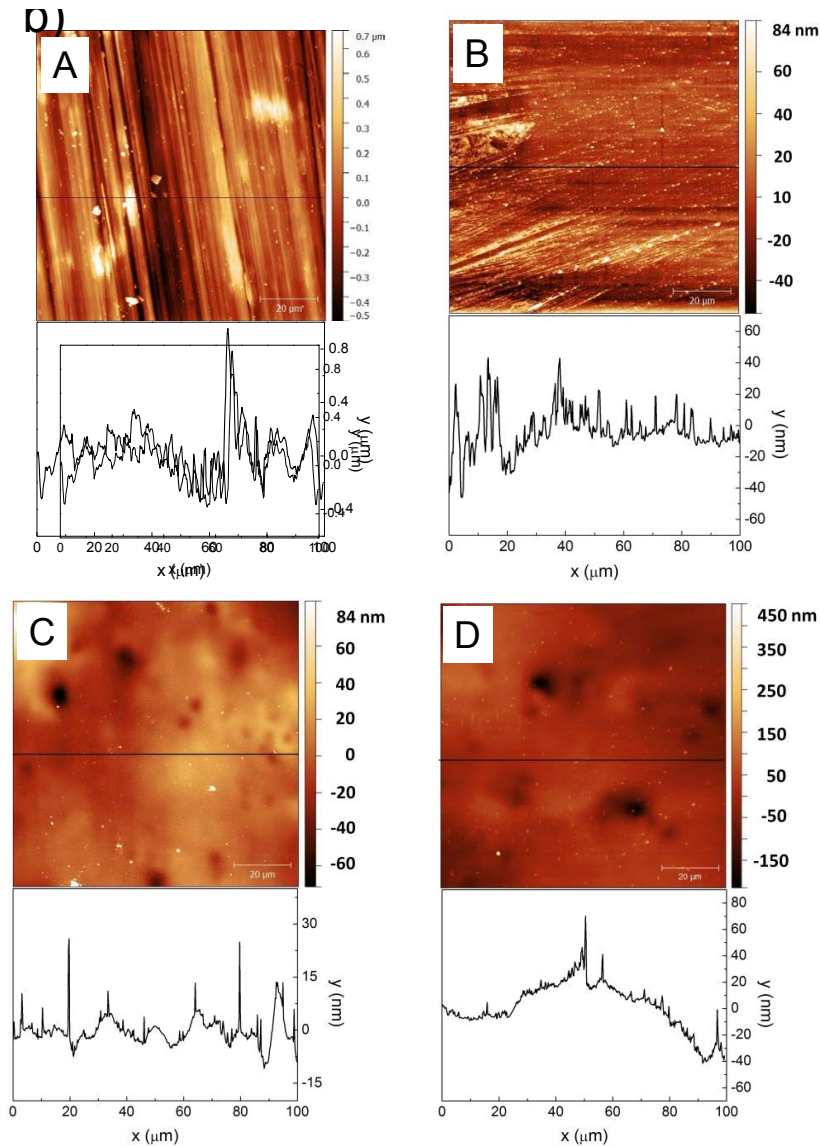


Figure 5. 22 (top) Topographical AFM images of A) Ti, and coatings B) P, C) A25, and D) A50. (bottom) Plot of selected cross-section lines from the images

Table 5.19 summarizes the root mean square roughness (RMS) calculated from the profile line defined on each image. RMS roughness of the bare metal is shown for the sake of comparison. Coated samples presented comparable RMS roughness between each other and reduced the roughness of the substrate one order of magnitude. The thickness of the coatings was also found to be similar and ranged between 12.0 and 16.5 μm . Despite the spherical topography of the coatings, their roughness remained on the nano-meter scale.

5.3.5 CELLULAR STUDY

Cellular studies were performed on the materials loaded with MOX to study the influence of the antibiotic on the cytotoxicity and the proliferation of cells. The material non-bio-functionalized material with MOX, P, was also evaluated and taken as the reference material. Control tests were performed in the absence of coating.

The **cytotoxic** results are shown in Figure 5.23(A) and demonstrated that the designed material did not induce cytotoxicity to the tested cells. All specimens showed almost 100% of viability. This proved that sol-gel coatings showed non-cytotoxicity, which is a critical requirement for biomaterials.

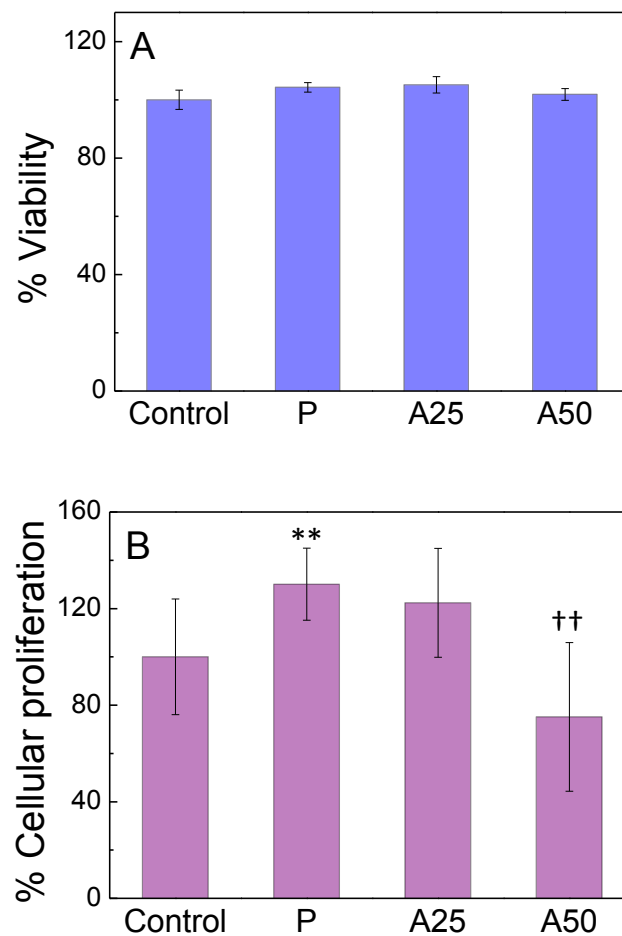


Figure 5. 23 A) Viability percentage and B) proliferation of MC3T3-E1 cells on the control and coatings P, A25 and A50. Control was considered in the absence of coating.

** : Probability ($p < 0.01$) for statistical contrast between control and coating P

†† : Probability ($p < 0.01$) for statistical contrast between coating P and coating A50

Figure 5.23 (B) depicts results of the **proliferation of cells** on the different systems. It was observed that the unloaded sol-gel coating (P) and the coating loaded with the lowest quantity of MOX (A25) had higher or similar cell proliferation than the control. An increment of the cellular proliferation in the presence of the materials can be explained by the addition of tris(trimethylsilyl) phosphite. This was already observed during the bio-functionalization with the organophosphite (section 5.2.4, Chapter 5). The cellular proliferation however, decreased with the increment of antibiotic (A50). But when taking into account the error bars it was observed that these differences were not significant. The statistical study performed between the coating P and the control (test without coating) revealed that the probability of coating P to enhance the proliferation of cells was small ($p < 0.01$). Also, the statistical study confirmed that between coating A50 and P the differences were also not relevant ($p < 0.01$). Indeed, it can be concluded with this study that the concentration of MOX did not compromise the proliferation of cells.

5.3.6 CONCLUSIONS

The bio-functionalization of the two coatings with **moxifloxacin** (MOX) was successfully achieved. The quantities of MOX added to the coating were: 25 mg/20.3 ml of sol and 50 mg/20.3 ml of sol. The following conclusions can be drawn from this study:

- (1) The additions of MOX did not modify the evolution of the reaction. Only the **viscosity** slightly **increased** due to a higher growth and connection of particles. The obtained values of viscosity however, were appropriated (1-10 mPa·s) for the deposition of sols on TiPM.
- (2) The **surface features** of the MOX-loaded coatings presented **similar** properties than the MOX-free coating (P). These surface features are expected to assist the **prevention and treatment of bacterial adhesion**.
- (3) Moreover, the **non-cytotoxicity** and the **proliferation of cells** were confirmed in the presence of the designed materials.

REFERENCES

- [1] H. Rahimi, R. Mozaffarinia, A. Hojjati Najafabadi, R. Shoja Razavi, and E. Paimozd, "Optimization of process factors for the synthesis of advanced chrome-free nanocomposite sol-gel coatings for corrosion protection of marine aluminum alloy AA5083 by design of experiment," *Prog. Org. Coatings*, vol. 76, no. 2–3, pp. 307–317, 2013.
- [2] D. Dutta, "Optimization of process parameters and its effect on particle size and morphology of ZnO nanoparticle synthesized by sol-gel method," *J. Sol-Gel Sci. Technol.*, vol. 77, no. 1, pp. 48–56, 2016.
- [3] Y. Tao, M. M. Ba-abbad, A. Wahab, N. Hanis, H. Hairom, and A. Benamor, "Synthesis of minimal-size ZnO nanoparticles through sol – gel method: Taguchi design optimisation," *JMADE*, vol. 87, pp. 780–787, 2015.
- [4] J. Gallo, M. Holinka, and C. S. Moucha, "Antibacterial surface treatment for orthopaedic implants," *Int. J. Mol. Sci.*, vol. 15, no. 8, pp. 13849–13880, 2014.
- [5] I. V Sukhorukova, A. N. Sheveyko, P. V Kiryukhantsev-korneev, and I. Y. Zhitnyak, "Toward bioactive yet antibacterial surfaces," *Colloids Surfaces B Biointerfaces*, vol. 135, pp. 158–165, 2015.
- [6] C. P. Stallard, K. A. McDonnell, O. D. Onayemi, J. P. O’Gara, and D. P. Dowling, "Evaluation of protein adsorption on atmospheric plasma deposited coatings exhibiting superhydrophilic to superhydrophobic properties," *Biointerphases*, vol. 7, no. 1–4, pp. 1–12, 2012.
- [7] S. Ghalme, A. Mankar, and Y. J. Bhalerao, "Optimization of wear loss in silicon nitride (Si₃N₄)– hexagonal boron nitride (hBN) composite using DoE – Taguchi method," *Springerplus*, 2016.
- [8] A. A. El hadad, D. Carbonell, V. Barranco, A. Jiménez-Morales, B. Casal, and J. C. Galván, "Preparation of sol-gel hybrid materials from γ -methacryloxypropyltrimethoxysilane and tetramethyl orthosilicate: study of the hydrolysis and condensation reactions," *Colloid Polym. Sci.*, vol. 289, no. 17–18, pp. 1875–1883, 2011.
- [9] R. M. A. Sumio Sakka, Ed., *Handbook of sol-gel science and technology. 2. Characterization and properties of sol-gel materials and products*, Springer S. 2005.
- [10] M. Criado, I. Sobrados, and J. Sanz, "Polymerization of hybrid organic-inorganic materials from several silicon compounds followed by TGA/DTA, FTIR and NMR techniques," *Prog. Org. Coatings*, vol. 77, no. 4, pp. 880–891, 2014.
- [11] N. S. Tomer, "Oxidation, Chain Scission and Cross-Linking Studies of Polysiloxanes upon Ageings," *Open J. Org. Polym. Mater.*, vol. 02, no. 02, pp. 13–22, 2012.
- [12] G. Camino, S. M. Lomakin, and M. Lagueard, "Thermal polydimethylsiloxane degradation. Part 2. The degradation mechanisms," *Polymer (Guildf)*, vol. 43, no. 7, pp. 2011–2015, 2002.
- [13] M. Hernández-Escolano, M. Juan-Díaz, M. Martínez-Ibáñez, a. Jimenez-Morales, I. Goñi, M. Gurruchaga, and J. Suay, "The design and characterisation of sol-gel coatings for the controlled-release of active molecules," *J. Sol-Gel Sci. Technol.*, vol. 64, no. 2, pp. 442–451, 2012.
- [14] F. Zhang, J. Dai, A. Wang, and W. Wu, "Investigation of the synergistic extraction behavior between cerium (III) and two acidic organophosphorus extractants using FT-IR, NMR and mass spectrometry," *Inorganica Chim. Acta*, vol. 466, pp. 333–342, 2017.
- [15] X. Wu, K. Gong, G. Zhao, W. Lou, X. Wang, and W. Liu, "Mechanical synthesis of chemically bonded phosphorus-graphene hybrid as high-temperature lubricating oil additive," *RSC Adv.*, vol. 8, no. 9, pp. 4595–4603, 2018.
- [16] B. Journal, L. Dong, W. Li, X. Zhou, Q. Kang, and W. Shen, "Liquid – Liquid Extraction of Matrine Using Trpo / Cyclohexane Reverse," vol. 26, no. 02, pp. 415–425, 2009.
- [17] V. B. and O. E. J. Schraml, M. Kvicalová, L. Soukupová, "Benzhydroximic acids - NMR study of trimethylsilyl derivatives," *J. Organomet. Chem.*, vol. 597, no. 1–2, pp. 200–205, 2000.

- [18] F. Uhlig and D. Dortmund, "Si NMR Some Practical Aspects," *Inorg. Chem.*, vol. 2, no. 46, pp. 208–222, 2000.
- [19] R. R. Lalmrahny, "The Michaelis-Arbuzov Rearrangement," pp. 415–430, 1981.
- [20] F. Varanda, M. J. Pratas De Melo, A. I. Caço, R. Dohrn, F. A. Makrydaki, E. Voutsas, D. Tassios, and I. M. Marrucho, "Solubility of antibiotics in different solvents. 1. Hydrochloride forms of tetracycline, moxifloxacin, and ciprofloxacin," *Ind. Eng. Chem. Res.*, vol. 45, no. 18, pp. 6368–6374, 2006.

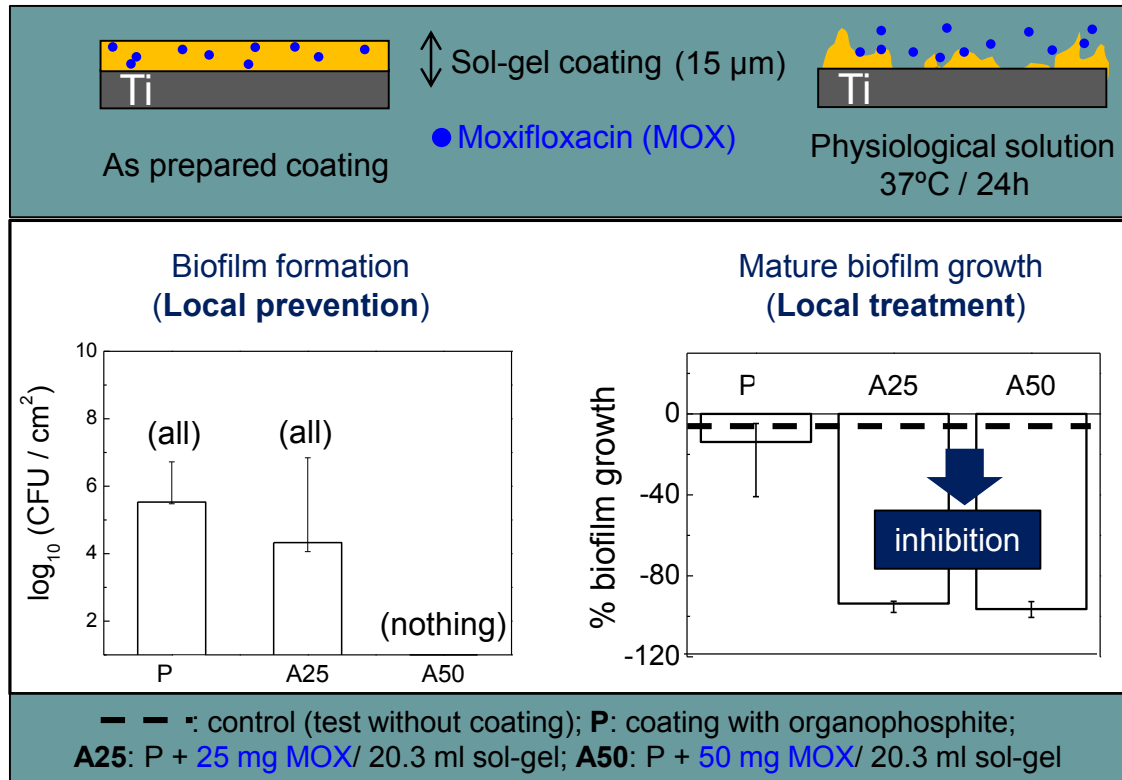
CHAPTER 6

ELECTROCHEMICAL CHARACTERIZATION

ABSTRACT.....	121
6.1 MATERIALS	123
6.2 ELECTROCHEMICAL CHARACTERIZATION.....	124
6.3 MICROBIOLOGICAL AND CELLULAR STUDY.....	138
6.4 CONCLUSIONS	142
REFERENCES.....	143

6. ELECTROCHEMICAL CHARACTERIZATION

ABSTRACT



A novel antibiotic-loaded sol-gel coating was developed to provide titanium with osseostimulating and antibacterial properties. The antibiotic (moxifloxacin) is locally released while the sol-gel coating is gradually degrading. The degradation kinetics of the coatings was studied using the Scanning Electrochemical Microscopy (SECM) and the Electrochemical Impedance Spectroscopy (EIS). It was observed that the degradation rate of the sol-gel coating increased with the concentration of antibiotic. Besides, the microbiological study showed that the sol-gel coatings inhibited the development of mature bacterial biofilm. The concentration of antibiotic was found to exert a strong influence on the degradation of coatings and the biofilm growth.

6.1 MATERIALS

Coatings with different concentrations of moxifloxacin (MOX) were prepared. A solution of 20.3 ml was prepared as described in section 3.1 of Chapter 3. Prior to the addition of water, which is the reactive inducing the hydrolysis-polycondensation reaction, the organic phase was prepared. The organic phase contains the organopolysiloxanes, the organophosphite and the ethanol. Each compound was added as follows: (1) 17.3 moles of MAPTMS; (2) 34.7 moles of TMOS; (3) 1 mole of tris(trimethylsilyl) phosphite; and (4) 104 moles of ethanol. Finally, 104 moles of water containing MOX were added. MOX was dissolved in the water added to the synthesis because the solubility of MOX in water is higher than in the organic phase (19.6 mg of MOX per 1 ml of water) [1]. The interaction between MOX and the sol-gel is physical because MOX is completely dissolved in the water.

Two coatings with two concentrations of MOX were prepared. One coating was saturated with MOX and contains 50 mg of MOX per solution, which is the highest quantity of MOX than can be dissolved in the water of the synthesis. This coating is identified as A50. The other coating contains 25 mg of MOX per solution and is denoted as A25. Sols were applied to the metallic substrates by dipping them into the solution. Then specimens were dried in a stove at 60°C and 2 bars for one hour. Table 6.1 summarizes the prepared systems. P is the blank coating (without MOX).

The content of MOX in the dried coatings ($m_{\text{MOX-coating}}$) was calculated with Equation 6.1:

$$m_{\text{MOX-coating}} = m_{\text{coating}} \frac{1}{d_{\text{solution}}} \frac{m_{\text{MOX}}}{V_{\text{solution}}} \quad (\text{Equation 6.1})$$

where m_{coating} is the mass of the dried coating calculated as the difference in mass between the uncoated and coated specimen, being 1.4 mg the mean value calculated for both coatings; d_{solution} , the density of the solution (1 g/ml); m_{MOX} , the quantity of MOX added to the synthesis (25 mg in coating A25, and 50 mg in coating A50); V_{solution} , the volume of the prepared sol-gel solution (20.3 ml).

The quantity of MOX contained in each coating is listed in Table 6.1. Coating A25 contains 0.0017 mg of MOX and coating A50 contains 0.0034 mg of MOX.

Table 6. 1 Coatings prepared with different additions of antibiotic (moxifloxacin, MOX)

Identification	MOX (mg)/ 20.3 ml of solution	MOX (mg)/ dried coating
P	--	--
A25	25	0.0017
A50	50	0.0034

6.2 ELECTROCHEMICAL CHARACTERIZATION

The evolution of the surface of the different sol-gel coatings with different concentration of MOX was studied with two electrochemical techniques: a high spatially-resolved one, the **scanning electrochemical microscopy** (SECM) and a conventional averaging technique, the **electrochemical impedance spectroscopy** (EIS). The characterization was performed by immersing specimens in PBS solution (Dulbecco's Phosphate Buffered Saline, Sigma Aldrich, USA) and 37°C.

Scanning Electrochemical Microscopy (SECM)

A selection of 4 maps of each specimen at different immersion times (2, 6, 12 and 24 hours) is depicted in Figure 6.1. The colour scale represents the normalized currents (I_N) measured at the SECM microelectrode. TiPM was evaluated in Chapter 4 but it is depicted in this section again and taken as reference system. The results for TiPM are shown in Figure 6.1(A). Maps showed mainly negative feedback response with normalized currents below 1, which corresponds to non-active behaviour. However, highly localised sites with a positive feedback response ($I_N > 1$) were detected after the first hours of immersion. Active sites increased with the immersion time as well as the normalized currents that reached values of 100. These sites changed on location with time, having a meta-stable behaviour. The amount of active sites increased with the immersion time. These active areas may be associated with local changes on the reactivity of Ti due to the heterogeneities on the natural passive layer that activate and repassivate with time. Nevertheless, there was no indication of stable events formed during the 24 hours of experiment.

For the case of the sol-gel coated samples, all maps (Figure 6.1(B-D)) showed negative feedback response ($I_N < 1$), which is indicative of non-active behaviour. This is expected for sol-gel coatings as the literature reports in a previous work where a similar sol-gel coating was applied on an aluminium alloy [2]. The behaviour of the unloaded sol-gel coating, P, is presented in Figure 6.1(B). The map recorded at 2 hours showed a heterogeneous distribution of currents that changed after 6 and 12 hours of immersion. These changes may be attributed to the heterogeneities of the coating layer and its evolution with time. The degrading mechanism of sol-gel coatings is known to consist of an initial swelling stage due to water uptake, with subsequent delamination and final deterioration of the coating [3], [4]. The changes on the topography of the coating can lead to variations on the tip-substrate distance, and therefore variations on the measured currents on negative feedback. However, the map for the unloaded sol-gel sample (P) at 24 hours showed an additional feature: localised positive feedback signal ($I_N > 1$), which suggests apparition of active sites. This response cannot be attributed to morphological changes because of the high recorded current (mean maximum $I_N \sim 12$). The detection of these localised active sites can be the first evidences of the degradation of the sol-gel coating. Therefore the microelectrode is detecting the response of the titanium substrate underneath, as observed in maps of Figure 6.1(A).

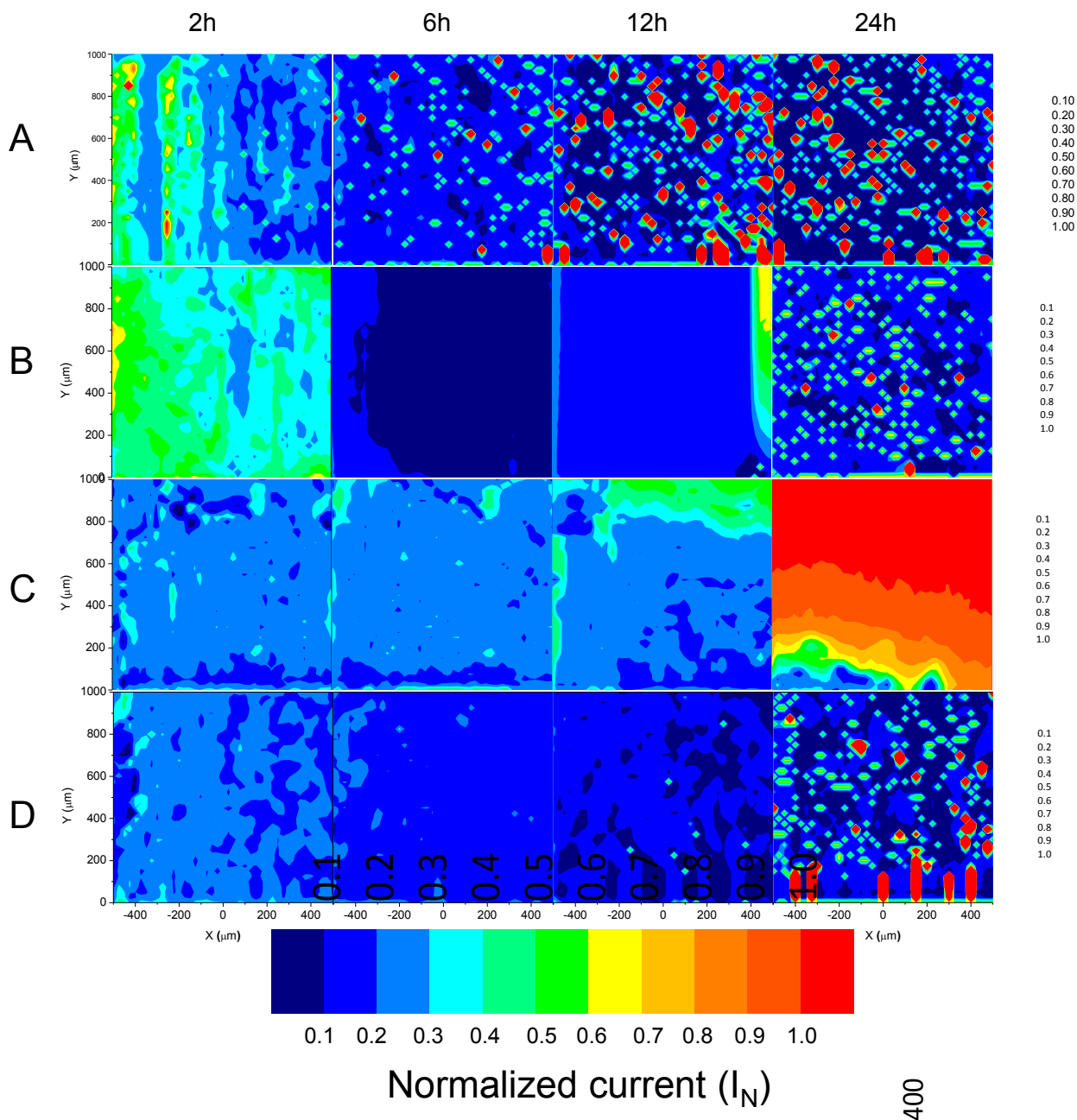


Figure 6. 1 SECM maps of $1 \times 1 \text{ mm}^2$ recorded after 2, 6, 12 and 24 hours exposed to a PBS solution at 37°C on A) TiPM sample and coated samples B) P, C) A25, and D) A50

In Figure 6.1(C) the SECM maps corresponding to sample A25 (low concentration of MOX-antibiotic) are shown. Maps showed similar non-active response with variations on the current distributions with time as it was observed for sample P. However, it was not observed so strong negative feedback as observed for sample P (Figure 6.1(B)), in which maps at 6 and 12 hours showed a strong decrease of the currents. This seems to indicate that sample A25 was under less aggressive degradation. At 24 hours, the map for sample A25 showed currents with active behaviour with higher normalized currents that remained however, close to one (mean maximum $I_N = 1.04$). This may indicate an increase on the distance between

the substrate and the microelectrode, which indicates the loss of sol-gel coating but without revealing the high active response of the titanium.

Figure 6.1(D) shows maps of sample A50, which contains higher concentration of MOX-antibiotic. Maps from 2 to 12 hours of immersion showed non-active response through the whole surface, similarly to sample A25. However, at 24 hours, local active sites were detected with high normalized currents (mean maximum $I_N \sim 930$). The presence of these active sites may be considered as an indication that the sol-gel has degraded leaving the Ti substrate exposed to the physiological solution. This can be interpreted as sample A50 showing faster degradation than samples P and A25 within the 24 hours of immersion. In order to gain some insight into the SECM results, the total active area was estimated with Equation 6.2 and referred as the recorded points with $I_N > 1$ per the total recorded points. Also the mean value of the registered $I_N > 1$ was obtained with Equation 6.3.

$$\% \text{ active area} = \frac{\text{total number of points with } I_N > 1}{\text{total number of points}} \times 100 \quad (\text{Equation 6.2})$$

$$\text{Mean } i_{I_N > 1} = \frac{\text{mean } I_N > 1}{\text{total number of points with } I_N > 1} \quad (\text{Equation 6.3})$$

The percentage of active area and the mean $I_N > 1$ of all the studied materials after 24 hours is depicted in Figure 6.2. The materials affected with localized metastable events, the uncoated TiPM and coatings P and A50, showed similar area affected with $I_N > 1$. Despite presenting similar percentage of active area, the mean $I_N > 1$ of coating A50 was remarkably higher than on the uncoated TiPM and coating P. This reveals more activity in coating A50 than in the other materials. In coating 25 almost the 50% of the area was affected by activity however, the current registered remained nearby one (mean $I_N = 1.04$). The low $I_N > 1$ of coating A25 suggests that the coating is still covering the whole metallic surface and acting as a protective layer, which retards the apparition of metastable events.

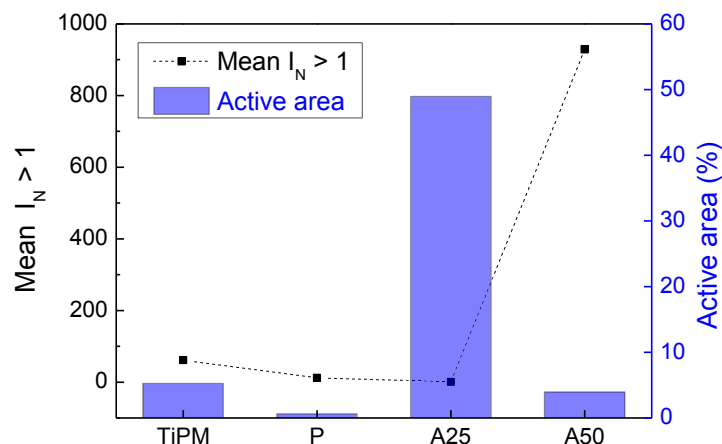


Figure 6. 2 Percentage of active area and mean normalized current with values above 1 calculated from maps of Ti, P, A25 and A50 recorded after 24 hours of exposure to the PBS solution at 37°C

Electrochemical Impedance Spectroscopy (EIS)

To complement the SECM experiments, electrochemical impedance spectroscopy (EIS) measurements were performed during 24 hours of immersion in PBS solution at 37°C. After the EIS experiments, the surface of the coated samples was inspected with SEM microscope. Impedances are depicted in three plots: A) Nyquist plot shows the real and imaginary components of the impedance, B) the logarithmic Bode plot depicts the evolution of the modulus of the impedance with the applied frequency, and C) the semi-logarithmic Bode plot represents the variation of the phase angle with the applied frequency. First, a qualitative analysis of the plots was performed. Then, a quantitative analysis was done using ZView software.

Figure 6.3 shows the EIS data for TiPM at the selected immersion times: 2, 6, 12 and 24 hours. As it was observed in Chapter 4, the barrier features of TiPM improved with the immersion time.

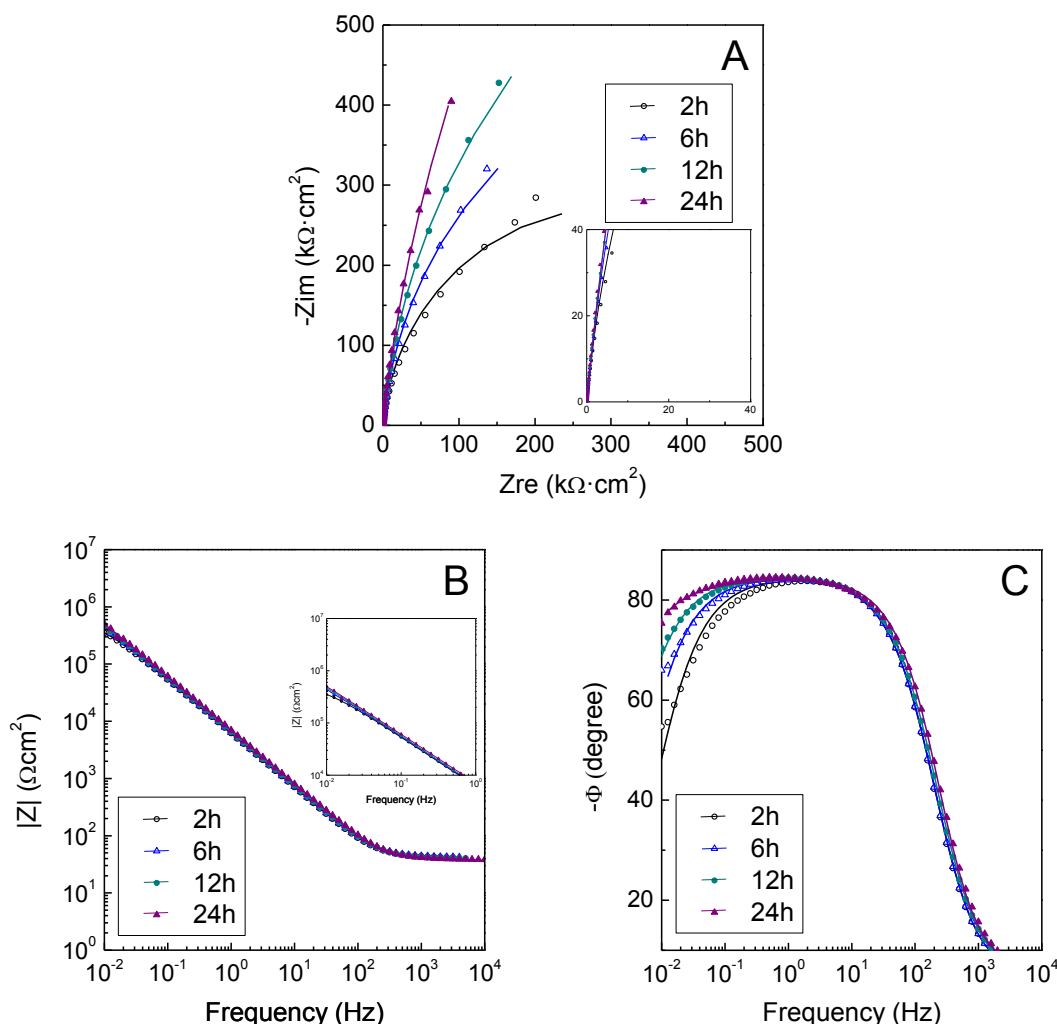


Figure 6. 3 Electrochemical impedance spectra of TiPM after 2, 6, 12 and 24 hours exposed to PBS solution at 37°C

Table 6. 2 Values of the modulus of the impedance ($|Z|$) and the phase angle (Θ) at 0.01 Hz

Material	$ Z $ $\Omega \cdot \text{cm}^2$	Θ (degrees)	$ Z $ $\Omega \cdot \text{cm}^2$	Θ (degrees)	$ Z $ $\Omega \cdot \text{cm}^2$	Θ (degrees)	$ Z $ $\Omega \cdot \text{cm}^2$	Θ (degrees)
Time (h)	2		6		12		24	
TiPM	3.5×10^5	54.7	4.4×10^5	66.0	4.6×10^5	70.4	5.0×10^5	75.3
P	1.7×10^5	61.0	1.9×10^5	66.4	2.1×10^5	71.7	2.4×10^5	73.4
A25	1.9×10^5	41.9	2.4×10^5	47.6	2.1×10^5	44.1	1.3×10^5	21.5
A50	1.5×10^5	49.7	2.1×10^5	69.6	2.3×10^5	75.8	2.5×10^5	79.6

The enhancement of the barrier features of TiPM can be observed with the aperture of the arc in Nyquist plot with time (Figure 6.3(A)). This is reinforced by observing the plot of the modulus of the impedance (Figure 6.3 (B)): the averaging impedance at low frequencies ($|Z|_{0.01\text{Hz}}$) increased with time from 3.5×10^5 to 5.0×10^5 . The values of the impedance at each time are listed in Table 6.2. The capacitive behaviour of TiPM is evidenced with the phase angle plot (Figure 6.3(C)) where it can be observed how the maximum phase angle reaches values close to 90 degrees. These results evidenced that there is not degradation of the Ti substrate. Then the local active sites observed in the SECM maps (Figure 6.3 (A)) did not affect the averaging resistance of the metal.

As it was expected, the presence of the sol-gel coating decreased the reactivity of the titanium surface acting as a protective layer. This was clearly observed in the results of sample P (Figure 6.4). The unloaded coating (P) provided to the metal a barrier against degradation during the duration of the experiments (24 hours) being the averaging impedance barely modified. Contrary to the SECM test, the averaging impedance response did not reveal the response of the metallic substrate despite that the phase angle at low frequencies shifted to higher values and reached values close to the ones registered in TiPM.

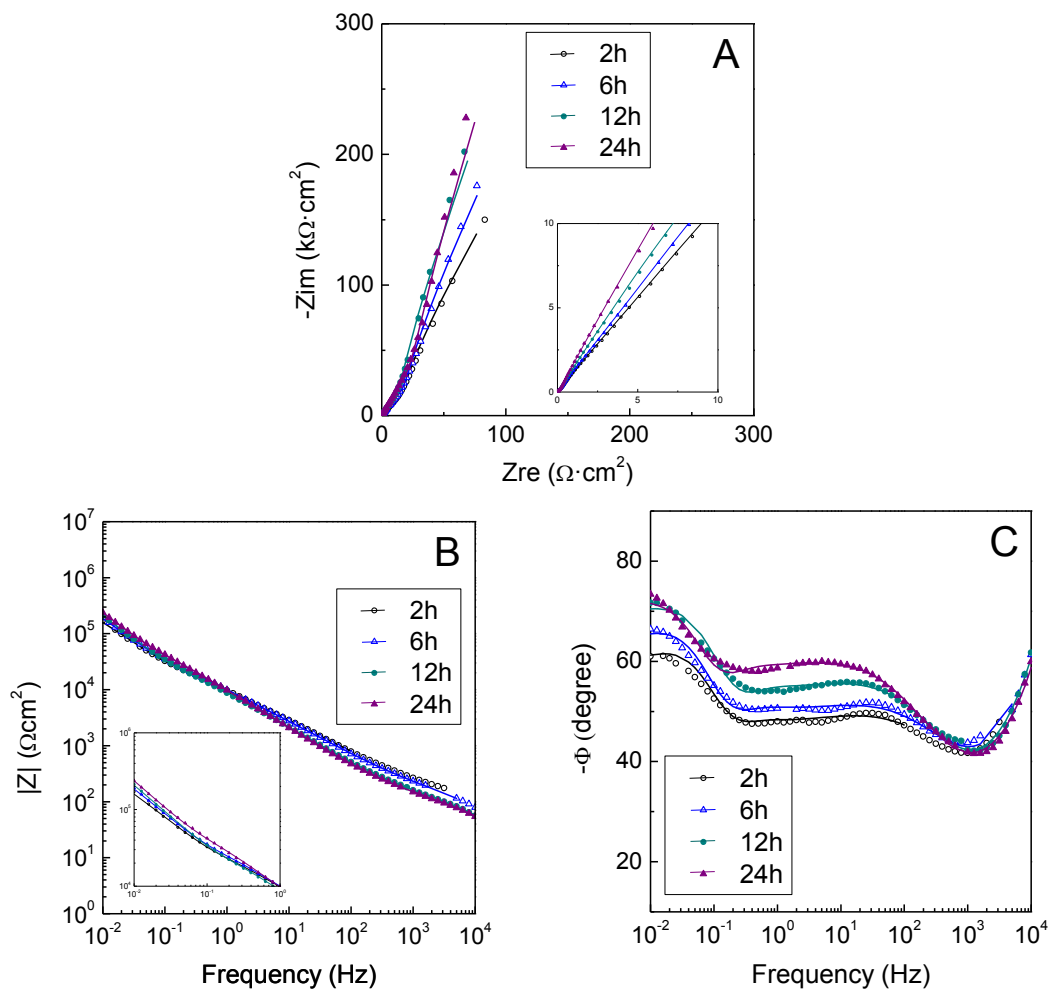


Figure 6. 4 Electrochemical impedance spectra of P after 2, 6, 12 and 24 hours exposed to PBS solution at 37°C

Impedance of the coating with the lower content of antibiotic (A25) is shown in Figure 6.5 and again it was evidenced that the coating acted as a protective layer of the metallic substrate. The presence of the antibiotic however, influenced the behavior of the coating. Coating A25 showed slightly signs of degradation from 2 to 12 hours. The electrochemical response only changed after 24 hours of immersion. The averaging impedance decreased and the phase angle at low frequencies shifted to lower values, being far from the response of the metallic substrate. These results support the SECM results and suggest that the coating is degrading and loosening its protective features but the coating is still covering the substrate.

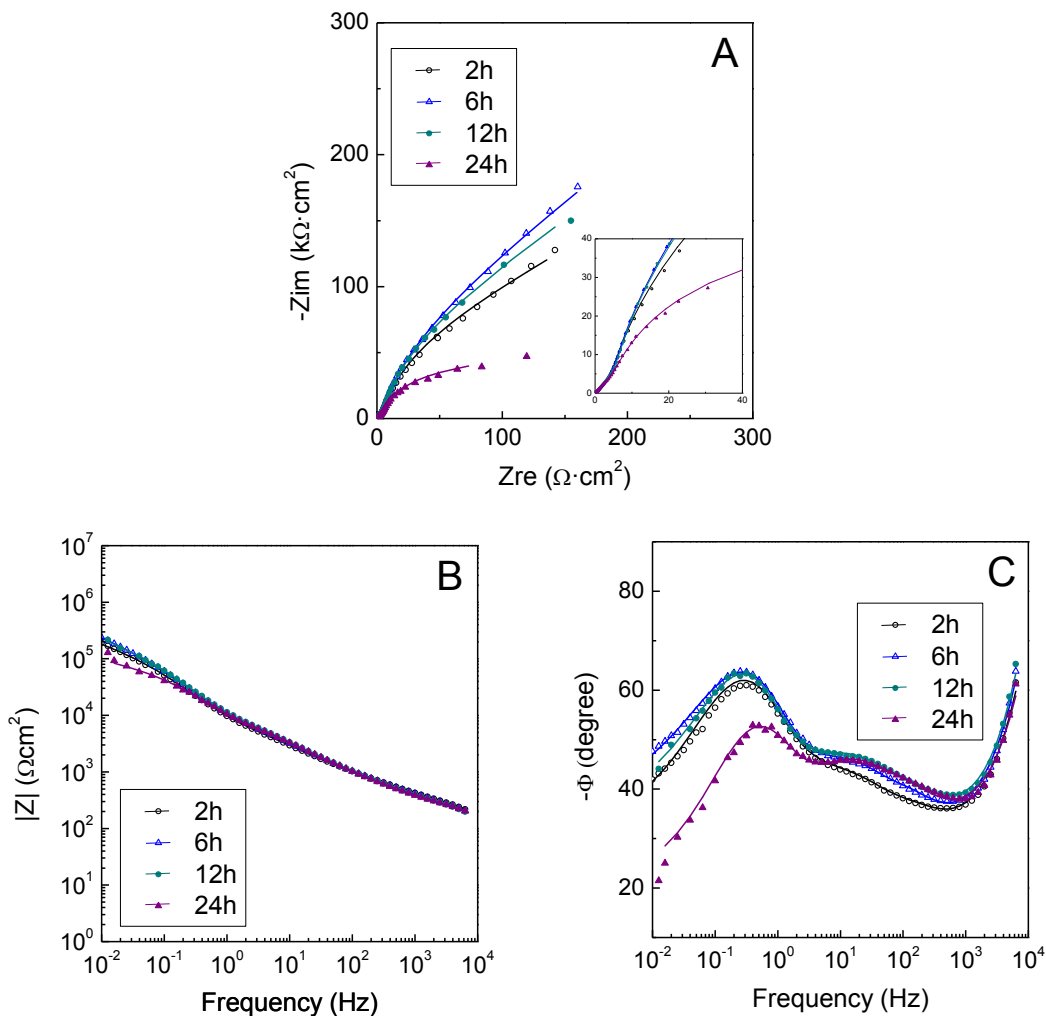


Figure 6. 5 Electrochemical impedance spectra of A25 after 2, 6, 12 and 24 hours exposed to PBS solution at 37°C

In the case of the sample with higher concentration of MOX (A50), the sol-gel showed clear signs of degradation after 1 day of experiment. Plots of coating A50 are shown in Figure 6.6. The behavior of the sample was very similar to the observation on the bare titanium after the same exposure time: in Nyquist plot the arc increased its amplitude with time and in the phase angle plot, the angle shifted to values very close to 90 degrees.

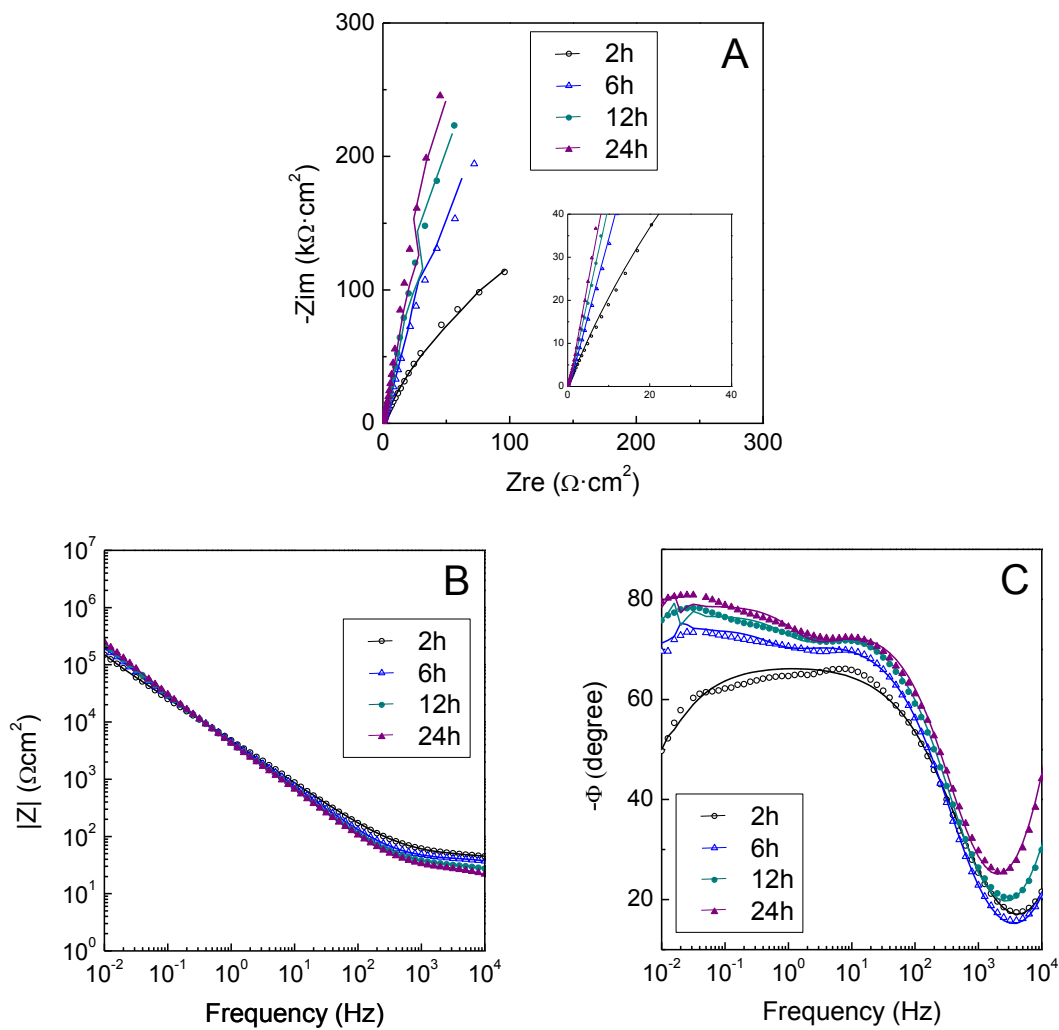


Figure 6. 6 Electrochemical impedance spectra of A50 after 2, 6, 12 and 24 hours exposed to PBS solution at 37°C

The impedance of TiPM was fitted using an **equivalent circuit** (EC) with two constant times placed in parallel. Results of TiPM were previously discussed in Chapter 4 where the electrochemical features of TiPM and the commercial Ti6Al4V alloy were compared. Sol-gel coatings have been assumed to present porosity among the surface. The presence of pores allows the electrolyte to interact with the metal. The EC used to fit the data of the coated specimens is presented in Figure 6.7.

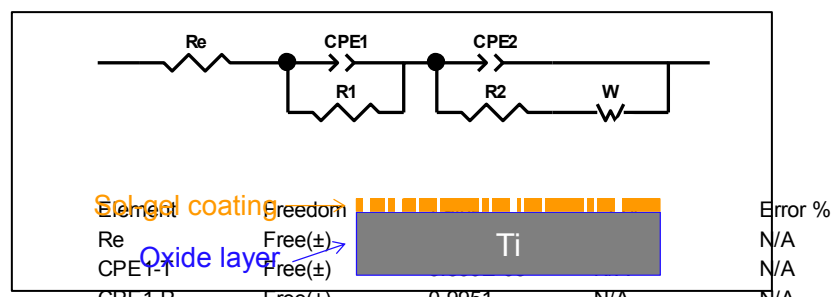


Figure 6. 7 The EC used to fit the impedance data of the coated specimens

Systems **sol-gel coating/metal** provides a bilayer barrier composed by a thin internal layer of the titanium oxide and an unsealed outer layer due to the presence of the sol-gel coating. The employed EC has two relaxation times placed in series because despite that sol-gel coatings are assumed to present pores, the thickness of these coatings are expected to be on the micro-metric scale. Thus, both phenomena are identified consecutively. The following circuit elements are considered in the EC. R_e represents the uncompensated resistance of the testing electrolyte. At high-middle frequencies the constant time corresponds to the dielectric features of the silane layer. The resistance and capacitance of the layer are represented with R_1 and CPE_1 , respectively. The constant time identified at middle-low frequencies corresponds to the interaction of the electrolyte with the metal due to the movement of the species of the electrolyte to the metallic substrate. The resistance of this phenomenon is represented with R_2 and refers to the charge transfer of the species through the metal. The capacitance of this constant time is identified as CPE_2 and is ascribed to the double layer phenomenon. A circuit element, a finite length Warburg element (W), to account for diffusional process is added to the EC. In both constant times a constant phase element (CPE) was employed instead of a pure capacitor (C) to take into account the intrinsic non-homogeneities of the coating and the metallic surface. This element is described with the Equation 6.4:

$$Z_{(CPE)} = \frac{1}{Y_0 (j\omega)^n} \quad \text{(Equation 6.4)}$$

where ω is the angular frequency and Y_0 is a constant, and the value of the exponent n indicates the deviation from ideal capacitive behaviour (e.g., when $n = 1$).

Table 6.3 summarizes the circuit elements obtained with the fitting of the specimens. Only values obtained after 2 and 24 hours are listed to evaluate first the variation of each material from the starting to the ending of the test.

Table 6. 3 Circuit elements obtained with the fitting of the impedance data of TiPM, and coatings P, A25 and A50 after 2 and 24 hours of immersion in PBS solution at 37°C

Material	TiPM		P		A25		A50	
	2	24	2	24	2	24	2	24
$R_1 / \Omega\text{cm}^2$	21.4	8.1	152.0	185.0	5659.0	3597.0	53.0	36.0
$CPE_1 / \mu\text{Fcm}^{-2}$	12.9	2.4	2.7	37.4	24.9	16.8	0.2	1.5
n_1	--	--	0.748	0.494	0.655	0.776	0.921	0.852
$R_2 / \Omega\text{cm}^2$	6.3×10^5	3.2×10^6	3.4×10^4	1.2×10^4	1.1×10^3	2.1×10^3	4.0×10^5	1.2×10^4
$CPE_2 / \mu\text{Fcm}^{-2}$	15.9	23.1	30.5	22.2	13.3	53.2	53.6	41.5
n_2	0.881	0.933	0.583	0.733	0.358	0.164	0.747	0.859
$\text{Chi-Sqr} \times 10^{-3}$	1.3	0.8	1.1	0.3	0.7	0.9	0.6	0.9

The good agreement between fitted and measured data is ensured because a chi-square smaller than 10^{-3} is obtained during the fitting [5]. The values of the resistance of the electrolyte, R_e , are not showed because values are incoherent and masked by R_2 , which is many orders of magnitude greater than R_e [5].

The **resistance of the coatings** (R_1) decreased from 2 to 24 hours as expected for sol-gel coatings that degraded in contact with an aqueous solution. The variation of R_1 with time is depicted in Figure 6.8(A). The averaging resistance of coating A50 reached values close to the ones registered in TiPM since the beginning of the EIS test. The resistance of coating P presented also stable values but the values were higher than the ones registered in coating A50. The coating with the lowest content of antibiotic (A25) showed meanwhile, a resistance 1-fold higher the ones registered in the other coatings. Despite these results correlate well with the SECM tests, the spatially-resolved technique, the SECM, allowed distinguishing the presence of coating in the specimen A50 at the beginning of the test. The SECM identified that between 12 and 24 hours the coating A50 started to degrade and revealed the response of the metallic substrate.

The evolution of the **capacitance of the coatings** (CPE1) with time is shown in Figure 6.8(B) and all the coatings showed similar values. The CPE1 of the silane coating can be estimated with the parallel plate capacitance approximation:

$$CPE1 = \frac{\epsilon\epsilon_0 A}{d} \quad (\text{Equation 6.5})$$

where $\epsilon_0 = 8.85 \times 10^{-10} \text{ F}\cdot\text{cm}^{-1}$; ϵ is the permittivity of the coating, which is assumed to be 2 [6]; d is the thickness (cm) of the coating whose values ranged between 12.0 and 16.5 μm (section 5.3.4, Chapter 5); and A (cm^2) is the area of the tested coating.

The calculated CPE1 of coatings is $1.24 \times 10^{-6} \text{ F}\cdot\text{cm}^{-2}$, which is one order of magnitude more ($10^{-5} \text{ F}\cdot\text{cm}^{-2}$) the CPE1 obtained with the fittings. This difference suggests that coatings are porous and permit the penetration of the electrolyte through the pores. The CPE1 values registered are close to the ones obtained in the uncoated metal. The values of CPE1 of coatings doped with MOX (A25 and A50) remained stable while the values of P increased after 12 hours immersed in PBS solution, meaning that coating P evidenced processes of degradation after 12 hours. The CPE1 of coating A50 was similar to the one registered in TiPM since the beginning of the test suggesting either coating A50 presented large pores that allowed to register the response of the metal or coating A50 was completely degraded.

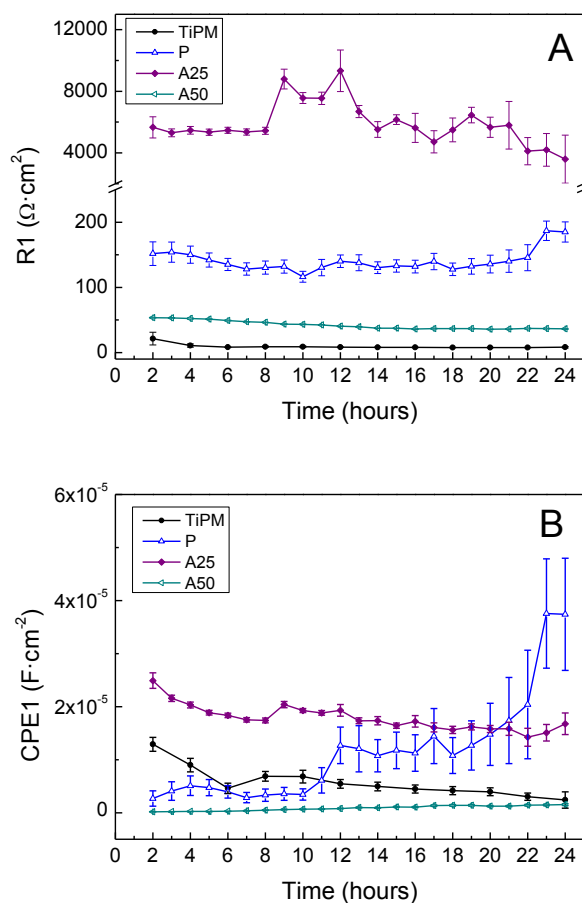


Figure 6. 8 Evolution with time of the EC circuit elements, (A) the resistance and (B) the capacitance, of the constant time registered at high-middle frequencies

The evolution of the circuit elements, the resistance (R2) and the capacitance (CPE2), of the second constant time is depicted in Figure 6.9. The **charge transfer resistance** (R2) is associated with the kinetically-controlled electrochemical reactions involving electrons and ions that either enter to the metal or diffuse to the electrolyte. The R2 of the coatings was 2-3 orders of magnitude lower the one of TiPM because the presence of the coatings hinders the electrochemical reactions with the metallic substrate. As it was observed with SECM, metastable events of the uncoated TiPM increased with the immersion time. This induces an increase of R2 from 2 to 24 hours due to the pronounced formation and dissolution of the passive layer. Contrary to the stability of R2 found in coatings P and A25, coating A50 showed remarkable variations of R2 with time. At the beginning of the test coating A50 showed similar values to the ones of TiPM. Then, R2 decreased and reached similar values to the ones registered in coatings P and A25. This can be explained as follows: first, coating A50 had similar values to TiPM because coating A50, as it was previously discussed with the evaluation of CPE1 variations, had large pores. Consequently, the oxide layer is exposed and its signal is registered. Then, between 12 and 24 hours, metastable events appeared, as it was observed with SECM results, giving rise to an increase on the corrosion processes accompanied with a decrease of R2.

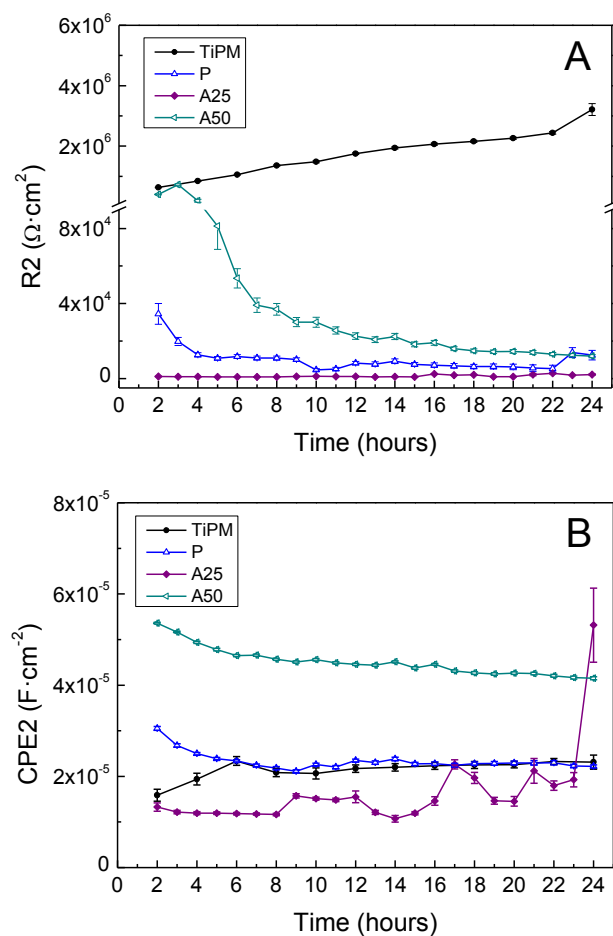


Figure 6. 9 Evolution with time of the EC circuit elements, (A) the resistance and (B) the capacitance, of the constant time registered at middle-low frequencies

As described in Chapter 4 when comparing the metallic substrates, the **corrosion rate** is proportional to CPE2. Coating A25, had the lowest corrosion rate and its CPE2 values varied with the immersion time. At 24 hours the CPE2 of coating A25 reached the highest value of all the tested materials. The instabilities found in coating A25 can be ascribed to variations on the features of the coating during the test, such as process of swelling due to the uptake of water [7]. Results showed that coating A50 was the material that experienced the highest corrosion rate with CPE2 values that doubled the values registered in the other materials. Indeed, the averaging response received supports the results obtained with SECM: despite the surface of coating A50 was less affected with active area ($I_N > 1$) than TiPM at 24 hours, the averaging $i_N > 1$ of coating A50 was found to be the highest (Figure 6.2).

First, the impedance at low frequencies (10 mHz) has been studied to compare the values of coatings with the ones of the metallic substrate. All the coated samples showed similar averaging response with values of $Z_{10\text{mHz}}$ similar to TiPM, with slightly changes after 24 hours. Where the presence and evolution of the sol-gel coatings on the Ti substrate can be elucidated is on the high-middle frequencies range of the Bode plot (Figure 6.(4-6)(B)). The evolution of the **modulus of the impedance at 100 Hz** ($|Z|_{100\text{Hz}}$) of each material with time is represented in Figure 6.10. All coated samples showed higher $|Z|$ than TiPM in this range of

frequencies. Coatings P2 and A25 showed very similar values at 2 hours of immersion, while A50 showed a lower value. This is already an evidence of the differences on the barrier properties of the coated samples. The specimen with higher concentration of MOX (A50) showed lower barrier properties than the rest at short immersion times. After 1 day, the values registered in coating A50 were very close to the ones registered in TiPM, meaning that coating A50 degraded almost completely. The evolution of the impedance of coating P2 at 100 Hz decayed with time while coating A25 did not change. This indicates that while coating P2 and A50 degraded, sample A25 with lower MOX content, is non-significantly affected.

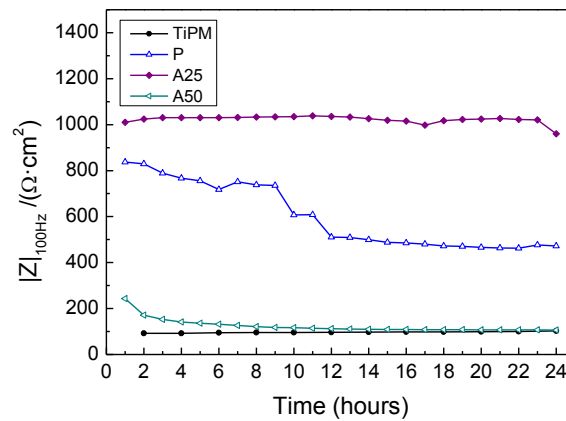


Figure 6. 10 Evolution of the modulus of the impedance at 100 Hz with the immersion time in PBS solution at 37°C of TiPM, and coatings P, A25 and A50

Again, as it was calculated in Chapter 5, the accumulative percentage of the capacitance of the coatings (CPE1) was evaluated using Equation 6.6.

$$\Delta\text{CPE1} = \frac{\text{CPE1}_t - \text{CPE1}_0}{\text{CPE1}_0} \times 100 \quad (\text{Equation 6.6})$$

where CPE1_0 is the capacitance of coatings after 2 hours of exposure to the electrolyte and CPE1_t the capacitance at the different recorded times.

The evolution of CPE1, which is proportional to the **water uptake**, with time is depicted in Figure 6.11. This plot confirmed that coating P and A50 experienced a gradual uptake of water and therefore, subsequent degrading process during the 24 hours of test. Coating A25 meanwhile, barely modified its dielectric features meaning that the coating was only slightly degraded.

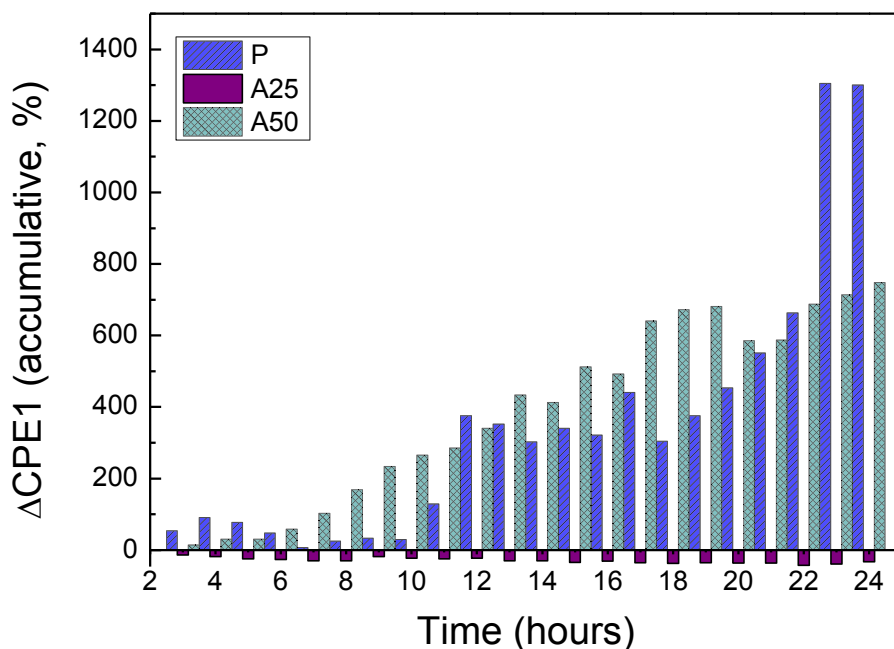


Figure 6. 11 Evolution of the accumulative CPE1 of coatings P, A25 and A50 immersed in PBS solution and 37°C during 24 hours

The EIS study supports the results obtained with SECM. While sample A25 showed scarcely presence of localised active sites, sample A50 showed the highest amount followed by sample P. It seems that after 24 hours, great part of the sol-gel coating of A50 is degraded. In the case of the coating P, it is partially degraded and for A25, it is less affected. This conclusion was confirmed by the inspection of the coated surface after EIS experiments using SEM. The images are shown in Figure 6.12.

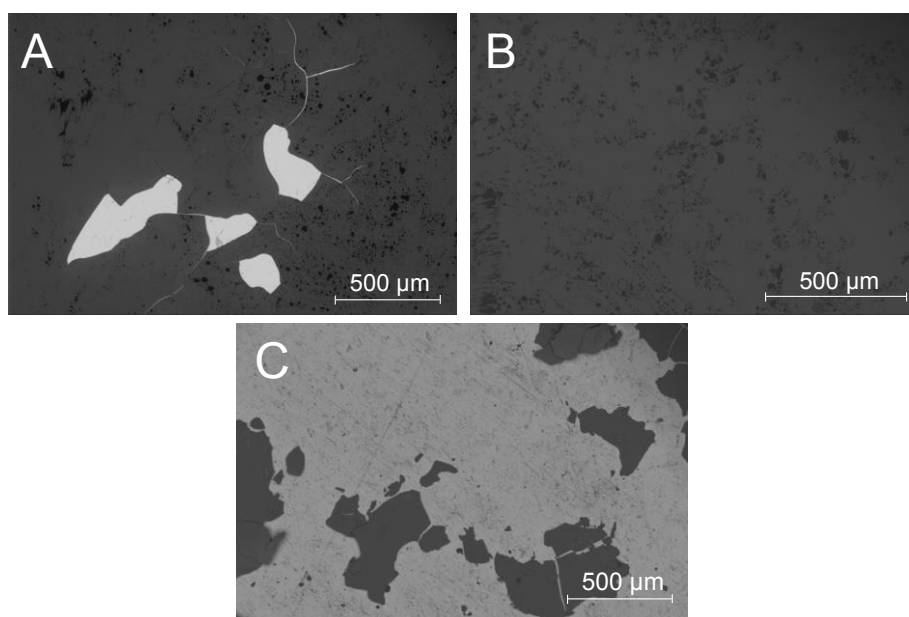


Figure 6. 12 SEM micrographs of coatings A) P, B) A25 and C) A50 after the 24 hours EIS test in PBS solution at 37°C

During the inspection of the surfaces, two contrasts were identified: the grey areas corresponding to the coating (EDS analyses revealed the presence of O, Si and C elements) and the bright areas corresponding to the metallic substrate. Ti was only detected in coatings P and A50. Meanwhile, for sample A25, the sol-gel coating still covered the whole substrate. These observations corroborated the results obtained with SECM and EIS experiments.

6.3 MICROBIOLOGICAL AND CELLULAR STUDY

The bacteria that cover the main etiological agents causing prosthetic joint infections were selected to test the biofilm formation and the treatment of mature biofilm growth [8], [9]. The selected strains for both tests were: *S. epidermidis* ATCC 35984, *S. aureus* 15981 and *E. coli* ATCC 25922.

Biofilm formation (prevention)

Bacteria can present two states during the biofilm growth: sessile bacteria adhered to the material and planktonic bacteria. When bacteria develop the biofilm, some bacteria detach and can be released to the medium as part of the natural development of the biofilm. The concentration of these detached planktonic bacteria estimates the efficiency of the released antibiotic to the medium because in this state microorganisms are more susceptible to antimicrobials than in their sessile state. Figure 6.13 shows the results of the biofilm formation on the reference and the loaded sol-gel coatings. Figure 6.13(A, C and E) shows the bacterial concentration per area unit that are attached to the surface (sessile bacteria) by means of colony forming units (CFU). Figure 6.13 (B, D and F) shows the planktonic bacterial concentration, which is proportional to the absorbance of the supernatant measured at 600 nm.

The microbiological study revealed two responses for the biofilm development and for the planktonic bacterial concentration. The biofilm development response was all-or-nothing for the staphylococci when their biofilms grew in presence of **P or A25 (all) and A50 (nothing)** (Figure 6.13(A and C)). The biofilm development of *E. coli* showed a low progression, which was influenced by the concentration of MOX (Figure 6.13(E)). The statistical study performed in this section compares the bacterial concentrations between each material and if the probability is found below 0.01 or 0.05, the bacterial concentration of the materials has been considered to be considerably different. Thus, it was identified that the bacterial concentration of coating A50 was remarkably different to the concentration on coatings P and A25 for all the tested species ($p < 0.05$). For coating A25 only with *S. aureus* the bacterial concentration was significant different when compared with coating P ($p < 0.05$).

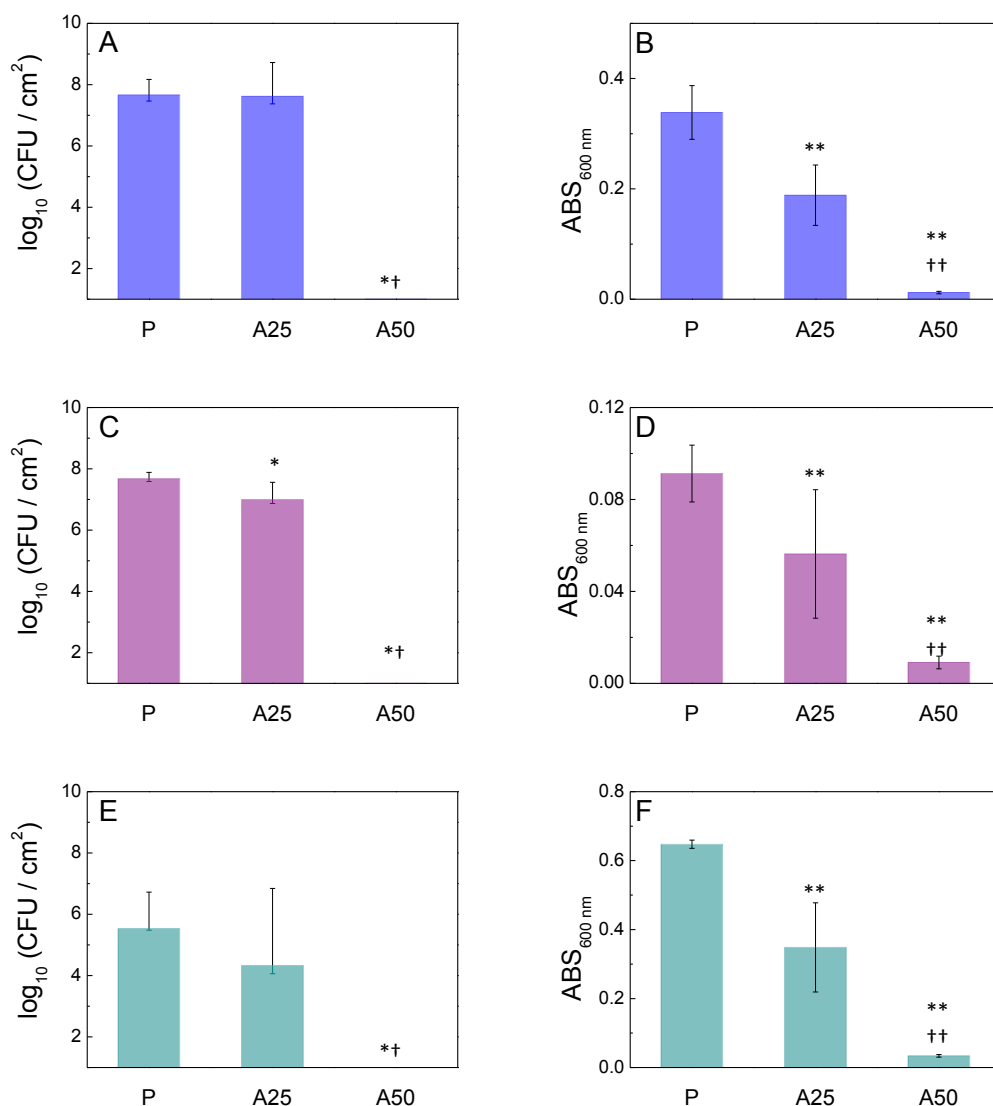


Figure 6. 13 Bacterial biofilm concentration per area unit (CFU) and planktonic bacterial concentration (ABS) of *S. epidermidis* ATCC 35984 (A and B), *S. aureus* 15981 (C and D) and *E. coli* ATCC 25922 (E and F) on coatings P, A25 and A50

- *: Probability ($p < 0.05$) for statistical contrast between coating P and coatings A25 and A50
- ** : Probability ($p < 0.01$) for statistical contrast between coating P and coatings A25 and A50
- † : Probability ($p < 0.05$) for statistical contrast between coating A25 and A50
- †† : Probability ($p < 0.01$) for statistical contrast between coatings A25 and A50

In contrast, the planktonic bacterial concentration was inversely proportional to the concentration of MOX in all the tested strains. Only A50 completely inhibited the formation of biofilm on the surface of the three tested species. A25 showed an intermediate inhibition degree between A50 and P, the latter taken as control. The statistical study confirmed that the bacterial concentrations on all the coatings were significantly different between each other ($p < 0.01$), meaning that the efficiency of the release MOX was higher.

Mature bacterial biofilm (treatment)

When a mature biofilm of each species was treated in the presence of coatings loaded with MOX, the biofilm growth decreased drastically (negative percentage values) when compared with the control (Figure 6.14). The statistical study was performed following the same protocol as in the study of the biofilm prevention. **Coatings loaded with MOX significantly inhibited** the mature biofilm growth (p -value <0.001). The unloaded coating (P2) did not inhibited (positive percentage values) the biofilm growth in the presence of *S. epidermidis* and *S. aureus* (Figure 6.14(A-B)). P showed however, inhibition in the presence of *E. coli* mature biofilm (Figure 6.14(C)). It was confirmed that a strong inhibition to the biofilm growth of the tested strains required the presence of the antibiotic. Though A25 and A50 inhibited in a similar degree the development of *S. epidermidis* and *E. coli* mature biofilm, A50 showed the highest inhibition in the presence of the *S. aureus* mature biofilm (p -value <0.001).

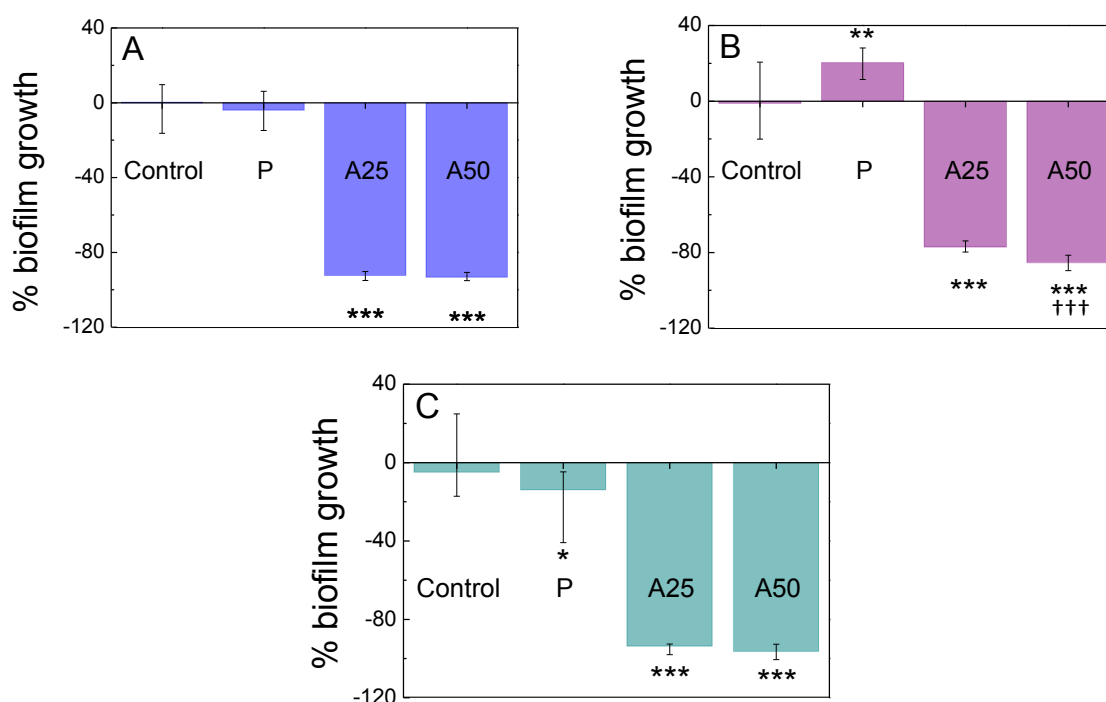


Figure 6. 14 Percentage of biofilm growth respect to the control of A) *S. epidermidis* ATCC 35984, B) *S. aureus* 15981, and C) *E. coli* ATCC 25922 on coatings P, A25 and A50

*: Probability ($p < 0.05$) for statistical contrast between the biofilm growth on the control and coatings

** : Probability ($p < 0.01$) for statistical contrast between the biofilm growth on the control and coatings

***: Probability ($p < 0.001$) for statistical contrast between the biofilm growth on the control and coatings

†††: Probability ($p < 0.001$) for statistical contrast between A25 and A50

For those cases where infection appears, the knowledge of the bacterial species allows selecting the best treatment with the optimal concentration of MOX. From the two concentrations studied in this work, the sample A50, containing higher concentration of MOX, presented the best inhibition against biofilm formation, especially on *S. aureus* strain.

Study of the release of antibiotic

The release of MOX in PBS solution (Dulbecco's Phosphate Buffered Saline, Sigma Aldrich, USA) and 37°C was monitored by ultraviolet-visible absorption spectroscopy. Figure 6.15 depicts the concentration of MOX released from coatings A25 and A50 after 6, 12, 24 and 48 hours of immersion. MOX was progressively detected with time in both coatings. The concentrations detected after 24 and 48 hours were nevertheless, lower than the total amount of MOX incorporated in the sol-gel. Interestingly, the amount of MOX released from the coatings was not very different between A25 and A50 at 24 hours. This suggests that the release of MOX is not directly related to the degradation of the sol-gel coating in this case. This is contradictory to previous studies that used inorganic sol-gel coatings loaded with vancomycin where S. Radin et al. stated a correlation between the release of the antibiotic and the degradation of the sol-gel coating [10].

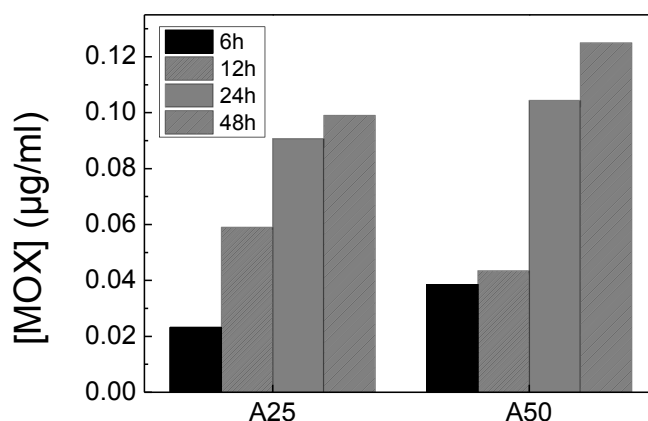


Figure 6. 15 Concentration of MOX released by coatings A25 and A50 after 6, 12, 24 and 48 hours of exposure to 10 ml of physiological solution at 37°C

The bacterial biofilm formation (CFU) tests (prevention) confirmed that A50 showed complete inhibition of the biofilm formation for the three tested bacteria while for A25 this inhibition was less pronounced. However, we did not observe the same agreement for the results of mature bacterial biofilm (treatment), where A25 and A50 showed very similar behaviour. It was expected to have better behaviour on A50 than on A25. This is only true for the case of *S. aureus*. This can be explained because the degradation of the coating was found to be non-proportional to the release of MOX. The antibiotic is physically entrapped into the coating, which is released to the medium. The study of mature bacterial biofilm (Figure 6.14) confirmed that despite A25 and A50 released the same quantity of MOX to the medium, the inhibition of the mature biofilm growth after 48 hours was enough (Figure 6.15). Then, is not only a matter of the liberation of the antibiotic, is also related to the efficiency of MOX.

6.4 CONCLUSIONS

In this work, sol-gel coatings containing moxifloxacin (MOX) as antibiotic were applied on titanium substrates prepared by powder metallurgy technology. The goal was to locally study the **degradation** and **microbiological performance** of the sol-gel coatings as function of the concentration of antibiotic. Two different concentrations were studied, **A25** (25 mg MOX per 20.3 ml sol-gel) and **A50** (50 mg MOX per 20.3 ml sol-gel). The following conclusions can be drawn:

- (1) SECM and EIS experiments demonstrated that the coating with high concentration of antibiotic (**A50**) **degraded faster** than coating with low concentration of antibiotic (A25).
- (2) With SECM maps the evolution of the sol-gel coatings was monitored. Changes of the morphology of the surface were detected that may be associated to the swelling and delamination processes of the coating. The detection of localised **active sites** ($i_N > 1$) was characteristic of the TiPM substrate, and there were an indication that the sol-gel coating degraded and exposed the metallic substrate. However, further research is required to understand in detail the degradation mechanism.
- (3) The release of MOX was found to be non-proportional to the degradation of coatings loaded with MOX. However, the **small quantities released of MOX** were enough to inhibit the growth of mature bacterial biofilms of the tested strains (**local treatment**).
- (4) In terms of local **prevention**, the coating loaded with high concentration of MOX (A50) showed the best bactericidal and broad-spectrum anti-biofilm response.

REFERENCES

- [1] F. Varanda, M. J. Pratas De Melo, A. I. Caço, R. Dohrn, F. A. Makrydaki, E. Voutsas, D. Tassios, and I. M. Marrucho, "Solubility of antibiotics in different solvents. 1. Hydrochloride forms of tetracycline, moxifloxacin, and ciprofloxacin," *Ind. Eng. Chem. Res.*, vol. 45, no. 18, pp. 6368–6374, 2006.
- [2] D. J. Carbonell, A. García-Casas, J. Izquierdo, R. M. Souto, J. C. Galván, and A. Jiménez-Morales, "Scanning electrochemical microscopy characterization of sol-gel coatings applied on AA2024-T3 substrate for corrosion protection," *Corros. Sci.*, vol. 111, pp. 625–636, 2016.
- [3] M. J. Juan-Díaz, M. Martínez-Ibáñez, M. Hernández-Escolano, L. Cabedo, R. Izquierdo, J. Suay, M. Gurruchaga, and I. Goñi, "Study of the degradation of hybrid sol-gel coatings in aqueous medium," *Prog. Org. Coatings*, vol. 77, no. 11, pp. 1799–1806, 2014.
- [4] L. C. Córdoba, M. F. Montemor, and T. Coradin, "Silane/TiO₂ coating to control the corrosion rate of magnesium alloys in simulated body fluid," *Corros. Sci.*, vol. 104, pp. 152–161, 2016.
- [5] A. El Hadad, E. Peón, F. García-Galván, V. Barranco, J. Parra, A. Jiménez-Morales, and J. Galván, "Biocompatibility and Corrosion Protection Behaviour of Hydroxyapatite Sol-Gel-Derived Coatings on Ti6Al4V Alloy," *Materials (Basel)*, vol. 10, no. 2, p. 94, 2017.
- [6] A. Perrotta, S. J. García, and M. Creatore, "Ellipsometric Porosimetry and Electrochemical Impedance Spectroscopy Characterization for Moisture Permeation Barrier Layers," *Plasma Process. Polym.*, vol. 12, no. 9, pp. 968–979, 2015.
- [7] M. Hernández-Escolano, M. Juan-Díaz, M. Martínez-Ibáñez, A. Jiménez-Morales, I. Goñi, M. Gurruchaga, and J. Suay, "The design and characterisation of sol-gel coatings for the controlled-release of active molecules," *J. Sol-Gel Sci. Technol.*, vol. 64, no. 2, pp. 442–451, 2012.
- [8] N. Benito, M. Franco, A. Ribera, A. Soriano, D. Rodríguez-Pardo, L. Sorlí, G. Fresco, M. Fernández-Sampedro, M. Dolores del Toro, L. Guío, E. Sánchez-Rivas, A. Bahamonde, M. Riera, J. Esteban, J. M. Baraia-Etxaburu, J. Martínez-Alvarez, A. Jover-Sáenz, C. Dueñas, A. Ramos, B. Sobrino, G. Euba, L. Morata, C. Pigrau, P. Coll, I. Mur, and J. Ariza, "Time trends in the aetiology of prosthetic joint infections: a multicentre cohort study," *Clin. Microbiol. Infect.*, vol. 22, no. 8, p. 732.e1-732.e8, 2016.
- [9] H. Wisplinghoff, T. Bischoff, S. M. Tallent, H. Seifert, R. P. Wenzel, and M. B. Edmond, "Nosocomial Bloodstream Infections in US Hospitals: Analysis of 24,179 Cases from a Prospective Nationwide Surveillance Study," *Clin. Infect. Dis.*, vol. 39, no. 3, pp. 309–317, 2004.
- [10] S. Radin and P. Ducheyne, "Controlled release of vancomycin from thin sol-gel films on titanium alloy fracture plate material," *Biomaterials*, vol. 28, no. 9, pp. 1721–1729, 2007.

CHAPTER 7

CONCLUSIONS

7. CONCLUSIONS

In this Doctoral Thesis **multifunctional** and **biodegradable sol-gel coatings** for prosthetic devices have been designed. These sol-gel coatings have been tested to fulfill the requirements to act as a prophylactic therapy in order to **prevent** and **treat bacterial infections** associated to joint prostheses. In addition, the developed coatings have been bio-functionalized with a phosphorus compound to enhance the **osseointegration** of the material with the host. The following conclusions can be drawn from this Doctoral Thesis:

- i. The sol-gel matrix has been optimized employing a **Taguchi** method by varying different parameters of the sol-gel synthesis (the molar ratio of the precursors, the reaction time of the sol-gel synthesis and the temperature of the drying step). The number of the prepared routes has been reduced from 27 to 9. It has been concluded that **molar ratio of the silanes** was the parameter of the sol-gel synthesis that contributed more to the variation of the **hydrophilicity/hydrophobicity** of the coatings. From the 9 prepared coatings, one has selected based on its homogenous and uniform surface features and its suitable degrading rate. The selected coating was: Coating S6: 1 mole MAPTMS / 2 moles TMOS, 24 hours of reaction and 60°C of drying temperature.
- ii. The bio-functionalization of the sol-gel coating with **phosphorus-based compounds** to enhance the osseointegration of the biomaterial with the host has been successfully accomplished by adding to the synthesis **tris(trimethylsilyl) phosphite (P)**. The concentration of this compound has been selected as the most suitable based in a compromise between the enhancement of the cellular proliferation and the adhesion of the coating to the substrate.
- iii. The bio-functionalization of the sol-gel coating containing P and the antibiotic, **moxifloxacin (MOX)**, has been achieved with two concentration: 25 mg MOX per 20.3 ml of sol (**A25**) and 50 mg of MOX per 20.3 ml of sol (**A50**). The parameters of synthesis and the surface features of the coatings have been not altered by adding MOX.
- iv. The **degradation kinetics** of sol-gel coatings has been studied with two **electrochemical techniques**: (1) an averaging technique, Electrochemical Impedance Spectroscopy (EIS), and a high spatially-resolved technique, Scanning Electrochemical Microscopy (SECM). The combination of both techniques demonstrated that the coating with more MOX (**A50**) degraded faster than the coating with less MOX (**A25**).
- v. The biological behaviour of coatings loaded with MOX has been evaluated with the study of the **bacterial adhesion** (prevention) and the **mature biofilm growth** (treatment) of the main species that causes infection (*S. aureus*, *S. epidermidis* and *E. coli*). It has been identified that coating A50 prevents better the adhesion of

bacteria than coating A25. Nevertheless, both coating inhibited in a similar degree the growth of mature biofilm. And, despite that the release of MOX has been found to be non-proportional to the degradation of coatings, the quantities of MOX released to the medium were enough to inhibit the growth of mature biofilm. Moreover, the **non-cytotoxicity** and the **cellular proliferation** of coatings have been verified.

CHAPTER 8

FUTURE PERSPECTIVES

8. FUTURE PERSPECTIVES

Due to the importance and relevance of enhancing the performance of prostheses in the biomedical field, the following recommendations to continue the development of sol-gel coatings are presented:

- (1) To introduce into the sol-gel coatings other antimicrobials agents such as antifungal compounds.
- (2) To incorporate into the formulation simultaneously several antimicrobials agents to broaden the efficiency of the prevention and treatment of prosthetic joint infections.
- (3) To perform an in-depth study of the release of the antimicrobials employing techniques with more resolution such as chromatographic techniques.
- (4) To in-depth study the contribution of the finite length Warburg element in the equivalent circuits of the Electrochemical Impedance Spectroscopy (EIS) data.
- (5) To perform *in vitro* test with bacteria and cells simultaneously.
- (6) To perform *in vivo* tests with animals.
- (7) To apply the sol-gel coating to catheters of polymeric nature, which are susceptible to bacterial infections.

